The Use of High-Velocity Air Fuel for Solid-State Additive Manufacturing

Peyman Khamsepour

A Thesis

In the Department of

Mechanical, Aerospace, and Industrial Engineering

Presented in Partial Fulfillment of the Requirements for the Degree of

Doctor of Philosophy (Mechanical Engineering) at

Concordia University

Montréal, Québec, Canada

March 2023

CONCORDIA UNIVERSITY

School of Graduate Studies

This is to certify that the thesis prepared

By: Peyman Khamsepour

Entitled: **The Use of High-Velocity Air Fuel for Solid-State Additive Manufacturing**

And submitted in partial fulfillment of the requirements for the degree of

Doctor of Philosophy (Mechanical Engineering)

Complies with the regulations of the University and meets the accepted standards with respect to originality and quality.

Signed by the final examining committee:

Dr. Ahmed Soliman	Chair
Dr. Tanvir Hussain	External examiner
Dr. Pantcho Stoyanov	External to program
Dr. Mehdi Hojjati	Examiner
Dr. Moussa Tembely	Examiner
Dr. Christian Moreau	Thesis supervisor
Dr. Ali Dolatabadi	Thesis supervisor

Approved by	Dr. Muthukumaran Packirisamy,	Graduate Program Director
March 27, 2023	Dr. Martin Pugh,	Dean

ABSTRACT

The Use of High-Velocity Air Fuel for Solid-State Additive Manufacturing

Peyman Khamsepour, Ph.D.

Concordia University, 2023

Ti-6Al-4V components used extensively in aero engines are prone to damage. When a part is damaged, it can be repaired or replaced. Compared to replacing, repairing methods such as solid-state additive manufacturing processes are more cost-efficient. Among solid-state additive manufacturing methods, cold spray (CS) is more promising because it fabricates samples at high deposition rates without oxidation or phase transformation. Using CS, it is possible to manufacture samples with low porosity levels; however, the existing pores that result from insufficient deformation of the solid-state particles adversely affect the mechanical properties. To enhance sample density, particle deformation should be increased by thermally softening them during deposition. As cold spray cannot deposit particles at elevated temperatures, this thesis proposes using high-velocity air-fuel (HVAF) as a solid-state additive manufacturing technology.

The numerical analysis reveals that through the thermal softening effect, particle deformation will increase by elevating the deposited particle temperature. This allows a denser structure to be fabricated. Nevertheless, the increase in particle deformation does not necessarily indicate better particle adhesion to the substrate. In order for the particle and substrate to adhere better, both the particle and the substrate oxide layer need to be broken and ejected. Particle and substrate oxide layer failures depend on particle velocity and temperature and particle velocity and substrate temperature, respectively.

The inner-diameter HVAF process (ID-HVAF) has been used as a solid-state deposition technique. Results showed that increasing nozzle length and air/fuel pressure enhanced the velocity of in-flight particles and the density of as-sprayed Ti-6Al-4V coatings. Using the spraying conditions that produced the densest coating, the ID-HVAF process was used to fabricate four-mm thick Ti-6Al-4V samples. Heat treatment was required to enhance the mechanical properties of the samples by transforming the brittle α-Ti phase into the more deformable β-Ti phase. Applying heat treatment decreased porosity from 1.18% to 0.98%. Lastly, the results show vanadium oxide presence in both as-fabricated and heat-treated samples. Oxygen content measurements revealed 1.6 wt% oxygen in both samples. This acts as an α-phase stabilizer and negatively affects the hardness of heat-treated samples.

Dedications

To my supportive, kind, and lovely wife, Hedieh

To my beloved supportive parents, Sima and Amir

To my brother, Parham

Acknowledgments

The opportunity to be supervised by Dr. Christian Moreau and Dr. Ali Dolatabadi is one of a lifetime, and I would like to express my deepest gratitude to both. Moreover, I would like to convey my gratitude to Dr. Jorg Oberste-Berghaus and Dr. Maniya Aghasibeig from the National Research Council of Canada (NRC) for entrusting me with this incredible project. My sincere thanks go out to Dr. Martin Pugh and Dr. Ivan Contreras for their support and assistance during my doctoral studies. Also, I would like to thank Miss Leslie Hosein for all her help.

It would be my pleasure to thank my colleagues at the thermal spray research center, especially Dr. Fadhel Benettouil, for all his help and wisdom during each challenge that we encountered in our work. In this regard, I would like to express my gratitude to Saeed Garmeh, Dr. Ali Nozari, and Dr. Navid Sharifi for their assistance and support. Thanks to my dearest friends, Dr. Saeed Mohammadkhani, Dr. Saeed Rahmati, and Farzam Arhami, for their friendship and help. Also, I would like to thank my closest friends, Amir Reza Malekian, Mohammad Reza Soltanloo, and Mahmood Soleimani, for being by my side throughout all the highs and lows of my life.

Thanks to the National Research Council and Concordia University for providing funding and financial support for my research and studies. Moreover, as the holder of the Gina-Cody Award, I would like to express my deepest gratitude to Dr. Gina Cody for generous contribution to our university.

I would like to conclude by thanking my parents, Sima and Amir, for dedicating their lives to me and my brother and helping us to achieve our goals. I would like to express my sincere gratitude to my amazing, supportive wife, Hedieh. There are no words to express how grateful I am to have her by my side every day of my life. Lastly, I would like to extend my gratitude to my brother, Parham.

Co-Authorship

To adhere to the requirements of a manuscript-based format, this thesis has been developed in accordance with these regulations. Coauthored works are therefore included in chapters 3, 4, 5, and 6. Following is a description of the contribution of each coauthor other than the author of this thesis:

Chapter 2 Article 1 "Numerical Simulation of the Effect of Particle and Substrate Pre-Heating on Porosity Level and Residual Stress of As-sprayed Ti-6Al-4V Components", Reprinted from the published article with the DOI of https://doi.org/10.1007/s11666-021-01286-9. Contribution of the Authors:

Peyman Khamsepour: Conceptualization, All the modeling, Analysis of the results, validation, writing the manuscript.

Christian Moreau: Conceptualization, Review & editing the manuscript, supervision, and funding acquisition.

Ali Dolatabadi: Conceptualization, Review & editing the manuscript, supervision, and funding acquisition.

Chapter 3 Article 2 "Effect of Particle and Substrate Pre-Heating on the Oxide Layer and Material Jet Formation in Solid-state Spray Deposition: A Numerical Study", Reprinted from the published article with the DOI of https://doi.org/10.1007/s11666-022-01509-7. Contribution of the Authors:

Peyman Khamsepour: Conceptualization, All the modeling, Analysis of the results, validation, writing the manuscript.

Christian Moreau: Conceptualization, Review & editing the manuscript, supervision, and funding acquisition.

Ali Dolatabadi: Conceptualization, Review & editing the manuscript, supervision, and funding acquisition.

Chapter 4 Article 3 "The Effect of Spraying Parameters of the Inner-Diameter High-Velocity Air-Fuel (ID-HVAF) Torch on Characteristics of Ti-6Al-4V In-Flight Particles and Coatings Formed at Short Spraying Distances", Reprinted from the published article with the DOI of https://doi.org/10.1007/s11666-023-01535-z. Contribution of the Authors:

Peyman Khamsepour: Conceptualization, Experimentations, All the characterizations, Analysis of the results, validation, writing the manuscript.

Christian Moreau: Conceptualization, Review & editing the manuscript, supervision, and funding acquisition.

Ali Dolatabadi: Conceptualization, Review & editing the manuscript, supervision, and funding acquisition.

Jorg Oberste-Berghaus: Conceptualization, Review & editing the manuscript, supervision, and funding acquisition.

Maniya Aghasibeig: Conceptualization, Review & editing the manuscript, supervision, and funding acquisition.

Fadhel Ben Ettouil: Technical support and assisting with preparation of coating samples.

Chapter 5 Article 4 "Tribological and Microstructural Properties of Ti-6Al-4V Samples Produced by Using High-Velocity Air Fuel (HVAF)", In Preparation:

Peyman Khamsepour: Conceptualization, Experimentations, All the characterizations, Analysis of the results, validation, writing the manuscript.

Christian Moreau: Conceptualization, Review & editing the manuscript, supervision, and funding acquisition.

Ali Dolatabadi: Conceptualization, Review & editing the manuscript, supervision, and funding acquisition.

Jorg Oberste-Berghaus: Conceptualization, Polishing the samples, Taking SEM images, Review & editing the manuscript, supervision, and funding acquisition.

Maniya Aghasibeig: Conceptualization, Review & editing the manuscript, supervision, and funding acquisition.

Fadhel Ben Ettouil: Technical support and assisting spraying and manufacturing the coating sample.

Appendix 1 Article 1 "The Effect of Water Layer Covering Substrate Surface on the Deformation of the Impacting Particle Deposited by Liquid Cold Spray", Reprinted from the published article with the DOI of https://doi.org/10.7939/r3-sm40-p514. Contribution of the Authors:

Peyman Khamsepour: Conceptualization, All the modeling, Analysis of the results, validation, writing the manuscript.

Christian Moreau: Conceptualization, Review & editing the manuscript, supervision, and funding acquisition.

Ali Dolatabadi: Conceptualization, Review & editing the manuscript, supervision, and funding acquisition.

Ali Akbarnozari: Conceptualization, Review & editing the manuscript.

Saeed Garmeh: Conceptualization, Review & editing the manuscript.

Appendix 1 Article 2 "The Effect of Water Film Surrounding the Deposited Particle on Bonding Area: A Numerical Study", Accepted in Journal of Thermal Spray Technology. Contribution of the Authors:

Peyman Khamsepour: Conceptualization, All the modeling, Analysis of the results, validation, writing the manuscript.

Christian Moreau: Conceptualization, Review & editing the manuscript, supervision, and funding acquisition.

Ali Dolatabadi: Conceptualization, Review & editing the manuscript, supervision, and funding acquisition.

Ali Akbarnozari: Conceptualization, Review & editing the manuscript.

Saeed Garmeh: Conceptualization, Review & editing the manuscript.

Table of Content

Table of Figures

Table of Tables

List of Abbreviation

Abbreviation	*Meaning (unit)*
CVD	Chemical Vapor Deposition
PVD	Physical Vapor Deposition
TST	Thermal Spray Techniques
HVOF	High-Velocity Oxy-Fuel
HVAF	High-Velocity Air-Fuel
SSAM	Solid-State Additive Manufacturing
ID-HVAF	Inner-Diameter HVAF
CEL	Coupled Eulerian-Lagrangian
HIP	Hot Isostatic Pressure
SLM	Selective Laser Melting
EoS	Equation of State
JC	Johnson-Cook
PTW	Preston-Tonks-Wallace
MZA	Modified Zerilli-Armstrong
VA	Voyiadjis-Abed
MKHL	Modified Khan-Huang-Liang
GZ	Gao-Zhang
ALE	Arbitrary Lagrangian-Eulerian
PEEQ	Equivalent Plastic Strain
TEMP	Temperature
SEM	Scanning Electron Microscope
TEMPMAVG	Average Temperature for the Eulerian Part

ASI	Adiabatic Shear Instability
BSE	Backscatter Electrons
XRD	X-Ray Diffraction
IR	Infrared
EDS	Energy Dispersive Spectroscopy
CoF	Coefficient of Friction

List of Symbols

Symbol	*Meaning (unit)*
v_{crit}	Critical Velocity (m/s)
σ_{TS}	Tensile Strength (MPa)
T_i	Particle Temperature (K)
T_R	Reference Temperature (293 K)
T_m	Melting Point (K)
c_p	heat capacity (J/K)
ρ	Density (Kg/m^3)
F_1	Material Constant
F_2	Material Constant
v_{crit}^{ref}	Reference Critical Velocity (650 m/s)
d_p	Particle Diameter (μm)
d_p^{ref}	Reference Particle Diameter (10 μm)
P	Total Pressure
E_m	Internal Energy per Unit Mass
P_H	Hugoniot Pressure
E_H	Hugoniot Energy
Γ_ρ	Gruneisen Coefficient
Γ_0	Material Constant
ρ_0	Material Constant
ρ	Pressure Stress
η	Nominal Compressive Volumetric Strain Equal to $1 - \rho_0/\rho$

$\rho_0 c_0^2$	The Elastic Modulus at Small Nominal Strains
c_0	Material Constant (m/s)
s	Material Constant
U_s	Shock Velocity (m/s)
U_p	Particle Velocity (m/s)
ε_p	Equivalent Plastic Strain
$\dot{\varepsilon}_p$	Plastic Strain Rate (1/s)
σ	Flow Stress (MPa)
$\dot{\varepsilon}_0$	Reference Strain Rate (1/s)
T_r	Reference Temperature (K)
T_m	Melting Point (K)
T	Particle Temperature (K)
A	Material Constant
B	Material Constant
C	Material Constant
n	Material Constant
m	Material Constant
$\Delta\bar{\varepsilon}$	Equivalent Plastic Strain
$\bar{\varepsilon}_f$	Equivalent Fracture Strain
d_1	Initial Failure Strain
d_2	Exponential Factor
d_3	Triaxiality Factor
d_4	Strain Rate Factor
d_5	Temperature Factor
$\bar{u}^{pl}$	Effective Plastic Displacement

L	Element Length
$\dot{\bar{u}}^{pl}$	Effective Plastic Displacement
$\dot{\bar{\varepsilon}}^{pl}$	Equivalent Plastic Strain Rate
$\bar{u}_f^{pl}$	Effective Plastic Displacement at the Failure Point
$\dot{d}$	Damage Variable Rate

Chapter 1

Introduction and Literature Review

1.1. Background

The components used in industrial applications are always prone to damage [1-4]. It has been reported that most of the time, the damage occurs on the surface of the samples [5-9]. Prior to the use of components in industry, their surface properties and lifespan can be improved by using coatings produced by different methods such as chemical vapour deposition (CVD), physical vapour deposition (PVD), and thermal spray techniques (TST) [10-13]. Even though coatings can enhance surface properties, samples are still susceptible to damage. A damaged part in an industrial machine can adversely affect its functionality; therefore, it is necessary to either replace it or repair it. Currently, repair methods have attracted attention due to their environmental benefits and cost-effectiveness [14]. In a recent study, it was shown that repairing a fractured wind turbine blade can cost up to 30,000 dollars, whereas the cost of replacing it can go up to 200,000 dollars [14]. Given this enormous gap between repair and replacement costs, more attention is being paid to repair methods, such as additive manufacturing processes [15].

As a result of the development of additive manufacturing techniques in the 1980s, components with complex shapes could be manufactured using a variety of materials as feedstock. Depending on the feedstock phase, additive manufacturing methods can be divided into three categories: liquid-based, solid-based, and powder-based as shown in Figure 1.1 [16]. Among all techniques, few methods, including binder jetting, powder bed fusion, sheet lamination, and solid based processes can be used to fabricate metallic samples [16]. Among additive manufacturing methods used to produce metallic samples, selective laser sintering (SLS) is a popular option, which belongs to the category of powder bed fusion methods. Powder bed fusion techniques require melting and altering the phases and properties of the feedstock, which make them appropriate for repairing damaged metallic components [16]. Another additive manufacturing method that can be used for repairing metallic damages components using the deposition of solid-state feedstocks is cold spray (CS) [15].

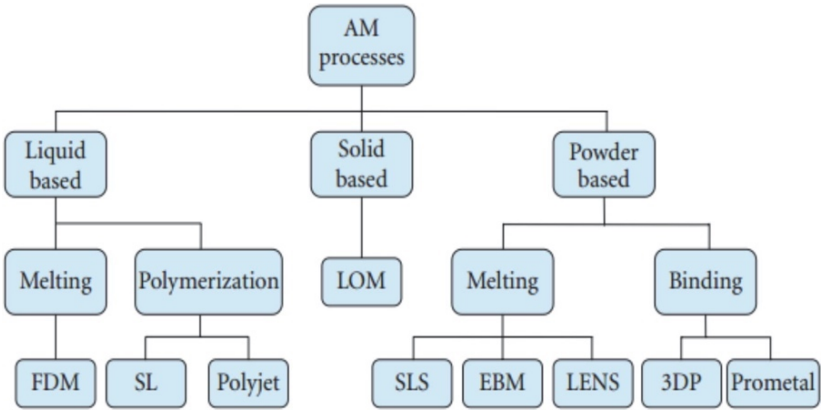

Figure 1.1. Classification of different additive manufacturing methods [16].

CS is mostly known as a thermal spray technique (TST) used to manufacture metallic coatings. In CS, solid-state particles are deposited at high velocity at around room temperature while maintaining their phases [13, 17-18]. Along with CS application as a TST, its high deposition rate makes it a cost-effective solid-state additive manufacturing method widely used to repair damaged metallic components [17-18]. However, as-fabricated CS samples exhibit poor mechanical properties which is resulted from the low adhesion strength among the deposited particles [17-21]. Numerical and experimental studies have shown that low adhesion strength is due to insufficient deformation of the deposited particles [22-23]. A post-deposition heat treatment is usually used to increase the adhesion strength and mechanical properties of CS samples. The other way to improve the sample's density and cohesion is through enhancing particle deformation by increasing particle velocity [24-26]. Both methods reduce the porosity level of samples, but the former is expensive, and the latter does not eliminate all pores which still needs to be followed by a post-spraying heat treatment. To avoid the need of heat treatments for metallic feedstocks with high strength and enhance their deformation upon impact during deposition, further particle deformation must be achieved by thermally softening the particles during the deposition [27]. One of these types of particles that have high strength which makes them hard to deposit using CS is Ti-6Al-4V [28-29]. This titanium alloy has unique set of properties such as high strength and stiffness, great fatigue resistance, and biocompatibility. The best combination of mechanical properties of Ti-6Al-4V has been observed when the microstructure has consisted of $\alpha + \beta$ Ti. The noted properties make this titanium alloy to be used in different industries such as aerospace, automotive, marine, power generation, sports, and biomedical [28]. However, Ti-6Al-4V coating manufactured using CS has low cohesion strength between the deposited particles and high porosity level because of low deformation of deposited particles upon impact. To overcome this issue and reduce the need of post sintering heat treatment for such a high strength material, heating the powders during spraying while keeping them in solid-state might be a good approach for improving the properties of the as-sprayed samples [29]. CS is not capable to elevate deposited particles temperature; therefore, another TST known as high velocity air-fuel (HVAF) can be introduced as an alternative solid-state additive manufacturing process [13]. HVAF is a combustion-based method that produce a flame for deposition using compressed air and combustible gas. Air containing 21 vol% of oxygen would result in a reduction in flame temperature that allows elevated temperature solid-state particles to be deposited with the minimum oxidation [13].

The purpose of this thesis is to gain a comprehensive understanding of how particle temperature affects the porosity level and the mechanical properties of as-fabricated samples. First, a numerical elastic-plastic investigation would be conducted to thoroughly comprehend the effect of preheating on the particle deformation. Then, HVAF would be used to deposit Ti-6Al-4V particles to fabricate thick coatings. Afterwards, the microstructural and tribological properties of as-sprayed Ti-6Al-4V samples will be examined to determine whether HVAF is a suitable solid-state additive manufacturing method for Ti-6Al-4V.

1.2. Solid-State Deposition Methods

The development of thermal spray technologies began in the last century based on using large droplets of materials, such as ceramics, metals, and composite to fabricate coatings [13, 30-46]. These deposited droplets can either be melted, partially melted, or stay solid which depends on the

process temperature, material melting point, and droplet size [13]. Thermal spray processes make it possible to spray particles in a large range of speed and temperature, Figure 1.1. This figure explains that the flame spray, arc spray and plasma spray processes deposit particles at very high temperature. During the last decades new processes at lower temperature and higher speed were developed. HVOF and HVAF in the 80ies, Cold spray in the 90ies and warm spray in the years 2000. Such evolution was motivated by the need to spray dense metal coatings while limiting the particle oxidation during spraying. A more in-depth explanation of solid-state deposition techniques and coating build-up is provided in this section.

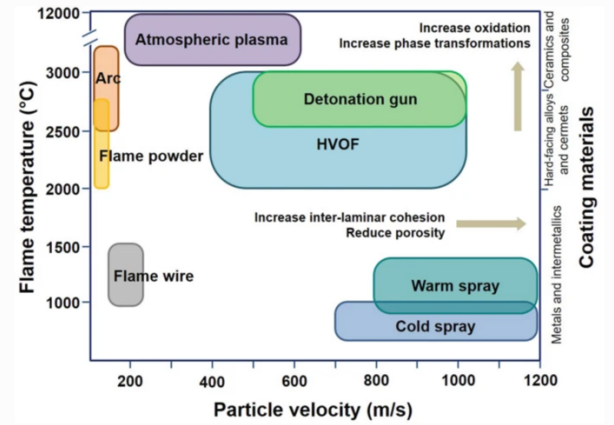

Figure 1.1. A schematic comparison between thermal spray methods [32].

1.2.1. Warm Spray

High velocity oxy-fuel (HVOF) and high velocity air-fuel (HVAF) are combustion-based thermal spray techniques. Using combustible gases and oxygen, both methods produce flames to deposit particles at high velocity and temperature [13]. The main difference between these two methods is the amount of oxygen used to ignite the fuel. Compared to HVAF that uses air (21 vol% O_2), HVOF uses pure oxygen, which leads to a higher particle temperature. As a result, HVOF can increase the likelihood of melting solid particles during the deposition process [13]. In recent years, a new HVOF method called “warm spray” has been developed capable of depositing solid-state particles at elevated temperatures, Figure 1.2. When warm spray is used, high pressure nitrogen is injected into the mixing chamber prior to the convergence-divergence nozzle. When the flow rate of nitrogen is controlled, it would be possible to lower the flame temperature and, consequently, the temperature of in-flight particles. This is because increasing nitrogen flow rate would unbalance the chemical equation between fuel and oxygen [13, 47]. R. M. Molak et al. [48] examined the effect of nitrogen flow rate on the deposition of Ti-6Al-4V by using warm spray. The result of this study illustrated that solid-state particles were successfully deposited and plastically deformed to adhere to the substrate, Figure 1.3. This study also demonstrates that warm spray can produce a dense Ti-6Al-4V coatings. However, they reported that due to the high in-flight particles temperature, solid particles' phases were altered by oxidation, resulting in poor mechanical properties [48]. Thus, to maintain the deposited particle phases, reduce oxidation, and enhance mechanical properties, the flame temperature needs to be reduced.

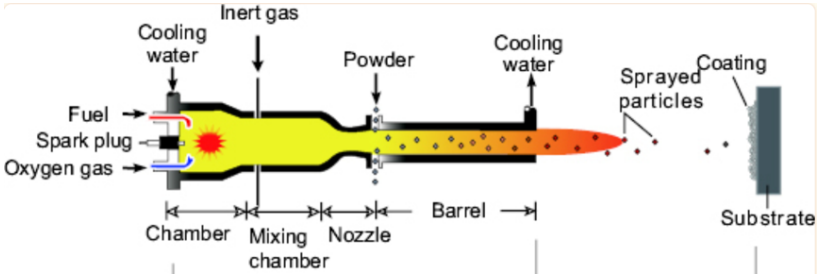

Figure 1.2. A schematic picture of warm spray technology [47].

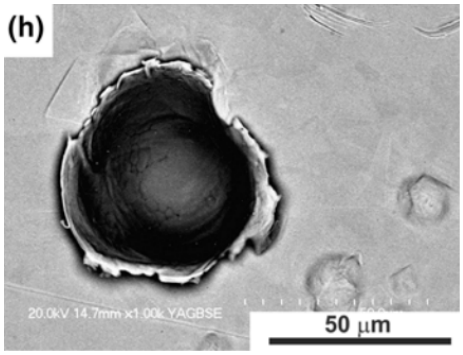

Figure 1.3. A single Ti-6Al-4V particle deposited using warm spray [48].

1.2.2. HVAF

To reduce flame temperature and the cost of operation, J. A. Browning created HVAF in 1982 by using compressed air instead of pure oxygen to generate the flame. HVAF deposition systems were not widely available until Uniquecoat Technology (USA) made the first commercial one in 1999 [49]. In comparison with HVOF, the use of air would result in a reduction in oxygen available for combustion to 21 vol%. The remaining 79 vol% of the air reduces the flame temperature which decreases in-flight particles temperature and increases their velocity [13, 52].

HVAF has been extensively used since the introduction of the commercial HVAF-M3 gun (Uniquecoat Technology, USA) which was introduced by V. E. Baranovski in 2010, Figure 1.4 [49]. An HVAF gun of a more recent generation, referred as inner-diameter HVAF (ID-HVAF) (Uniquecoat Technology, USA), enables manufacturing coatings on the inner surface of a tube. ID-HVAF is a miniature version of the HVAF-M3 with a narrower jet that allows producing samples with near-net shapes [59]. Both guns would ignite compressed air and fuel in the combustion chamber where the feedstock powders are injected axially. As part of HVAF design to increase particle velocity, a convergent-divergent nozzle is used, the shape and dimensions of which significantly influence the coating properties [13, 55, 59]. In addition, the size of the combustion chamber, powder injector, and spraying parameters, including air/fuel pressures, spray distance, and carrier gas pressure affect the properties of the as-sprayed coatings [55].

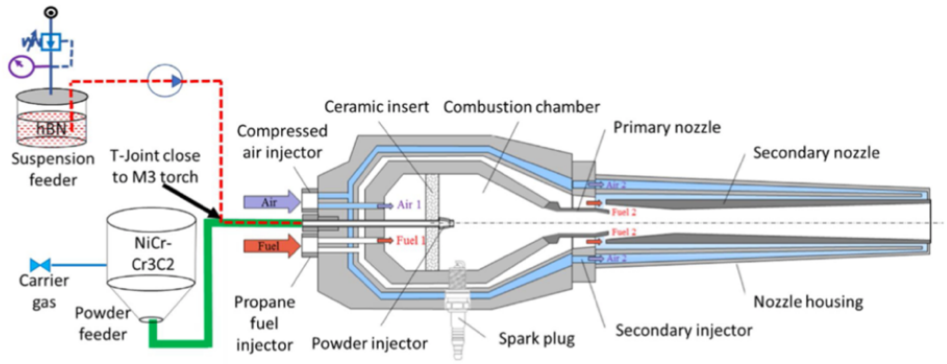

Figure 1.4. A schematic figure of an HVAF process [55].

Many studies have been devoted to investigating either the fundamentals or the potential of the HVAF process to manufacture coatings [51-57]. A. Vardelle et al. [52] studied the ability of HVAF to preserve the crystalline phases of the deposited particles. The purpose of this study was to compare the phases of WC-Co-Cr coatings sprayed by using HVOF and HVAF. Comparing the properties of coatings produced by each method, it was concluded that HVAF coatings are less subjected to phase transformation and oxidation. This is due to reduced oxygen availability and lower particle temperatures during spraying [56-57]. S. Liu et al. [51] found that HVAF deposits can be very dense due to the high velocity of the in-flight particles. In another work conducted by A. K. Gujba et al. [58], WC-based coatings fabricated with HVAF have less than 5% porosity level [58]. In other studies, HVAF has been used to deposit wear resistance materials on substrates to enhance their tribological properties [51-55]. Y. Korobov et al. [53] used HVAF to apply WC-10Cr-4Co coatings on stainless steel substrates with high impact velocity. As a result of the coating's high density, they have great tribological and cavitation resistance [53]. Recently, HVAF has been investigated for its potential to produce wear-resistant composite coatings by depositing liquid feedstocks. A. Ganvir et al. [55] used a HVAF-M3 gun to deposit wear-resistant Cr_3C_2-NiCr coatings. To produce a composite coating, they used a hybrid powder-suspension method that incorporated boron nitride as a solid lubricant. The study showed that the resulting coatings have high wear resistance. They also reported that the coating resistance to wear was further increased by elevating the testing temperature. Due to the success of creating coatings with HVAF to enhance tribological properties, some new attempts used numerical examinations to study the gun's structure effect on the flame stability and HVAF flame's influence on in-flight particles behavior [60-61].

F. Liu et al. [60] studied the effect of each gun's component (Figure 1.5), such as an axial inlet and porous ceramic sheet, on flame stability using computational fluid dynamics (CFD). This work demonstrated that porous ceramic sheet reduces the turbulent dissipation of airflow. It was also shown that, in the combustion chamber, the presence of an axial inlet could increase gas residence time and stroke. Another study using CFD modeling was conducted by H. Jiang et al. [61] to examine the characteristics of in-flight Fe-based alloy particles deposited by HVAF. Their calculation showed that in the combustion chamber, the static pressure and flame temperature of the combustion would be up to 515,000 Pa and 1600 K, respectively. In addition, they found that particle size and nitrogen (carrier gas) flow rate are the two parameters that affect in-flight particle characteristics and nozzle clogging. Their investigation also revealed that smaller particles are

more likely to be affected by gas flow, while larger ones have more inertia and momentum to maintain. In this study, the particle temperature increased significantly when the radial injection diverged from the central axis, meaning that in-flight particle temperature depends on the position of powder injection and turbulent dispersion [61].

In conclusion, aside from the advantages of using HVAF to manufacture coatings, to avoid phase transformation and oxidation of in-flight particles, the process temperature might be further reduced by using the cold spray (CS) technology.

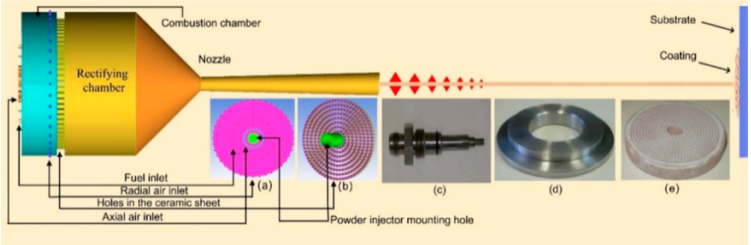

Figure 1.5. The schematic and real-life example of the components of an HVAF gun [60].

1.2.3. Cold Spray

Cold spray (CS) is one of the newest members of the thermal spray family. Because CS process does not contain any combustible gases, it is considered as an environmentally friendly TST [52]. This coating method was accidentally discovered by Dr. Papyrin while he was studying the erosion of the target sample in the 1990s. To further develop this method, Dr. Papyrin and his team successfully deposited a variety of metallic materials onto a variety of substrates [64].

In CS process, particles are deposited using a high-velocity gas, such as air, helium, or nitrogen, as a propellant. This process involves passing a high-pressure gas through an electrically heater to increase the gas temperature up to 1000 °C. By passing the elevated temperature gas through a convergent-divergent de Laval nozzle (Figure 1.6), the gas can reach supersonic speeds in the range of 300-1200 m/s [13, 60-64]. Depending on the location where the particles are injected, whether before or after the nozzle throat, CS can be classified as a high-pressure or a low-pressure process, respectively [13].

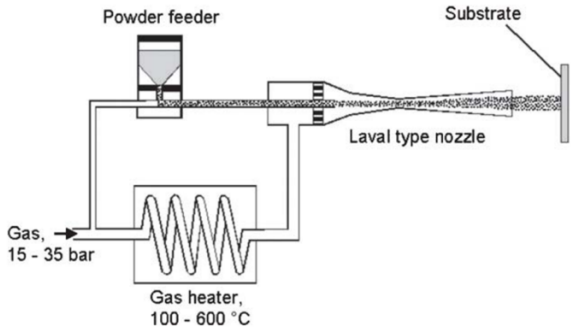

Figure 1.6. A schematic figure of the Laval type nozzle used in CS deposition [62].

In the CS process, the particles are relatively small (between 10 to 40 μm) and are deposited at a high velocity (up to 1200 m/s) around room temperature. In this method, a supersonic gas is used

to maintain particles' temperatures below their melting point, making it possible to deposited solid-state particles. Thus, CS can successfully deposit temperature-sensitive materials such as copper and titanium while preserving the phases of the initial feedstocks [52, 65-67]. It is worth noting that CS as a solid-state thermal spray technique builds up coatings based on severe plastic deformation of the deposited particles and substrate [13].

1.2.4. Fundamentals of Bonding Mechanism in Solid-State Deposition

Upon impact, the deposited solid-state particles and substrate would deform severely in tens of nanoseconds which is an adiabatic process. In this process, the heat generated by deformation only increases the temperature in a particular region. In some cases, this increase in temperature can melt the particle and/or substrate locally [13, 68, 69]. In the absence of melting, only metallurgical bonding and mechanical interlock can adhere the particle to the substrate [13]. As a result of mechanical interlocking, deposited particles are trapped within the substrate's topography. By contrast, metallurgical bonding results in high adhesion strength. For metallurgical bonding to occur, two fresh metallic surfaces must come into contact after the oxide surrounding the particle and substrate is broken [13]. To break the oxide layer and to eject the broken pieces, the particle impact velocity must be greater than a critical value [70-74].

The critical velocity is determined by the particle size, particle temperature, substrate characteristics, and material properties. T. Schmidt et al. [72] reported that a higher critical velocity is measured for particle adhesion when titanium is selected over tin or copper due to its greater strength. They observed a 250 m/s drop in critical velocity while increasing aluminum particles' diameter by 5 μm. Therefore, it can be said that the critical velocity is affected by all parameters that can alter the deformation of the particle and substrate [72]. Ultimately, they proposed two models that accurately estimate the critical velocity (Eq. 1.1 and Eq. 1.2) [72, 74].

$$v_{crit} = \sqrt{\frac{F_1 . 4 . \sigma_{TS} . (1 - \frac{T_i - T_R}{T_m - T_R})}{\rho} + F_2 . c_p . (T_m - T_i)} \tag{1.1}$$

$$v_{crit} = v_{crit}^{ref} \frac{0.42(^{d_p}/_{d_p^{ref}})^{0.5} \sqrt{1 - {}^{T_i}/_{T_m}} + 1.19\sqrt{1 - {}^{0.73T_i}/_{T_m}}}{0.65 + (^{d_p}/_{d_p^{ref}})^{0.5}} \tag{1.2}$$

Where, v_{crit} is critical velocity, σ_{TS} is tensile strength, T_i is particle temperature, T_R is reference temperature equals to 293 K, T_m is the melting point, c_p is heat capacity, ρ is density, and F_1 and F_2 are material constants. v_{crit}^{ref} is a reference critical velocity equal to 650 m/s, d_p particle diameter, and d_p^{ref} is reference particle diameter equals 10 μm [72, 74].

To understand the importance of critical velocity, M. Hassani-Gangaraj et al. [75] monitored the deposition of a 15 μm aluminum particle once its velocity was lower (Figure 1.7(a)) and once it was higher than the critical value (Figure 1.7(b)). In the former case, the impact of the particle on the substrate caused both to be plastically deformed. However, since the velocity was lower than

its critical value, the particle detached from the surfaces. In the latter case, both the particle and the substrate deformed significantly, which caused the particle to adhere to the substrate. To gain a deeper understanding of how impact velocity affects particle bonding to the substrate and to avoid using expensive advanced monitoring methods, numerical studies are useful [77, 76, 78-85].

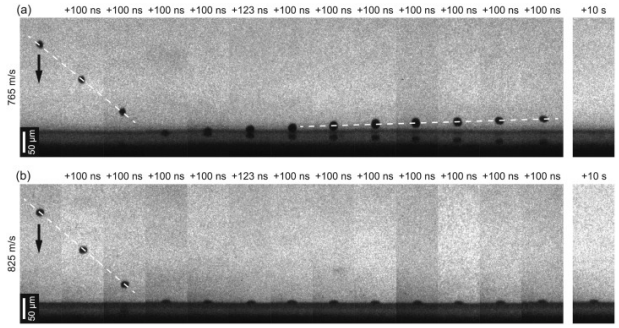

Figure 1.7. In-situ monitoring of the impact of (a) a 15-µm aluminum particle impacting an aluminum substrate at a velocity of 756 m/s which is lower than critical velocity and (b) a 16-µm aluminum particle impacting an aluminum substrate at a velocity of 825 m/s which is around the critical velocity [75].

F. Meng et al. [76] used numerical modeling to better understand the influence of the particle velocity on bonding formation, Figure 1.8. They showed that when the particle velocity was below the critical value, deformation and deposition efficiency would be low. As particle velocity increased up to its critical value, particle deformation increased, resulting in a rise in deposition efficiency. It was reported that to achieve very high deposition efficiency, impact velocity had to be increased beyond the critical value [76].

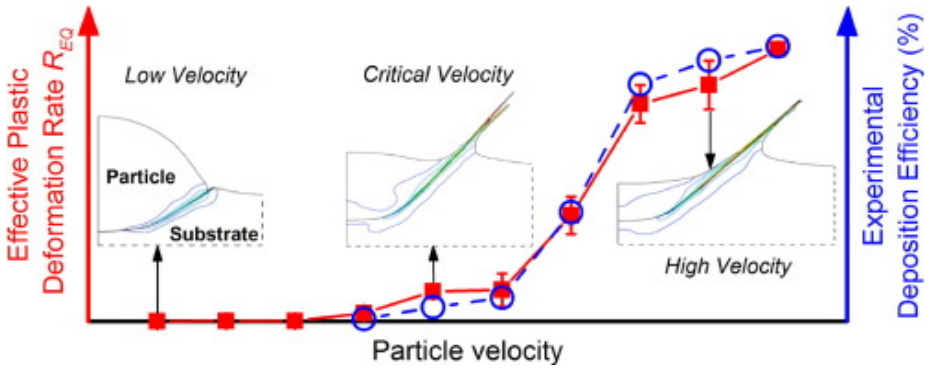

Figure 1.8. Effect of particle velocity on the deposition efficiency and deposited particle deformation while Cu particle impinged on Cu substrate using CS [76].

Bonding is created by deforming the particle and substrate. Metallic materials are highly susceptible to oxidation; therefore, a layer of oxide surrounds both the deposited metallic particles and the substrate. Metallurgical bonding occurs whenever the particle velocity is higher than the critical value, causing the oxide surrounding the particle and substrate to be broken off and ejected [13, 72, 77]. Based on Figure 1.9, W. Y. Li et al. [86] suggested that the oxide layer of the particle and substrate would break up upon impact. In this case, the breakage would occur in the region with the greatest pressure and shear stress [87]. With enhancing the deformation, the broken oxide pieces would be extruded, allowing fresh metallic surfaces of the particle and substrate to come

into contact and to create metallurgical bonding. To increase the area of the surface capable of producing metallurgical bond, it is necessary to eject the oxide debris using material jet [86].

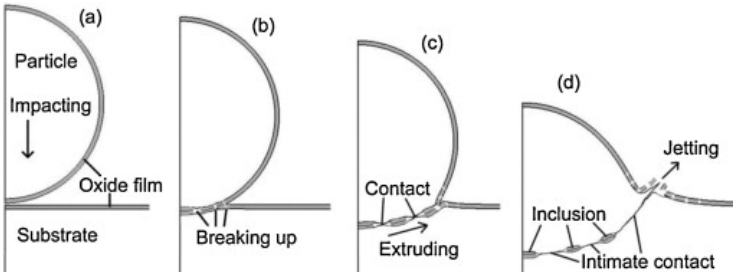

Figure 1.9. The proposed theory showing the oxide layer breakage during the deformation of an impacted solid particle deposited using CS [86].

Material jet formation is explained by the deformation of the particle and substrate when the particle velocity exceeds the critical value, resulting in the distribution of a high-pressure gradient in both particle and substrate. As a result of deformation, this gradient becomes localized in a ring-shaped region known as adiabatic shear instability (ASI) [71-72]. In this region, the temperature increases significantly, resulting in the softening of the deposited particles and substrate. Thermal softening facilitates deformation and forms a viscous fluid conducive to material jet [72]. A contrary study by M. Hassani-Gangaraj et al. [77] argues that localized shear stress cannot lead to material jet formation by focusing on the ineffectiveness of thermal softening. Accordingly, material jet is caused by solid pressure waves interacting with edges of the deposited particle and substrate. As a result, a tensile gradient would develop on the edge of the contact area, which eject materials and broken oxide pieces, Figure 1.10 [77].

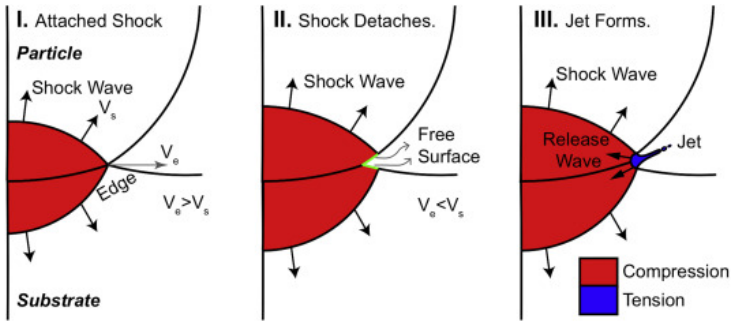

Figure 1.10. The theory proposed by M. Hassani-Gangaraj et al. [77] responsible for creating material jet.

Y. Xie et al. [88] developed a new theory for the adhesion of deposited particles to substrate. To begin with, they examined the impact of one single high strength Ni particle on a soft aluminum substrate. As a result of this impact, no material jet was formed, and the particle was mechanically interlocked to the substrate. Then, they fabricated a Ni coating on the Al substrate, and they found metallurgical bonding between the first layer of deposited Ni particles and aluminum substrates without material jet formation. Hence, the authors presented a new theory (Figure 1.11) that allows metal-to-metal contact. According to this theory, in the beginning, the first layer of the particles would be deposited on the substrate. Upon the impact, the oxide layer of the particles and the substrate break, and the broken oxide pieces form a bridge-like structure that prevents metal-to-metal contact. When the coating is being manufactured, the particles that have already been

deposited will deform more due to the peening effect. A greater deformation would result in a greater number of oxide pieces to be broken, forming more oxide debris. Increasing the deformation of already deposited particles by peening effect results in filling of pores between oxide debris, thereby causing discontinuous metal-to-metal contact and metallurgical bonding [88].

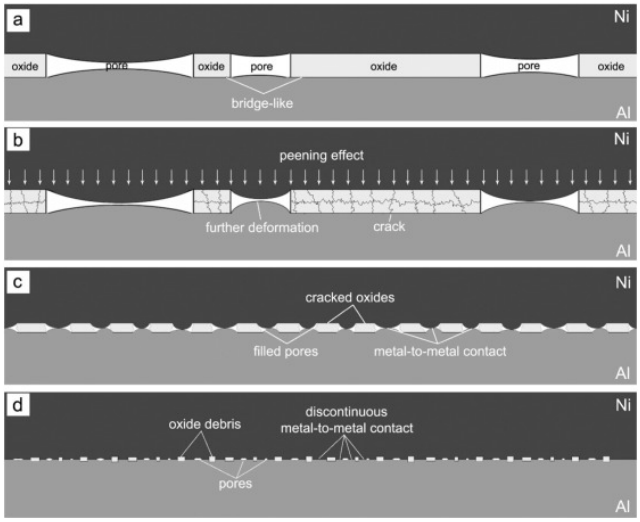

Figure 1.11. A schematic coating adhesion mechanism to the substrate [88].

1.2.5. Modelling the Particle Impact

In solid-state deposition techniques, particle deformation occurs within tens of nanoseconds resulting in a very high strain rate deformation (up to 10^9 s^{-1}). Since this nonlinear deformation is governed by dynamic rules, it cannot be studied experimentally without expensive sophisticated tools. However, the particle impact can be studied numerically as long as an elastic-plastic model capable of analyzing high strain deformations is developed [73, 78-85].

Since the deformation occurs at a high strain rate, Hook's law cannot be applied to study the elastic behavior. To study the elastic section of a sample deforming at high strain rates, a model called the Mie-Gruneisen Equation of State (EoS) has been developed. This model has been established based on a linear relationship between pressure and internal energy. The full description of this model is presented in Chapter 2. To study plastic behavior, six different models have been introduced in the literature [73]. Among them, the Johnson-Cook (JC) model (Eq. 2.3) has accurately estimated the shape and characteristics of the deformed particles after impact [73, 89-90].

$$\sigma = \left(A + B\varepsilon_p^n\right)\left(1 + C ln\frac{\dot{\varepsilon}_p}{\dot{\varepsilon}_0}\right)\left(1 - (\frac{T - T_r}{T_m - T_r})^m\right) \tag{1.3}$$

where σ is flow stress. A, B, C, n, and m represent material constants. Additionally, ε_p, $\dot{\varepsilon}_p$, σ, $\dot{\varepsilon}_0$, T_r, T_m, and T are illustrating equivalent plastic strain, plastic strain rate, flow stress, reference strain rate, reference temperature, melting point, and temperature, respectively [73]. In this model, the first bracket related to the strain hardening, the second bracket considered the strain rate hardening, and the last bracket is for taking the thermal softening into account [73].

Several finite element methods can be applied to solve elastic-plastic models, including Arbitrary Lagrangian-Eulerian (ALE), Coupled Eulerian-Lagrangian (CEL), and Smoothed-Particle Hydrodynamics (SPH) [91-95]. When a designed sample is assumed to be Lagrangian, both the mesh and the material must deform together, leading to significant element distortion. This problem has been addressed by the ALE method, which is capable of remeshing [68, 91-92]. ALE has been used to accurately estimate the deformed Cu particle shape compared to experimental results [73, 91]. S. Rahmati et al. [87, 96] used ALE method to examine bonding formation and oxide layer failure when a Cu particle impacts a Cu substrate. A study by H. Assadi et al. [69] used ALE to investigate the effect of the impact velocity on the particle deformation and material jet formation during the deposition of a Cu particle towards a Cu substrate. They found that ALE and remeshing avoid the presence of highly distorted elements and can accurately predict the material jet formation and particle deformation [69]. However, Xie et al [68] found that the final deformed shape and characteristics of deposited particles are highly dependent on the remeshing constants. Thus, it is necessary to develop another method that can predict the results without relying on these remeshing constants [68].

To overcome ALE limitation, the Coupled Eulerian-Lagrangian (CEL) method has been developed with the particles or substrate assumed to be Eulerian, i.e., the mesh is constant, and the material moves within it [68, 93]. This prevents any significant distortion of the elements, making CEL method ideal to study the effect of particle and substrate initial conditions on particle deformation and porosity level [68, 93, 97-98]. M. Yu et al. [99] used CEL to study the effect of preheating the particle and substrate on their deformation [99]. J. Xie [100] investigated the potential of CEL method to predict the density of the Cu and Al samples manufactured by CS. He concluded that CEL accurately predicted porosity level compared to the experimental results [100]. A study by X. Song et al. [93] examined the potential of CEL to estimate porosity levels in as-sprayed Ti-6Al-4V deposits by comparing the results to experiments. They found that CEL method was accurate in examining the effect of the impact velocity on porosity levels [93]. Although CEL accurately predicts the final deformed shape, it numerically underestimates the value of each parameter, including plastic strain, stress, and temperature, which is because available commercial software such as ABAQUS reports the mean value of the parameters of a Eulerian part [68].

Lastly, there is another method, called Smoothed-Particle Hydrodynamics (SPH), in which no mesh is found within the system, assuming that the selected part is composed of smoothed particles [83, 68, 94-95]. Based on a comparison of the SPH method with the ALE method, it was found that SPH can accurately predict single particle deformation at different impact angles [83, 94]. Furthermore, B. Gnanasekaran et al. [83] found that SPH is capable to study the structure of as-fabricated deposits. J. Xie et al. [68] used SPH to study the deformation of an aluminum particle impacting on an aluminum substrate at a velocity of 700 m/s. The result of their study showed that SPH method has limitations when it comes to considering thermomechanical effects of deformation [68].

To this point, the deposition mechanisms and techniques to build up the coatings have been thoroughly reviewed. It will therefore be easier to explain each observed property in solid-state additively manufactured samples. In the next section, we will discuss the potential of solid-state additive manufacturing methods such as CS to repair damaged metallic components.

1.3. The Use of Cold Spray as a Solid-State Additive Manufacturing Method

Cold spray (CS) offers the opportunity to produce near-net-shape samples at high deposition rate without any oxidation or phase transformation, which makes it suitable for repairing damaged metallic components [13, 101]. Nevertheless, the existing porosity level of CS as-fabricated samples negatively affects their mechanical properties [102]. A detailed discussion of the reasons why CS as-fabricated samples have poor mechanical properties will be presented in this section.

1.3.1. Porosity Level

One of the main disadvantages of using CS as a solid-state additive manufacturing technique is poor mechanical properties of the as-fabricated samples [103-107,112]. Y. Kim et al. [112] studied the potential of CS as a solid-state additive manufacturing by depositing copper particles. In this work, nitrogen and helium were used as carrier gases to produce thick copper deposits. They reported a porosity level of 0.02% and 0.01% with nitrogen and helium, respectively. In this study, EBSD mapping showed that by choosing helium as the carrier gas, grains were deformed further, indicating higher in-flight particle velocity. Consequently, they concluded that using helium as propellant enhances particle velocity and, as a result, particle deformation, fabricating a very dense structure while CS deposits deformable and soft materials like copper [112, 133]. In another work, M. Amiri et al. [108] deposited Ni using CS with different carrier gases: air with low pressure, air with high pressure, nitrogen, and helium to investigate the porosity level of as-fabricated samples. Using nitrogen, a sample with a porosity of 3.5% was produced. Using air at high and low pressure led the porosity level to decrease down to 2% and 1.5%, respectively. And using helium as the carrier gas produced a sample with porosity of 0.4% [108]. A study by C. Chen et al. [105] showed that accelerating deposited particles enhances density of the as-fabricated samples. In this work, they deposited Ti-6Al-4V particles using helium and nitrogen as the propellant. To determine the internal porosity, they used X-ray computed tomography (XCT), Figure 1.12 [105]. As it can be seen, while nitrogen is the carrier gas, the deposited particles deformed less significantly, resulting in higher porosity level. By using helium, it is possible to increase the in-flight particle velocity, thereby reducing the inter-particle porosity [105, 133]. In conclusion, CS cannot produce fully dense structures by depositing high strength materials such as Ti or Ni alloys [105, 106].

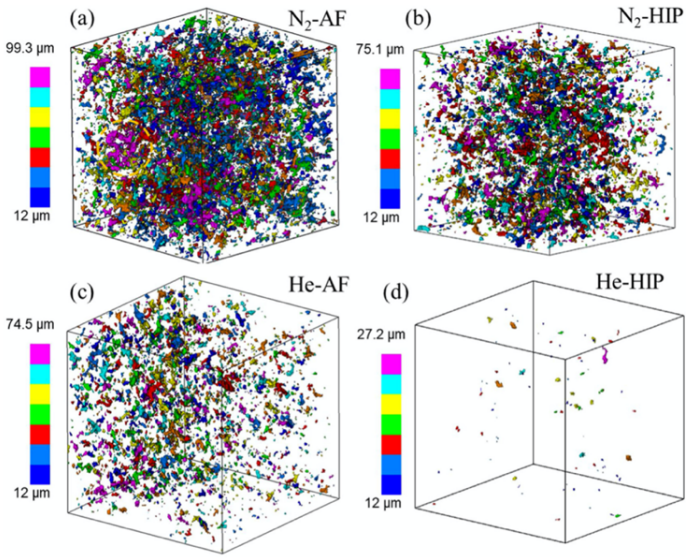

Figure 1.12. XCT analysis of the (a) as-fabricated using nitrogen, (b) HIPed sample produced using nitrogen, (c) as-fabricated using helium, (b) HIPed sample produced using helium [105].

Increasing particle velocity not only deforms the deposited particle further, but also increases the peening effect, meaning that deposited particles can further deform already deposited ones [13]. N. H. Tariq et al. [114] discussed the peening effect on porosity reduction in an as-fabricated Al sample. As shown in Figure 1.13, the first layers of deposited particles have a denser structure due to the peening effect. When it comes to the last deposited layers, the peening effect becomes less significant [114]. Therefore, the peening effect cannot reduce the overall porosity of the as-fabricated samples.

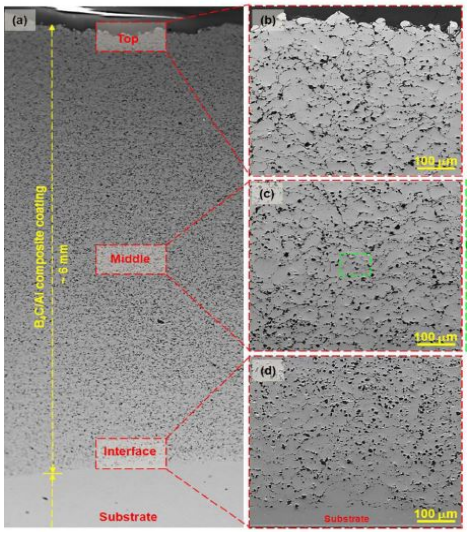

Figure 1.13. The examination of peening effect for manufacturing aluminum composite using CS [114].

As some point, increasing the particle velocity did not significantly reduce porosity level of an as-fabricated sample. For this reason, many researchers have worked on sintering deposited samples using heat treatment processes. S. Bagherifard et al. [106] investigated CS's potential as an additive manufacturing method to produce Inconel 718 samples [106]. The authors concluded that the high hardness and low deformability of Inconel 718 prevent CS from depositing dense structures. In this study, as-fabricated samples were reported to have a porosity level around 1.2%. After three hours of heat treatment at 1050 °C in an argon environment, they reported a porosity of 0.9% [106]. A. Singh et al. [109] deposited SS316L with high-pressure cold spray. According to their measurements, the porosity of the as-fabricated sample was 6%. Following a heat treatment at 1100 °C, the effect of the cooling rate on porosity level was examined. They found that the porosity of the sample decreased to 1.2% by cooling it to the ambient temperature in the furnace (slow cooling rate). When the sample is cooled in the air, the porosity of the sample decreased to 0.95% [109]. It is worth noting that during the sintering heat treatment, small pores would disappear, while large pores would only shrink, Figure 1.14 [109]. Thus, to further decrease the porosity level by sintering heat treatment, a method known as hot isostatic pressing (HIP) has been suggested [105].

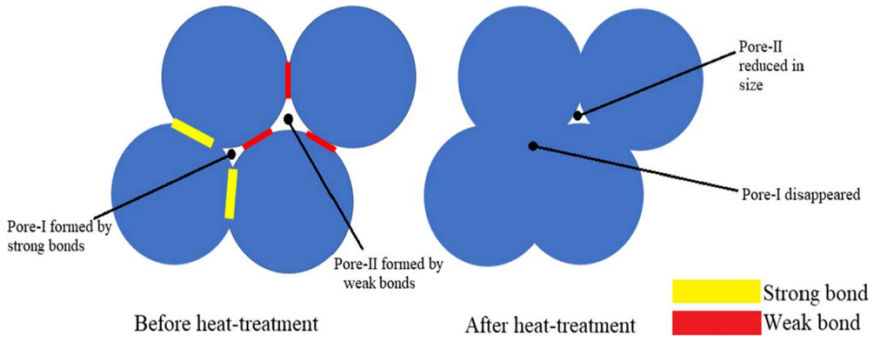

Figure 1.14. The deposited particles behavior during heat treatment [109].

The hot isostatic pressing (HIP) process has been used to significantly reduce the porosity level of as-fabricated samples. P. Petrovskiy et al. [111] used nitrogen as the carrier gas to fabricate thick Ti-6Al-4V deposits by CS. In comparison with the as-fabricated sample, which has a porosity level of 7.5%, the HIP sintered samples have a porosity level of 0.2% [111]. Another study conducted by C. Chen et al. [105] investigated the capability of HIP to sinter CS samples manufactured by either nitrogen or helium as the carrier gas. With HIP applied, the porosity of both samples significantly decreased, Figure 1.12. Precisely, the porosity level of the as-fabricated sample was 2.45% while using nitrogen as the propellant and 1.5% using helium. HIP reduced each sample's porosity to 1.15 % and 0.03 %, respectively [105]. The results show that the helium sample is further densified since its initial pores were smaller. This is in accordance with the founding discussed previously by A. Singh et al., Figure 1.14 [109].

Therefore, in CS process, using helium alone cannot deposit fully dense samples of high-strength materials. Further reduction of porosity was achieved by HIP and annealing. In this case, the costly process of HIP has proven to be more promising than annealing [105].

1.3.2. Mechanical Properties

The mechanical properties of any component have a significant impact on its lifetime. The mechanical properties of as-fabricated CS samples, including hardness, tensile behavior, and fracture surface, are examined in more detail in this section.

The first mechanical property discussed in this section is the hardness of the as-fabricated samples. These samples are expected to have a high hardness since they are manufactured by the deformation of deposited particles [115-117]. C. Chen et al [105] utilized CS to deposit Ti-6Al-4V particles using nitrogen or helium as the carrier gas. Compared to nitrogen, helium deposits particles at higher velocity. As a result, deposited particles deformed more, creating a higher dislocation density. This means that the hardness of the as-fabricated sample manufactured by helium as the carrier gas (420 micro-Vickers) was significantly greater than the one manufactured using nitrogen (390 micro-Vickers). In this work, as a result of applying HIP heat treatment, the sample went through recovery and recrystallization processes, resulting in a decrease in hardness. The hardness of samples manufactured by helium and nitrogen was reduced to 280 and 200 micro-Vickers, respectively [105]. S. Bagherifard et al. [106] observed the same reduction in hardness after recovery and recrystallization of Inconel 718 samples fabricated using CS.

The fracture behavior of the CS as-fabricated samples is the next mechanical property discussed in this section. Tensile testing of as-fabricated samples reveals brittle-like fractures, which are a result of the pores structure of the samples. Precisely, the pores within a sample can function as crack initiation sites. A sintered sample will withstand higher strains until its brittle fracture is eventually converted to a ductile fracture [105-106, 118-123]. C. Chen et al. [105] examined the fracture behavior of as-fabricated and HIPed Ti-6Al-4V samples, Figure 1.14. According to their work, due to the high porosity level of Ti-6Al-4V samples (using nitrogen as the carrier gas), the fracture occurred at a low strain and based on brittle mechanism without showing any signs of dimples, Figure 1.14(a). When helium was used as the propellant, sample density increased, and some localized dimples were found in the fracture surface, Figure, 1.14(b). They concluded that increasing the density of as-fabricated samples is positively associated to increase in their ductility. They also found that sintering the as-fabricated samples using HIP, particularly when helium is used as a carrier gas, the sample fractures occurred at high strains based on ductile mechanisms. This means that large dimples are observed on the fracture surface, Figure 1.14(g) [105]. In another study, K. Tsaknopoulos et al. [119] deposited Al F357 with nitrogen as the carrier gas. Heat treatments then were used to transform brittle fractures into ductile fractures in as-fabricated samples. The first heat treatment involved heating the samples at 230 °C for 75 minutes, while the other one involved heating them at 385 °C for 6 hours. Due to the presence of dimples on the fracture surfaces of both heat-treated samples, the researchers concluded that both would fail based on ductile mechanism; however, the samples would have different strengths and elongations. The elongation of the sample heat-treated at 385 °C was significantly higher indicating that the heat treatment at a higher temperature for a longer period enhanced the ductility further [119].

In conclusion, heat treatment not only reduces porosity but also affects mechanical properties. Heat treatment can recover and recrystalize the samples and reduce their hardness. Further, these methods can reduce the porosity by sintering the samples, leading to an enhancement in ductility [105-106, 118-122].

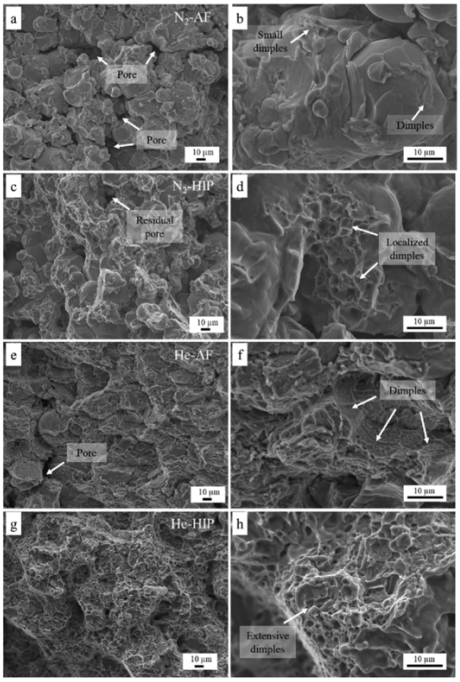

Figure 1.14. The examination of the fracture surface of Ti-6Al-4V samples manufactured using CS. In the right column, a smaller magnification is used [105].

1.3.3. Tribological Properties

There is always the possibility that the surface of spray components is damaged and worn. It is essential to examine the tribological properties of as-sprayed samples [78, 116, 123]. In this regard, Kuhn et al. [116] investigated the tribological properties of Ti-6Al-4V as-fabricated samples and found that the samples are not able to form tribo-layers during the test, Figure 1.15(a). Their study revealed that particle detachment is the cause of wear, resulting from insufficient bond strength between the deposited particles, Figure 1.15(b). Accordingly, the detachment wear mechanism is illustrated by pits that have formed between the deposited particles [116].

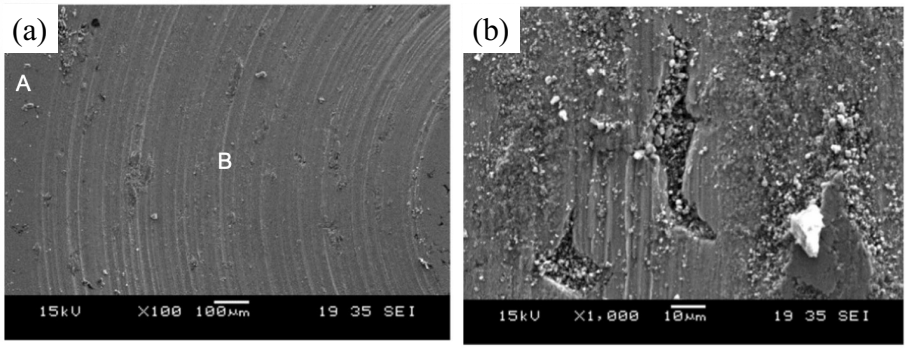

Figure 1.15. The morphology of Ti-6Al-4V sample tested for tribological properties with (a) lower and (b) higher magnification [116].

Another study examined the tribological properties at various temperatures of as-fabricated Ti-6Al-4V samples [78]. This study found that the coefficient of friction (CoF) increased with increasing temperature to 400°C. By increasing the temperature higher than 400°C, CoF decreased significantly due to the formation of a tribo-layer. In addition to CoF, wear rate is also affected by the test temperature. By raising the temperature, the wear rate of the material decreased significantly. To determine the underlying reasons for these changes, they examined the microstructure of the wear track. Based on this analysis, it was concluded that under 200°C, abrasive wear is occurring without the formation of tribo-layers. In contrast, by increasing the temperature up to 400°C, a tribo-layer was formed on the wear track [78]. Moreover, an increase in temperature enhances the oxidation of the material, which results in a significant increase in wear resistance [78]. Thus, by increasing the operational temperature of Ti-6Al-4V samples, it can be expected to enhance their tribological properties.

In another study by P. Sirvent et al. [123], the effect of heat treatment on the tribological properties of as-fabricated Ti-6Al-4V samples were examined in greater detail [123]. As-fabricate Ti-6Al-4V samples were subjected to a solution heat treatment followed by a precipitation heat treatment which formed deformable β-Ti phase on the grain boundaries of unfavorable equiaxial α-Ti. Then, the tribology test was conducted at room temperature and at 450°C under two different conditions: oscillating and sliding. While using the sliding method, both the CoF and the wear rate were found insensitive to the heat treatment and tribological test temperature. Moreover, testing the sample at room temperature resulted in the formation of abrasive grooves and some detached particles. It is possible to observe a much smoother wear track when the test temperature is increased. Using the oscillating method, the application of heat treatment or increasing the test temperature resulted in improved CoF and reduced wear rate. Also, the wear track was found to have abrasive grooves and some detached particles. Lastly, they concluded that more oxidations occurs during the oscillating test, enhancing the wear resistance properties of the heat-treated samples [123].

1.5. Objectives of Work

As reported in the work done for developing CS as an additive manufacturing technique, poor mechanical properties and the need for post-heat treatment keep it from becoming widely accepted. It was well established that the porosity level plays an important role in the mechanical properties of the samples. To reduce operating costs, as-fabricated samples must be made denser. This can be achieved by deforming the deposited particles to a greater extent upon impact. Since particle velocity cannot be enhanced infinitely, particle temperature should be considered as an additional parameter to enhance the deformation of deposited particles. Therefore, in this thesis, solid-state particles are heated during deposition with the objective of enhancing the density and mechanical properties of as-sprayed samples. This can be accomplished by first numerically investigating the effect of the particle temperature on particle deformation, porosity level, and binding area. Afterwards, the tribological and microstructural properties of Ti-6Al-4V samples produced by HVAF would be examined to evaluate its potential as a solid-state additive manufacturing method. The more-detailed objectives of this thesis are listed as below:

- To investigate the effects of heating the particles and substrate during spraying on their deformation, material jet formation, particle adhesion, porosity level, and residual stress of deposited Ti-6Al-4V particles using an elastic-plastic finite element method.
- To understand the effects of inner diameter HVAF gun (ID-HVAF) spraying parameters on in-flight particle characteristics.
- To evaluate the protentional of ID-HVAF as a solid-state additive manufacturing process by studying the tribological and microstructural properties of as-fabricated Ti-6Al-4V samples.

1.6. Thesis Layout

The thesis consists of six chapters and is written according to the manuscript-based thesis regulations. In this study, numerical and experimental methods were used to investigate the effects of heating the deposited solid-state particles on the porosity level and mechanical properties of Ti-6Al-4V samples fabricated using HVAF.

The purpose of Chapter 1 was to describe the benefits of repairing damaged samples over replacing them. This chapter discussed the benefits of using CS as a solid-state additive manufacturing technique for repairing damaged metallic samples. To understand the obtained properties of as-fabricated CS samples, an in-detail explanation of coating builds up and bonding mechanism are provided in this chapter. Then, this chapter discusses the microstructure and mechanical properties of as-fabricated samples to address the main drawbacks associated with using CS for repair purposes. Lastly, to overcome the drawbacks of CS, the proposed idea and thesis's objective are provided.

In Chapter 2, elastic-plastic models are used to investigate the effect of heating the particle and substrate during spraying on the particle and substrate deformation. Following this, a simulation is used to study the effects of heating the particle and substrate on porosity levels and residual stresses of as-fabricated Ti-6Al-4V samples using HVAF.

The purpose of Chapter 3 is to utilize a proper elastic-plastic finite element method to investigate the effects of heating the particle and the substrate on the failure of the oxide layer, the formation of material jet, and bonding area.

It is the purpose of Chapter 4 to investigate experimentally how a ID-HVAF gun can be used to deposit solid particles at elevated temperatures to produce Ti-6Al-4V coatings. To examine the effects of ID-HVAF spraying parameters on in-flight particle characteristics, a diagnostic system known as DPV was used. In a subsequent step, the influence of the spraying parameters on the properties of the as-sprayed coatings were studied.

In Chapter 5, the optimum conditions obtained from Chapter 4 were used to manufacture a Ti-6Al-4V thick deposit. In this study, the tribological and microstructural properties of as-fabricated and heat-treated samples are examined to evaluate the potential of the HVAF process as a solid-state additive technique.

Chapter 6 summarizes the obtained results and makes some suggestions for future research.

In Appendix 1, the potential of another innovative solid-state deposition technique known as liquid cold spray has been studied. This process deposits solid-state metallic particles at high velocity at room temperature using water as propellant. Due to the inability to study particle deformation experimentally, numerical methods have been used to study the effect of water propellent on particle deformation. The appendix consists of two papers. The first one examines the effect of water wetting the substrate on particle deformation. The other study examines the effect of water wetting the particle on its deformation and adhesion to the substrate.

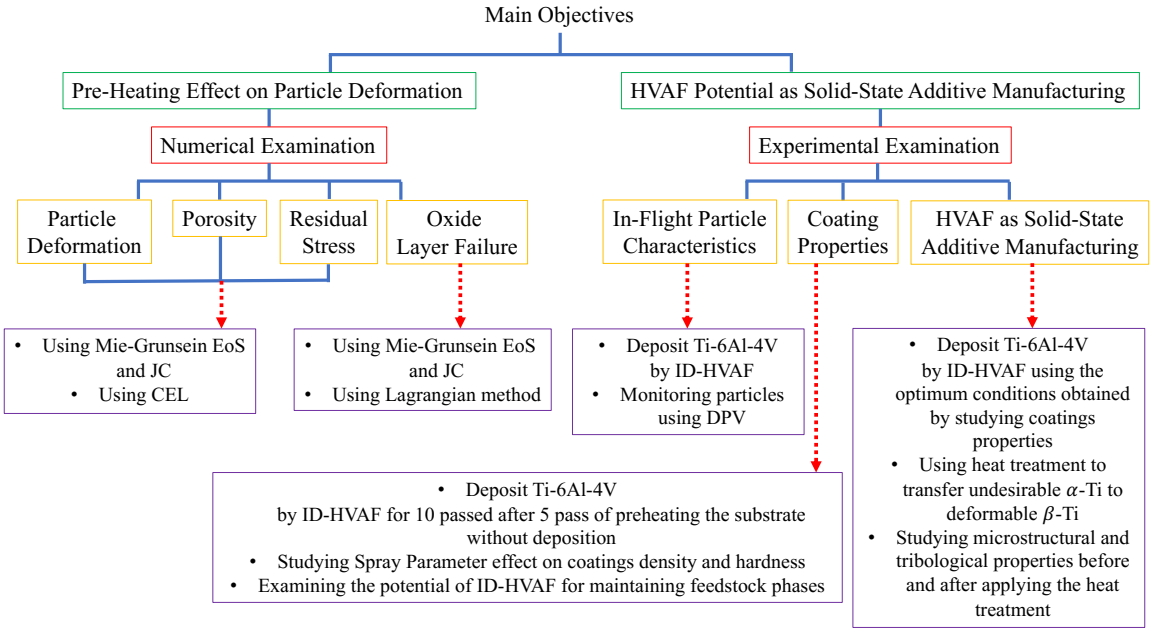

Figure 1.16. A schematic of the thesis layout.

Chapter 2

Numerical Simulation of the Effect of Particle and Substrate Pre-Heating on Porosity Level and Residual Stress of As-sprayed Ti-6Al-4V Components[1]

2.1. Abstract

Nowadays, in the aerospace industry, additive manufacturing and repairing damaged metallic components like Ti-6Al-4V samples has grabbed attention. Among repairing techniques, solid-state additive manufacturing processes like cold spray is promising because of their unique benefits such as high deposition rate with almost no oxidation in the deposited materials. However, its main drawback is the level of porosity of as-sprayed samples. To increase density and inter-particle bonding, deposited particles must go through more degrees of deformation by increasing particle velocity and particle temperature. To increase these two parameters simultaneously, high-velocity air fuel (HVAF) can be utilized. For understanding the effect of using HVAF on particle deformation, a proper elastic-plastic finite-element-based simulation is required. The obtained outcomes show that enhancing particle velocity and providing more kinetic energy will increase particle deformation and sample density. Importantly, increasing particle temperature will seize particle deformation by thermal softening effect i.e. enhancing as-sprayed sample density, while rising substrate temperature by pre-heating will soften the substrate resulting in a decrease in particle deformation.

2.2. Introduction

In the aerospace industry, a considerable amount of research has been devoted to developing new strategies to enhance the durability of different parts of the current aero engines. Turbine blades, as an example, are manufactured by Ti-6Al-4V alloy because of its unique set of properties as high melting point and high tensile strength [124-129]. The metallic Ti-6Al-4V components used in industry are suspectable to damage, therefore the need for repairing is raised. Among repairing techniques, solid-state additive manufacturing methods like cold spray seems to be more promising because of their characteristics, such as high deposition rate and no oxidation. Nevertheless, cold spray as a solid-state additive manufacturing technique has a main drawback associated with high porosity levels in as-fabricated samples. These pores have been resulted from insufficient bonding, caused by inadequate particle deformation upon its impact on the substrate surface [19, 105-106, 130-133].

Particle deformation can cause bonding in a ring-shaped region known as “adiabatic shear instability.” To understand the formation of this area, at the first nanoseconds of the impact, a pressure gradient spread in both particle and substrate, creating localized shear straining at the gap

---

[1] Khamsepour, P., Moreau, C., & Dolatabadi, A. (2021). Numerical simulation of the effect of particle and substrate preheating on porosity level and residual stress of as-sprayed Ti6Al4V components. *Journal of Thermal Spray Technology*, 1-14. DOI: https://doi.org/10.1007/s11666-021-01286-9

between two bumping interfaces. The localized shear strain will become adiabatic shear instability by accumulating the impact pressure, which means that thermal softening is now overriding strain and strain-rate hardening. This can cause a discontinuous increase in strain and temperature values [13, 72, 77]. Besides, the out-flowing material jet is formed because of the viscous flow. Finally, this material jet can eject out the broken oxide layers, leading to bonding [13, 72]. However, Hassani-Gangaraj et al. [77] oppose the idea that localized shear stress is the cause of bonding. This investigation was mainly focused on the ineffectiveness of thermal softening on material jet formation. They proposed that material jet is produced because of solid pressure waves interacting with deposited particles' edges.

For realizing the importance of particle deformation more profoundly, some experimental investigations have been carried out. For instance, Chen et al. [105] deposited Ti-6Al-4V particles with cold spray by two different carrier gases: nitrogen and helium. He concluded that particle velocity is further increased by using helium compared to nitrogen. Hence, more deformation was observed in deposited particles resulting in a decrement in porosity levels. However, this reduced porosity level still can alter mechanical properties, as a result, a post-heat treatment approach like annealing or hot isostatic pressure (HIP) is required. These heat treatment methods force the particles to go through the sintering process, reducing the porosity level significantly [105-106]. Accordingly, to minimize the need for a post-heat treatment approach, particle's ability to deform must increase even more. For this purpose and because of the limitations on enhancing particle velocity, increasing particle temperature is proposed as a viable solution [99].

For considering particle temperature and having a high deposition rate simultaneously, high-velocity air fuel (HVAF) process can be employed as a solid-state additive manufacturing method. In the HVAF process, by combining air and a combustible fuel like propylene, combustion occurs. This combustion can increase both particle velocity and temperature instantaneously. Also, by contemplating flame temperature, particle melting point, and particle size, it is possible to deposit elevated temperature solid particles [13, 134-136]. Moreover, it is essential to observe the effect of using HVAF on particle deformation and porosity level of as-sprayed samples.

For investigating the deformation of deposited solid particles, experimental approaches are incompetent because the deformation happens in tens of nanoseconds, follows dynamic rules, and is nonlinear [73, 137]. Hence, a proper set of elastic-plastic models capable of examining high strain rate deformations is required. For elastic exploration, Mie-Gruneisen equation of state (EoS) and for plastic examination, Johnson-Cook (JC) model have been used frequently [73, 137]. For solving the noted models, a finite-element-based method like Coupled Eulerian-Lagrangian (CEL) is needed. Compared to other finite-element-based approaches like Arbitrary Lagrangian-Eulerian (ALE), CEL's advantage is based on assuming an Eulerian particle, which avoids the need of remeshing and having highly distorted elements [137]. Xie et al. [137] compared CEL and ALE approaches by studying the impact of an aluminum particle on an aluminum substrate. They concluded that CEL could not study particle deformation numerically because only the mean value of each variable is reported for the Eulerian particle. However, it is the most accurate approach to analyze substrate deformation and predict the porosity level of as-fabricated samples [137].

Besides attempts to study particle deformation deposited by cold spray [69, 73, 77, 96, 105, 137-139], the effect of copper particle temperature up to 700 °C was investigated when substrate is at room temperature. By rising particle temperature because of the thermal softening effect, the

particle flattening ratio increases, and the material jet is produced only from the particle. On the other hand, by increasing copper substrate temperature up to 700 °C while the deposited particle is at room temperature, particle deformation decreases significantly [99]. Furthermore, some attempts have been devoted to estimating the porosity level of as-fabricated samples. For example, the effect of particle temperature up to 523 K has been investigated while copper particles are impinged on an aluminum substrate. The results show that increasing particle temperature and velocity enhances the density of as-sprayed samples [100].

Conclusively, due to the lack of studies of the porosity level of as-sprayed samples produced by solid particles at elevated temperatures, this paper aims to numerically investigate the feasibility of using HVAF as a solid-state additive manufacturing technique. Therefore, the effect of particle and substrate initial temperature on particle deformation and porosity level of as-fabricated samples are scanned for fulfilling this goal. Accordingly, a proper elastic-plastic finite-element-based method based on Mie-Grunsien EoS and JC model is used.

2.3. Numerical Methodologies

2.3.1. Mie-Gruneisen EoS

Mie-Gruneisen EoS is capable of handling the elastic sections of a high strain rate deformation. This model is developed based on crystal structure and a connection among internal energy, thermal vibrational energy, and the potential energy at zero temperature. It is worth noting that the relationship between vibration energy and thermal vibration pressure is dependent on vibration frequency and volume but independent of temperature. Using the vibrational theorem and Gruneisen equation, the primary form of Mie-Gruneisen EoS can be illustrated via Eq. 2.1 below [140-141].

$$P - P_H = \Gamma_\rho (E_m - E_H) \tag{2.1}$$

where P is total pressure, E_m is internal energy per unit mass, P_H is Hugoniot pressure, and E_H is specific energy. Also, Γ_ρ is Gruneisen coefficient which can be calculated by Eq. 2.2 [141]:

$$\Gamma_\rho = \Gamma_0 \frac{\rho_0}{\rho} \tag{2.2}$$

where Γ_0 and ρ_0 are material constants and ρ represented pressure stress. Also, the value for both Hugoniot pressure and Hugoniot energy can be found with the help of Eq. 2.3 and Eq. 2.4, respectively [137, 141].

$$E_H = \frac{P_H \eta}{2\rho_0} \tag{2.3}$$

$$P_H = \frac{\rho_0 c_0^2 \eta}{(1 - s\eta)^2} \tag{2.4}$$

where η is equal to $1 - \rho_0/\rho$ and represents the nominal compressive volumetric strain. $\rho_0 c_0^2$ expresses the elastic modulus at small nominal strains. Furthermore, c_0 and s are material constants used for drawing an association between shock velocity (U_s) and particle velocity (U_p) [137].

Finally, by considering all noted formulas together, the final form of Mie-Gruneisen EoS can be formed as Eq. 2.5 [137]:

$$P = \frac{\rho_0 c_0^2 \eta}{(1 - s\eta)^2} \left(1 - \frac{\eta \Gamma_0}{2}\right) + \Gamma_0 \rho_0 E_m \tag{2.5}$$

In the end, this model only can study the hydrostatic behavior, therefore for examining the deviatoric behavior, a linear elastic model and shear modulus are required [73].

2.3.2. Johnson-Cook Model

Johnson-Cook model is a plastic model able to examine a high strain rate deformation. This model is represented by Eq. 2.6 [73].

$$\sigma = \left(A + B\varepsilon_p^n\right)\left(1 + C ln\frac{\dot{\varepsilon}_p}{\dot{\varepsilon}_0}\right)\left(1 - (\frac{T - T_r}{T_m - T_r})^m\right) \tag{2.6}$$

where, ε_p, $\dot{\varepsilon}_p$, σ, $\dot{\varepsilon}_0$, T_r, T_m, and T are equivalent plastic strain, plastic strain rate, flow stress, reference strain rate, reference temperature, melting point, and temperature, respectively. Constants in this formula are considered as A, B, C, n, and m. This model has been utilized noticeably for examining the deformation of a deposited particle [73, 137].

2.3.3. Coupled Eulerain-Lagrangian (CEL) Method

In the CEL approach, the mesh is unchanged through the analysis, so the submitted job will not get aborted because of highly distorted elements. Also, CEL can only study substrate behavior numerically because, for the Eulerian particle, only the mean value of each variable can be reported. On the other hand, because CEL can predict particles' final deformed shape, it is considered the approach used in this paper using ABAQUS to investigate Ti-6Al-4V particles deformation deposited by the HVAF process [137].

For carrying this simulation, the required material constants for the Ti-6Al-4V particle and the substrate are shown in Table 2.1 [142]. Also, the changes of physical properties like density, heat conductivity, heat capacity, and shear modulus with temperature have been taken into account by the formulations noted in the reference [143] The friction coefficient is assumed to be 0.3 in all the conditions, and the mesh size of the particle and the substrate area under the impact is equal to 1 μm which has already been used in the literature [137, 144]. The Lagrangian substrate's mesh type is C3D8RT (An 8-node thermally coupled brick, trilinear displacement, temperature, reduced integration, hourglass control). For Eulerian particle, mesh type is EC3D8RT (An 8-node thermally coupled linear Eulerian brick, reduced integration, hourglass control). The particle is extracted from the Eulerian part by defining a discrete field, and the interaction between particle and substrate is defined as “General” since there is no specific surface existing for an Eulerian section. The step used for carrying these simulations is considered as “Dynamic, Temp-disp, Explicit” and the time of studying particles deformation is chosen in a way that particle detachment is just about to begin. This is the reason that no particle detachment can be seen in the obtained results. In the end, the boundary condition for Lagrangian substrate is defined as “PINNED” for the bottom and perimeter and only the displacement in “Z-direction” in locked in the symmetric

surface perpendicular to "Z-direction". For the Eulerain part, the velocity of Z is assumed to be zero in the symmetric surface perpendicular to "Z-direction" [137].

Table 2.1. Material constants are used for simulating the deformation of a Ti-6Al-4V particle deposited by HVAF [143-144].

Property	Ti6Al4V
Density $(^{kg}/_{m^3})$	4430
Shear modulus (GPa)	41.9
C_0 $(\frac{m}{s})$	5130
s_0	1.03
Γ_0	1.23
A (MPa)	862
B (MPa)	331
C	0.012
m	1.1
n	0.34
$T_m(K)$	1903
$T_r(K)$	298
Conductivity$(^{W}/_{m.K})$	6.6
Heat Capacity$(^{J}/_{Kg.K})$	536

2.3.4. Single Particle Impact

This paper's first concern is devoted to examining the effect of particle temperature, particle velocity, and substrate temperature (Table 2.2) on the deformation of a 29 μm solid Ti-6Al-4V particle impacts on the substrate of the same material, as shown in Figure 2.1 [145]. The noted initial particle and substrate temperature has been assumed in a way that no melting will occurs during the deformation to maintain the accuracy the noted elastic-plastic simulation. Also, in this examination, the flattening ratio will be utilized to understand particle deformation by using the Eq. 2.7 below. Also, the effect of noted parameters on substrate deformation will be investigated by the changes of equivalent plastic strain (PEEQ) and temperature (TEMP) for a specific node by the passage of time.

$$Flatenning\ ratio\ (\%) = \frac{The\ maximum\ hieght\ of\ a\ deformed\ particle}{The\ initial\ diameter\ of\ impacted\ particle} \times 100 \qquad (2.7)$$

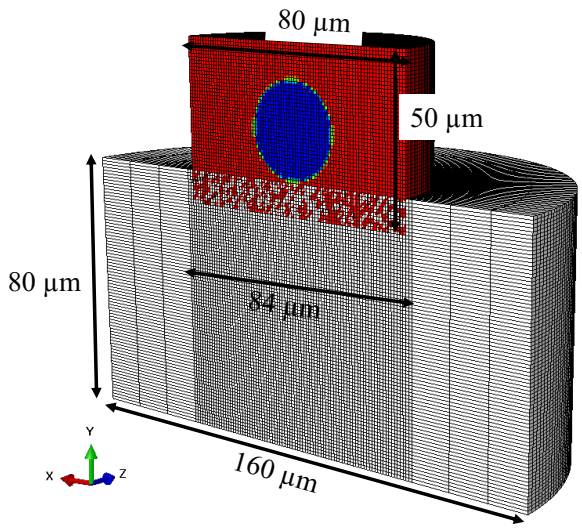

Figure 2.1. Preliminary state and computational mesh for examining the effect of particle and substrate initial conditions on the deformation of a deposited Ti-6Al-4V particle on a Ti-6Al-4V substrate by HVAF process.

Table 2.2. The conditions utilized for investigating the effect of particle temperature, particle velocity, and substrate temperature on particle and substrate deformation upon the impact of a Ti-6Al-4V particle deposited by the HVAF process.

Condition	Particle temperature (K)	Particle velocity (m/s)	Substrate temperature (K)
V1	873	600 / 650 / 700	673
V2	873 / 973 / 1073 / 1173 / 1273	600	673
V3	1073	600	473 / 573 / 673 / 773

2.3.5. Multiple Particles Impact

After understanding the influence of particle and substrate initial condition upon impact on their deformation, the porosity level of as-fabricated Ti-6Al-4V samples is investigated through modeling multiple particle impact. In order to make the modeling tractable, it is assumed that some agglomerated particles are impinging on the substrate by the pattern shown in Figure 2.2. Based on actual Ti-6Al-4V powders, the Dv (10) and Dv (50) values shown in Figure 2.3 will be utilized to capture the particle size distribution effect. Therefore, for different sets of particles and substrate initial conditions, once it is assumed only a unisize 10 µm particles are impinging and alternatively a combination of 5 and 10 µm particles are considered, Table 2.3.

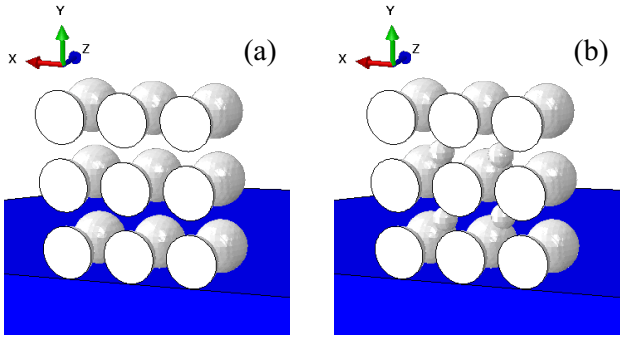

Figure 2.2. The initial condition for examining the porosity level, which a) only 10 µm Ti-6Al-4V particles and b) 5 & 10 µm Ti-6Al-4V particles are deposited by HVAF.

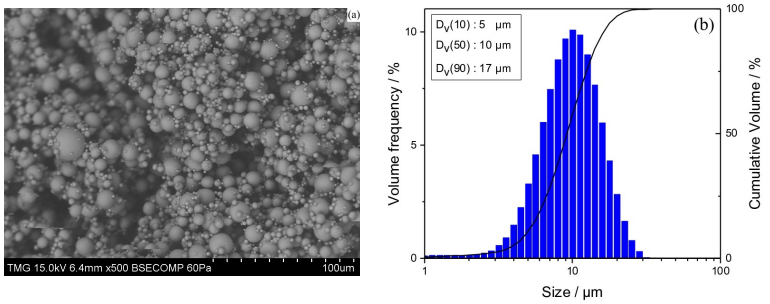

Figure 2.3. a) Scanning electron microscope (SEM) image of Ti-6Al-4V powders and b) particle size distribution of Ti-6Al-4V powders.

Table 2.3**.** Various conditions for examining the effect of particle and substrate initial conditions and particle size distribution on porosity level of as-fabricated samples with Ti-6Al-4V powders.

Name of the case	Particle size (µm)	Particle temperature (K)	Particle velocity (m/s)	Substrate temperautre (K)
P1	10	873	600 / 650 / 700	673
P2	10	873 / 1073 / 1273	650	673
P3	10	1073	650	573 / 673 / 773
P4	5 & 10	873	600 / 650 / 700	673
P5	5 & 10	873 / 1073 / 1273	650	673
P6	5 & 10	1073	650	573 / 673 / 773

2.3.6. Porosity Level Investigation

To investigate the porosity level of as-sprayed samples, a method based on extracting a constant cube shape from each as-fabricated sample is required. For each condition, with the help of Eq. 2.8 and counting the number of total elements and the number of elements containing less than 85% void, the porosity level can be calculated. It is worth noting that the benefit of utilizing this approach is based on considering the internal porosity in each as-fabricated sample [142].

$$\%\ of\ Porosity = \frac{Number\ of\ void\ elements}{Number\ of\ total\ elements} \tag{2.8}$$

2.4. Results and Discussion

2.4.1. Model Validation

Before examining the effect of particle and substrate initial conditions on particle deformation, it is necessary to assure the accuracy of the simulation approach. It is assumed that a 29 µm Ti-6Al-4V particle is deposited by cold spray, which means that both particle and substrate temperatures are at 298 K. Also, particle velocity is assumed to be 741 m/s [145]. After simulating the noted condition, the final deformed shape of both particle and substrate can be represented by Figure 2.4. As illustrated, particle and substrate are significantly deformed, and the particle temperature (TEMPMAVG) the substrate equivalent plastic strain (PEEQ) values are higher in the edges where adiabatic shear instability can occur. Also, a uniform ring-shaped area with the highest PEEQ can be achieved on the substrate surface. These prove that CEL can predict substrate deformation, particle final deformed shape, and adiabatic shear instability region as it has already been proven by Xie et.al [137].

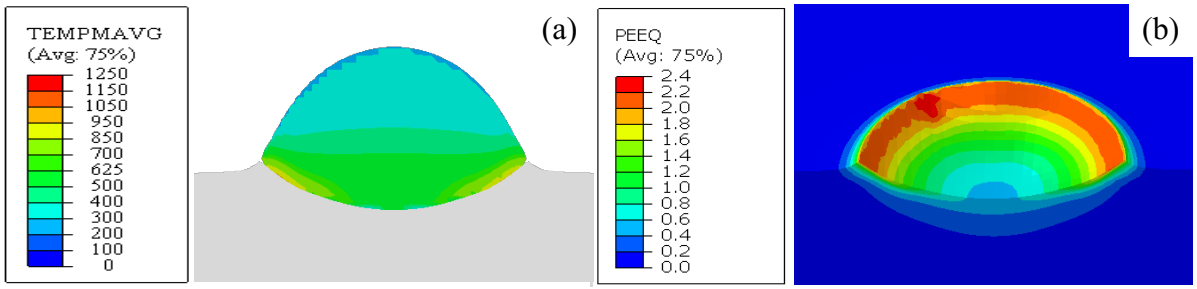

Figure 2.4. a) Particle final deformed shape and b) PEEQ distribution on the substrate surface after 20 ns of the impact of a 29 µm Ti-6Al-4V particle with the velocity of 741 m/s and the temperature of 298 k on a Ti-6Al-4V substrate at the temperature of 298 k.

On the other hand, by studying the changes of equivalent plastic strain and temperature for substrate and particle as shown in Figure 2.5, it is observed that CEL is only capable of studying substrate deformation numerically, which is because of the fact that the value of equivalent plastic strain and temperature should reach a steady state situation. On the other hand, for the Eulerian particle only the mean value of each variable can be reported which is lower than the actual value. The initial zero value for particle equivalent plastic strain and temperature is based on the fact that the material has not reached that specific node yet. Also, the high increase at the beginning of the impact in both equivalent plastic strain and temperature is because of the high strain rate [137].

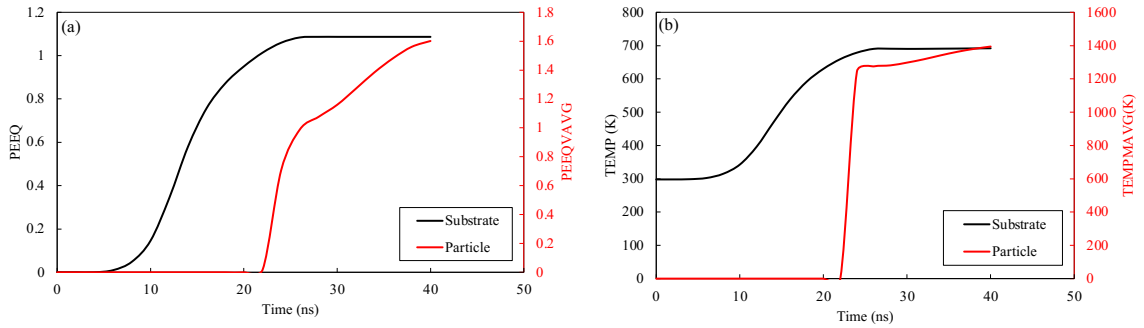

Figure 2.5. Changes of a) particle and substrate PEEQ and b) particle and substrate temperature versus time.

Finally, it is necessary to make sure the mesh size is appropriate for the problem to be solved. For that, the ratio of artificial strain energy and internal energy should be less than 5% in the region where a steady-state is reached. This is because at the beginning of the impact, due to noises, this ratio might be higher than 5%. In the case of the noted simulation, this ratio is around 3%, Figure 2.6. This shows that the mish size was defined accurately to control the hourglass and eliminate the propagation of zero-energy modes, leading to inaccurate outcomes [137].

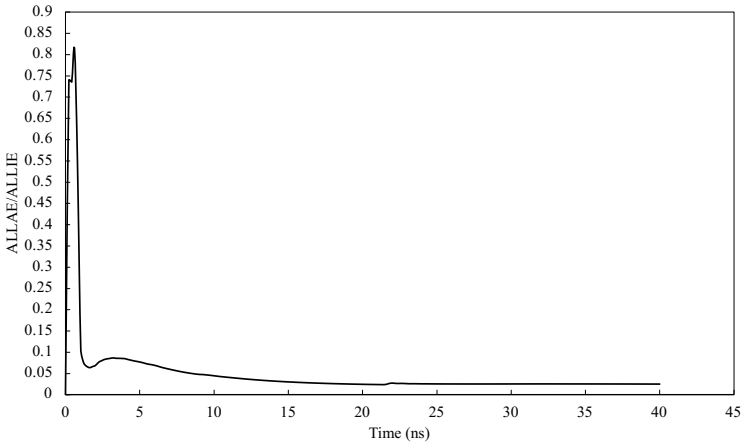

Figure 2.6. a) Changes in the ratio of artificial strain energy and internal energy by the passage of time.

2.4.2. Effects of Particle and Substrate Initial Condition on Particle Deformation

2.4.2.1. Particle Velocity

While using HVAF process as a solid-state additive manufacturing technique, an elevated solid particle will be imping on the substrate surface at high velocity [13]. Therefore, it is necessary to examine the effect of particle velocity on its deformation. For this purpose, a solid Ti-6Al-4V particle with a temperature of 873 K and velocity of 600, 650, or 700 m/s is impacting on a Ti-6Al-4V substrate with the temperature of 673 K, condition V1 in Table 2.2. The results show that enhancing particle velocity will increase particle deformation significantly because of improving particle's kinetic energy required for the deformation, Figure 2.7 and Figure 2.8.

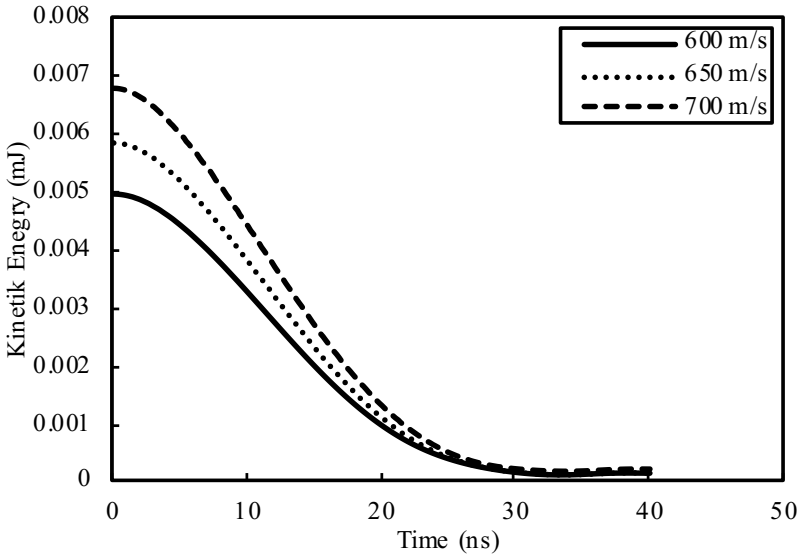

Figure 2.7. The effect of particle velocity on kinetic energy.

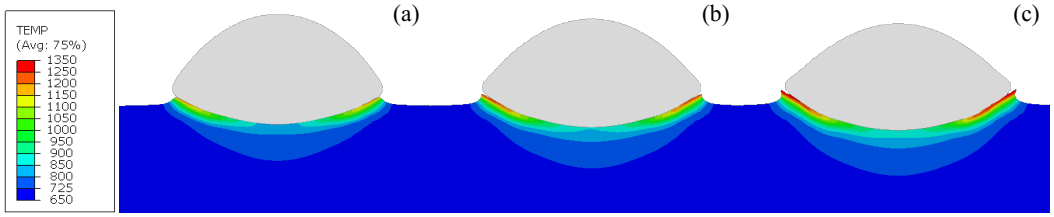

Figure 2.8. The final shape of a Ti-6Al-4V particle impacted with the initial temperature of 873 K on a Ti-6Al-4V substrate with an initial temperature of 673 K and particle velocity is a) 600, b) 650, and c) 700 m/s.

By boosting particle velocity, substrate deformation will also be affected, which means that the substrate will deform more, and its equivalent plastic strain (PEEQ) will increase. This increase will be more significant at the first five nanoseconds (ns) of the impact, which can be because of high strain rate deformation. In addition, due to the heat produced during the deformation, the final substrate temperature will rise as shown in Figure 2.9. For instance, at 40 ns after the impact, when particle velocity increases from 600 m/s to 700 m/s, PEEQ of the substrate will increase almost 22%, and the maximum temperature of the substrate will also increase by 50 K.

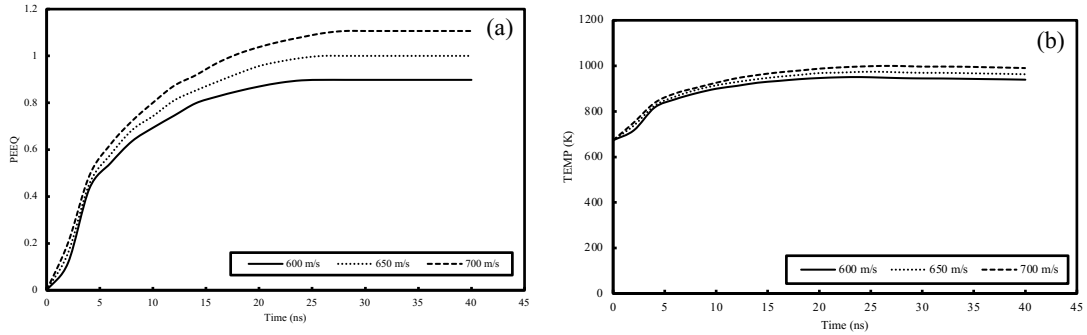

Figure 2.9. The examination of particle velocity effect on the changes of substrate a) PEEQ and b) temperature by the passage of time.

2.4.2.2. Particle Temperature

Another factor that can alter particle deformation is the temperature which has been taken into account by considering a 29 µm Ti-6Al-4V particle with the velocity of 600 m/s and temperature of 873, 973, 1073, 1173, and 1273 K impacting on a Ti-6Al-4V substrate with a temperature of 673 K, "Case V2" in Table 2.2. Since increasing a component temperature will seize the deformation with the help of thermal softening, a particle will deform more noticeably as its initial temperature is enhanced, Figure 2.10. Moreover, when an elevated temperature particle is impinging on a substrate, the produced material jet is only formed of the particle itself. On the other side, a softer particle will apply less force on the substrate surface for its deformation, so it can be expected that substrate deformation is affected negatively by enhancing particle temperature. Also, because of having an adiabatic heat exchange system in the contact area of deposited particle and substrate, no heat will exchange, which means that particle temperature has a limited effect on the final substrate temperature as shown in Figure 2.11.

When a solid particle is impinging on a substrate, adhesion requires to happen to produce a coating. Some researchers hypothesize that adhesion comes from a welding-like process which a localized melting occurs in the contact area. As a result, particles and substrate will diffuse into each other, and bonding will occur. On the other hand, some other works the bonding is described only by plastic deformation [137]. In this simulation, in all conditions, neither particle nor substrate temperature exceeds the melting point. Therefore, it can be expected that only plastic deformation and having a pressure gradient is the cause of adhesion.

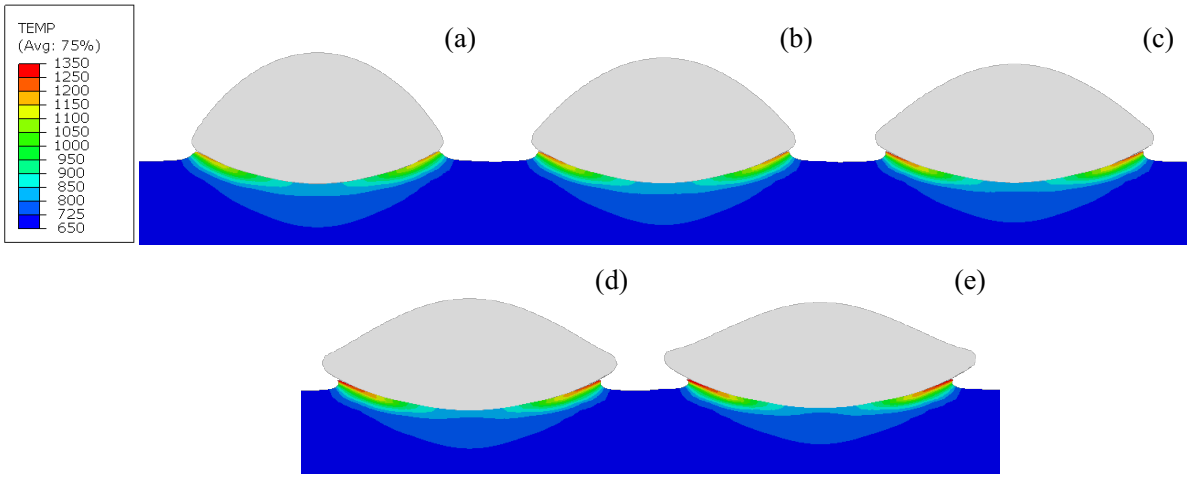

Figure 2.10. The final deformed shape when a Ti-6Al-4V particle with the velocity of 600 m/s impacted on a Ti-6Al-4V substrate with the temperature of 673 K when initial particle temperature is a) 873, b) 973, c) 1073, d) 1173, and e) 1273 K.

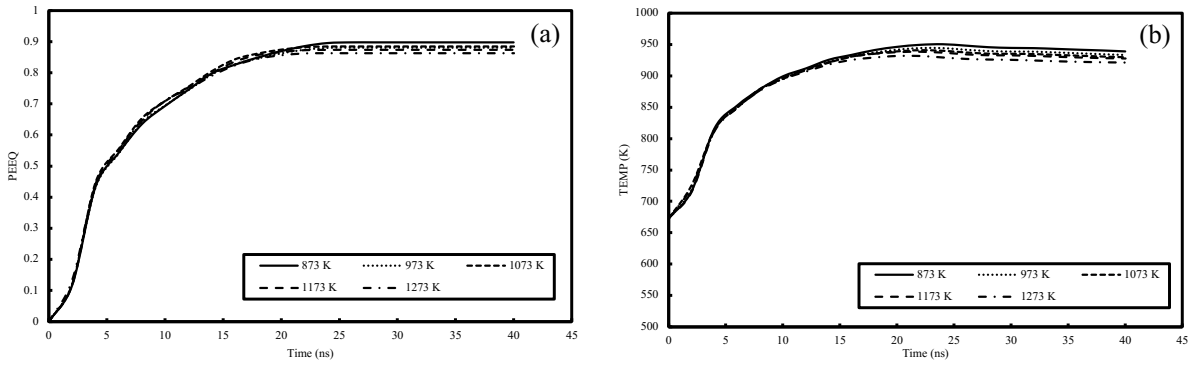

Figure 2.11. Effect of particle temperature on the substrate a) PEEQ and b) temperature by the passage of time.

2.4.2.3. Substrate Temperature

In HVAF process, because of the existing flame, heating the substrate is inevitable. In addition, pre-heating the substrate is an effectual factor to increase the adhesion of particles to the substrate. So, it is essential to take substrate temperature into account [13]. For inspecting the effect of the noted variable on the particle and substrate deformation, it is assumed that a particle with the temperature equal to 1073 K and with the velocity of 600 m/s is impinging on a substrate surface with the temperature of 473, 573, 673, or 773 K, "V3" in Table 2.2. By having higher substrate temperature, particle deformation will decrease, and the importance of material jet becomes less critical, Figure 2.12. This reduction in particle deformation is based on increasing substrate temperature, which cause the solid deposited particle impacts on softer surface. So, the particle will deform less and substrate deformation increases which can be understood by studying PEEQ and TEMP changes by the passage of time, Figure 2.13 [99, 137]. For instance, by increasing substrate temperature from 473 K to 773 K, the value of PEEQ and TEMP will increase around 20 % and 30 %, respectively.

To put it in other words, a higher initial temperature enhances the role of the thermal softening effect. Thermal softening will decrease the material resistance to shear flow so that the elevated temperature part will deform more noticeably by the same amount of provided energy comparing to the cooler part. As a result, the plastic strain will increase, and more heat will be produced. This will increase the final temperature even to values higher than the melting point [137].

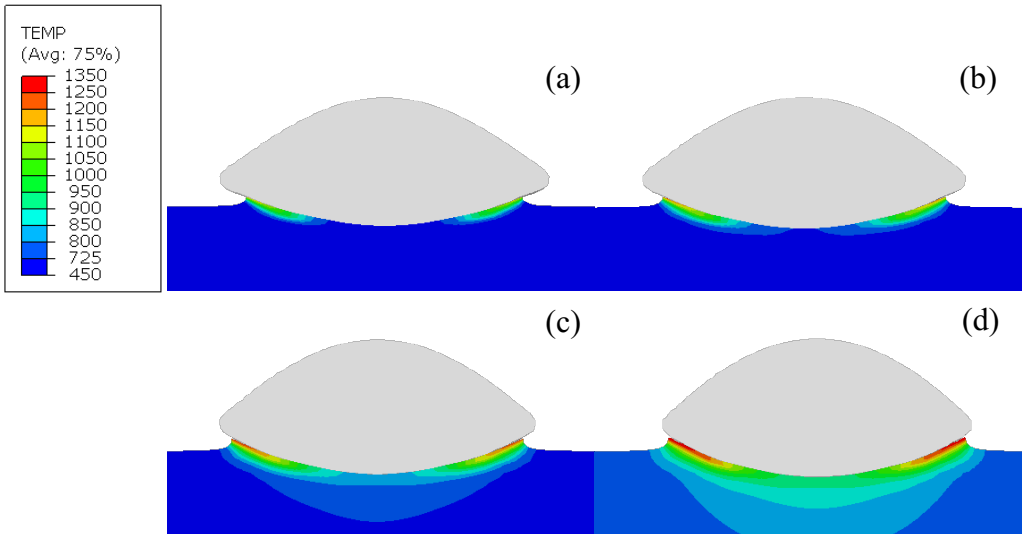

Figure 2.12. The final deformed shape when a Ti-6Al-4V particle with the velocity of 600 m/s and the temperature equal to 1073 impacted on a Ti-6Al-4V substrate when its initial temperature is a) 473 K, b) 573 K, c)673 K, and d)773 K.

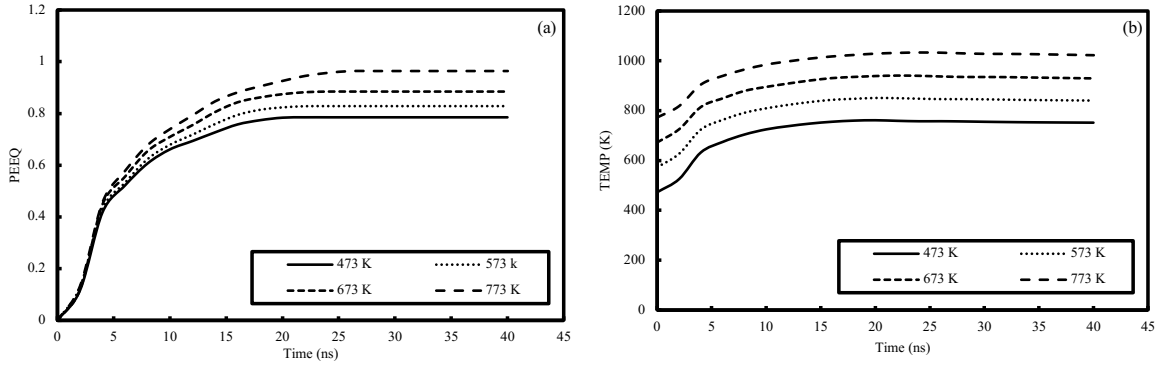

Figure 2.13. Effect of substrate temperature on the substrate a) PEEQ and b) TEMP by the passage of time.

2.4.2.4. Flattening Ratio

Particle deformation is quantified by investigating the flattening ratio has been calculated via Eq. 8 and reported as shown in Figure 2.14. As illustrated, particle deformation will increase by enhancing particle velocity because of improving particle initial kinetic energy. For instance, by increasing particle velocity from 600 to 700 m/s, the flattening ratio improves by 13.5%. In addition, increasing particle temperature will lead to thermal softening, which will boost particle flattening ratio and deformation. For example, flattening ratio will increase by 49.4% when particle temperature raises from 873 to 1273 K. On the other hand, rising substrate temperature and having a softer substrate will decrease particle deformation and the flattening ratio [99]. To be more specific, increasing substrate temperature from 473 to 773 K will decrease flattening ratio by 7.63%. Hence, it can be concluded that increasing particle temperature can increase flattening ratio and particle deformation more significantly comparing to increasing particle velocity. This shows that for sufficiently large particle speeds particle deformation is affected more noticeably by particle thermal softening compared to particle kinetic energy.

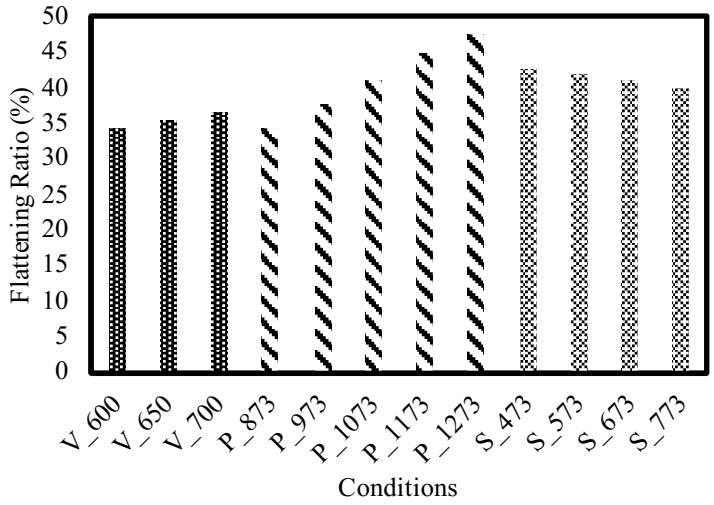

Figure 2.14. Effect of particle velocity, particle temperature, and substrate temperature on a deposited Ti-6Al-4V particle flattening ratio.

2.4.3. Porosity Level of As-Fabricated HVAF Samples

In this step, based on the conditions mentioned in Table 2.3, the effect of particles and substrate initial conditions on porosity level are examined. First, it is essential to visualize the density of as-sprayed samples. For that purpose, the conditions in which particle temperature is 1273 K, particle velocity is 650 m/s, and the substrate temperature is 673 K will be used as the example of as-sprayed samples to study the particle size distributions effect. As shown in Figure 2.15, both final shapes are highly dense. However, for examining the internal porosity, i.e. Figure 2.16, each deformed shape's outer surface is eliminated. This presents that when 5 µm particles are in-between 10 µm particles, more porosity can be achieved, which is because of blocking the deformation of 10 µm particles. Therefore, it is important to use an approach to count internal pores in as-fabricated samples for measuring porosity level, which has already been explained in previous section.

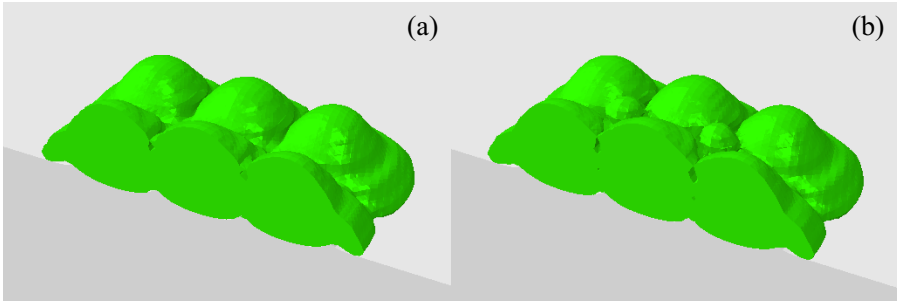

Figure 2.15. The final deformed shape of conditions which Ti-6Al-4V particles temperature is 1273 K, particles velocity is 650 m/s, the substrate temperature is 673 K, and a) only 10 µm particles and b) 5 & 10 µm particles impacted on Ti-6Al-4V substrate.

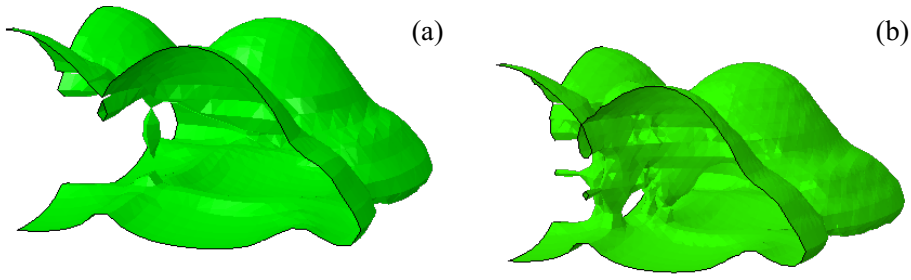

Figure 2.16. Investigating the internal porosity of the conditions that Ti-6Al-4V particles temperature is 1273 K, particles velocity is 650 m/s, the substrate temperature is 673 K, and a) only 10 µm particles and b) 5 & 10 µm particles impacted on Ti-6Al-4V substrate.

Based on the described approach, for the condition when only 10 µm with initial temperature equals to 1273 K and velocity of 650 m/s are impacting on the substrate at the initial temperature equals to 673 K, a cube has been extracted, Figure 2.17. Then the porosity level is calculated and reported in Figure 2.18. For both cases, the porosity level will decrease by enhancing particle temperature and velocity because of having particle thermal softening and improving particle kinetic energy, respectively. For instance, when only 10 µm particles impact substrate, by increasing particle velocity from 600 to 700 m/s, the porosity level decreases by 75%. This value for the conditions in which both 5 and 10 µm are impacting on the substrate is equal to 53%. Moreover, by increasing impinging particles temperature from 873 to 1273 K, the porosity level decreases almost by 81% and 60 % when only 10 µm particles and a combination of 5 and 10 µm particles are impacting on the substrate, respectively. On the other hand, although enhancing substrate deformation will decrease particle deformation, but because of the peening effect, the porosity level remains almost unchanged (as described in [99, 114]. To provide more details, by increasing substrate temperature from 573 to 773 K, the porosity level of as-sprayed samples once only 10 µm particles and a mixture of 5 and 10 µm particles drop almost by 34 % and 14 %, correspondingly.

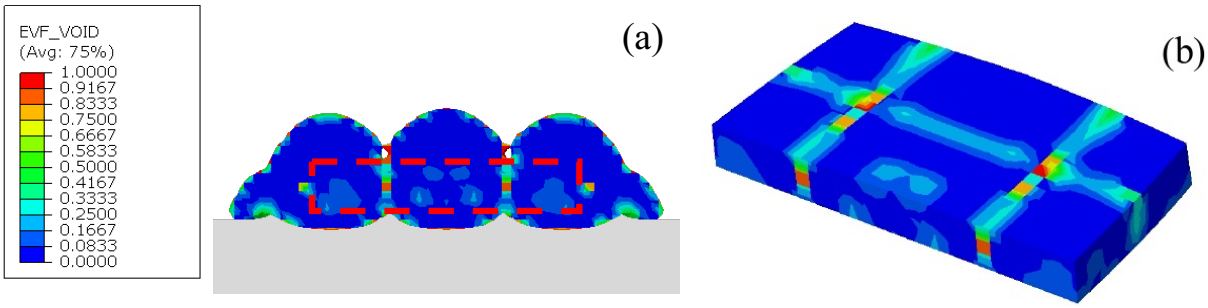

Figure 2.17. (a) Cross section view of 18 particles with 10 micrometers deposited Ti-6Al-4V particles with a temperature of 1273 K and velocity of 650 m/s impacting on the substrate with initial temperature equals to 673 K, (b) Extracting a cube in the middle of the deposited part.

It can be concluded that for enhancing samples' density, the most influential parameters are particle velocity and temperature. On the other side, increasing substrate temperature will have an insignificant effect on density enhancement of as-sprayed coatings. Also, by adding 5 µm particles in between 10 µm ones, the porosity level will increase because the amount of inter-particle pores

will rise. This can be related to the type of particle impact pattern, which will cause deformation blockage of 10 μm particles by 5 μm particles.

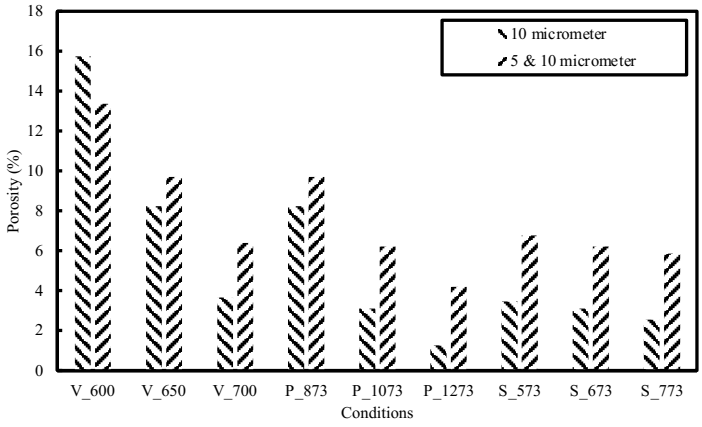

Figure 2.18. The porosity level of each condition is noted in Table 2.3 when only 10 μm or 5 & 10 μm Ti-6Al-4V particles are deposited on Ti-6Al-4V substrate by HVAF process.

2.4.4. Residual Stress of As-sprayed HVAF Components

During cold spray process, the residual stress can be rooted in peening effect, thermal stress, and quenching. Peening effect occurs because of the impact of high velocity particles. Thermal stress can be based on the mismatch of thermal expansion coefficient between particles and substrate, which can lead to have either tensile or compressive residual stress. In the end, quenching is defined by fast cooling rate of the deposited particles or substrate [100]. While particles are impinging on already deposited layers, peening effect and quenching will define the final residual stress. The prominence of peening effect (compressive stress) or quenching (tensile stress) is based on the temperature difference between depositing particles and the temperature of already deposited particles, the ability to be plastically deform, and work hardening properties [146].

In this paper, for examining the residual stress, the pressure stress values at 34 ns after the impact has been selected on the symmetric axis (Y-axis), Figure 2.19. In the presented outcomes, the normal distance has been used, which zero value is the contact area between deposited particles and substrate and -1 represent the bottom surface of substrate. Also, it is worth noting that compressive stress is presented by positive sign and tensile stress is reported by negative sign. In the end, because the density of samples was higher when only 10 μm Ti-6Al-4V particles were impinging, only the residual stress in these as-sprayed samples will be investigated in this section.

First, in all conditions, the residual stress in substrate near the contact surface is compressive, which represents the importance of peening effect. To be more specific, when particle velocity increases from 600 to 700 m/s because of rising the impact kinetic energy, the peening effect becomes more significant. Therefore, the value of maximum compressive stress in substrate will increase from 461 to 521 MPa. On the other hand, increasing particle temperature will have more noticeable effect on particle itself because of thermal softening. This leads to the fact that increasing particle temperature from 873 to 1273 K while substrate temperature is 673 K will decrease substrate residual stress from 406 to 368 MPa. This can be related to the fact that increasing particle temperature will seize its deformation and decrease equivalent plastic strain of substrate and its deformation, Figure 2.11. Finally, when substrate temperature increases from 573

to 773 K, because of thermal softening effect, its deformation will increase. Therefore, Ti-6Al-4V substrate residual stress near the contact surface will decrease gradually from 483 to 438 MPa. Having higher substrate temperature will increase the influence of thermal softening resulting in lower residual stress.

In the next step, it is important to study the effect of particle and substrate initial conditions on the residual stress of deposited particles. For initial deposited layers, by increasing all three variables, i.e., particle temperature, particle velocity, and substrate temperature, the residual stress will be compressive because of peening effect. On the other side, on the top layer of deposited particles, because peening effect is not significant, particles cannot deform expressively, so the residual stress will be tensile. To examine each variable's effect in more detail, when particle velocity increases from 600 to 700 m/s, because of providing more kinetic energy and particle deformation, the maximum residual compressive stress will increase from 843 to 871 MPa. Also, the maximum residual compressive stress will increase from 926 up to 1170 MPa when particles initial temperature increases from 873 to 1273 K due to thermal softening. In the end, increasing substrate temperature has a unsignificant negative effect on porosity level, but a noticeable undesirable consequence on particle deformation, Figure 2.14 and Figure 2.18. Therefore, because of insignificant changes in porosity level, the changes in residual stress will also become unimportant. For instance, by increasing substrate temperature from 573 to 773 K, the maximum residual compressive stress increases only for 50 MPa. In the end, it can be concluded that particle temperature can increase compressive residual stress in a more noteworthy way comparing particle velocity or substrate temperature.

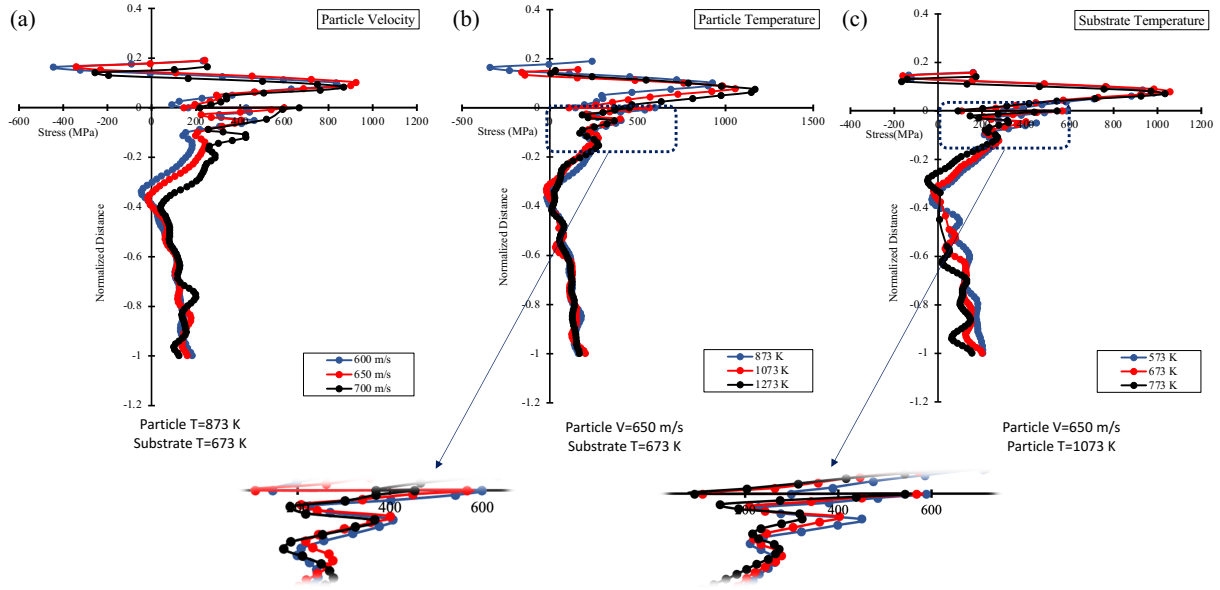

Figure 2.19. Effect of a) particle velocity, b) particle temperature, and c) substrate temperature on residual stress distribution in deposited 10 µm Ti-6Al-4V particles on Ti-6Al-4V based on conditions noted in Table 2.3.

2.5. Conclusion

This paper targets to investigate the effect of using HVAF to enhance deposited solid Ti-6Al-4V particle velocity and temperature with the hope to increase the density of as-sprayed samples. Thus, a proper simulation method must be applied for fulfilling this purpose by considering the Mie-Gruneisen equation of state and Johnson-Cook for elastic and plastic parts of the simulation, correspondingly. Moreover, a finite-element-based approach known as coupled Eulerian-Lagrangian (CEL) is required to solve the noted models.

Applying the noted simulation shows that enhancing particle velocity will provide more kinetic energy for the deformation, which increases particle deformation. This can enhance the density of as-sprayed samples and increase the residual compressive stress in deposited particles. Also, providing more particle temperature will seize particle deformation because of thermal softening, which can increase sample's density more extensively alongside the residual compressive stress in as-fabricated components. On the other hand, by enhancing substrate temperature, the substrate will go through the thermal softening process and becomes soft. Therefore, the particle impinging on a softer surface and its deformation will decrease noticeably. Although enhancing substrate temperature will decrease particle deformation, its effect on porosity level and residual stress is insignificant due to the pining effect. In the end, because of the chosen pattern when multiple 5 and 10 μm Ti-6Al-4V particles are impinging on a Ti-6Al-4V substrate, the enhancement in density will not be as significant as when only 10 μm Ti-6Al-4V particles are impacting. This can be because of deformation blockage role that 5 μm are performing.

So far, by the help of depositing Ti-6Al-4V particles by using cold spray, it has been shown that enhancing particle velocity by using helium as the carrier gas will lead to more particle deformation and density [105]. However, to the author's knowledge, the effect particle and substrate preheating by using another thermal spray technique like HVAF as a solid-state additive manufacturing technique has not been investigated. Hence, to validate the outcomes noted above and to understand the effect of particle and substrate preheating, it is necessary to use HVAF process to manufacture Ti-6Al-4V samples by depositing powders represented in Figure 2.2.3 above.

Chapter 3

Effect of Particle and Substrate Pre-Heating on the Oxide Layer and Material Jet Formation in Solid-state Spray Deposition: A Numerical Study[2]

3.1. Abstract

In a solid-state deposition technique such as cold spray (CS) or high-velocity air-fuel (HVAF), particle and substrate initial conditions play a crucial role in particle deformation and its adhesion strength to the substrate. In these thermal spray techniques, the deposited particle and the substrate are required to deform plastically; hence, both components are usually metallic. An oxide layer at the surface of these metallic components may avoid producing a metallurgical bonding and strong adhesion between them. To better understand the effect of particle and substrate initial conditions, e.g. particle velocity, particle temperature, and substrate temperature, on the formation of metallurgical bonding, it is necessary to examine particle and substrate oxide layer failure. In this work, the effect of a 20 µm Ti-6Al-4V particle and a Ti-6Al-4V substrate initial conditions on the failure of their oxide layer during impact has been studied. The results show that the presence of an oxide layer increases the required critical velocity for particle adhesion on the substrate. Furthermore, regardless of the chosen initial conditions, the particle oxide layer would fail in the adiabatic shear instability region because of the severe deformation that the particle experiences upon impact. This study shows that a stronger bonding between the deposited particle and the substrate can be achieved by increasing the particle velocity and substrate temperature, as they increase the extent of the failed oxide layer region of the substrate. Rising particle temperature increases particle deformation and has no significant effect on the adhesion between the particle and substrate.

3.2. Introduction

Cold spray is a unique thermal spray technique that allows solid-state deposition without oxidation or decomposition [105-160]. In this process, solid particles impact the substrate surface at a high velocity while retaining their low temperature. Upon impact, particles severely deform at a very high strain rate (up to 10^9 s^{-1}), leading to the oxide layer failure followed by a metallurgical bonding, and eventually the formation of coatings [13, 73, 133]. In fact, the brittle oxide layer will not undergo the same significant amount of deformation that a particle or a substrate goes through which results in its failure [87]. The failure of the oxide layer produces small oxide debris and provides two new metallic surfaces in direct contact [147].

The produced oxide debris must be ejected with the help of adiabatic shear instability (ASI) and the material jetting [88, 148]. ASI is a transformed local shear strain caused by the pressure gradient created during the particle deformation. ASI helps thermal softening, governs the deformation, and significantly increases the particle temperature. The higher temperature and

[2] Khamsepour, P., Moreau, C. & Dolatabadi, A. Effect of Particle and Substrate Pre-heating on the Oxide Layer and Material Jet Formation in Solid-State Spray Deposition: A Numerical Study. *J Therm Spray Tech* (2022). DOI: https://doi.org/10.1007/s11666-022-01509-7

thermal softening combination create an out-flowing material jet that ejects the broken oxide layer [72]. Hassani-Gangaraj et al. [77] suggested that the thermal softening is not the cause of material jet formation. They state that the produced tensile stress at the edges of the contact area of the deposited particle and substrate is the reason for material jet formation. Chen et al. [149] also studied the de-bonded sprayed solid particles and showed that a metallurgical bonding could be formed only after the oxide layer fails and the newly formed metallic surfaces are put in direct contact.

The effects of particle velocity on the adhesive strength of cold spray deposited particles have been investigated previously [145, 150-154]. As an example, Legoux et al. used a low-pressure cold spray system to show that increasing particle velocity could enhance adhesive strength and deposition efficiency [145]. However, it is not possible to increase particle velocity limitless [145]. For increasing the adhesive strength even more, it has been proposed that increasing substrate temperature can play a key role [145, 150-154]. A study by Xie et al. suggests that substrate pre-heating can cause softening, crater depth enhancement and more substrate deformation. As a result, a material jet can be produced from the deposited particle and the substrate leading to bonding with higher adhesive strength [152]. However, it is worth noting that increasing the substrate temperature can increase the substrate oxide layer thickness and alter the required critical velocity for bonding [150].

Considering current capabilities, the study of particle deformation and oxide layer failure using experimental techniques is very difficult because these phenomena occur in tens of nanoseconds [137]. This necessitates the use of a modeling system as an alternative approach. The finite element method (FEM) has been widely used for studying the deformation of deposited particles using CS on the assumption that a particle is in an Eulerian or Lagrangian framework [69, 99, 139]. In the previous studies, FEM was also utilized to assess the effect of the velocity and temperature of a particle on its deformation upon impact [99, 155]. The behavior of the oxide layer of a particle when impacting the substrate during the CS process has been widely studied [87, 156-158]. Rahmati et al. [87] assumed that the oxide layer could deform until it reaches failure displacement which has a low numerical value because of its brittleness. They showed that the particle core dominates the deformation process. This means that the material response of the oxide layer is insignificant due to the high kinetic energy of the impact. Hence, that oxide layer would deform independent from its material properties and its failure would only depends on displacement at the failure. They also investigated the effect of the failure displacement of the oxide layer of copper on its failure, by developing a model to illustrate the bonded and de-bonded areas of the impacted particle [87].

This study tries to continue the work that has been carried out before by Rahmati et al. [87] by taking the effect of particle and substrate temperature on oxide layer failure into consideration. Since a nanometric-scale oxide layer has been proven to show ductile behavior, both using experiment and molecular dynamic methods [87, 158], an elastic-plastic damage numerical examination has been developed by assuming that a 20 μm Ti-6Al-4V particle is deposited using HVAF toward a Ti-6Al-4V substrate while both parts are covered with an 80 nm oxide layer.

3.3. Numerical Methodology

3.3.1. Mie-Grüneisen Equation of State

The Mie-Grüneisen Equation of State (EoS) was used to investigate the elastic deformation of deposited particles. This model is based on crystal structure and a connection among internal energy, thermal vibrational energy, and potential energy at zero temperature [5-8). The initial form of the Mie-Grüneisen EoS is obtained using the vibrational theorem and the Grüneisen equation, presented as Eq. 3.1 [140-141]:

$$P - P_H = \Gamma_0 \frac{\rho_0}{p}(E_m - E_H) \tag{3.1}$$

where P is total pressure, E_m denotes internal energy per unit mass, P_H stands for Hugoniot pressure, and E_H indicates specific energy. Moreover, $\Gamma_0$is material constant and ρ_0 is reference density, and p represents pressure stress. The values of internal energy per unit mass and Hugoniot pressure can respectively be calculated via Eq. 3.2 and Eq. 3.3 [140-141]:

$$E_H = \frac{P_H \eta}{2\rho_0} \tag{3.2}$$

$$P_H = \frac{\rho_0 c_0^2 \eta}{(1 - s\eta)^2} \tag{3.3}$$

where η (nominal compressive volumetric strain) is equal to $1 - \rho_0/\rho$ and $\rho_0 c_0^2$ designates the elastic modulus at a low nominal strain rate. Furthermore, c_0 and s are material constants that can make a link between shock velocity (U_s) and particle velocity (U_p). The final form of the Mie-Grüneisen EoS is obtained using Eq. 3.4 [140-141]:

$$P = \frac{\rho_0 c_0^2 \eta}{(1 - s\eta)^2} \left(1 - \frac{\eta \Gamma_0}{2}\right) + \Gamma_0 \rho_0 E_m \tag{3.4}$$

As this model can only represent the hydrostatic behavior, elastic models and shear modulus were used to examine the deviatoric behavior [73].

3.3.2. Johnson-Cook Model

A Johnson-Cook plasticity model was used to investigate deformation at a high strain rate. This model is reproduced in Eq. 3.5 below [73]:

$$\sigma = \left(A + B\varepsilon_p^n\right)\left(1 + C ln\frac{\dot{\varepsilon}_p}{\dot{\varepsilon}_0}\right)\left(1 - (\frac{T - T_r}{T_m - T_r})^m\right) \tag{3.5}$$

where A, B, C, n, and m are material constants, ε_p, $\dot{\varepsilon}_p$, σ, $\dot{\varepsilon}_0$, T_r, T_m, and T are equivalent plastic strain, plastic strain rate, flow stress, reference strain rate, reference temperature, melting point, and temperature, respectively.

3.3.3. Johnson-Cook Damage Model

A damage model assumes that damage or a crack is initiated when the ratio of equivalent plastic strain ($\Delta\bar{\varepsilon}$) to equivalent fracture strain ($\bar{\varepsilon}_f$) equals 1, as shown in Eq. 3.6 [141, 159-161]:

$$D = \sum \frac{\Delta\bar{\varepsilon}}{\bar{\varepsilon}_f} = 1 \tag{3.6}$$

The present study used the Johnson-Cook damage model in connection with the Johnson-Cook plasticity model to examine fracture initiation. To calculate the equivalent fracture strain ($\bar{\varepsilon}_f$), Eq. 3.7 was used [141, 159-161]:

$$\bar{\varepsilon}_f = [d_1 + d_2.\exp(d_3\eta)] \times \left[1 + d_4.\ln\left(\frac{\dot{\bar{\varepsilon}}}{\dot{\bar{\varepsilon}}_0}\right)\right] \times \left[1 + d_5.\left(\frac{T - T_{room}}{T_m - T_{room}}\right)\right] \tag{3.7}$$

where d_1, d_2, d_3, d_4, and d_5 represent initial failure strain, exponential factor, triaxiality factor, strain rate factor, and temperature factor, respectively. It is necessary to consider damage evolution to examine the oxide layer's failure pattern during the deformation of the deposited particles [141, 159-161]. Since it is well-established in the literature, both experimentally and numerically, that the thin brittle oxide layer presents some important and non-negligible ductility [87, 158, 162-169], a ductile fracture model like Johnson-Cook has been selected to analyse the failure of the thin brittle layer [87, 170].

3.3.4. Damage evolution law

The reduction rate of material stiffness can be defined using the damage evolution law. In the current study, this rate was determined on the basis of effective plastic displacement ($\bar{u}^{pl}$) and through the use of evolution equations, Eq. 3.8 and Eq. 3.9 [87, 141].

$$\dot{\bar{u}}^{pl} = L\dot{\bar{\varepsilon}}^{pl} \tag{3.8}$$

$$\dot{d} = \frac{L\dot{\bar{\varepsilon}}^{pl}}{\bar{u}_f^{pl}} = \frac{\dot{\bar{u}}^{pl}}{\bar{u}_f^{pl}} \tag{3.9}$$

where L is element length, $\dot{\bar{u}}^{pl}$ indicates effective plastic displacement, $\dot{\bar{\varepsilon}}^{pl}$ denotes equivalent plastic strain rate, $\bar{u}_f^{pl}$ is the effective plastic displacement at the failure point, and $\dot{d}$ stands for the damage variable rate.

A linear type of damage evolution was used, where material stiffness is assumed to be fully reduced (d=1) when effective plastic displacement reaches the fracture value ($\bar{u}^{pl} = \bar{u}_f^{pl}$), as shown Figure 3.1. In the damage evolution law for examining brittle fracture, the value of $\bar{u}_f^{pl}$ was set to zero. However, for ductile fracture, the $\bar{u}_f^{pl}$ value depends on mesh size, and its accurate value must be obtained using the experimental examination. Here, in this research, the same range tested in the literature [87, 141] was used to investigate the failure of the oxide layer since carrying out the experimental work was beyond the scope of this study.

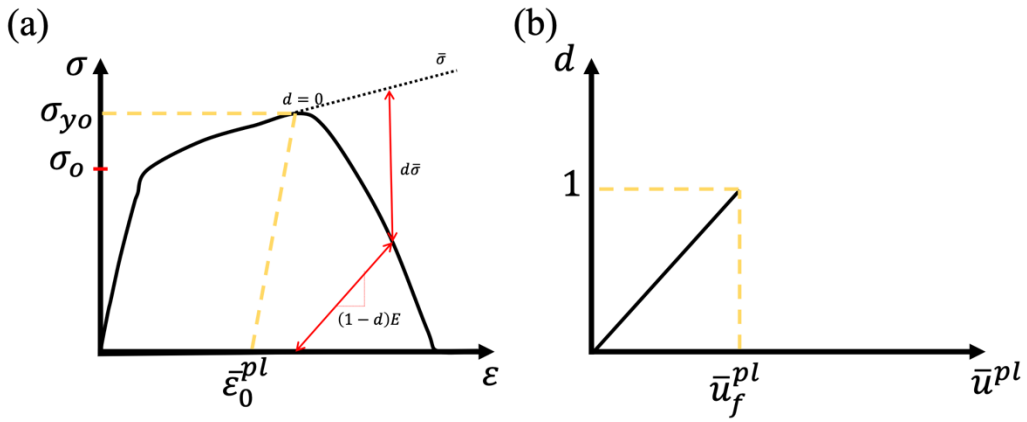

Figure 3.1. (a) Schematic stress-strain diagram of material with progressive damage reduction and (b) linear damage evolution in terms of plastic displacement.

3.3.5. Finite Element Method

The deformation of a Ti-6Al-4V solid-state particle deposited using either HVAF or CS was studied, drawing upon the Lagrangian technique on the FEM software ABAQUS/Explicit [87]. All simulations have been carried on for 8 ns which is because the oxide layers fail at the first nanoseconds of the impact. After oxide layer breakage, the particle and substrate deformation cause the production of material jet. Hence, the selected duration for examining the oxide layer failure would not only provide a fair comparison of the oxide layer failure but also avoids having highly distorted elements. Scanning electron microscopy (SEM) micrograph as well as particle size distribution curve of Ti-6Al-4V powder are shown in Figure 3.3.2. Ti-6Al-4V powder consists of spherical particles with particle diameters centered along a single mode, with maximal volume frequency at 22 µm. The D_{10}, D_{50}, and D_{90} values are 14, 20, and 29 µm, respectively, showing that the particle size distribution of Ti-6Al-4V powder is very narrow (Figure 3.3.2(b)). Thus, for this simulation, it was assumed that the 20 µm Ti-6Al-4V particle impacts a Ti-6Al-4V substrate. Figure 3.3.3 demonstrates the initial conditions of Ti-6Al-4V particle and substrate used to investigate oxide layer failure during the deposition process. An 80 nm thin brittle layer which can act as the similar to the brittle titanium oxide layer was assumed at the surface of the substrate and particle to examine oxide layer failure during the particle impact (Figure 3.3.3(a)). This thickness falls in the range used in the previous studies [6, 24-26, 32-33]. Additionally, during depositing solid particles using HVAF, due to the high temperature of the existing flame, oxidation happens which can increase the oxide layer thickness significantly. A 3D geometry is also given in Figure 3.3.3(b). It is worth noting that the particle diameter with oxide is exactly 20.16 µm; however, to simplify the reading of the text, it would namely be called a 20 µm Ti-6Al-4V particle. All the material constants used for this simulation are laid out in Table 3.1 [142-143, 162, 171]. The same material constant used for the core particle was used for the oxide layers. This is because the particle kinetic energy is significantly high which deforms the oxide films independently from their own properties. Hence, the only parameters that is important is the brittleness of the oxide film which is defined by using the formulation noted in the literature [87]. It must be noted that changes in density, shear modulus, heat conductivity, and heat capacity with temperature were considered using the formulations noted in the literature [35]. Also, according to the literature [172-173], when a Ti-6Al-4V sample is subjected to an elevated temperature environment,

titanium oxide can be formed. Hence, in this study, it is assumed that titanium oxide covered both deposited particles and the substrate surface.

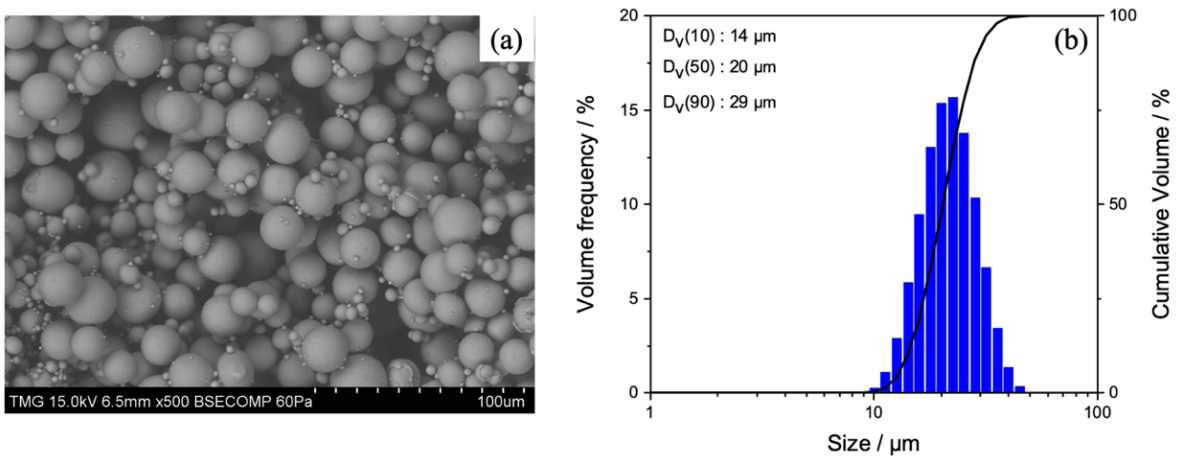

Figure 3.2. (a) SEM micrographs and (b) size distribution of the Ti-6Al-4V powder.

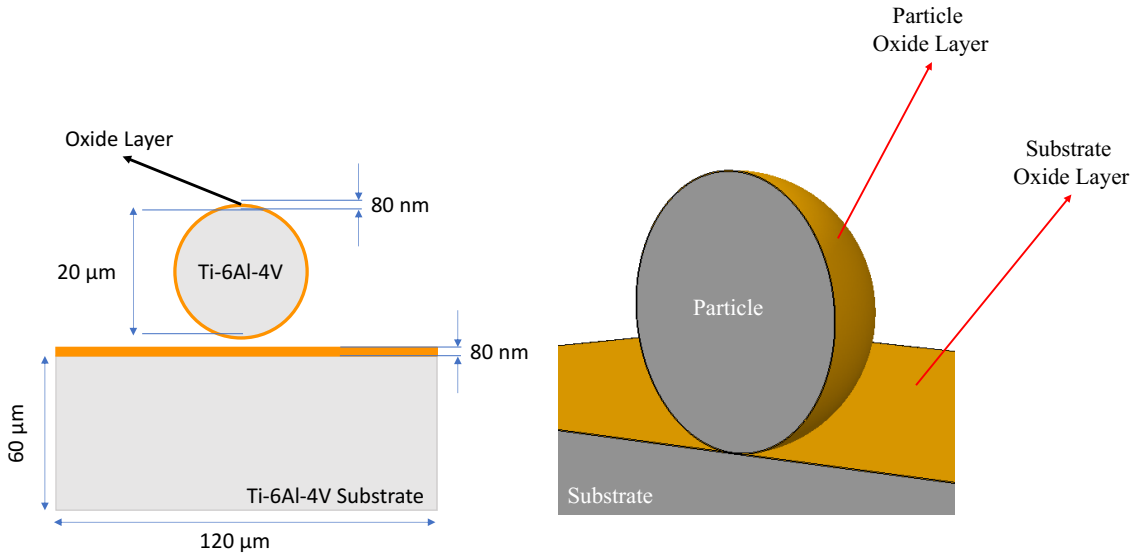

Figure 3.3. The geometry was used to investigate the oxide layer failure during the impact of a Ti-6Al-4V particle.

Table 3.1. Ti-6Al-4V material constants were used in the simulation [141, 159-161].

Property	Ti6Al4V
Density $(^{kg}/_{m^3})$	4430
Shear modulus (GPa)	41.9
$C_0\ (\frac{m}{s})$	5130
s_0	1.03
Γ_0	1.23
A (MPa)	862
B (MPa)	331
C	0.012
m	1.1
n	0.34
$T_m(K)$	1903
$T_r(K)$	298
Conductivity $(^{W}/_{m.K})$	6.6
Heat Capacity $(^{J}/_{Kg.K})$	536
d_1	-0.09
d_2	0.25
d_3	-0.5
d_4	0.014
d_5	3.87

All simulations were performed in the Lagrangian framework. After the application of material constants, the dynamic explicit solver was used. Once the parts were assembled, the interaction was defined using a friction coefficient of 0.3 and the "penalty" option. The exchange between the surfaces was assumed "general" [87, 88, 155]. To define the tie between the deposited particle and its oxide layer, the "surface to surface" option was the most efficient one. After applying initial velocity and temperature to the particle and the substrate, each part was meshed. The mesh size for the particle, the substrate area under the impact, and the oxide layer were assumed to be 0.5 μm, which is 1/40 of particle diameter and falls in an acceptable. range based on the mesh size presented in the literature [87, 137]. It is worth noting that six elements have been selected on substrate oxide layers thickness and one element on particle oxide layer thickness. The mesh type for all the parts was defined as C3D8RT (an 8-node thermally-coupled brick, trilinear displacement, temperature, reduced integration, and hourglass control) with mesh distortion control to increase the accuracy of the results [87, 137].

The present study assumed that the Ti-6Al-4V particle deposited using CS (particle and substrate temperature was 298 K) impacted the Ti-6Al-4V substrate once without considering oxide layers and the other time both parts are covered with an 80 nm oxide layer. The effective plastic displacement of the oxide layer at the failure point ($\bar{u}_f^{pl}$) was assumed 0.00025 [87]. Such numerical investigations were conducted to examine the effect of the oxide layer on the final deformed shape of the deposited particle. Also, during depositing solid particles using HVAF, deposited particles and substrate initial conditions play a key role in the failure of the oxide layer and bonding strength. Hence, to study the role of particle velocity, particle temperature, and substrate temperature on particle and substrate oxide layer failure, the selected initial conditions shown in Table 3.2 were used. It is worth noting that particle velocity effect on particle oxide layer

failure was examined in previous literature [87]. However, since the substrate oxide layer was not taken into account, this paper investigates particle velocity to gain more understanding on its effect on the failure of both particle and substrate oxide layer.

Table 3.2. Particle and substrate initial conditions were used to study the oxide layer failure.

Studied Initial Condition	Particle Velocity (m/s)	Particle Temperature (K)	Substrate Temperature (K)
Particle Velocity Effect	**550**	1073	298
	750	1073	298
	950	1073	298
Particle Temperature Effect	750	**873**	298
	750	**1073**	298
	750	**1273**	298
Substrate Temperature Effect	750	1073	**298**
	750	1073	**373**
	750	1073	**473**

All noted initial conditions noted in Table 3.2 are obtained using experimental data acquired during deposition of Ti-6Al-4V particles using an internal-diameter HVAF (ID-HVAF) system (Uniquecoat Technologies LLC, Oilville, USA). ID-HVAF has three different convergent-divergent nozzles which their difference is their length. The spraying distance for depositing coatings is in the range of 50 to 75 mm. During the experimental examination of the potential of ID-HVAF for producing Ti-6Al-4V coatings, Substrate temperatures were selected from the experimental observation using an infrared camera (Teledyne FLIR, A320) while Ti-6Al-4V particles were impinging on already deposited Ti-6Al-4V particles, as shown in Figure 3.3.4(a). The in-flight particles velocity and temperature were measured by the DPV-evolution (company, model) using light signal radiated from the heated particles above 1273 K. However, when DPV was worked in hot particle mode with an inactive laser, only the small burning particles were detected. Therefore, the cold particle mode of DPV with an active laser was used to monitor the velocity of larger and cooler in-flight particles. Figure 3.3.4(b) shows the distribution of the obtained particle velocity using the spraying condition in which air/fuel pressure are 841/827 KPa and the spraying distance is 50 mm. It is worth noting that a difference of 14 KPa between air and fuel pressure is necessary to obtain a stable flame for the deposition. The range of in-flight particle velocity was between 450 and 1050 m/s. Therefore, the selected initial particle velocity noted in Table 3.2 falls into the in-flight particles velocity measured by DPV. However, it was not possible to produce coating by depositing the particles shown in Figure 3.3.2 due to the low in-flight particle velocity. Hence, in this study, a higher particle velocity (950 m/s) compared to DPV measurement was also selected as one of the initial conditions. As mentioned above, DPV is not able to measure particle temperature below 1273 K; hence, 873, 1073, and 1273 K were selected as particle temperature [39-40]. However, computational fluid dynamic (CFD) models can be used to accurately estimate in-flight particles temperature which was beyond the scope of this paper. In the end, it is worth noting that the detected in-flight particle size was compared to the initial particle size (Figure 3.2(b)) to calibrate the DPV cold mode.

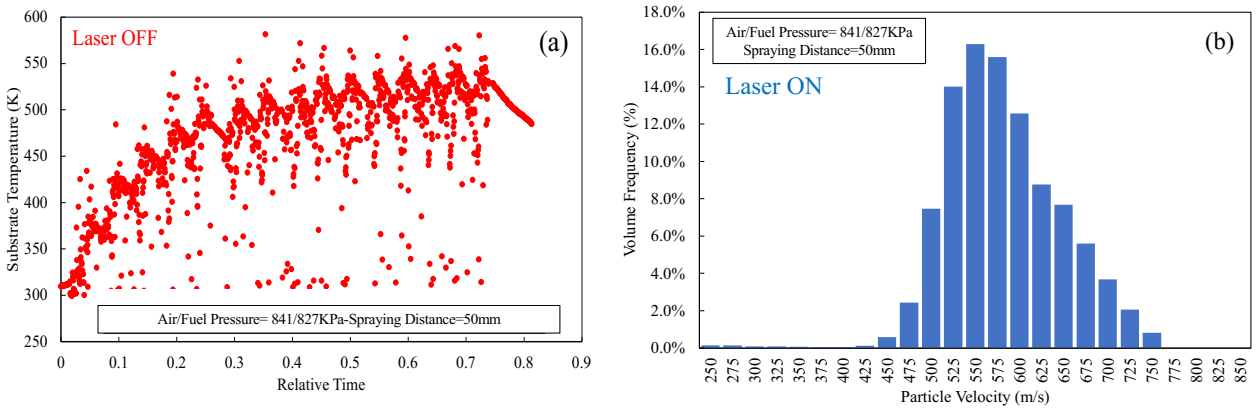

Figure 3.4. The variation in (a) substrate temperature monitored using an IR camera and (b) the distribution of in-flight particle velocity detected using cold mode of DPV using an active laser during the deposition of a Ti-6Al-4V coating using an inner-diameter HVAF gun.

3.4. Results and Discussion

3.4.1. Effect of Oxide Layer on Particle Deformation

Figure 3.3.5 shows the final deformed shape of the particle at 30 ns after the impact for the cases with and without oxide layers. For comparison purposes, the SEM micrograph of an around 20 µm Ti-6Al-4V particle deposited on a Ti-6Al-4V substrate using a cold spray (298 K) at an average velocity of 782152 m/s is also shown in Figure 3.3.5(d) [175]. Two different simulations were carried out to explore the effect of the oxide layer on the final shape of the particle. First, an 80 nm oxide layer was assumed to be around the 20 µm Ti-6Al-4V particle and at the surface of the substrate. Then, it was assumed that the particle impacted without any oxide layer. In both cases, particle temperature and substrate temperature were 298 K, and particle velocity was once 750 m/s for the time no oxide layer has been considered and 750 and 850 m/s for the time that particle and substrate were covered with an 80 nm oxide layer. Effective plastic displacement at the failure point for both oxide layers was assumed 0.00025. In Figure 3.3.5(a) and Figure 3.3.5(b), the dark blue color represents the substrate oxide layer while the orange color represents the particle oxide layer. Also, the white area in all the oxide layer examinations illustrates the region in which the oxide layer is only broken. As depicted in Figure 3.3.5, the particle in all three conditions deformed significantly. Figure 3.3.5(a) shows that when particle velocity is 750 m/s, substrate oxide did not fail meaning that no bonding can be formed. Additionally, Figure 3.3.5(c) shows that the deformed particle does not have the same dimension compared to the reported experimental results (Figure 3.3.5(f)). Hence, to enhance the deformation and to fail substrate oxide layer, it is necessary to increase impact velocity from 750 m/s to 850 m/s. Figure 3.3.5(b) shows that when impact velocity is 850 m/s, some parts of oxide layers present a curvature-like shape illustrating that the oxide layer deformed plastically before its failure due to the particle's high level of kinetic energy like the results presented in the literature [87]. By comparing the simulated and the experimental results [175], it was found that regardless of the presence of the oxide layer, the numerical method can predict accurately the shape of the deformed Ti-6Al-4V particle. However, in the numerical study, to accurately predict the deformed particle size when both particle and substrate are covered with an oxide layer, the impact velocity should be increased by 100 m/s, Figure 3.3.5(b) to Figure 3.3.5(d). This finding is aligned with previous literature suggesting that the presence of oxide layer affects the required critical velocity [22, 175]. This means that having an oxide layer around the

particle and/or substrate would increase the required velocity in which the particle can adhere to substrate metallurgically. This finding is aligned with previous literature suggesting that the presence of oxide layer affects the required critical velocity [22, 175].

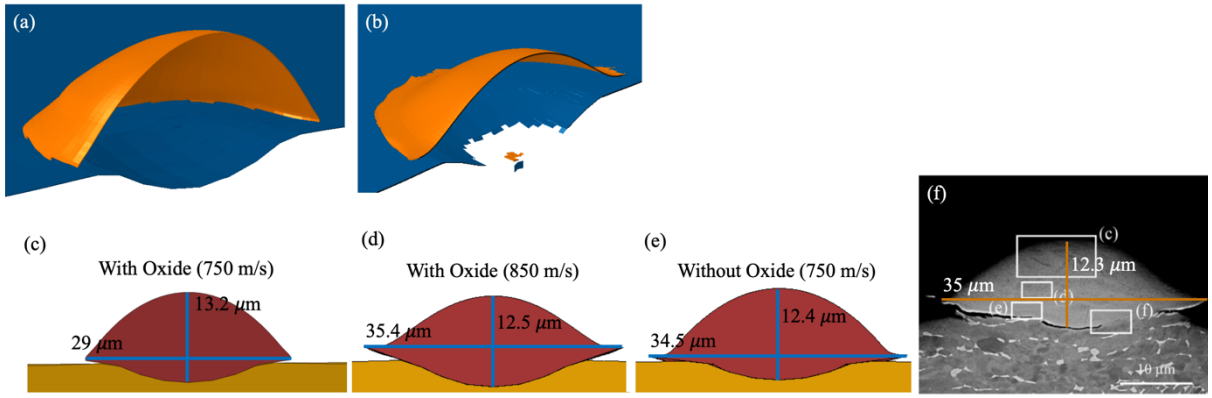

Figure 5. (a) Oxide layer when impact velocity is 750 m/s, (b) oxide layer when impact velocity is 850 m/s, (c) the final deformed shape of the particle with oxide layers impacted at 750 m/s, (d) the final deformed shape of the particle with oxide layers impacted at 850 m/s, (e) the final deformed shape of the particle without oxide layers impacted at 750 m/s, and (f) the experimental result of a 20 μm Ti-6Al-4V particle deposited on a Ti-6Al-4V substrate using the cold spray at a velocity of 782152 m/s [175].

3.4.2. Effect of Oxide Layer on Material Jet Formation

In the next step, to analyze the material jet formation, it is assumed that by using HVAF, an elevated temperature solid particle impacts a substrate, both covered with an oxide layer. To do so, particle temperature and velocity are assumed to be1073 K and 950 m/s, respectively, while the substrate temperature is kept at 298 K. The effective plastic displacement for the oxide layer was 0.0005. Figure 3.3.6 compares the pressure stress distribution in particle and substrate as a function of time after the impact. A pressure gradient is distributed in both particle and substrate when the particle impacted the substrate surface. Over time, this pressure gradient increased in a ring-shaped region known as the ASI region [72, 77]. As shown in Figure 3.3.6, pressure stress was higher in the ring-shaped ASI region, in both particle and substrate. The simulation results in Figure 3.3.6 demonstrate that at the beginning of the impact, the pressure stress is distributed at the contact area but with the passage of time tensile stress is formed at the tip of the contact area (red circles). This tensile stress becomes more significant with time leading to the ejection of the materials. In the end, it is worth noting that the gray and black colors seen in Figure 3.3.6 are regions with the stresses higher or lower than the used range in the color bar. The plastic strain (PE) distribution, as shown in Figure 3.3.7, indicates that an increase in the pressure stress causes more deformation in the ASI region. Figure 3.3.8 shows the temperature distribution at the interface of the particle and substrate. In the ASI region, due to the high amount of deformation, the temperature raised significantly which caused thermal softening. Also, the produced tensile stress at the edge of the impact surface has ejected the softened material of the particle and substrate and produced a material jet, as illustrated in Figure 3.3.6. Therefore, the same reported behavior that causes the formation of a material jet in cold spray [72, 77, 149] can be observed for deposited solid particle covered with oxide layer using HVAF.

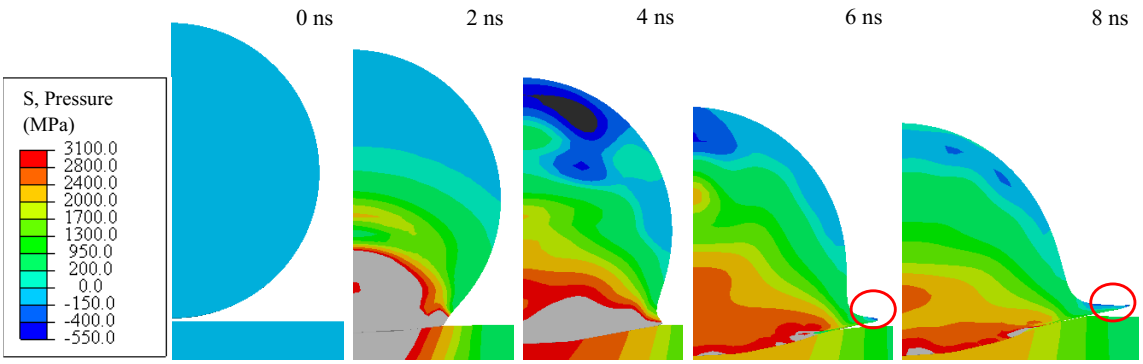

Figure 3.6. The examination of the pressure stress distribution in both particle and substrate as a function of time while Ti-6Al-4V particle temperature is 1073 K and its velocity is 950 m/s, and the substrate temperature is 298 K.

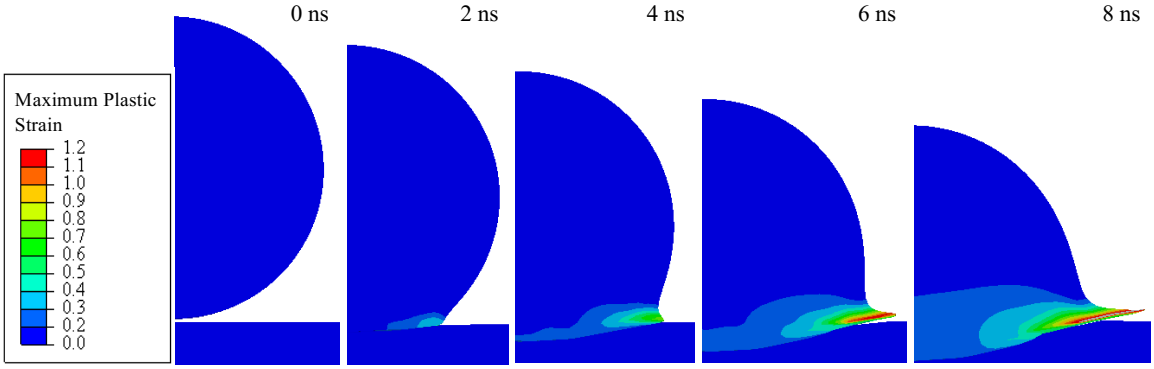

Figure 3.7. The examination of the plastic strain distribution in both particle and substrate by the passage of time while Ti-6Al-4V particle temperature is 1073 K and its velocity is 950 m/s, and the substrate temperature is 298 K.

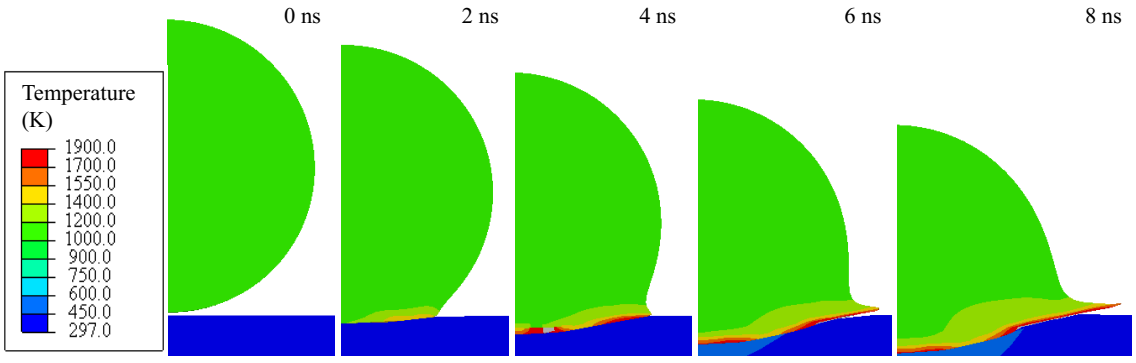

Figure 3.8. The examination of the temperature distribution in both particle and substrate by the passage of time while Ti-6Al-4V particle temperature is 1073 K and its velocity is 950 m/s, and the substrate temperature is 298 K.

In addition, as illustrated in Figure 3.3.9, the oxide layer failure occurs on the path of the ASI region where the plastic strain is higher due to larger deformation. The fractured pieces of the oxide layer are ejected with the help of the material jet before the formation of metallurgical bonding. Figure 3.3.9(a) shows that at 1.4 ns, the oxide layer went through a plastic deformation before it started to fail. At 1.6 ns (Figure 3.3.9(b)), the oxide layer went through a higher degree of deformation and failed in the regions where the plastic strain was higher. At the same time, the oxide layer on the substrate surface failed with a similar mechanism, as illustrated in Figure 3.3.9(c)-(d), which means that when the plastic strain in a ring-shaped ASI region increases, the oxide layer fails.

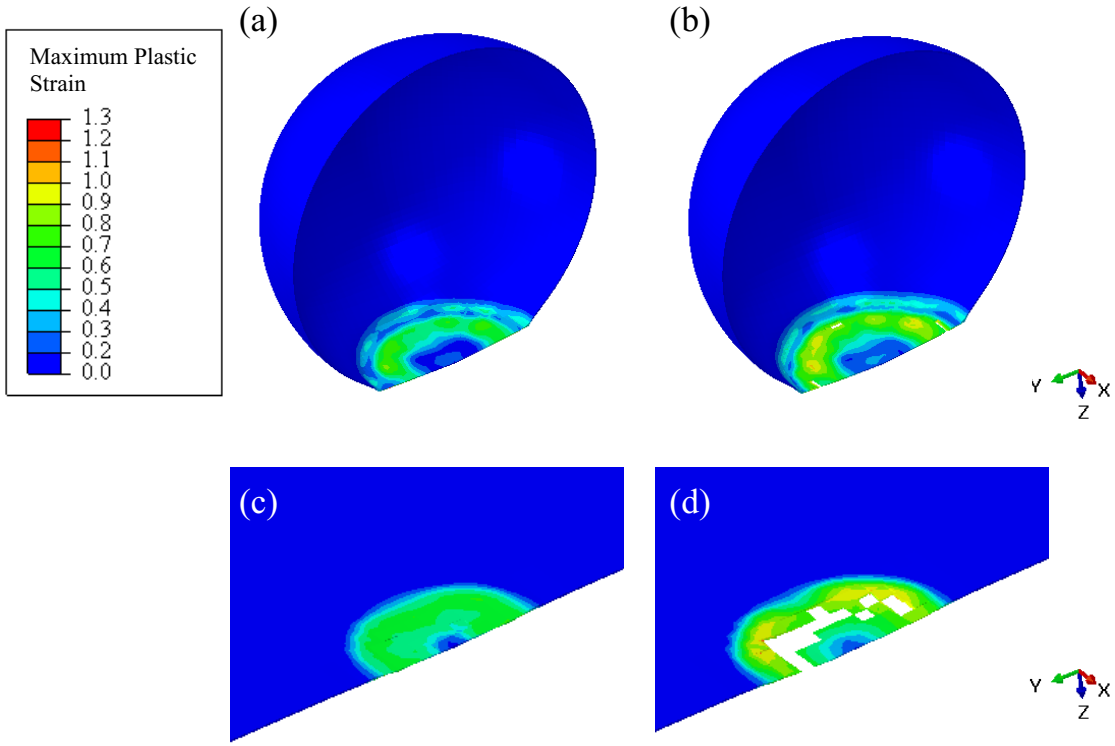

Figure 3.9. The investigation of the plastic strain of (a) particle oxide layer at 1.4 ns, (b) particle oxide layer at 1.6 ns, (c) substrate oxide layer at 0.8 ns, and (d) substrate oxide layer at 1 ns, before and after the oxide layer fracture occurs.

3.4.3. Parameters Influencing the Oxide Layer Failure

3.4.3.1. Particle Velocity

To analyze the effect of particle velocity on oxide layer failure and the adhesion of the particle and substrate, it was assumed that a 20 µm Ti-6Al-4V particle was deposited using HVAF at the temperature of 1073 K and various velocities between 550 and 950 m/s while substrate temperature stayed constant at 298 K. Increasing particle velocity provides more kinetic energy required for particle deformation; hence, the particle can go through more deformation. Figure 3.3.10 shows the equivalent plastic strain changes by the passage of time of the deposited particle and substrate. As shown in Figure 3.3.10(a), an increase in particle velocity raises the equivalent plastic strain value showing an increase in particle deformation. Additionally, increasing the particle velocity

enhanced substrate equivalent plastic strain and substrate deformation (Figure 3.3.10(b)). The increase in the deformation of the deposited particle and substrate accelerates oxide layer failure.

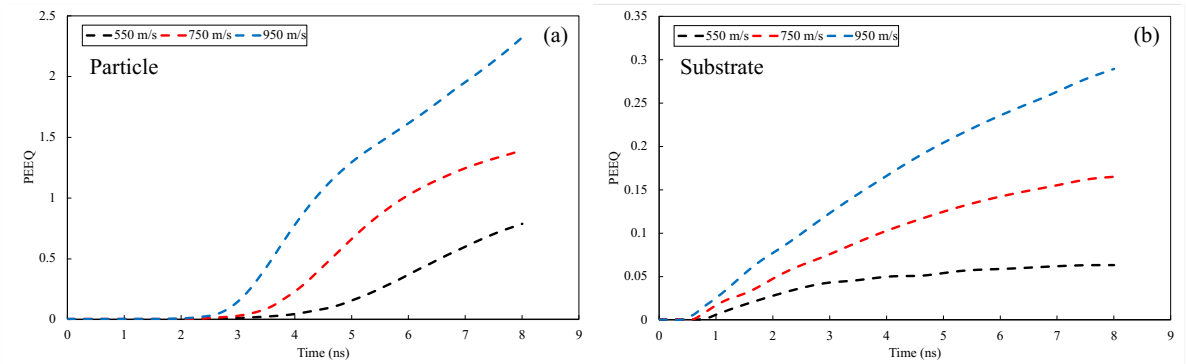

Figure 3.3.10 The effect of impact velocity on the equivalent plastic strain (PEEQ) evolution in the (a) particle and (b) substrate. Initial particle temperature 1073 K and substrate temperature 298 K.

Figure 3.3.11 shows the effect of impact velocity on the oxide layer failure while the particle temperature is 1073 K, and the substrate temperature is 298 K. The simulation results shown in Figure 3.3.11 indicate that as the particle velocity rises, the particle flattening ratio and deformation increase. Also, a higher particle velocity causes more deformation of the substrate surface and increases the particle penetration into the substrate. For the particle, as the velocity increases from 550 to 950 m/s, the particle goes through more degrees of deformation, and its oxide layer quickly fails. To produce a region with the possibility of making a metallurgical bonding, the oxide layer of the substrate needs to be eliminated as well. This only can be achieved when particle velocity is 950 m/s, as shown in Figure 3.3.11(c). These results confirm the significant impact of particle velocity on the formation of metallurgical bonding. The noted findings can be validated by previous studies [176-177]. As such, Huang et al. [176] studied the effect of the particle velocity on the tensile strength of the coatings manufactured by cold spray. They concluded that increasing particle velocity could enhance particle and substrate deformation, increasing the coating's adhesive strength and tensile strength. Additionally, an interesting experimental examination showed that a higher particle velocity can increase the possibility of oxide layer delamination. However, at the south pole of the impacted particle an island of oxide layer would be oxide due to the low degree of deformation [177]. Conclusively, increasing particle velocity can improve the deformation and facilitate substrate oxide layer failure, leading to a stronger adhesion between the particle and the substrate.

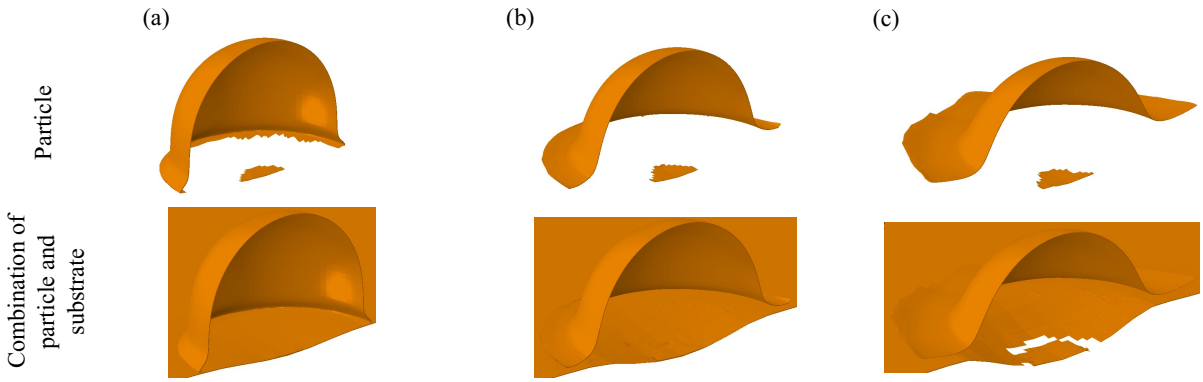

Figure 3.11. The effect of impact velocity (a) 550 m/s, (b) 750 m/s, and (c) 950 m/s on particle and substrate oxide layer failure while particle temperature is 1073 K, and the substrate temperature is 298 K.

3.4.3.2. Particle Temperature

The influence of particle temperature on the oxide layer failure was studied by assuming that the particle impact on the substrate surface at the velocity of 750 m/s while particle temperature is 873 K, 1073 K, or 1273 K and the substrate temperature is 298 K. Figure 3.3.12 shows the equivalent plastic strain behavior of a particular node of the substrate and the particle. According to Figure 3.3.12(a), particle equivalent plastic strain improved by increasing the particle temperature due to the enhancement of particle thermal softening. Also, Figure 3.3.12(b) illustrates that increasing particle temperature, reduced substrate equivalent plastic strain and substrate deformation. Hence, it can be concluded that increasing initial particle temperature accelerates the initiation time of particle's oxide layer failure due to an increase in the particle deformation and subsequently the thermal softening effect.

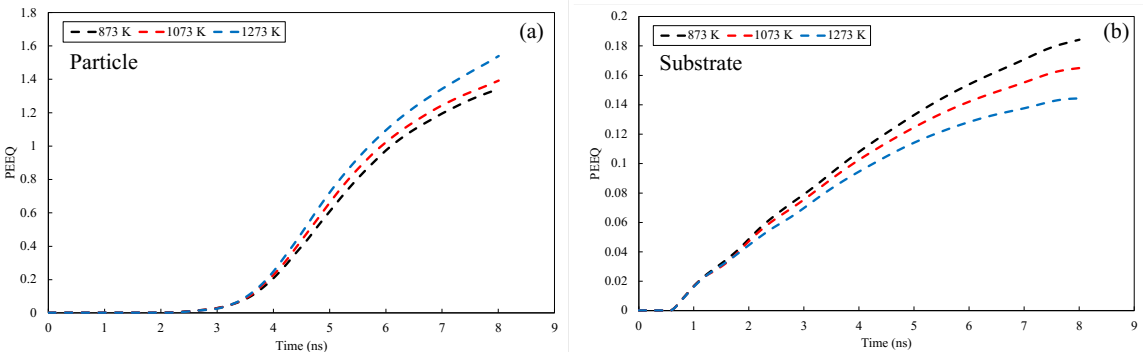

Figure 3.12. The effect of particle temperature on the equivalent plastic strain changes by the passage of time for the (a) particle and (b) substrate while particle velocity is 750 m/s, and the substrate temperature is 298 K.

The effect of initial particle temperature on the area where the oxide layer had failed was investigated. As shown in Figure 3.3.13, when particle temperature increases, a larger part of the oxide layer of the particle fails due to the larger degree of particle deformation. This leads to an increase in ASI and the size of the area where two new metallic surfaces were in contact with each other. However, Figure 3.3.13 confirms that at any given particle temperature, the substrate oxide layer remains unaffected and does not fail. This is because the substrate deformation is negatively

associated with the particle temperature. Increasing the initial temperature of the particle results in more particle deformation; however, it does not lead to a metallurgical bonding because it is ineffective for substrate deformation and substrate oxide layer failure. However, it is worth noting that increasing particle deformation by boosting its temperature can decrease the porosity level of the as-fabricated coating [155]. To our knowledge, the effect of particle temperature on the failure of the oxide layer and adhesive strength between the deposited particle and the substrate has never been experimentally studied. Thus, it is necessary to measure the in-flight particle temperature during the deposition by an inner-diameter HVAF gun for validating the reported simulated outcomes. Also, comparing the results shown in Figures 3.11 and 3.13 suggests that the particle velocity has a greater impact than the particle temperature on the oxide layer failure and the adhesion between particle and substrate (and eventually a metallurgical bonding between the particle and the substrate).

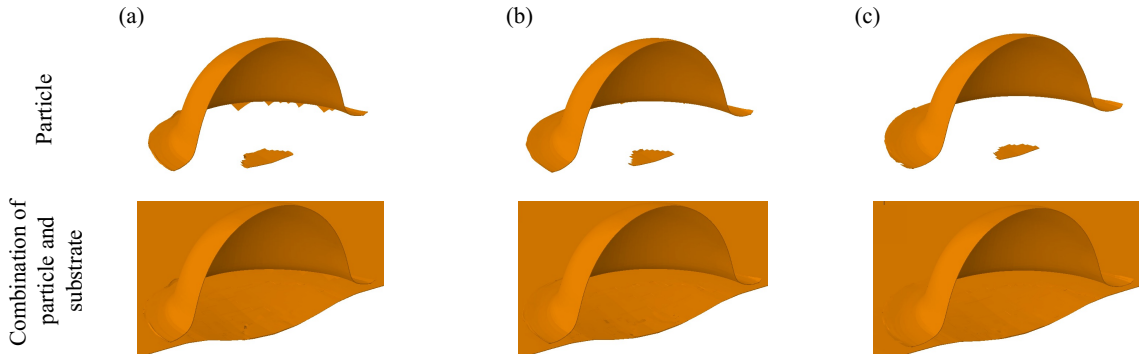

Figure 3.13. The effect of particle temperature (a) 873 K, (b) 1073 K, and (c) 1273 K on particle and substrate oxide layer failure while particle velocity is 750 m/s, and the substrate temperature is 298 K.

3.4.3.3. Substrate Temperature

The effect of substrate temperature on oxide layer behavior was investigated by assuming that the particle impact on the substrate surface at the particle velocity of 750 m/s and temperature of 1073 K while the substrate temperature varied between 298 and 473 K. Figure 3.3.14 shows the equivalent plastic strain behavior of the particle and the substrate. According to Figure 3.3.14(a), as substrate temperature increases from 298 to 473 K, the deposited particle plastic strain and deformation have not changed significantly. This is because the heat exchange system between the substrate and particle is adiabatic meaning that no heat would exchange from the substrate to the particle to enhance the particle thermal softening effect in the examined 8 ns. However, the substrate temperature effect on particle deformation has been examined in our previous work for the duration that the particle deformation is completed. It was shown that increasing the substrate temperature can decrease particle flattening ratio and deformation [153]. By increasing substrate temperature, the substrate undergoes a thermal softening effect leading to a rise in equivalent plastic strain. This means that by keeping particle velocity and input kinetic energy constant and increasing substrate temperature, substrate deformation increases, Figure 3.3.14(b).

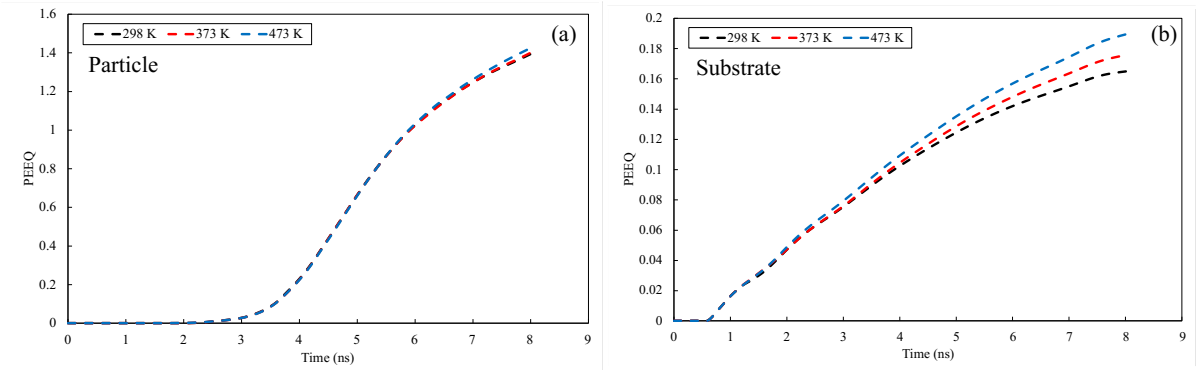

Figure 3.14. The effect of substrate temperature on the equivalent plastic strain changes by the passage of time for the (a) particle and (b) substrate while particle velocity is 750 m/s and particle temperature is 1073 K.

Finally, the influence of substrate temperature on oxide layer failure is simulated. Figure 3.3.15 shows that increasing substrate temperature does not affect the particle oxide layer failure. However, when the substrate temperature is 373 or 473 K, due to the thermal softening effect, the substrate goes through a higher degree of deformation leading to the failure of its oxide layer. Increasing the initial substrate temperature results in the failure of a larger area of its surface. This means that a higher substrate temperature enhances substrate deformation but its effect on particle deformation is negligible. However, a higher substrate temperature can result in producing an area for metallurgical bonding which was not possible when only the particle temperature was increased (Figure 3.3.13).

Particle and substrate deformation can be altered by increasing substrate temperature and substrate thermal softening effect. This means that by increasing the substrate temperature, the softened substrate would deform more while impacted particles are found to be less deformed [155]. However, pre-heating the substrate can increase substrate oxide layer thickness. The enhanced deformation of the pre-heated substrate provides the opportunity to eliminate the substrate thick oxide layer and produce a higher adhesive strength between the particle and substrate [152].

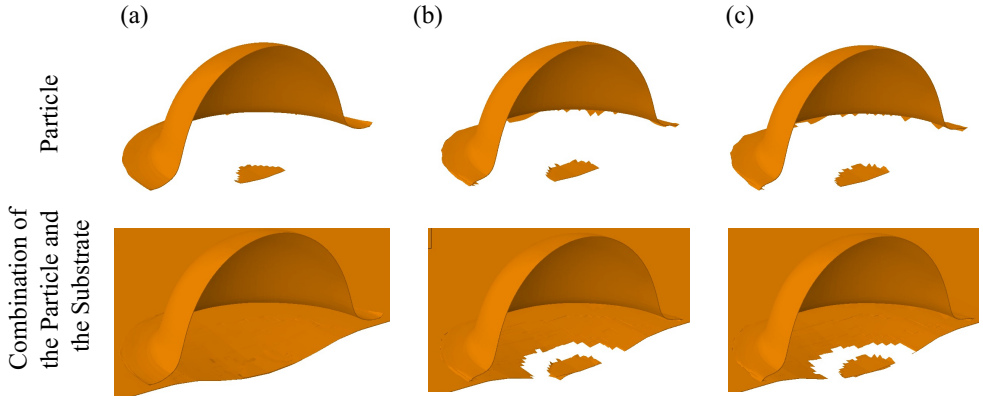

Figure 3.15. The effect of substrate temperature (a) 298 K, (b) 373 K, and (c) 473 K on particle and substrate oxide layer failure while particle velocity is 750 m/s and particle temperature is 1073 K.

3.5. Conclusion

In this study, a numerical method has been used to investigate the particle and substrate initial conditions on their 80 nm oxide layer failure upon the impact of a deposited Ti-6Al-4V particle using HVAF. Due to the higher gas flow temperature in the HVAF process compared to cold spray, the oxide layer at the surface of the particle and substrate might be thicker, affecting the particle critical velocity. By assuming the existence of an 80-nm oxide layer, it was shown that increasing the particle velocity and substrate temperature can increase the failure of the substrate's oxide layer and, consequently, the adhesion of the particle to the substrate. On the other hand, increasing the particle temperature only affects the particle deformation and has no significant influence on the failure of the substrate oxide layer and the adhesion. However, increasing particle temperature can reduce the porosity level of as-deposited coating. Conclusively, to put on to other words, increasing substrate temperature can enhance the size of the region in which the oxide layer is broken and the possibility of producing metallurgical bonding exists. This can only be altered by increasing particle velocity and substrate temperature. Conclusively, this paper illustrated that regardless of material selection, for adhering the particle to the substrate, substrate oxide layer should be broken which is only depended on substrate temperature and impact velocity.

Chapter 4

The Effect of Spraying Parameters of the Inner-Diameter High-Velocity Air-Fuel (ID-HVAF) Torch on Characteristics of Ti-6Al-4V In-Flight Particles and Coatings Formed at Short Spraying Distances [3]

4.1. Abstract

High-velocity air-fuel (HVAF) is a combustion process that allows solid-state deposition of metallic particles with minimum oxidation and decomposition. Although HVAF and cold spray are similar in terms of solid-state particle deposition, a slightly higher temperature of HVAF may allow further particle softening and because of it, more particle deformation upon impact. The present study aims to produce dense Ti-6Al-4V coatings by utilizing an inner-diameter (ID) HVAF gun. The ID gun is considered a scaled-down version of the standard HVAF with a narrower jet, beneficial for near-net-shape manufacturing. To explore the potential of the ID gun in the solid-state deposition of Ti-6Al4V, an investigation was made into the effect of spraying parameters (i.e., spraying distance, fuel pressure, feeding rate, traverse speed, and nozzle length) on the characteristics of in-flight particles and the attributes of the as-fabricated coatings such as porosity, phases, and hardness. For studying in-flight particles characteristics, using online diagnostics is challenging due to the exothermic oxidation reaction of fine particles, while larger particles are too cold to be detected from their thermal emission. However, DPV diagnostic system was successfully employed to differentiate the non-emitting solid particles from the burning ones. It was found that increasing air and fuel pressure of the ID-HVAF jet as well as increasing the nozzle length led to an increase in the velocity of the in-flight particles and resulted in improved density and hardness of the as-sprayed samples. However, increasing the spraying distance had a negative effect on the density and hardness of the manufactured coatings.

4.2. Introduction

The Ti-6Al-4V alloy has a unique set of mechanical and physical properties, making it suitable for manufacturing turbine blades in the aerospace industry. However, Ti-6Al-4V components are prone to damage because of the extensive use of turbine blades [124-129]. According to previous study, replacing a turbine blade would cost almost 7 times more than repairing it [14]. To be more cost-effectiveness, this necessitates the importance of repairing through the use of solid-state additive manufacturing techniques, such as cold spray (CS) [19, 105-106, 130-133].

In CS process, the deformation of the deposited particles upon impact plays a crucial role in bonding and deposit density [13, 72, 77, 105-106]. For instance, Chen et al. [105] produced Ti-6Al-4V deposits via CS using nitrogen as the propelling gas. It was noted that the main problem

[3] Khamsepour, P., Oberste-Berghaus, J., Aghasibeig, M., Ben EttouilMoreau, F., Moreau, C., & Dolatabadi, A. (2023). The Effect of Spraying Parameters of the Inner-Diameter High-Velocity Air–Fuel (ID-HVAF) Torch on Characteristics of Ti-6Al-4V In-Flight Particles and Coatings Formed at Short Spraying Distances. *Journal of Thermal Spray Technology*, Vol. 1, Issue 1-2. DOI: https://doi.org/10.1007/s11666-023-01535-z

with the as-sprayed samples was poor mechanical properties due to inadequate bonding between the deposited particles. When they used helium as the propelling gas, particle velocity was increased leading to more particle deformation and as-fabricated sample density [105]. Additionally, using post heat treatment methods such as annealing or hot isostatic pressure (HIP) to sinter the deposited particles has also been shown to enhance the density and mechanical properties of CS samples [105-106]. Among these two methods, the former one does not eliminate the need for post-heat treatment and the latter one is considered to be expensive [105-106]. Hence, to become more cost-effectiveness, it is necessary to increase the deformation of deposited particles. In this regard, account should be taken of particle temperature to activate the thermal softening effect and to facilitate particle deformation [73, 99-100, 137].

To deposit elevated temperature solid-state particles at high deposition rates, combustion-based thermal spray techniques, such as high velocity oxy-fuel (HVOF), warm spray, or high velocity air-fuel (HVAF) should be selected [13]. The flame temperature of HVOF is higher than those of other techniques due to the use of pure oxygen in the combustion process [13]. In this way, there would be a greater chance of melting the solid particles [13]. Fortunately, warm spray technology has been developed to overcome this drawback and lower the flame temperature. In this method, nitrogen is injected into the mixing chamber prior to the nozzle to unbalance the combustion chemical equation and lower the flame temperature [47, 13]. R. Molak et al. [48] deposited solid Ti-6Al-4V particles using the warm spray. In spite of their success in depositing solid particles, the high oxide content in the coatings resulted in the need to further reduce the flame temperature.

Flame temperatures can be further reduced by using the HVAF process [59]. In this method, combustible gases are burned with air. The use of air will not only result in a decrease in oxygen levels, but also an increase in nitrogen levels, which will reduce the flame temperature and particle oxidation [72, 51-53]. As a result, HVAF is a combustion-based process that maintains the solid-state of metallic particles during deposition [72]. To the best of our knowledge, no specific attempt has been made to deposit solid metallic particles using the HVAF process with the purpose of studying the effect of the in-flight particle characteristics on the properties of the as-sprayed coatings.

Two main types of HVAF guns are available: the full-scale M3 and the inner-diameter HVAF (ID-HVAF) gun. The main goal of this project is to introduce HVAF as a solid-state additive manufacturing method for repairing damaged parts; hence, inner diameter HVAF is an appropriate option since its main advantage is that its narrower jet permits the production of near-net-shaped samples [13, 59]. However, this work is limited to studying the effect of spraying parameters of ID-HVAF guns on depositing the outer surface of substrates. Consequently, most the concerns associated with depositing on an inner surface would be eliminated [178-180].

ID-HVAF has been developed in order to fabricate coatings on the inner surface. In other words, ID-HVAF operates mostly at short spraying distances. As an instance, J. Pulsfor et al. [179] examined the wear resistance of inner diameter coatings produced using high velocity oxy-air fuel (HVOAF) at three short spraying distances (30, 50, and 70 mm). It was found that the coating's hardness and fracture toughness increased with an increase in spraying distance from 30 mm to 50 mm. If the spraying distance is further increased, neither mechanical property would decrease significantly. Additionally, all samples showed good wear resistance regardless of spraying distance; however, the 50 mm spraying distance resulted in a lower wear rate. According to

Katranidis et al. [181] spraying distance affects the coating thickness and porosity of inner diameter coatings. In their study, they found that increasing spraying distance would result in increased thickness and porosity. Therefore, one of the main objectives of this paper is to investigate the effects of spraying distance on coating properties.

The purpose of this study is to examine the effects of spraying parameters on coating properties by using ID-HVAF to deposit solid-state particles. Therefore, the DPV diagnostic system would be used to monitor temperature and velocity of in-flight particles. Following that, the effect of spraying parameters on coating thickness, hardness, and density will be studied in more detail.

4.3. Experimental Procedure

4.3.1. Materials and Spraying Technique

In this study, solid-state Ti-6Al-4V metallic powders (AP&C, Canada) with d_{50} of 10 and 20 µm were deposited using an ID-HVAF system (Uniquecoat Technologies LLC, Oilville, USA). The particle size distributions of the particles and their scanning electron microscopic (SEM) micrographs presenting the spherical shape of the particles are shown in Figure 4.1. During depositing, the effect of spraying parameters (i.e., spray distance, feeding rate, nozzle length, traverse speed, fuel pressure, and air pressure (Table 4.1)) on the characteristics of in-flight particles and the properties of the deposited coatings were investigated.

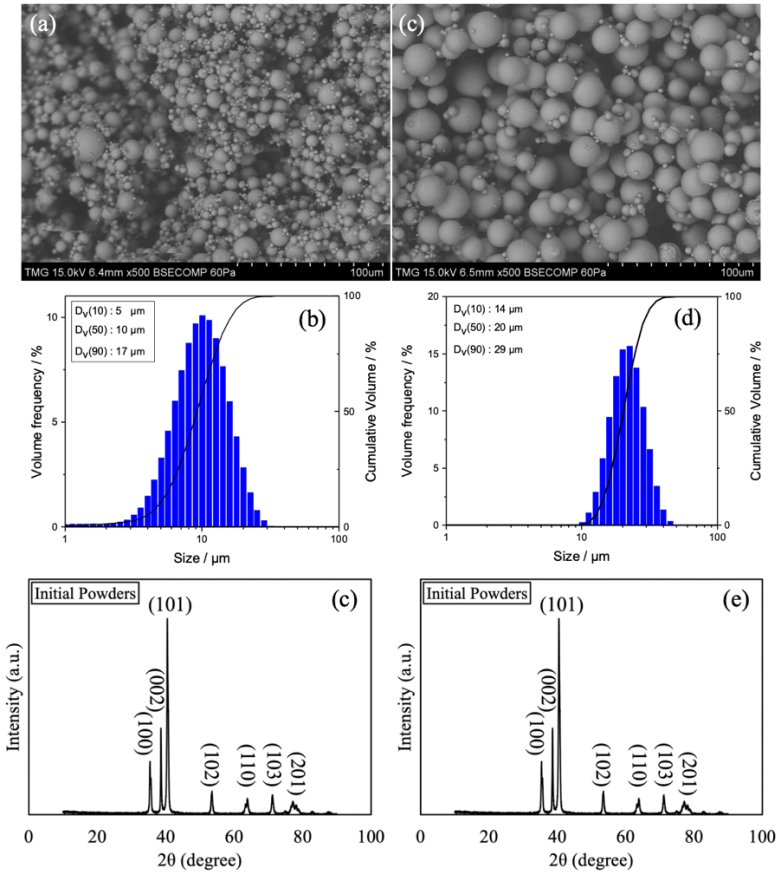

Figure 4.1. (a) and (d) SEM image of Ti-6Al-4V particles; (b) and (e) size distribution of Ti-6Al-4V particles; (c) and (f) X-Ray Diffraction (XRD) result of the Ti-6Al-4V particles.

Table 4.1. ID-HVAF spray parameters.

Parameter	Value
Spraying Distance (mm)	50/75
Spraying Step (mm)	3
Spraying Anlge	90 º
Torch Traverse Speed (mm/s)	500/1000
Air Presusre (KPa)	758/786/813/841
Fuel (Propylen) Pressure (KPa)	744/772/799/827
Carier Gas (Nitrogen) Pressure (KPa)	275
Hopper Feeder Setting (%)	5/6/7
Nozzle	i7-1L4/i7-2L4/i7-3L4

4.3.2. Characteristics of In-Flight Particles and Coatings

Modern diagnostic sensors can be useful in elucidating the effect of the spray parameters on in-flight particles characteristics and thus the coating properties. However, utilizing such a diagnostic system to monitor the temperature and velocity of Ti-6Al-4V particles is challenging as high temperature fine titanium particles go through an exothermic oxidation reaction while other larger particles remain too cold to be detected. However, by using laser illumination instead of thermal emission from the particle alone, the DPV (Tecnar, Canada) diagnostic system can successfully differentiate the non-emitting solid particles from the burning ones. This allows capturing most of the in-flight particles in the spray jet. In-flight particle characteristics were measured for the Ti-6Al-4V powder with the d_{50} of 20 μm at different combinations of air and fuel pressure (air pressure = 786, 813, and 841 KPa; fuel pressure = 772, 799, and 827 KPa), spraying distances of 50 or 75 mm, and different nozzle lengths (Figure 4.3 and Table 4.3) at the hopper setting of 1%. An actual set-up of the DPV system with respect to the spray gun is shown in Figure 4.2. The effect of the nozzle length on the characteristics of in-flight particles was considered using the three different convergent-divergent nozzles shown in Table 4.3. Table 4.2 shows the specific sample numbering that has been used for reporting the results obtained from DPV (Figure 4.5). Also, During the spraying process, the temperature of the center of substrates was monitored during deposition using an infrared (IR) Camera.

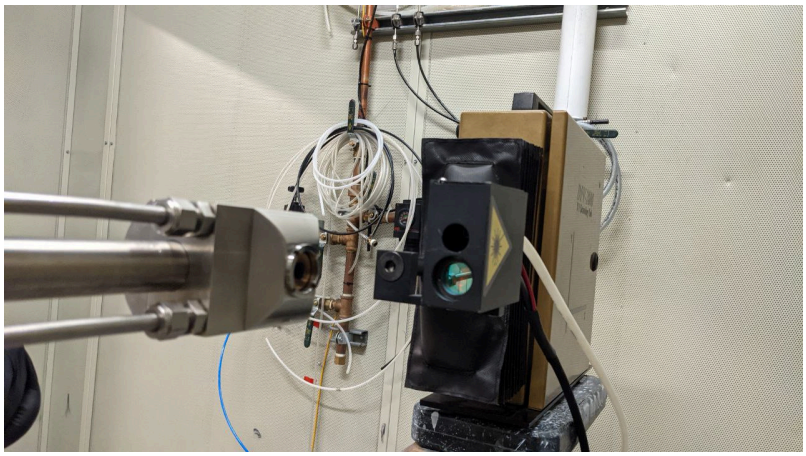

Figure 4.2. The actual set-up used for examining the Ti-6Al-4V in-flight particle characteristics using DPV at the spraying distance of 50 mm when the short nozzle was used with the ID-HVAF gun.

Table 4.2 Spraying Parameters used based on sample number shown in Figure 4.5.

Sample Number	Air Pressure (KPa)	Fuel Pressure (KPa)	Spraying Distance (mm)
1	786	772	50
2	813	799	50
3	841	827	50
4	786	722	75
5	813	799	75
6	841	827	75

(a) (b)

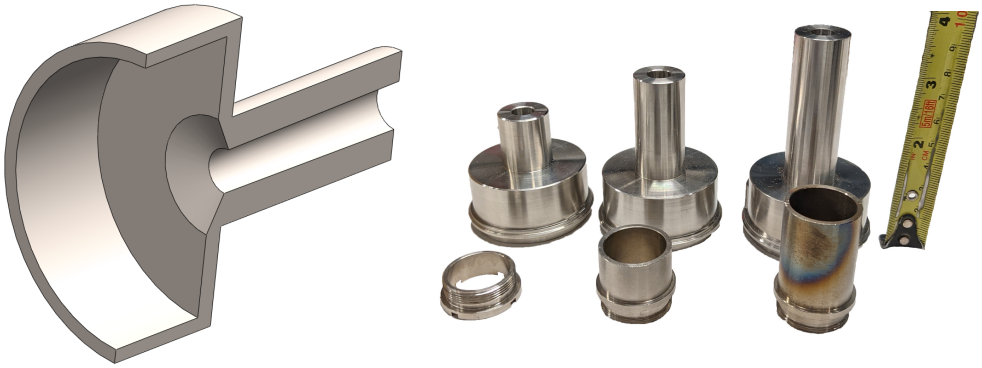

Figure 4.3. (a) A schematic figure of an ID-HVAF nozzle and (b) actual nozzles used in the study.

Table 4.3. Lengths of the nozzles used with the ID-HVAF gun.

Nozzle Name	Nozzle Length (mm)
i7-1L4 (Short)	26.17
i7-2L4 (Medium)	46.75
i7-3L4 (Long)	70

4.3.3. Spraying Parameter Effect on Coating Properties

All coatings have been manufactured on a sandblasted stainless-steel substrate with an initial roughness of 5.4±0.7 μm. To enhance the deposition efficiency, the substrate was pre-heated by the ID-HVAF jet without powder injection for 5 passes. Lastly, in all manufactured coatings, particles were deposited on the substrate surface for 10 spray passes. Below, more detail on the spraying parameters for studying each spraying parameters effect (i.e., spray distance, feeding rate, nozzle length, traverse speed, fuel pressure, and air pressure) would be provided in more detail.

4.3.3.1. Feeding Rate Effect

For studying the feeding rate, the feeding speed had been changed from the hopper setting of 5% to 7% which can increase the feeding rate. It is worth noting that hopper setting of 7% corresponds to approximately a feeding rate equal to 18 gr/min. In the meanwhile, the air and fuel pressure are 813/799 KPa and 841/827 KPa, and spraying distance was 50 mm. Table 4 provide the naming for each used condition that would be used throughout the manuscript.

2.3.2. Air/Fuel and Spraying Distance Effect

For examining the air and fuel pressure, they have been increased in increments of 27.5 KPa from 758 KPa to 841 KPa and 744 KPa to 827 KPa, respectively. This has been done while feeding rate was 18 gr/min and the spraying distance were 50- and 75-mm. It is worth noting that a stable flame was achieved when air pressure was 13.75 KPa higher than fuel pressure. Table 4 provide the naming for each used condition that would be used throughout the paper.

4.3.3.3. Nozzle Length Effect

The nozzle length effect has been examined by using all three nozzles shown in Fig. 2. This means that particles have been deposited at the feeding rate of 18 gr/min while spraying distance was 50 m/s and air/fuel pressure were 813 KPa/799 KPa, respectively. It is worth noting that in ID-HVAF configuration, nozzle configurations are shown in Fig. 3 and their sizes are summarized in Table 3. In all the nozzles, particles are injected axially into the mixing chamber. The nozzles are cooled by air. Each hallow cylinder in front of each nozzle in Fig. 3(b) has an inner diameter slightly larger that outer diameter of the nozzle. Hence, the turbulence of air in that space would be responsible for cooling the nozzles. Table 4 provide the naming for each used condition that would be used throughout this study.

4.3.3.4. Traverse Speed Effect

Lastly, traverse speed which indicates the speed of the gun moving parallel to the substrate surface during deposition was 1000 mm/s in all conditions except it is indicated otherwise. This means that the traverse speed effect by selecting one 1000 mm/s and once 500 mm/s on coating properties was examined while air/fuel pressure was 813/799 KPa and spraying distance was 50 mm. Table 4 provide the naming for each used condition that would be used throughout the paper.

Table 4.4. Naming each condition used for examining Ti-6Al4-V coating properties manufactured using ID-HVAF.

Name of Experiment	Studying Spraying Parameter	Air Pressure (KPa)	Fuel Pressure (KPa)	Spraying Distance (mm)	Traverse Speed (mm/s)	Feeding Hopper Setting (%)	Nozzle Length (mm)
F1	Feeding Rate	813	799	50	1000	5	46.75
F2	Feeding Rate	813	799	50	1000	6	46.75
F3	Feeding Rate	813	799	50	1000	7	46.75
F4	Feeding Rate	841	827	50	1000	5	46.75
F5	Feeding Rate	841	827	50	1000	6	46.75
F6	Feeding Rate	841	827	50	1000	7	46.75
AS1	Air/Fuel Pressure and Spray Distance	744	758	50	1000	7	46.75
AS2	Air/Fuel Pressure and Spray Distance	786	772	50	1000	7	46.75
AS3	Air/Fuel Pressure and Spray Distance	813	799	50	1000	7	46.75
AS4	Air/Fuel Pressure and Spray Distance	841	827	50	1000	7	46.75
AS5	Air/Fuel Pressure and Spray Distance	744	758	75	1000	7	46.75
AS6	Air/Fuel Pressure and Spray Distance	786	772	75	1000	7	46.75
AS7	Air/Fuel Pressure and Spray Distance	813	799	75	1000	7	46.75
AS8	Air/Fuel Pressure and Spray Distance	841	827	75	1000	7	46.75
N1	Nozzle Length	813	799	50	1000	7	26.17
N2	Nozzle Length	813	799	50	1000	7	46.75
N3	Nozzle Length	813	799	50	1000	7	70
T1	Traverse Speed	813	799	50	500	7	46.75
T2	Traverse Speed	813	799	50	1000	7	46.75
T3	Traverse Speed	813	799	50	500	7	70
T4	Traverse Speed	813	799	50	1000	7	70

4.3.4. Metallographic, Phase, and Hardness Analysis

After the coatings were produced, the samples were cut and polished for microstructural analysis using standard metallography techniques. A scanning electron microscope (SEM, Hitachie) in the backscatter (BSE) mode was used to examine the microstructure of the coatings. Porosity levels and thickness of the coatings were analyzed by image analysis software. Phase composition of the coatings as well as the deposited powders were assessed by X-ray diffraction (XRD) using CuKα radiation at scanning angles (2θ) from 25º to 85º. The Microhardness of the polished cross-sections was measured with a Mitutoyo MVK-H1 microhardness tester by applying a force of 300 g for 10 seconds.

4.4. Results and Discussion

4.4.1. Characteristics of In-flight Particles

The DPV diagnostic system was used to measure the temperature and velocity of in-flight particles via the emitted or reflected radiation. As an example, DPV was used with and without laser under the spraying condition in which Ti-6Al-4V particles were deposited using the short nozzle with the air pressure of 841 KPa, the fuel pressure of 827 KPa, and spraying distance of 75 mm. The first necessary step was to study the distribution of the detected energies. Without laser, significant noises were found in received signals (Figure 4.4(a) and Figure 4.4(c)). By using a laser, as suggested in the literature [113], the detected energies from both cooler and elevated temperature deposited particles showed a more continuous distribution of states, with less noise and with a higher intensity range, suggesting a more robust and reliable measurement (Figure 4.4(b) and Figure 4.4(d)). Hence, for studying cold large in-flight particle characteristics, an active laser was employed. It is worth noting that activating the laser would enable the DPV to study the reflected laser from the surface of cooler particles while still studying the emitted heat wave of burning ones. However, by activating the laser, one of the detecting lenses of DPV becomes inactive which disables the possibility of computing the temperature of a detected particle [113].

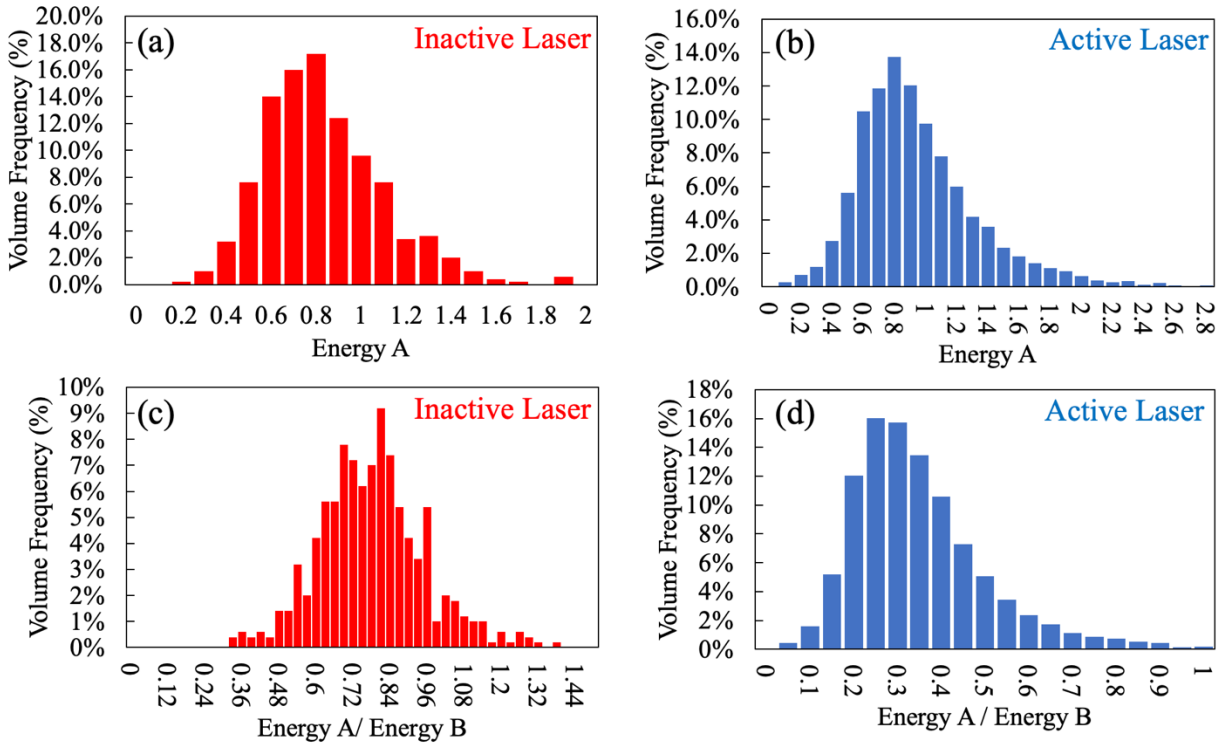

Figure 4.4. (a) Energy A detected with inactive laser, (b) energy A detected with active laser, (c) the ratio of two detected energies with inactive laser, and (d) the ratio of two detected energies with active laser obtained from the DPV diagnostic system when the short nozzle was used to deposit particles at an air pressure of 813 KPa, a fuel pressure of 799 KPa, and a spraying distance of 75 mm.

As it was shown, a more reliable measurement was attained when the DPV system detects non-emitting particles using an active laser. By using this technique, the average velocities for different spraying conditions were measured, Figure 4.5. The spraying parameters for each sample are also shown in Table 4.2. This figure shows that the effect of increasing the spraying distance was not as significant as the increase of air pressure and fuel pressure on the velocity of in-flight particles. The most noticeable increase in particle velocity was observed with an increase in nozzle length. As an example, increasing the nozzle length from the shortest nozzle to the longest nozzle with air pressure of 813 KPa, fuel pressure of 799 KPa, and spraying distance of 50 mm, can increase the average of in-flight particle velocity by 130 m/s approximately. While by using the same nozzle length and spraying distance, the increase in air and fuel pressure did not have an effective impact on particle velocity. As another instance, by increasing air and fuel pressure from 786 and 772 KPa to 841 and 827 KPa while using the moderate nozzle, the average in-flight particle velocity boosted by 25 m/s approximately. Thus, by comparing all conditions, it is found that the most effective spraying parameter on increasing in-flight particle velocity is nozzle length and the highest velocities were obtained with the medium and long nozzles at high air and fuel pressures.

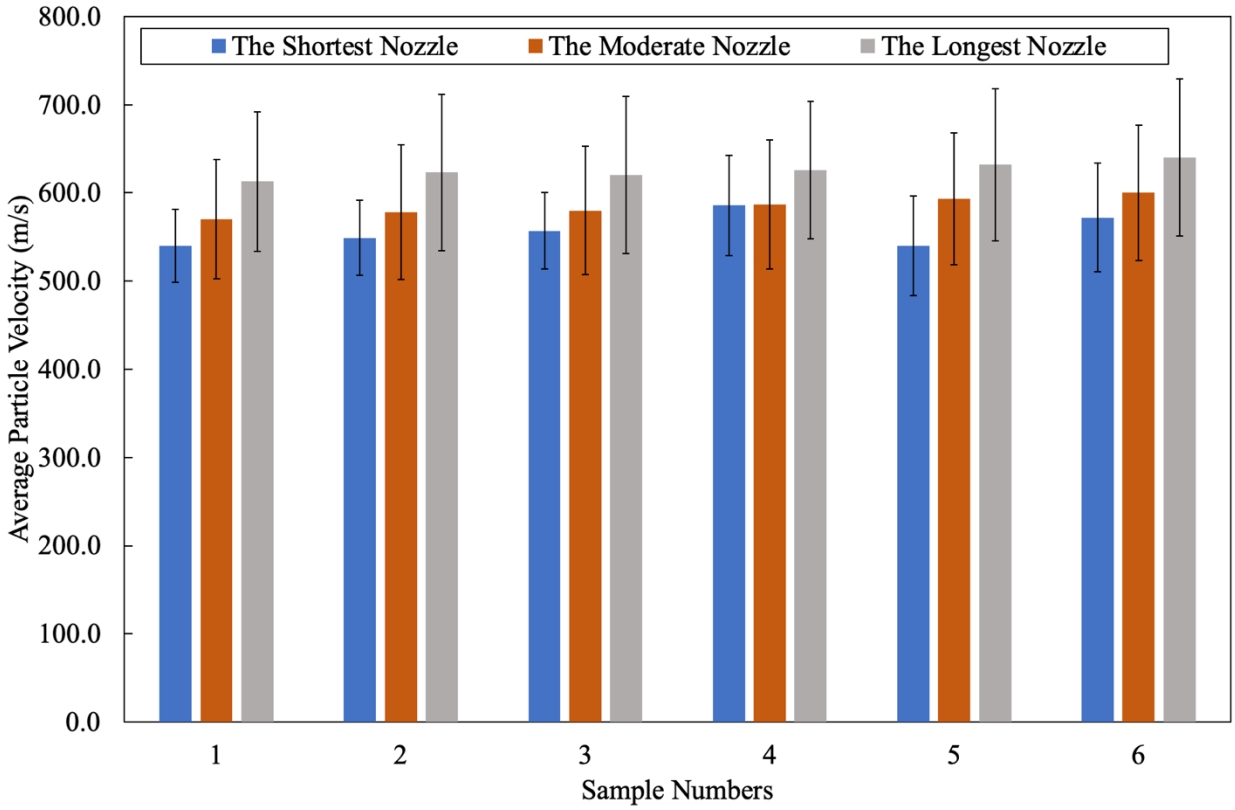

Figure 4.5. The effect of air pressure and fuel pressure at two different spraying distances (50 or 75 mm) on the velocity of in-flight Ti-6Al-4V particle. Error bars represent standard deviation.

After studying the in-flight particle velocity, both particle size distributions of Ti-6Al-4V noted in Figure 4.1 were deposited at the spraying distance of 75 mm using the moderate nozzle size and the hopper feeder of 6%. It is worth noting that the medium nozzle was selected because it provides higher average of in-flight particles velocity compared to the short nozzle, and the chance of clogging the medium nozzle was less compared to the long nozzle. The purpose of these depositions was to investigate the potential of making a coating at a high deposition rate. The microstructure images of the manufactured coatings are presented in Figure 4.6. As illustrated, regardless of the particle size, particles are deformed significantly, red arrows. This deformation is more noticeable in the first deposited layers because of the peening effect. With the higher thickness and deposition efficiency of coatings produced using the Ti-6Al-4V particles with the d_{50} of 10 µm, the peening effect and particle deformation are more significant compared to the time that the other particle size distribution was used. On the other hand, while depositing Ti-6Al-4V particles with the d_{50} of 10 µm, due to the low air and fuel pressure, some particles kept their spherical shape meaning they have not gone through deformation, yellow arrows. Conclusively, due to the larger mass of Ti-6Al-4V particles with the d_{50} of 20 µm, their impact velocity is much lower than the required critical value leading to a lower coating thickness and density. As a result of this, for studying the effect of ID-HVAF spraying parameters on as-sprayed Ti-6Al-4V coatings, Ti-6Al-4V particles with the d50 of 10 mm would be used.

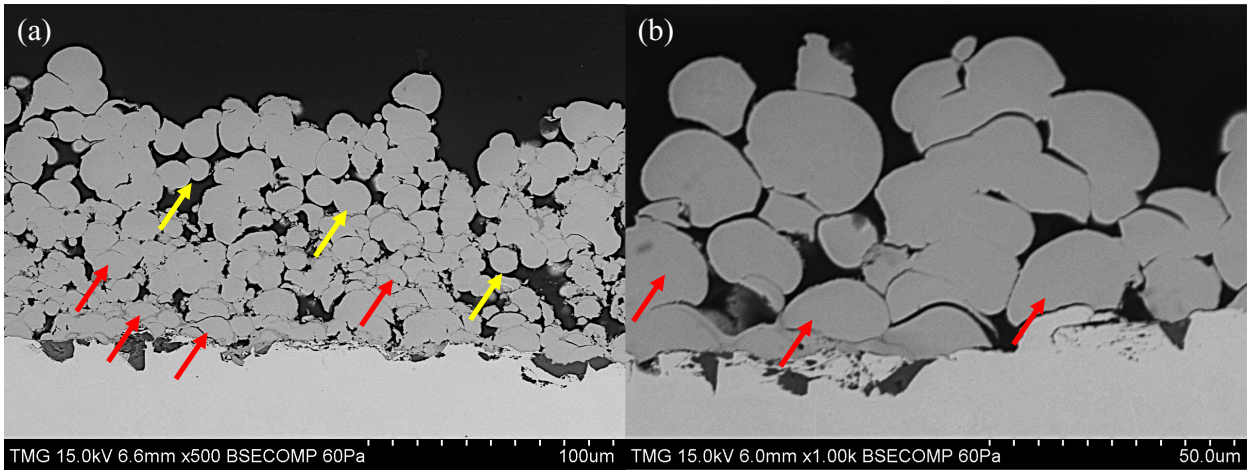

Figure 4.6. Using ID-HVAF minimum power for assessing the possibility of manufacturing coatings using (a) Ti-6Al-4V powders with d_{50} equals 10 µm to and (b) Ti-6Al-4V powders with d_{50} equals to 20 µm while air and fuel pressure were 744 KPa, spaying distance was 75 mm, and the moderate nozzle was used.

4.4.2. The Effect of Feeding Rate on the Microstructure of the Coatings

The effect of feeding rate at hopper settings of 5%, 6%, and 7%, two air/fuel combinations of 813/799 KPa and 841/827 KPa, and spraying distance of 50 mm was investigated (F1 to F6 in Table 4.4). The medium nozzle length has been chosen to deposit particles at elevated temperatures, and the resulting coatings are presented in Figure 4.7. As illustrated from the microstructural images, at each combination of air and fuel pressures, increasing the feeding rate led to the deposition of a denser and thicker coating.

According to Figure 4.7 and Figure 4.8, increasing the feeding rate by changing the hopper setting from 5% to 7% (F1 to F3) resulted in a 13% decrease in porosity and a 74 μm increase in sample thickness when lower air and fuel pressures were used. The change in porosity and coating's thickness became more significant at higher air and fuel pressures. This means that when air and fuel pressures were 841 and 827 KPa, respectively, by increasing the feeding rate (F4 to F6), porosity was decreased by 26% and thickness was increased by 39 μm. The low increase in thickness at higher air and fuel pressures and the highest feeding rate (7% hopper setting) might be due to the bounced back particles from the substrate surface. In both combinations of air and fuel pressures, the density remains stable at 6% and 7% of the hopper setting; however, the difference between these two conditions is noticeable in the enhancement of the thickness and deposition efficiency.

Increasing the air and fuel pressures for each selected feeding rate could produce a denser structure since particle velocity increases, and as a result of it, the peening effect becomes more significant. Because the densest structure with higher thickness has been created while the feeding rate is 7%, this rate has been chosen for the subsequent tests.

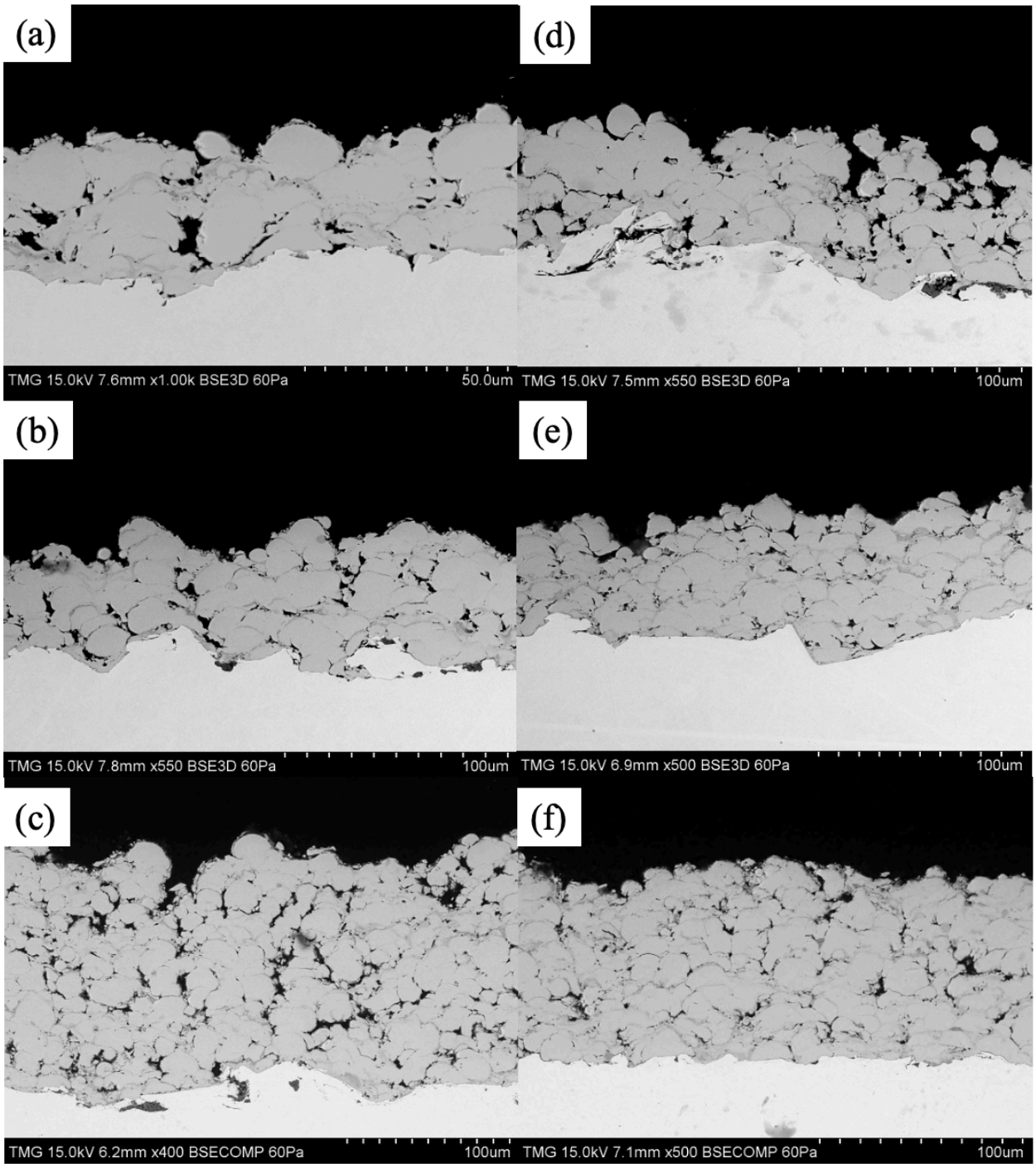

Figure 4.7. The SEM images of the deposited coatings using the medium nozzle and at a spraying distance of 50 mm and (a) F1, (b) F2, (c) F3, (d) F4, (e) F5, and (f) F6.

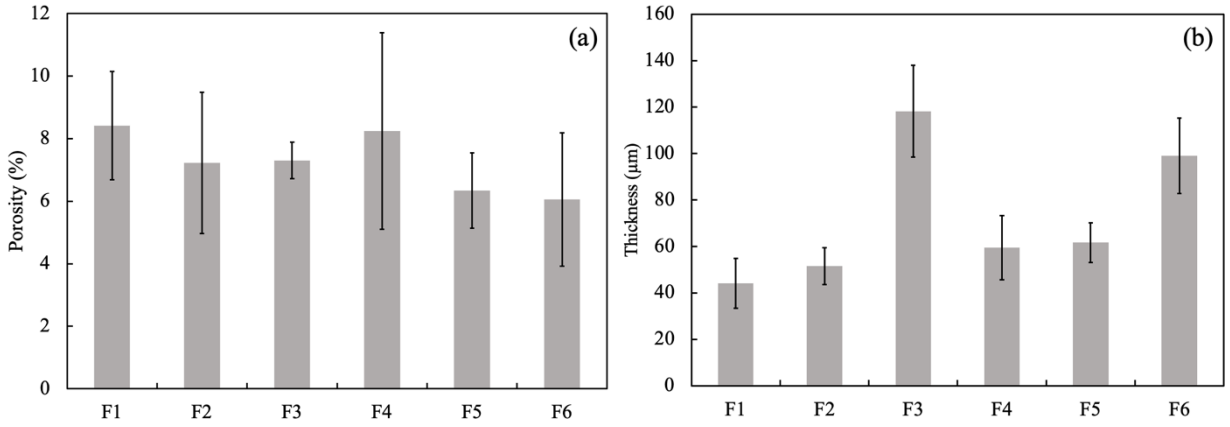

Figure 4.8. Examination of feeding setting effect on (a) porosity level and (b) thickness of as-sprayed Ti-6Al4V coatings sprayed at the distance of 50 mm with the medium nozzle. Error bars are standard deviation.

4.4.3. Effect of spray parameters on the Microstructure of the Coatings

Coatings by using the medium nozzle for depositing the smaller particles at the two different spraying distances and increased air/fuel pressures of 758/841 KPa to 744/827 KPa were produced (AS1 to AS8 in Table 4.4). The porosity level of the coatings is given in Figure 4.9 and Figure 4.10. As the microstructure clearly shows, at the spraying distance of 50 mm, increasing air and fuel pressure led to a decrease of 4% in average porosity level (AS1 to AS4). At the spraying distance of 75 mm, the change in average porosity level was 1.8% under the same conditions (AS5 to AS8). On the other hand, at the same air pressure and fuel pressure, by increasing the spraying distance the average porosity level increased noticeably. To put it in other words, the porosity decreased with rising gas pressure due to the higher particle velocities. However, this effect is more pronounced at the 50 mm spraying distance as compared to the 75 mm spraying distance. Further, the coating thickness, and the associated deposition rate, increased with gas pressure at the 75 mm spraying distance, while no distinct trend can be seen at the 50 mm spraying distance. This suggests that at the shorter spraying distance, a significant part of the particles may not deposit but bounce off the substrate. The pronounced densification at 50 mm may then be related to a higher peening effect of the non-depositing particles at the shorter spray distance. This indicates that the density of the coatings is highly dependent on the air pressure, fuel pressure, and spraying distance.

The change in deposit density and thickness is pertinent to particle deformation [105]. An increase in air pressure and fuel pressure leads to increased particle velocity and its kinetic energy. More particle deformation brings about more bonding between the deposited particles and thus lower coating porosity. As Figure 4.11 illustrates, increasing spraying distance had a negative effect on the temperature of the substrate as it decreased. This drop-in temperature plays down the role of thermal softening and results in reduced particle deformation.

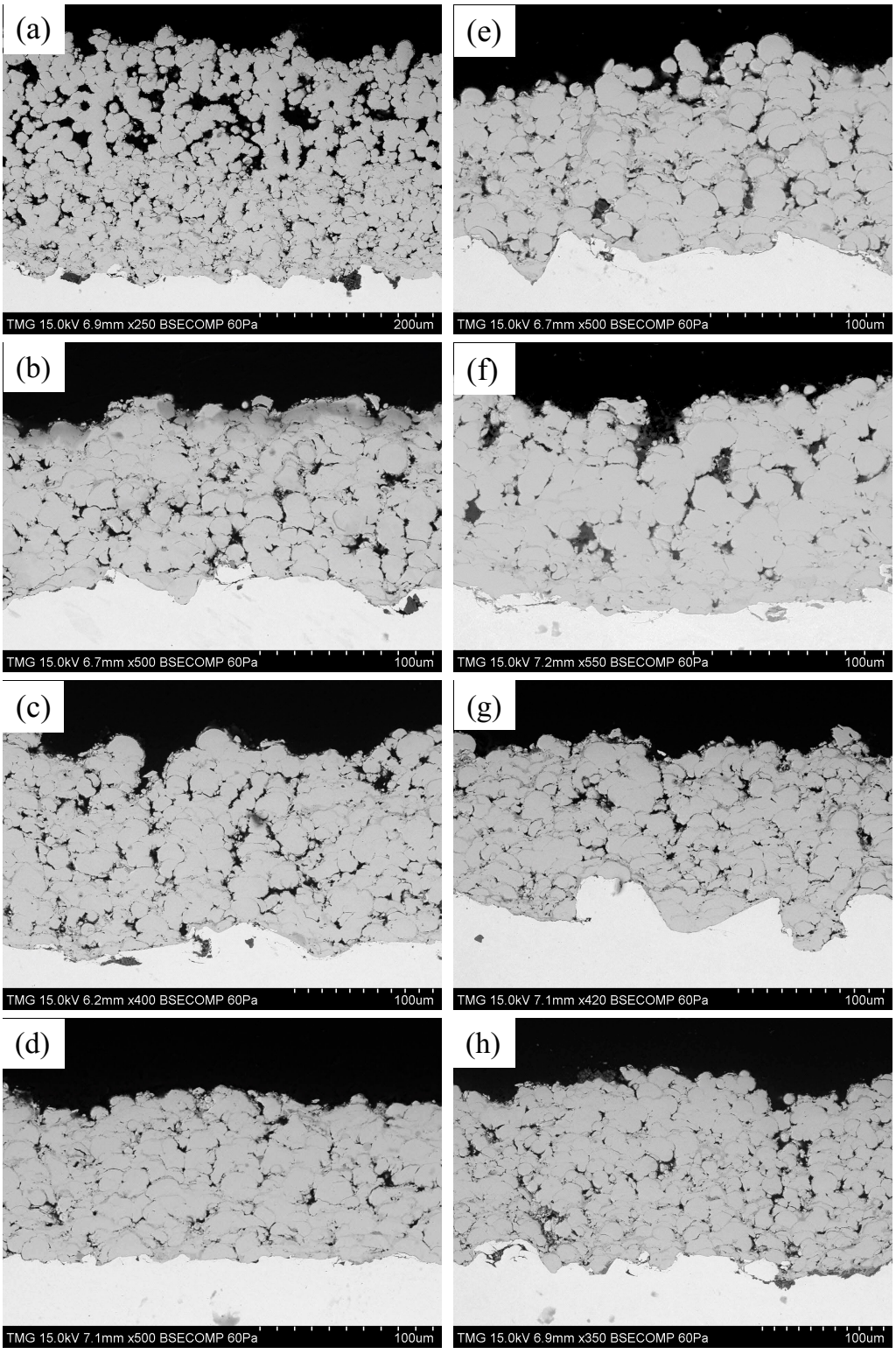

Figure 4.9. The SEM images of the deposited coatings using the condition of (a) AS1, (b) AS2, (c) AS3, (d) AS4, (e) AS5, (f) AS6, (g) AS7, and (h) AS8.

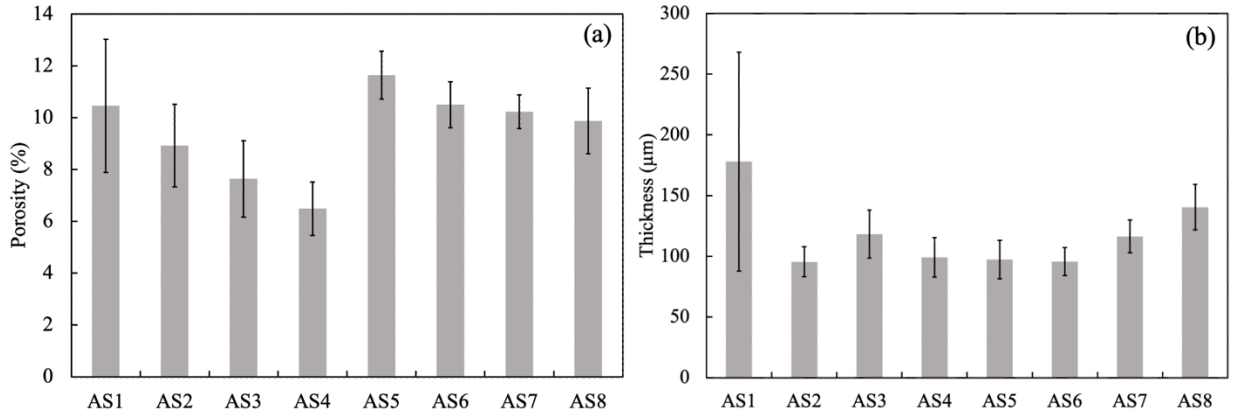

Figure 4.10. The effect of air pressure and fuel pressure at two different spraying distances on the porosity level (a) and thickness (b) of as-fabricated coatings. Error bars exemplify standard deviation.

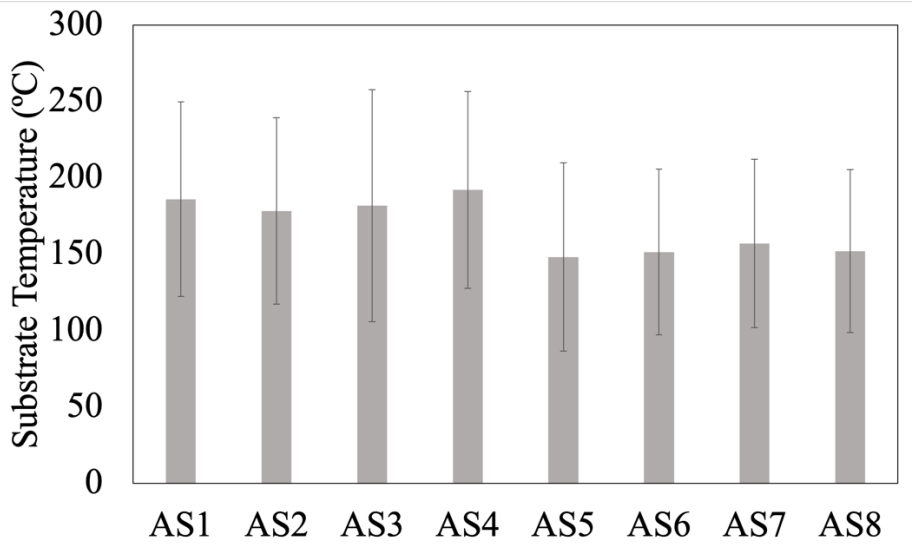

Figure 4.11. The effect of air pressure and fuel pressure at two different spraying distances of 50 mm and 75 mm on the temperature of the substrate.

After studying the microstructure, it is important to examine the potential of ID-HVAF in maintaining phases of deposited particles and the hardness of the coatings, Figure 4.12. For this investigation, some selected coatings which represented a dense structure have been chosen. According to the obtained XRD results, the produced coatings contained vanadium oxide phase. In contrast with CS, HVAF is not able to maintain the deposited particle phases [105]. Energy dispersive spectroscopy (EDS) mapping of the sample AS3 has been studied to assure the accuracy of XRD results, Figure 4.13. The EDS mapping showed that the oxygen content is higher in the regions shown by yellow arrows which has higher vanadium compared to titanium or aluminum. Regarding the hardness, Figure 4.12(b), increasing air pressure and fuel pressure leads to slightly higher particle velocity and more particle deformation. This could result in an increase in dislocation density leading to higher hardness [105]. For example, at the spraying distance of 75 mm, with an increase in air/fuel pressures from 813/799 to 841/827 KPa (AS7 and AS8, respectively), average microhardness increased by 30 HV. On the other hand, hardness was not

affected significantly by increasing spraying distance from 50 to 75 mm when air and fuel pressures are kept constant (AS3 and AS7, respectively). This can be put down to an increase in substrate temperature, which facilitates dislocation motion and brings on a decrease in stored dislocation density.

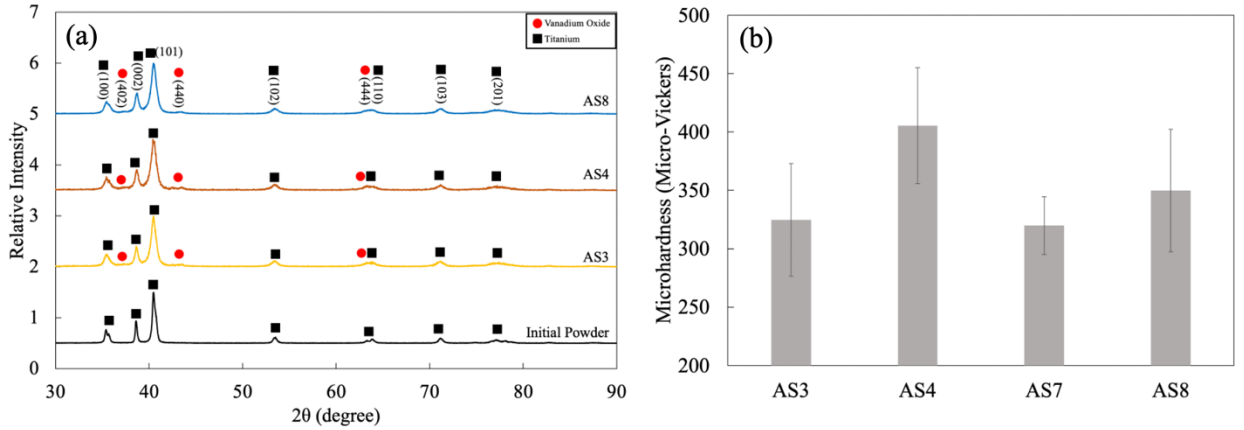

Figure 4.12. (a) XRD analysis of the two densest coatings and (b) microhardness examination of four of the densest coatings manufactured using ID-HVAF process parameters. Error bars represent standard deviation.

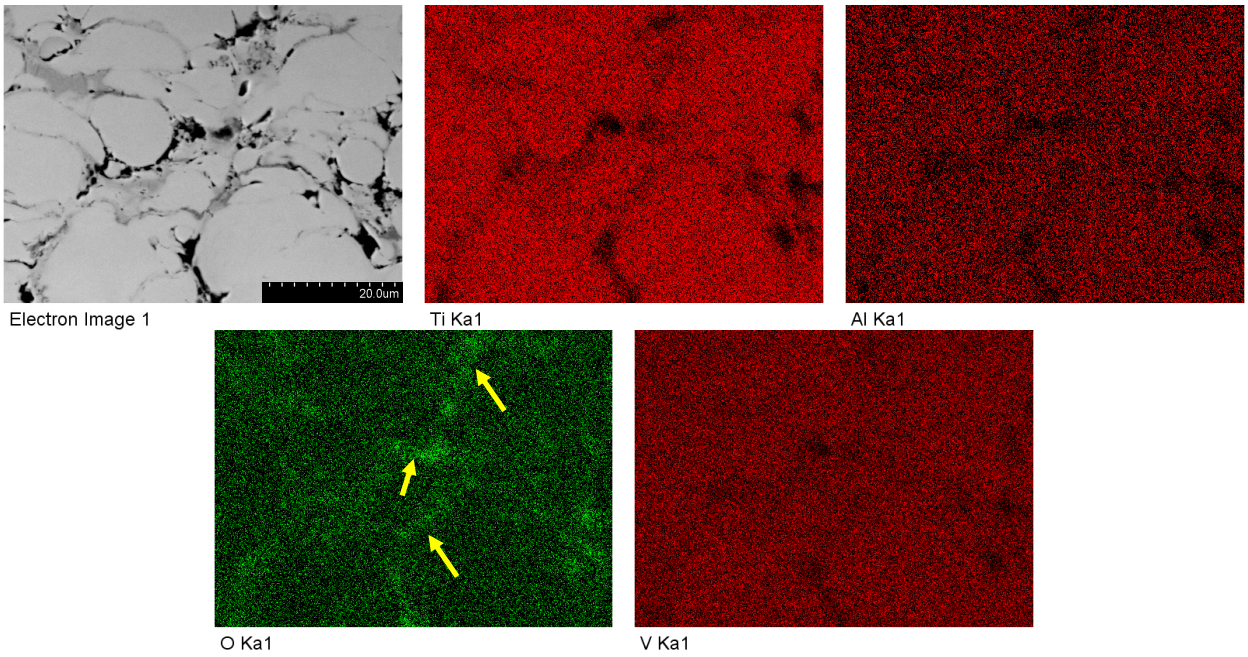

Figure 4.13. Energy dispersive spectroscopy (EDS) mapping of the Ti-6Al-4V sample produced using ID-HVAF at the spraying distance of 50 mm, air pressure is 813 KPa, and fuel pressure is 799 KPa (AS3).

4.4.4. Nozzle Length Effect of Coatings Properties

The effect of nozzle length is studied at the quasi-optimized condition. The microstructure in Figure 4.14 illustrates an increase in coating thickness and associated deposition efficiency with increasing nozzle length. Further, the coating porosity decreased significantly with the medium-sized nozzle as compared to the short one. By using the long nozzle, the particle velocity increases significantly, as shown by using the DPV, which led to a dense structure at the first deposited layers, Figure 4.14 (c). On the other hand, this enhancement of the particle deformation with nozzle length may be influenced by the increased residence time available for particle heating and the thermal softening effect [13]. It is worth noting that using a long metallic nozzle for depositing fine metallic particles increases the possibility of clogging the nozzle.

Figure 4.15 shows that increasing the nozzle length from 26 mm (short nozzle) to 70 mm (long nozzle) reduced the porosity by 53 % and increased the thickness by 57 µm (N1 to N3). However, the average thickness of as-sprayed deposits using medium and long nozzle were 118 µm and 111 µm, respectively, which are rather similar. Thus, for avoiding the nozzle blockage and having more uniform deposits, in subsequent tests, the medium size nozzle was chosen.

According to XRD results, Figure 4.16(a), regardless of the length of the nozzle, ID-HVAF is not capable to maintain the phases of deposited particles. By assuming that air pressure, fuel pressure, and spraying distance are constant while nozzle length increases (M_50_A813_F799 and L_50_A813_F799 in Figure 4.16(b)), the hardness has boosted. This is rooted in the enhancement of particle velocity, which eases particle deformation and, as a result of it, improved stored dislocation density.

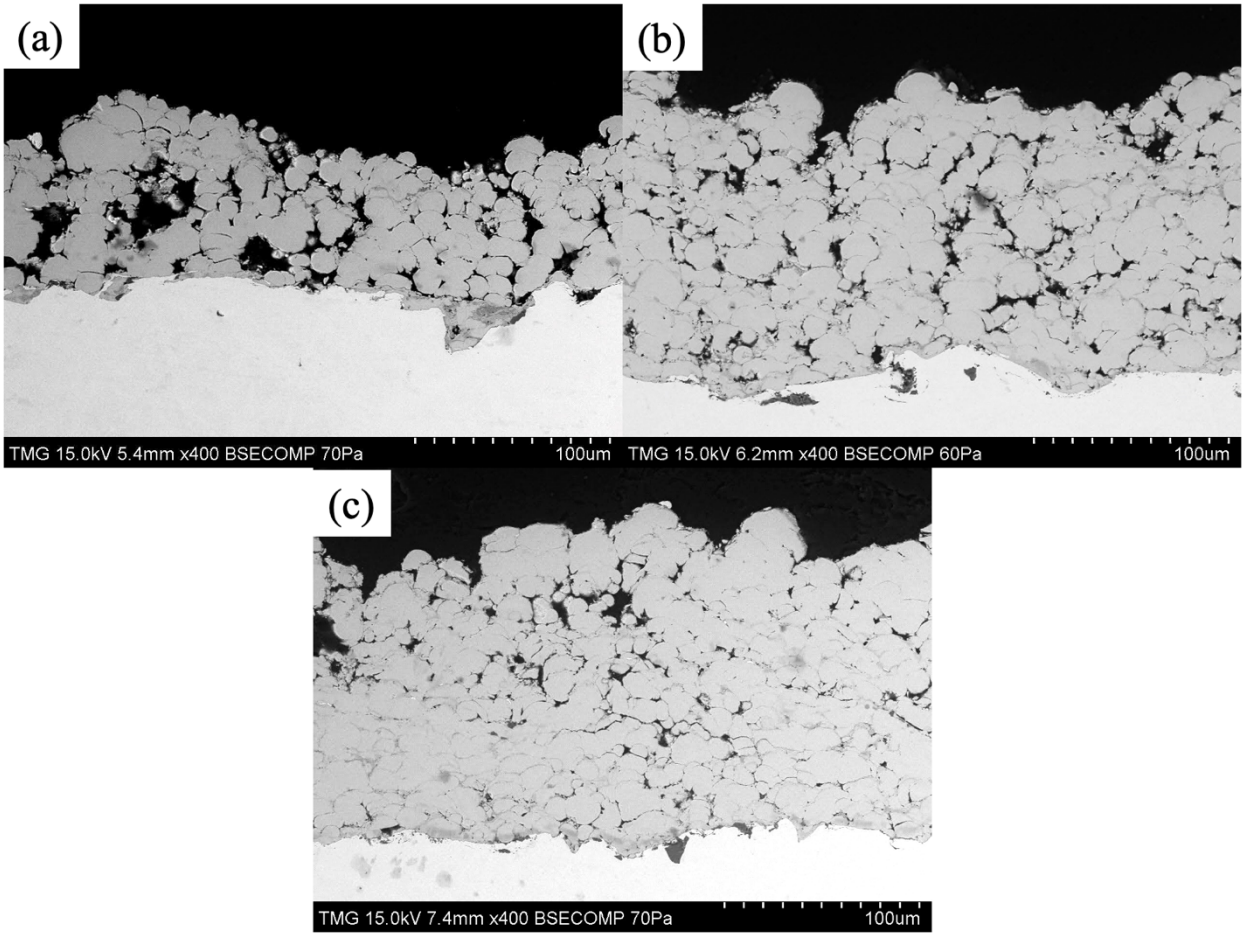

Figure 4. 14. SEM images of the coatings (a) N1, (b) N2, and (c) N3.

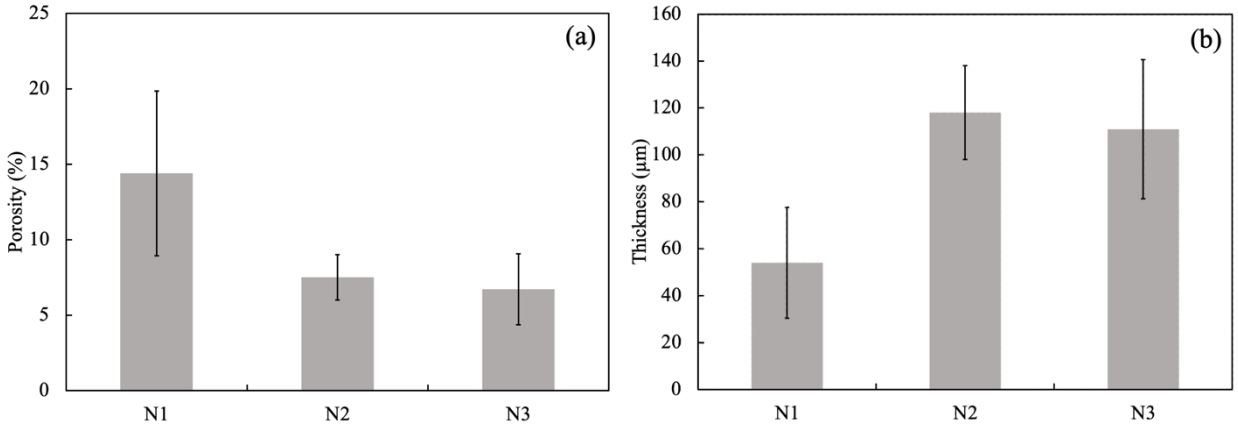

Figure 4.15. Examining the effect of nozzle length on obtained (a) porosity and (b) thickness of the manufactured coating.

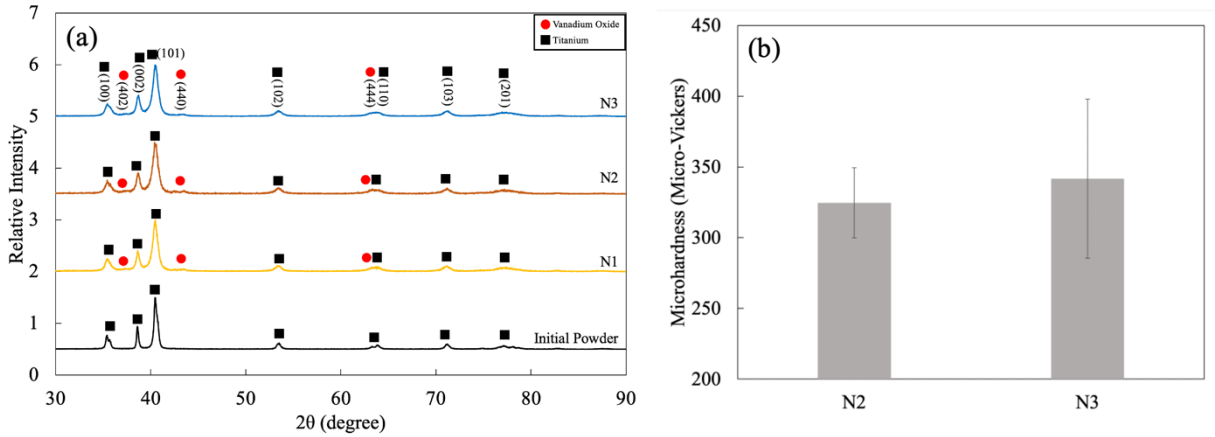

Figure 4.16. (a) XRD analysis of the densest coatings and (b) microhardness examination of the densest coatings manufactured using different nozzle lengths. Error bars show standard deviation.

4.4.5. Effect of Traverse Speed

The effect of the traverse speed on the coating porosity was investigated at the deposition condition of 813/799 KPa air/ fuel pressures and 50 mm of spraying distance (T1 to T4). It is worth noting that both medium size (T1 and T2) and long size nozzles (T3 and T4) were used in this investigation at the traverse speeds of 500 and 1000 mm/s. Figure 4.17 shows the substrate temperature when using the long nozzle (T3 and T4) showing that by decreasing the traverse speed, the average substrate temperature was increased 50 °C as the torch spends a longer time on the substrate.

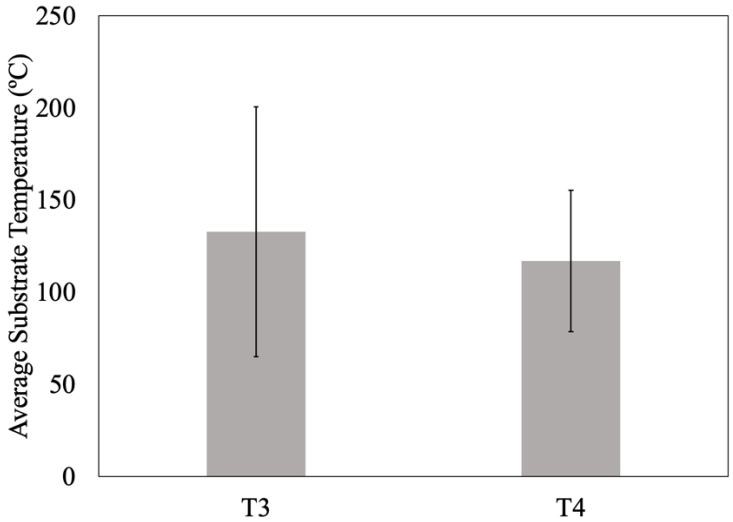

Figure 4.17. Average substrate temperature for T3 and T4 samples. Error bars show standard deviation.

Figure 4.18 illustrates the microstructure of as-sprayed deposits. Due to the peening effect, the density increased in the first deposited layers significantly regardless of the nozzle length and traverse speed. The peening effect depends on particle velocity and already deposited particles temperature. Therefore, the peening effect becomes more significant by using the long nozzle and lower traverse speed that increases particle velocity and substrate temperature, respectively. The thickness of the manufactured coatings increased around 112 µm in both nozzles while traverse speed was lower because more particles impinged on top of each other, Figure 4.19. The boost in traverse speed from 500 to 1000 mm/s led the average porosity level to drop by 15 % and 37 % for the long and medium nozzle, respectively.

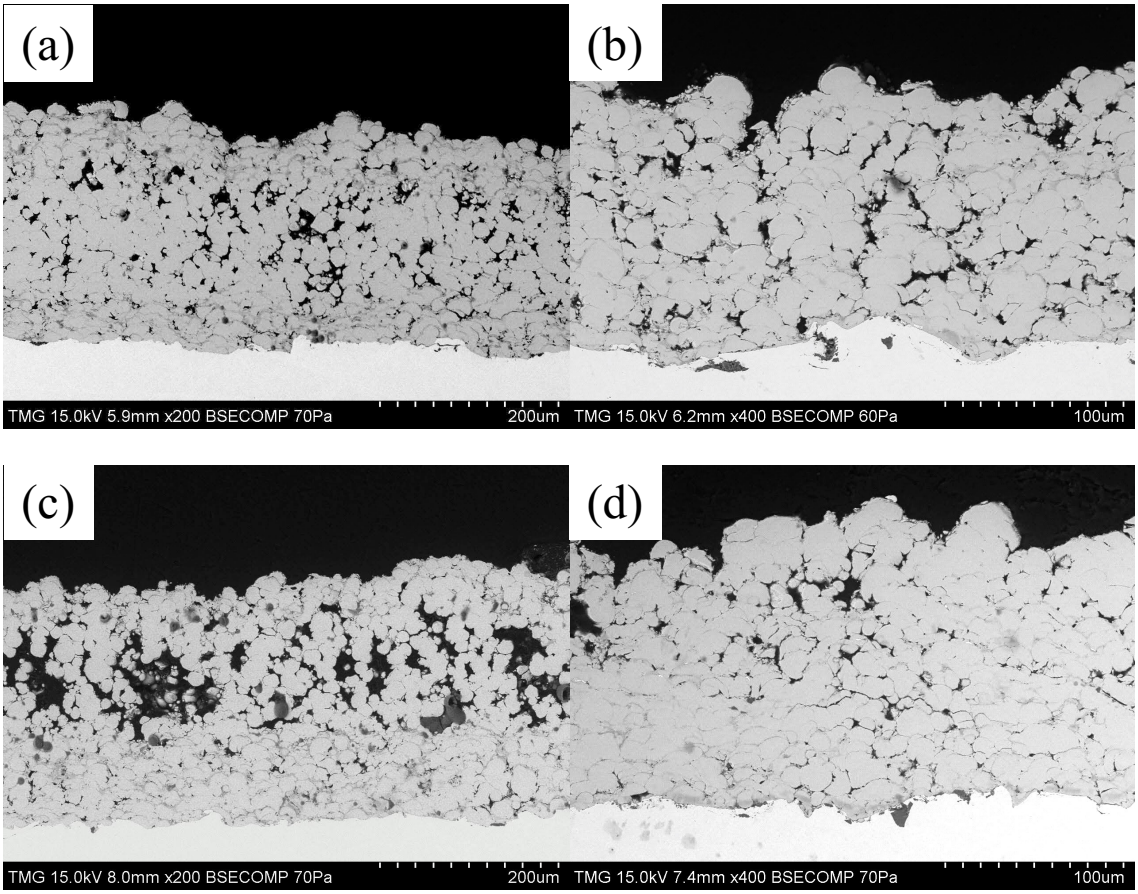

Figure 4.18. The microstructure examination of the coatings (a) T1, (b) T2, (c) T3, and (d) T4.

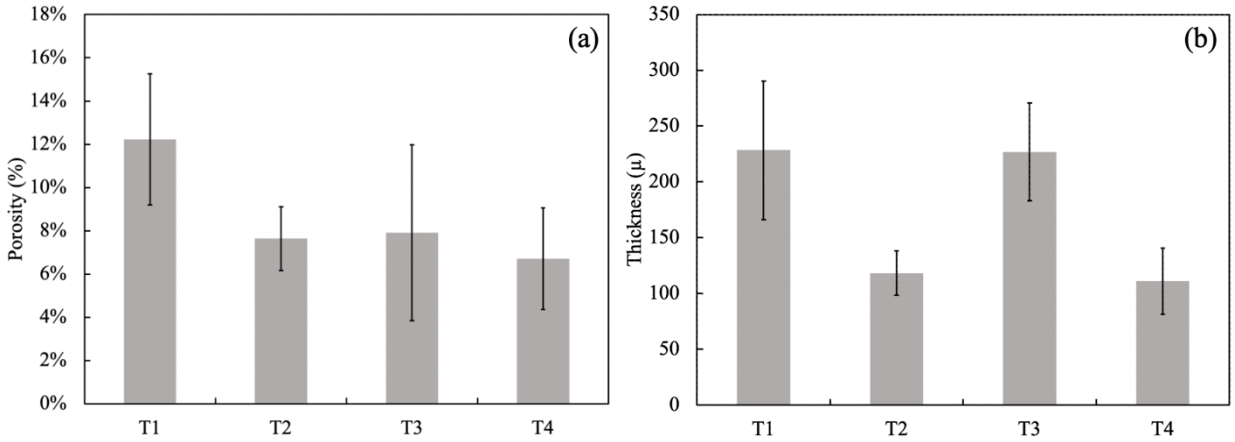

Figure 4.19. The effect of traverse speed on (a) Porosity level and (b) thickness of the Ti-6Al-4V coatings produced using ID-HVAF.

As it was shown before, ID-HVAF led to find the vanadium oxide phase in as-sprayed samples; hence, regardless of the traverse speed, ID-HVAF cannot maintain the phases of the deposited particles, Figure 4.20(a). On the other hand, lowering the traverse speed enhanced the significance of the peening effect leading to a higher degree of particle deformation and coatings' microhardness, especially, when the large nozzle is used, Figure 4.20(b).

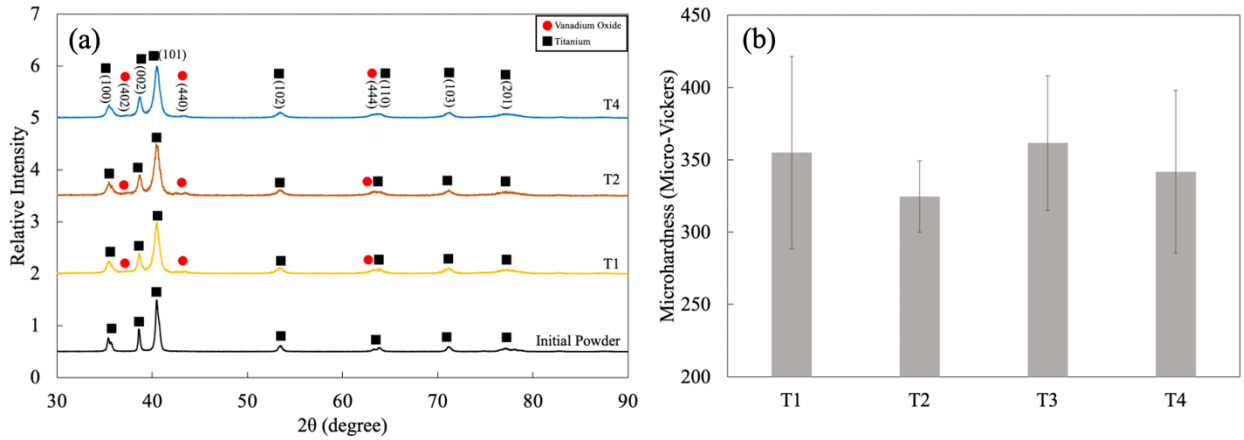

Figure 4.20. (a) XRD analysis of the densest coatings and (b) microhardness examination of the densest coatings manufactured using different traverse speeds. Error bars are standard deviation.

4.5. Conclusion

The focus of the study was to examine the potential of using the ID-HVAF process to produce Ti-6Al-4V deposits demonstrating a suitable combination of porosity, thickness, and microhardness. The effect of different spray parameters such as air pressure, fuel pressure, feeding rate, nozzle length, traverse speed, and spraying distance on the characteristics of in-flight particles and the as-sprayed deposits were investigated.

The obtained results showed that DPV as a diagnostic system could not detect in-flight particles responsible for manufacturing the coating due to their low temperature. Hence, with the help of a laser, the non-emitting particles were detected. As illustrated, increasing nozzle length, air

pressure, and fuel pressure significantly affected in-flight particles velocity. In the next step, the ID-HVAF gun parameter's effect on as-sprayed samples was examined. It was shown that increasing the feeding rate would enhance the deposition efficiency and density of the sample. Additionally, boosting air and fuel pressure would increase particle velocity, density, deposition efficiency, and hardness. However, increasing the spraying distance would provide the particle with more time to cool down and to impact a cooler substrate which led to a drop in density, deposition efficiency, and hardness. Using a long nozzle was positively associated with higher sample density compared using the short one. This is because the long nozzle increases particle velocity significantly, and as a result of it, a harder sample would be produced while other spraying parameters are constant. Decreasing traverse speed had the potential to enhance the coating's thickness while reducing the deposit density. Also, because lower traverse speed enhances the peening effect, the hardness of the produced coatings was higher compared to the time that the ID-HVAF gun moves faster in front of the substrate. In the end, due to the exothermic reaction that Ti-6Al-4V particles might go through, it is inevitable to maintain initial particle phases, and in all samples, vanadium oxide has been found. To conclude, this paper showed that ID-HVAF is capable to be considered as a solid-state deposition technique like cold spray process; however, HVAF does not maintain the phases just like cold spray and the produced samples are not as dense as as-fabricated samples using CS [182]. Then, in the future, the potential of ID-HVAF as a solid-state additive manufacturing method capable of repairing damaged metallic parts can be studied.

It is worth noting that, in this paper, outer layer of a cubic substrate has been coated using ID-HVAF torch. Hence, the obtained conclusions cannot be related to characteristics of an inner diameter surface coated using ID-HVAF. This is because in such a confined space, the turbulence can directly affect the entrapment of bounced back particles. Also, the substrate temperature cannot easily be controls. These can adversely affect the coatings properties and diverge them from what has been reported in this paper.

4.6. Acknowledgment

The authors would like to thank the National Research Council of Canada (NRC) for their financial support for this work.

Chapter 5

Tribological and Microstructural Properties of Ti-6Al-4V Samples Produced by Using High-Velocity Air Fuel (HVAF)[4]

5.1. Abstract

Cold spray (CS) and high-velocity air-fuel (HVAF) are known as solid-state deposition techniques. In both methods, deposited particles deform severely upon impact on a substrate. For some materials with high hardness and/or strength, the low process temperature of CS may result in insufficient deformation of deposited particles; consequently, low density deposits with poor mechanical properties are formed. For such materials, using HVAF to deposit solid particles at elevated temperatures could be a practicable method. In this work, inner-diameter HVAF (ID-HVAF) has been used to manufacture a four mm thick Ti-6Al-4V deposit. To enhance mechanical properties, post-spray heat-treatment has been performed for phase transformation of α-Ti to β -Ti. The porosity level in the as-fabricated and the heat-treated sample was 1.2% and 0.9%, respectively, both exhibit a dense structure. Both as-fabricated and heat-treated samples of Ti-6Al-4V deposits have a high oxygen content, which is the main concern regarding ID-HVAF.

5.2. Introduction

Ti-6Al-4V is a common alloy used in a variety of industries, such as aerospace that operates in harsh environments, in which the components are prone to damage [124-128]. To be cost effective, repairing damaged metallic components using solid-state additive manufacturing techniques such as CS has gained attention [130-133]. CS deposits metallic particles at supersonic velocities and low temperatures. As a result of the impact, both the deposited solid particle and substrate deform plastically to create bonding [13, 19, 72-73, 77, 100]. Increasing deposited particle deformation improves as-fabricated sample density. However, CS cannot deform high strength materials sufficiently to deposit a dense structure [87, 105-106, 137, 153, 155].

Chen et al. [105] investigated using both helium and nitrogen as the CS propellant gas to deposit Ti-6Al-4V particles. The purpose of using helium was to increase in-flight particles velocity and, as a result, particle deformation and sample's density. Although the attempt was successful, the obtained properties were still far from a bulk-like sample's characteristics. To sinter the deposit, relieve residual stresses, and enhance mechanical properties, post-heat treatment methods such as annealing and hot isostatic pressure (HIP) were used [105-106, 137]. To produce a very dense structure and to be cost-effective, the increased deformation of the deposited particles is desirable. This can be accomplished by depositing the particles at enhanced temperatures to soften the particles prior to impact [183].

For this purpose, another thermal spray method, known as high velocity air-fuel, can be used to elevate deposited particles temperature and manufacture a sample at a high deposition rate. In a

[4] Submitted to Surface and Coating Technology Journal in February 2023.

previous study, ID-HVAF was successfully used to manufacture metallic Ti-6Al-4V coatings. It was shown that air pressure, fuel pressure, spraying distance, traverse speed, and nozzle length can have a significant effect on inflight particle characteristics, coating density, and hardness [183]. As we have illustrated in our previous work, increasing the air/fuel pressure and nozzle length improves inflight particle velocity and produces a denser coating while maintaining the α -Ti phase of deposited particles [183].

Because ID-HVAF maintained the α-Ti phase of the deposited particles, fatigue strength, creep resistance, and fracture toughness are likely to be poor [183-186]. To enhance the deposit's mechanical properties, it is essential to transfer α-Ti to β-Ti. This is because β-Ti has a body-centered cubic (bcc) structure making it deformable compared to the hexagonal α-Ti. In a previous study by Molak et al. [185], the warm spayed Ti-6Al-4V deposits have been heat-treated to form β-Ti. It was illustrated that the applied heat treatment not only sintered the sample and significantly decreased porosity levels but also enhanced the deposit's ductility by transferring α-Ti to β-Ti [186]. In another study carried out by C. Chen et al. [105], HIP was shown to sinter the Ti-6Al-4V particles in as-fabricated sample and to significantly enhance the ductility of the part.

To overcome the mechanical properties drawback of as-fabricated CS deposits and to reduce the operational costs of heat treatment, this study proposed thermal softening of the particles during deposition to enhance particle deformation. For this purpose, deposition of particles at elevated temperatures and high velocities using ID-HVAF were performed to examine the potential of this process as a solid-state additive manufacturing method for repairing Ti-6Al-4V parts. Based on our previous results [183], spraying parameters that led to dense microstructures with high hardness were used to manufacture a four mm thick deposit. Then, a heat treatment process was applied to sinter the deposited particles and enhance the mechanical properties by transferring α-Ti to β-Ti.

5.3. Experimental Methodology

An ID-HVAF gun (Uniquecoat Technologies LLC, Oilville, USA) was selected to be used due to its narrow jet that facilitates manufacturing near-net shape parts. Ti-6Al-4V grade 5 particles (AP&C, Canada) with oxygen content of 0.25 wt% measured by LECO 836 Elemental Analyzer were deposited using the ID-HVAF system to manufacture a four mm thick coating on a stainless-steel cylinder with the Outer diameter of 213 mm. The Ti-6Al-4V feedstock powder particles had a spherical shape (Figure 5.1(a)) with d_{10}, d_{50}, and d_{90} of 5, 10, and 17 µm, respectively, Figure 5.1(b). During deposition, the substrate was rotating at the speed of 167 rpm while the gun was moving at the speed of 8 mm/s perpendicular to the surface of the cylinder at the spraying distance of 50 mm. This translates to a tangential speed of 1000 mm/s. The remaining spraying parameters (Table 5.1) were selected based on the results of the previous study [183]. The ID-HVAF nozzle used for the deposition is shown in Figure 5.2.

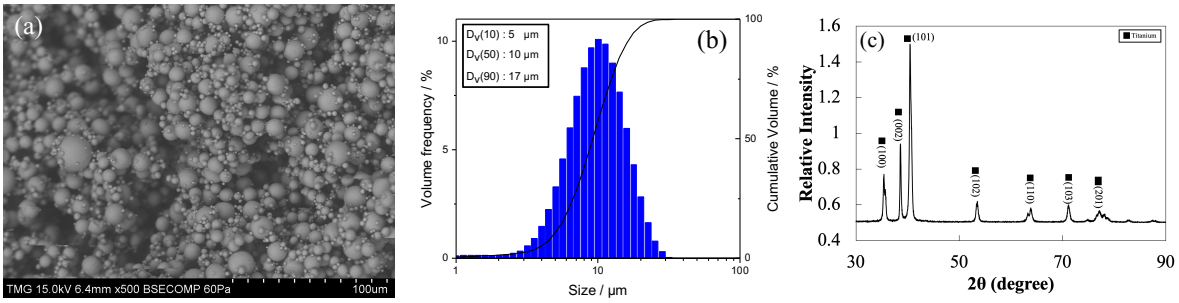

Figure 5.1. Ti-6Al-4V powder (a) Scanning electron microscope (SEM) image, (b) particle size distribution analyses, (c) XRD analysis.

Table 5.1. ID-HVAF spraying parameters for manufacturing Ti-6Al-4V deposit.

Parameter	Value
Spraying Distance (mm)	50
Spraying Step (mm)	3
Rotation Speed (rpm)	167
Spraying Angle (º)	90
Torch Traverse Speed (mm/s)	8
Air Pressure (KPa)	813
Fuel Pressure (KPa)	799
Carier Gas (Nitrogen) Pressure (KPa)	275
Feed Rate (gr/min)	18
Nozzle Length (mm)	46.75

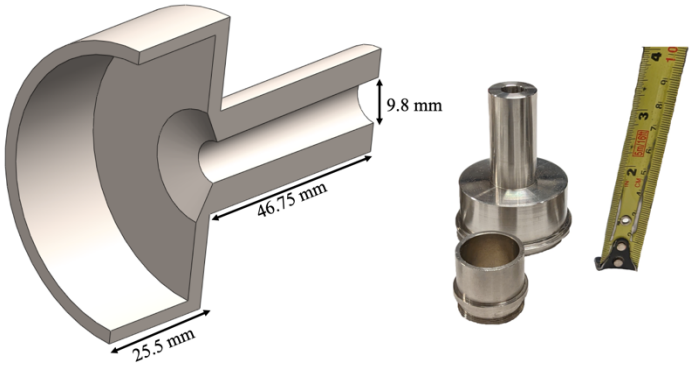

Figure 5.2. Used ID-HVAF nozzle for manufacturing the thick Ti-6Al-4V sample.

Prior to spraying of the coating, a total of five passes were used to preheat the surface with the spray jet and without any powder injection. In total, 250 passes at feed rate of 18 g/min produced a 4 mm thick Ti-6Al-4V coating. During spraying, the substrate temperature was monitored using an infrared camera (FLIR, A320). To minimize the oxidation of the deposited particles, the

substrate was cooled from both inside and outside of the cylinder with high-pressure air vortexes (Figure 5.3).

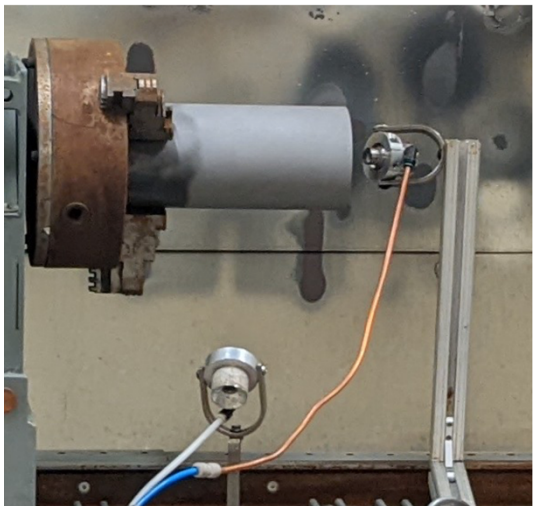

Figure 5.3. The used set-up for cooling the substrate during deposition.

Samples of 10*80 mm were cut out of the coated cylinder using EDM machining. Then, the extracted samples were heat treated to produce β-Ti to enhance the mechanical properties of the deposited Ti-6Al-4V coatings [184-185]. The first step of the heat treatment was done above the transformation temperature at 1025 °C for one hour in Argon, followed by cooling with compressed air. In the next step, to avoid excessive grain growth, an annealing process at a temperature slightly higher than transit temperature was applied to the coupon. In this step, the sample was heated at 760 °C for 2 hours in argon, followed by cooling to room temperature outside of the furnace [186].

To study the microstructure of both as-fabricated and heat-treated samples, metallographic samples were prepared using the standard metallography techniques. Kroll's etchant (water 92.82 wt%, nitric acid 6.11 wt%, hydrofluoric acid 1.07 wt%) was used to reveal the microstructure [187]. The microstructure was studied using an optical microscope (OM) and scanning electron microscope (SEM) in the backscatter electrons (BE) and secondary electron (SE) modes. Porosity levels were estimated using SEM images and an image analyzer software called ImageJ. In addition, Energy Dispersive Spectroscopy (EDS) was utilized for elemental mapping of both as-fabricated and heat-treated samples. X-Ray Diffraction (XRD) was used to analyze the initial powder and fabricated deposit using a source emitting CuK radiation at scanning (2) angles between 25º to 85º. Oxygen measurement was performed by a LECO 836 Elemental Analyzer. Microhardness of the deposits was evaluated by applying a force equal to 100 g for 10 seconds.

5.4. Results and Discussion

5.4.1. Samples Appearance

This section discusses both spray monitoring as well as the visual characteristics of the fabricated samples. To minimize oxidation and phase transformation during spraying, substrate temperature should be as low as possible. Using an inferred camera, the substrate temperature has been monitored during the spraying, Figure 5.4. As illustrated, the maximum substrate temperature during spraying was around 220 °C. Additionally, Figure 5.4 shows the two times that spraying was paused intentionally to check the nozzle, as ID-HVAF nozzles are initially designed to deposit ceramic particles and are prone to clogging when injecting fine metallic particles.

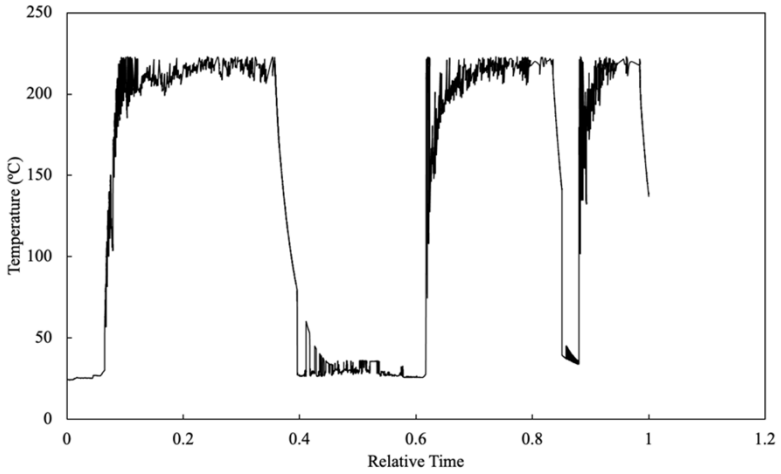

Figure 5.4. Substrate temperature during deposition of Ti-6Al-4V particles using ID-HVAF gun.

After 250 passes of deposition, a 4 mm Ti-6Al-4V coating shown in Figure 5.5(a) was produced. Following extraction of test coupons from the coated cylinder, one coupon was heat treated according to the previously described procedure. The horizontal cracks (yellow arrows) within the coating made it impossible to cut out any tensile test samples, Figure 5.5(b). Also as shown in Figure 5.5(b), a non-uniform coating thickness was obtained, which could be related to from the feeder's incapability to deliver fine metallic particles at a stable feeding rate.

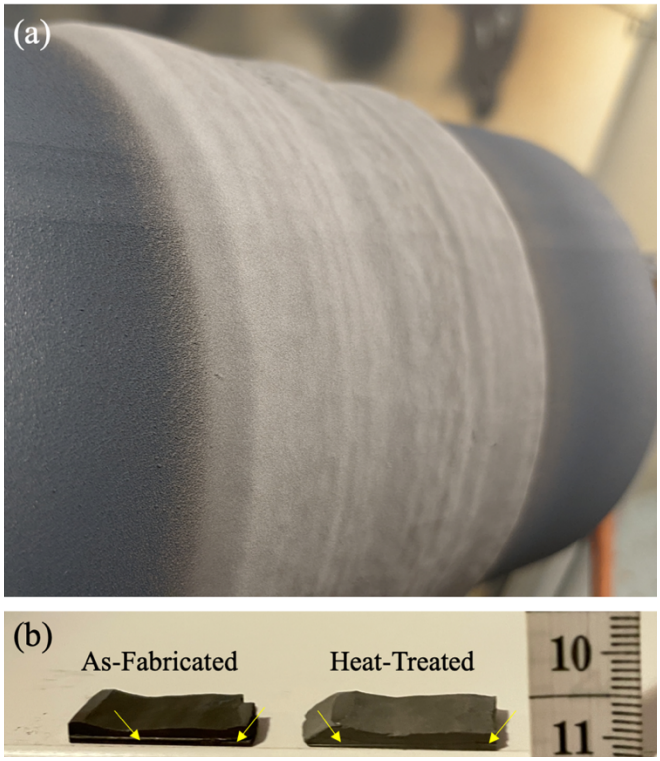

Figure 5.5. (a) The manufactured 4 mm-thick Ti-6Al-4V coating using ID-HVAF and (b) extracted coupons from the coatings before and after heat treatment.

5.4.2. Microstructural Examination

The top surface of the as-fabricated and heat-treated deposits was examined to find evidence of particle deformation, and to confirm that ID-HVAF was successfully used as a solid-state additive manufacturing process. In the micrographs of Fig.6, material jet of deformed particles (yellow arrows) indicates that ID-HVAF successfully deposited Ti-6Al-4V solid-state particles.

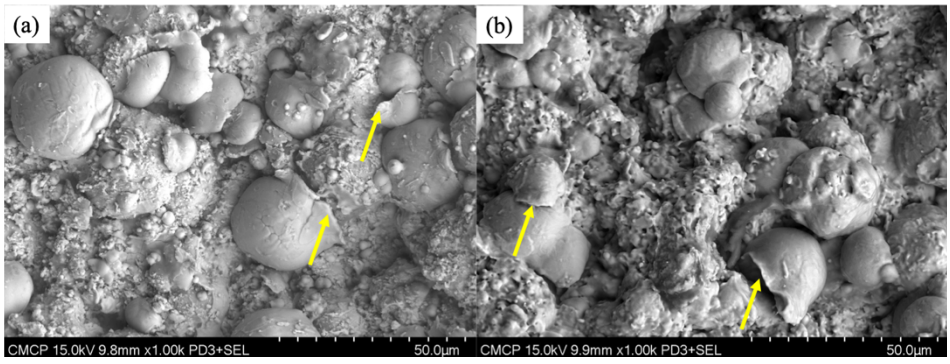

Figure 5.6. SEM images of top surface of (a) as-fabricated sample and (b) heat-treated sample.

The cross-sectional microstructure of as-fabricated and heat-treated samples are shown Figure 5.7. The top layer of the as-fabricated sample (green arrows) is porous due to insignificant peening effect. Two other porous strips within the coating correlate with the pauses taken during spraying to ensure that the nozzle was not clogged (yellow arrows). These highly porous regions are

responsible for the horizontal cracks shown in Figure 5.5(b). After applying heat treatment, the deposited particles experienced some level of sintering, which increased the deposit density, Figure 5.7(b). The two porous strips within the coatings (yellow arrows in Figure 5.7(a)) are less evident due to this sintering effect. It is worth noting that the porosity level is higher after the longer first pause than after the shorter second pause. This can be due to surface cooling and surface oxidation which results in the less deformation of the deposited particles caused by the peening effect. However, some large pores were remained (blue arrows), that could be the result of coalesce of the smaller pores. In the heat-treated sample, some horizontal cracks can be seen (red arrows) which made it impossible to extract tensile test coupons for examining the mechanical properties of the coating. In the higher magnification image of the as-fabricated sample, the deformed particles are clearly visible. However, by applying heat treatment, the particles are fully defused into each other and reconstructed an equiaxial α-Ti and intergranular β-Ti.

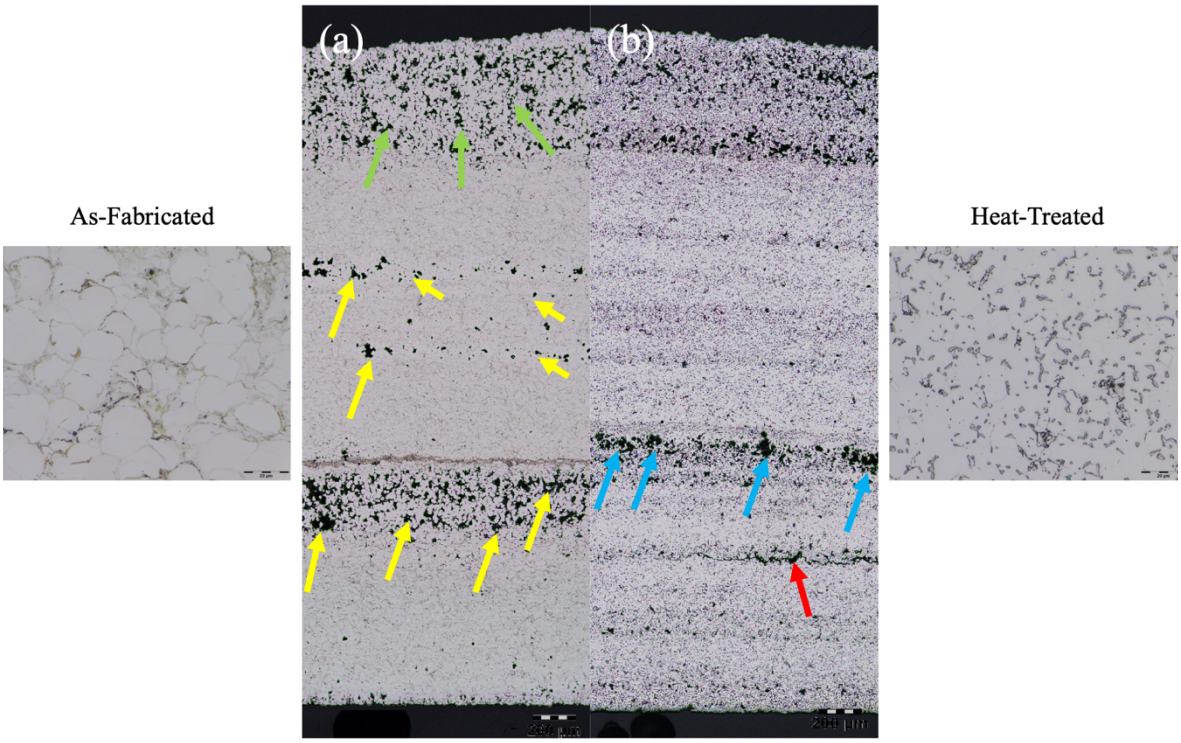

Figure 5.7. The optical microscopic (OM) image of the cross-section view of (a) as-fabricated and (b) heat-treated Ti-6Al-4V sample produced using ID-HVAF gun.

To study the microstructure of the coatings in more detail, a scanning electron microscope (SEM) was used, Figure 5.8. The microstructure of the as-fabricated coating at different magnifications is shown in Figure 5.8(a), Figure 5.8(c), and Figure 5.8(e). Figure. 8(b), Figure 5.8(d), and Figure 5.8(f) illustrate the microstructure of the heat-treated Ti-6Al-4V deposit. According to Figure 5.8(a) and Figure 5.8(b), the samples are dense prior and after heat treatment, and only few pores could be observed (yellow arrows). By increasing the magnification of the as-fabricated sample (Figure 5.8(c)), the splats shown by red-dashed-circles prove the existence of burned and/or highly oxidized particles in the deposit. By further increasing the magnification, Figure 5.8(e), the deformed particles are clearly visible, demonstrating the success of ID-HVAF in depositing solid-state particles. Figure 5.8(f) reveals a complete change in microstructure after heat treatment. Due

to the sintering process, a dense coating structure was clearly seen, and intergranular β-Ti has been formed in between of equiaxial α-Ti grains (green arrows).

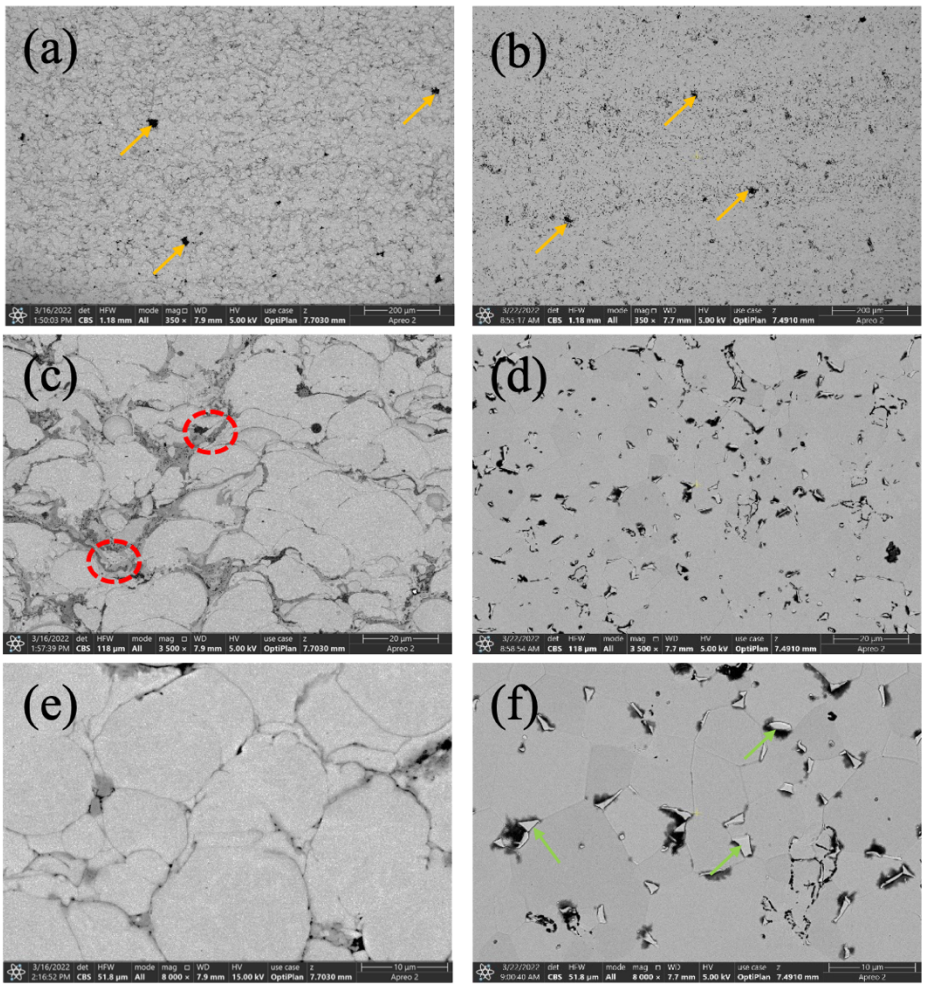

Figure 5.8. SEM images of (a), (c), and (e) non-etched as-fabricated Ti-6Al-4V deposit and (b), (d), and (f) etched heat-treated Ti-6Al-4V deposit at different magnifications.

The porosity level in the densest area of each coating was measured, and the results are shown in Figure 5.9. The as-fabricated sample has a porosity of 1.2%. Applying heat treatment decreased the porosity down to 0.9%. The obtained results were compared with those acquired for cold sprayed Ti-6Al-4V coatings in a study by Chen et al. [105]. They used nitrogen and helium as carrier gases to fabricate CS Ti-6Al-4V deposits which resulted in the porosity levels of 2.5% and 1.5%, respectively. The comparison shows that denser as-fabricated structures were produced with ID-HVAF, even when helium was employed as the propellant gas with cold spray, showing the positive effect of higher particle temperatures and thus particle softening with the HVAF process. It is worth noting that the particle size used in the noted work was slightly larger than what was used in this study. After sintering of the coatings by HIP, Chen et al. [105] found porosity levels of 0.037% and 1.67 % when helium and nitrogen were used as the propellant gas, respectively [105]. The proposed heat treatment in this study produced a denser structure than the HIPed coatings deposited using nitrogen, however, the heat-treated coating microstructure appears to be

more porous than the CS coating produced by helium as the carrier gas post-HIP. This could be due to the presence of less oxides on particle boundaries in the CS coating sprayed with helium compared to the HVAF coating, promoting atomic diffusion and sintering of the particles.

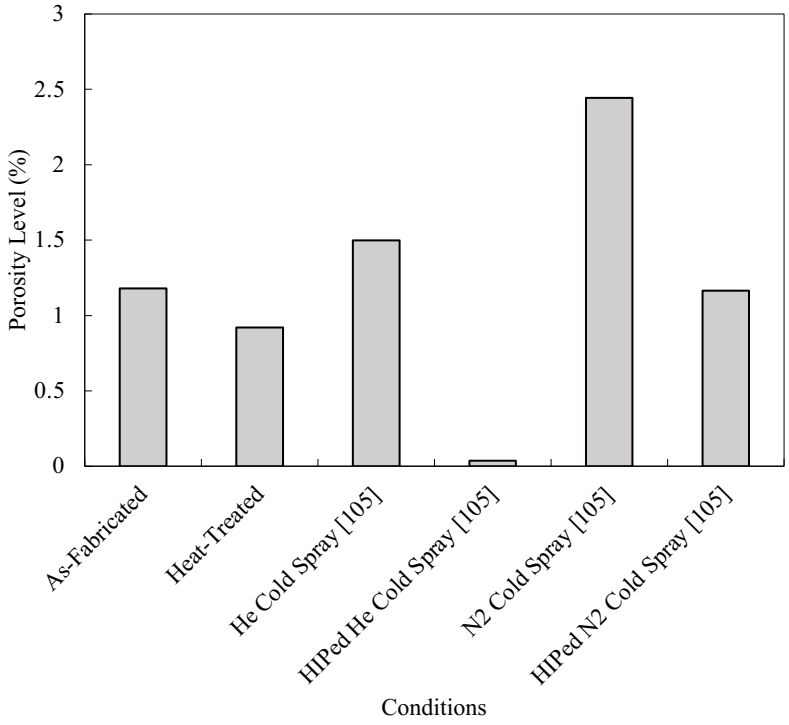

Figure 5.9. Comparison between the porosity levels of Ti-6Al-4V deposits manufactured by ID-HVAF and CS [105] before and after sintering.

5.4.3. Phases and Elements Analysis

XRD phase analysis results of as-fabricated and heat-treated coatings compared to the starting powder are shown in Figure 5.10. It shows that titanium remained in the -phase in the as-fabricated coating, however, vanadium oxide was formed. This illustrates that the temperature of the process was not high enough to transfer α-Ti to β-Ti. After applying heat treatment, some new insignificant peaks of β-Ti appeared. The low intensity of these peaks is consistent with the microstructural examination results, as only a small portion of β-Ti was observed, Figure 5.9(f). Since the heat treatment was done in an inert environment, no new oxide component was formed compared to the as-fabricated coating.

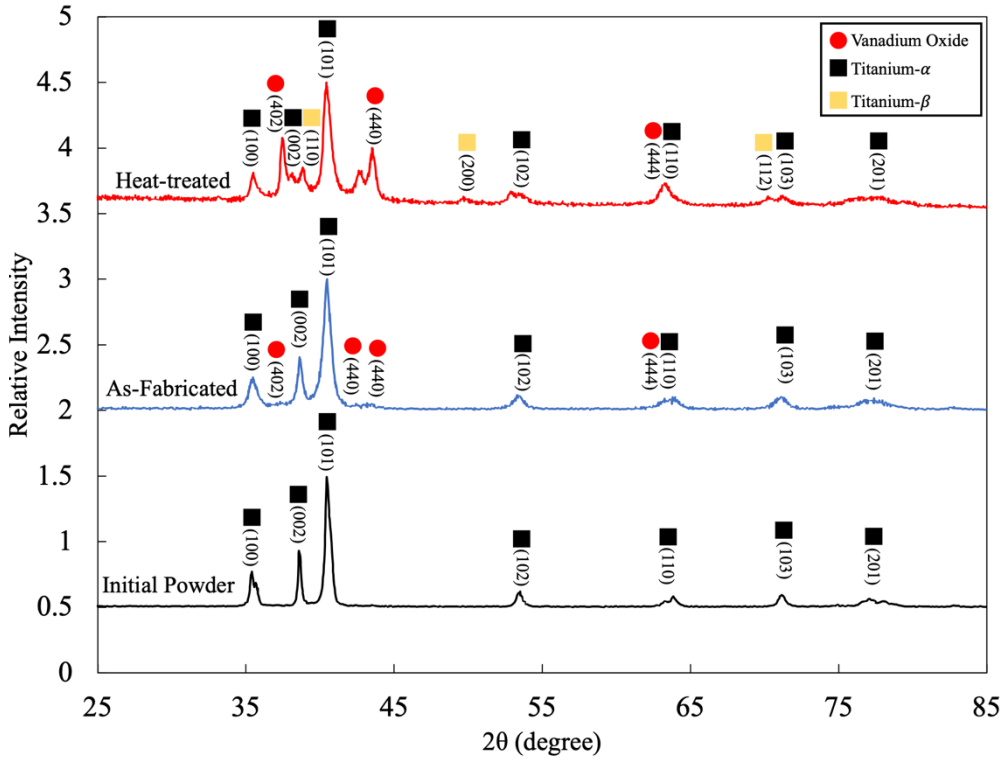

Figure 5.10. XRD phase analysis of as-fabricated and the heat-treated Ti-6Al-4V coatings compared to the starting powder.

The results of this study demonstrate that although combustion-based HVAF technique can be successfully used for solid-state deposition of metallic particles, the higher temperature of the jet could result in oxidation and burning of the fine feedstock particle. This is what leads to the formation of new phases like vanadium oxide in as-fabricated coatings. In addition, presence of large α-Ti grains after the heat treatment could be resulted from the high oxygen (α phase stabilizer) content. The oxide content of the coatings, measured using a LECO device, are shown in Figure 5.11. As-fabricated coating contains a significant amount of oxygen at around 1.75 wt%. By applying heat treatment, the average oxygen content measured in the coating was reduced to 10.3%. Considering the error bars, it can be said that the heat treatment process did not have a significant effect on the oxygen content.

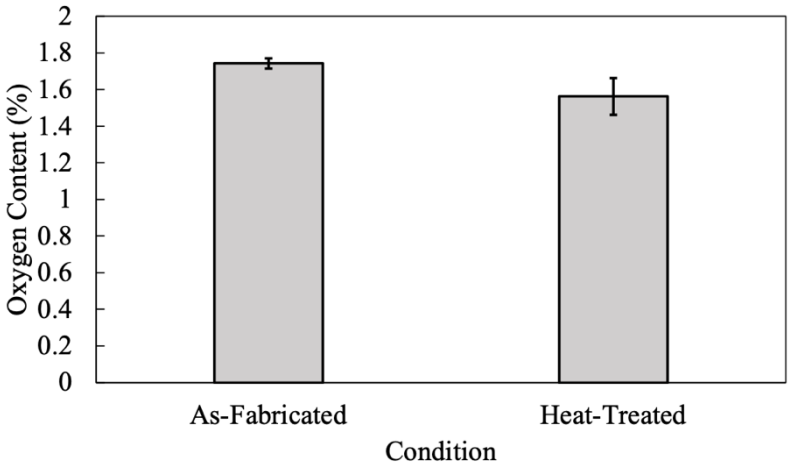

Figure 5.11. The measured oxygen content in as-fabricated and heat-treated Ti-6Al-4V deposits manufactured by ID-HVAF. The error bars are standard deviation.

5.4.4. Coating Hardness

According to Figure 5. 12, the as-fabricated coating had a microhardness of approximately 442 Vickers. By applying heat treatment, the average microhardness was increased by about 27%. This can be related to the presence of large α-Ti grains. Having a high level of oxygen content which acts as α phase stabilizer can prohibit the heat treatment to transit $\alpha \rightarrow \beta$. As shown in Figure 5.8(f), heat-treated sample has a low distribution of small β phases but has large harder α grains. This is in-line with the finding of a previous study by Molak et al. [186]. They used Ti-6Al-4V particles with d_{50} of 30 μm to manufacture as-fabricated parts using warm spray. Then, $\alpha \rightarrow \beta$ transition heat treatment was used at a temperature same as what was used in this study. They related the increase of hardness to oxygen diffusion into the titanium matrix from the interface between the particles during the heat treatment and thus strengthening of the α-phase. This effect is reported to be more pronounced when the sample as high oxygen content. Also, the increase in the hardness can be related to sintering the particles and producing metallic bonding through solid-state diffusion [186]. The hardness values of this study were also compared to those fabricated with CS using helium as the carrier gas before and after applying HIP [105], where hardness values of 410 and 380 Vickers were reported, respectively [105]. The comparison revealed that the ID-HVAF as-fabricated coating has a similar hardness to the CS coating; however, the proposed heat treatment of this study increased the coatings hardness, which is in contrast with what was reported for the CS coatings after HIP process [105]. This is due to the fact that in their work the heat treatment was below $\alpha \rightarrow \beta$ transition temperature and they did not have any oxide formed during spaying. Hence, the used heat treatment for an as-fabricated HVAF sample with high oxygen content would increase the hardness of the samples.

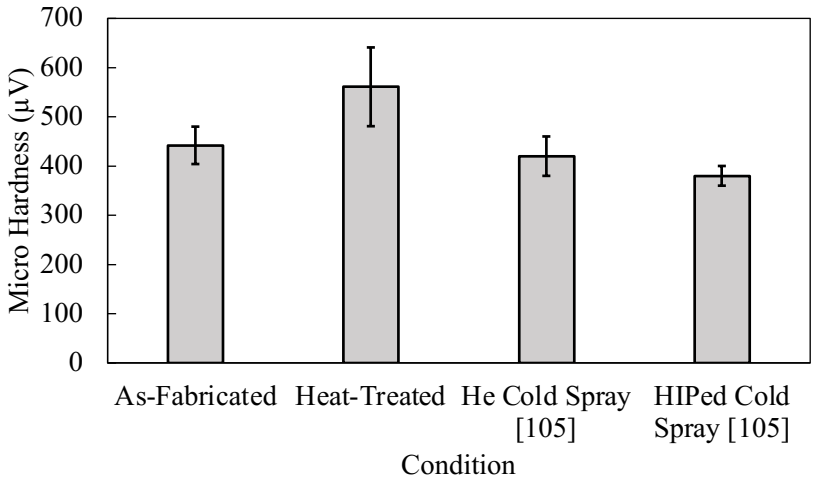

Figure 5.12. The measured micro-hardness of as-fabricated and heat-treated Ti-6Al-4V samples manufactured using ID-HVAF. The error bars represent standard deviation.

5.5. Conclusion

It was demonstrated that HVAF could successfully be employed for solid-state deposition of Ti-6Al-4V particles, producing a 4 mm thick Ti-6Al-4V coating. A post-spraying heat treatment process was used to sinter the deposited particles and transform brittle and hard α-Ti into deformable β-Ti. Microstructural, phase analysis and mechanical properties of the as-fabricated and heat-treated coatings, in addition to their tribological wear behavior were investigated.

Porosity level of the as-fabricated samples was about 1.2%, which was reduced to less than 1% by applying heat treatment, forming a dense coating microstructure. Two main disadvantages were identified for the as-fabricated ID-HVAF coating: a multilayered stirp in the samples and high oxygen content. Heat treatment of the as-fabricated sample that has high oxygen content prevents the formation of the β-Ti phase, causing the α-Ti grains to become coarser. This increases the hardness of heat-treated samples.

5.6. Acknowledgment

The authors would like to acknowledge the financial support of the National Research Council of Canada (NRC) for carrying out this research.

Chapter 6

Summary, Conclusion, Limitations, and Recommendation

6.1. Summary

Repairing damaged metallic parts has gained considerable attention in recent years due to its financial efficiency compared to replacing them. Among repair methods, cold spray offers a promising potential since it can produce metallic samples at a high deposition rate without oxidation. As-fabricated CS samples have poor mechanical properties due to existing pores in the microstructure which arises from insufficient deformation of the deposited particles. Currently, two methods have been employed to enhance density and mechanical properties of as-fabricated samples, which are enhancing deposited particle deformation by increasing impact velocity and/or sintering the deposited particles. Even though the density of as-fabricated samples increased due to enhanced particle velocity and deformation, sintering the samples was still needed to further enhance mechanical properties. In contrast, sintering methods like annealing and HIP were always considered expensive processes. To address these limitations, one approach would be to thermally soften the particles during spraying to increase their deformation further by preheating them during the deposition. In view of the inability to deposit solid-state particles at elevated temperatures using cold spray, this thesis proposed another thermal spray method known as HVAF. The first step in this study was to use numerical analysis to verify that heating the particles during spraying enhances the particle deformation and increases the density of as-fabricated samples. The potential for using HVAF as a solid-state additive manufacturing technique was then assessed through the examination of mechanical, microstructural, and tribological properties of fabricated Ti-6Al-4V samples.

6.2. Conclusion

As a solution to increase the density and mechanical properties of as-fabricated samples, this thesis proposed heating in-flight particles during spraying. Numerical methods can be used before conducting any experiment involving HVAF to test whether elevating the in-flight particle temperature significantly improves the particle deformation. According to the numerical analysis:

- Increasing the velocity of an elevated Ti-6Al-4V particle enhances its deformation and the density of as-fabricated sample.
- When the particle temperature increases upon impact, it becomes softer, resulting in increased particle deformation and sample density.
- Increased substrate deformation leads to softer surfaces for particles to impact on, resulting in a decrease in particle deformation without affecting sample density significantly.

Once it has been demonstrated that increasing particle temperature can increase sample density and particle deformation, it is necessary to examine its effect on the bond produced between the particle and substrate. For this purpose, it is necessary to examine the effect of particle and substrate initial conditions on the failure of their oxide layers. The numerical analysis of oxide layer failure illustrates that:

- In any given condition, the particle oxide layer will fail easily, and the bond will be defined by the failed area of the substrate oxide layer.
- By increasing particle velocity, the substrate would be more deformed more, and the area of failed substrate oxide layer would increase. As a result, increasing particle velocity increases the area on which the particle can bond to the substrate.
- As particle temperature increases, it softens the particle and has no noticeable effect on the bonding and the area of failed substrate oxide layer.
- Increasing substrate temperature would soften the substrate and enhance its deformation. As a consequence, the oxide layer on the substrate fails in more areas, resulting in easier particle-substrate bonding.
- Substrate oxide layer failure is a major factor in determining the critical velocity required for creating bonding. In other words, even at impact speeds below the reported critical value, bonding would still be possible by preheating the substrate.

As a result of confirming that preheating the deposited particles enhances the sample's density, solid-state Ti-6Al-4V particles were deposited at elevated temperatures using HVAF. First, a study of the potential of HVAF for manufacturing solid-state metallic coatings revealed that:

- HVAF is imperative to maintaining the phases of deposited particles.
- Based on the analysis of the effects of the HVAF spraying parameters, it was revealed that increasing feeding rate, the air/fuel pressure, and nozzle length can enhance particle velocity, resulting in a denser and harder structure.
- Due to a reduction in peening effect, increasing traverse speed would decrease substrate temperature, sample density, and hardness of as-sprayed deposits.
- Increasing spraying distance would decrease in-flight particle velocity and substrate temperature leading to a drop in density and hardness of as-sprayed sample.
- HVAF is fully capable to deposit solid-state Ti-6Al-4V and create a dense coating without clogging the nozzle.

In the final step, the best combination of spraying parameters was selected to produce a thick Ti-6Al-4V coating to study the potential of HVAF as a solid-state additive manufacturing process. The results illustrate that:

- HVAF was successfully used as a solid-state additive manufacturing method to produce a dense sample that contained a high amount of oxygen.
- HVAF maintain the α phase of the Ti; however, it did not maintain the phases of Ti-6Al-4V by producing vanadium oxide.
- The clogging of the nozzle and inevitable stops during spraying resulted in distinctive layers on the sample, making it impossible to extract samples for tensile testing.
- Heat-treatment was applied to sinter the particles and to transfer α-Ti to β-Ti which has better mechanical properties. However, since the as-fabricated sample has high level oxygen, which is α phase stabilizer, this heat-treatment affects the hardness adversely.

6.3. Limitation of the Research

Although the work was successfully completed and the results met the thesis' objective, some limitations prevent the work from being further developed. These drawbacks are listed as below:

- It was impossible to correlate numerical results with observed experimental outcomes due to the lack of a proper method to monitor the in-flight particle temperature.
- By using elastic-plastic analysis, bonding could not be considered.
- The ID-HVAF gun does not have a nozzle developed for depositing metallic particles. Therefore, depositing fine metallic particles always caused nozzle clogging, which increased the operational cost.
- When it came to depositing fine particles, the available feeding system was not able to maintain the deposition rate. A possible solution was to fill the feeder with more powder, but this produced electricity in the system, which was not considered safe.

6.4. Recommendation

Lastly, it is necessary to make some recommendations regarding the follow-up work on this dissertation. These recommendations are noted as below:

- Developing a CFD-based analysis or using new monitoring techniques to have better understanding of spraying parameters effect on in-flight particles temperature.
- Studying the effect of in-flight particle temperature on bonding strength of a single particle adhered to the substrate using pull-out test.
- Developing a proper ID-HVAF nozzle appropriate for depositing metallic particles.
- Studying the effect of spraying parameters including particle size distribution of clogging the nozzle.
- Increasing the rotational velocity of the substrate to avoid having burned particles in the as-fabricated samples.
- Controlling the flow rate of the air and fuel to decrease the process temperature and oxidation of in-flight particles.

Chapter 7

References

[1] Lin, H., Binoniemi, R. R., Fett, G. A., Woodard, T., Punch, E. F., Van Tyne, C., Taylor, B. C., & Matlock, D. K. (2006). Investigation of the Effect of Sample Size on Fatigue Endurance Limit of a Carburized Steel. *SAE Transactions*, *115*, 525–540.

[2] Evans, A. G. (1991). Brittle Fracture: Micromechanics. *Concise Encyclopedia of Advanced Ceramic Materials*, 29-47.

[3] Kalainathan, S., Sathyajith, S., & Swaroop, S. (2012). Effect of laser shot peening without coating on the surface properties and corrosion behavior of 316L steel. *Optics and Lasers in Engineering*, *50*(12), 1740-1745.

[4] Sharma, G. S., Sugavaneswaran, M., Vijayalakshmi, U., & Prakash, R. (2019). Influence of γ-alumina coating on surface properties of direct metal laser sintered 316L stainless steel. *Ceramics International*, *45*(10), 13456-13463.

[5] Abbasi, Z., Shamsaei, E., Leong, S. K., Ladewig, B., Zhang, X., & Wang, H. (2016). Effect of carbonization temperature on adsorption property of ZIF-8 derived nanoporous carbon for water treatment. *Microporous and Mesoporous Materials*, *236*, 28-37.

[6] TAN, H., CHEN, J., & WANG, J. (2010). Study on Carbonization of Heat Resisting Cast Steel. *Hot Working Technology*, *2010*, 22.

[7] Sharifahmadian, O., Salimijazi, H. R., Fathi, M. H., Mostaghimi, J., & Pershin, L. (2013). Relationship between surface properties and antibacterial behavior of wire arc spray copper coatings. *Surface and Coatings Technology*, *233*, 74-79.

[8] Ramlakhan, M., Wu, C. Y., Watano, S., Dave, R. N., & Pfeffer, R. (2000). Dry particle coating using magnetically assisted impaction coating: modification of surface properties and optimization of system and operating parameters. *Powder Technology*, *112*(1-2), 137-148.

[9] Yang, X., Zhu, L., Zhang, Y., Chen, Y., Bao, B., Xu, J., & Zhou, W. (2014). Surface properties and self-cleaning ability of the fluorinated acrylate coatings modified with dodecafluoroheptyl methacrylate through two adding ways. *Applied surface science*, *295*, 44-49.

[10] Liang, J., Hu, L., & Hao, J. (2007). Characterization of microarc oxidation coatings formed on AM60B magnesium alloy in silicate and phosphate electrolytes. *Applied Surface Science*, *253*(10), 4490-4496.

[11] Johnson, R. W., Hultqvist, A., & Bent, S. F. (2014). A brief review of atomic layer deposition: from fundamentals to applications. *Materials today*, *17*(5), 236-246.

[12] Heberlein, J., Postel, O., Girshick, S., McMurry, P., Gerberich, W., Iordanoglou, D., ... & Tymiak, N. (2001). Thermal plasma deposition of nanophase hard coatings. *Surface and Coatings Technology*, *142*, 265-271.

[13] Fauchais, P. L., Heberlein, J. V., & Boulos, M. I. (2014). *Thermal spray fundamentals: from powder to part*. Springer Science & Business Media.

[14] Mishnaevsky Jr, L., & Thomsen, K. (2020). Costs of repair of wind turbine blades: Influence of technology aspects. *Wind Energy*, 23(12), 2247-2255.

[15] Sousa, B. C., Tsaknopoulos, K., & Cote, D. L. (2022). Microstructural and Micromechanical Characterization of Feedstock for Cold Spray Additive Manufacturing and Processing. *Powders*, 1(3), 129-154.

[16] Singh, D. D., Mahender, T., & Reddy, A. R. (2021). Powder bed fusion process: A brief review. *Materials Today: Proceedings*, 46, 350-355.

[17] Hutasoit, N., Rashid, R. R., Palanisamy, S., & Duguid, A. (2020). Effect of build orientation and post-build heat treatment on the mechanical properties of cold spray additively manufactured copper parts. *The International Journal of Advanced Manufacturing Technology*, *110*(9), 2341-2357.

[18] Tan, A. W. Y., Sun, W., Phang, Y. P., Dai, M., Marinescu, I., Dong, Z., & Liu, E. (2017). Effects of traverse scanning speed of spray nozzle on the microstructure and mechanical properties of cold-sprayed Ti-6Al-4V coatings. *Journal of Thermal Spray Technology*, *26*(7), 1484-1497.

[19] Xie, X., Ma, Y., Chen, C., Ji, G., Verdy, C., Wu, H., ... & Liao, H. (2020). Cold spray additive manufacturing of metal matrix composites (MMCs) using a novel nano-TiB2-reinforced 7075Al powder. *Journal of Alloys and Compounds*, *819*, 152962.

[20] Gavras, A. G., Lados, D. A., Champagne, V. K., & Warren, R. J. (2018). Effects of processing on microstructure evolution and fatigue crack growth mechanisms in cold-spray 6061 aluminum alloy. *International Journal of Fatigue*, *110*, 49-62.

[21] Wahab, D. A., & Azman, A. H. (2019). Additive manufacturing for repair and restoration in remanufacturing: An overview from object design and systems perspectives. *Processes*, *7*(11), 802.

[22] Rokni, M. R., Nutt, S. R., Widener, C. A., Champagne, V. K., & Hrabe, R. H. (2017). Review of relationship between particle deformation, coating microstructure, and properties in high-pressure cold spray. *Journal of thermal spray technology*, *26*(6), 1308-1355.

[23] Tan, A. W. Y., Sun, W., Bhowmik, A., Lek, J. Y., Marinescu, I., Li, F., ... & Liu, E. (2018). Effect of coating thickness on microstructure, mechanical properties and fracture behaviour of cold

sprayed Ti-6Al-4V coatings on Ti-6Al-4V substrates. *Surface and Coatings Technology*, *349*, 303-317.

[24] Ma, W., Xie, Y., Chen, C., Fukanuma, H., Wang, J., Ren, Z., & Huang, R. (2019). Microstructural and mechanical properties of high-performance Inconel 718 alloy by cold spraying. *Journal of Alloys and Compounds*, *792*, 456-467.

[25] Cao, C., Han, T., Xu, Y., Li, W., Yang, X., & Hu, K. (2020). The associated effect of powder carrier gas and powder characteristics on the optimal design of the cold spray nozzle. *Surface Engineering*, *36*(10), 1081-1089.

[26] Yin, S., Yan, X., Jenkins, R., Chen, C., Kazasidis, M., Liu, M., ... & Lupoi, R. (2019). Hybrid additive manufacture of 316L stainless steel with cold spray and selective laser melting: Microstructure and mechanical properties. *Journal of Materials Processing Technology*, *273*, 116248.

[27] Lan, L., Zhou, W., Kong, X., & Qiu, C. (2017). Hot plastic deformation behavior and its effect on microstructure of low carbon multi-microalloyed steel. *Procedia engineering*, 207, 651-656.

[28] Boruah, D., Zhang, X., McNutt, P., Khan, R., & Begg, H. (2022). Effect of Post-Deposition Thermal Treatments on Tensile Properties of Cold Sprayed Ti6Al4V. *Metals*, *12*(11), 1908.

[29] Garrido, M. A., Sirvent, P., & Poza, P. (2018). Evaluation of mechanical properties of Ti6Al4V cold sprayed coatings. *Surface Engineering*, *34*(5), 399-406.

[30] Ang, A. S. M., Sanpo, N., Sesso, M. L., Kim, S. Y., & Berndt, C. C. (2013). Thermal spray maps: Material genomics of processing technologies. *Journal of thermal spray technology*, *22*(7), 1170-1178.

[31] Richards, B. T., & Wadley, H. N. (2014). Plasma spray deposition of tri-layer environmental barrier coatings. *Journal of the European Ceramic Society*, *34*(12), 3069-3083.

[32] Ramirez, J. M. H., Bustamante, R. P., Merino, C. A. I., & Morquecho, A. M. A. (2020). Unconventional techniques for the production of light alloys and composites. Springer.

[33] Abu-Warda, N., López, A. J., Pedraza, F., & Utrilla, M. V. (2020). Fireside corrosion on T24 steel pipes and HVOF NiCr coatings exposed to different salt mixtures. *Corrosion Science*, *173*, 108747.

[34] Akbarnozari, A., Ben-Ettouil, F., Amiri, S., Bamber, O., Grenon, J. D., Choquet, M., ... & Moreau, C. (2020). Online Diagnostic System to Monitor Temperature of In-Flight Particles in Suspension Plasma Spray. *Journal of Thermal Spray Technology*, *29*, 908-920.

[35] Zhu, J., Wang, X., Kou, L., Zheng, L., & Zhang, H. (2020). Prediction of control parameters corresponding to in-flight particles in atmospheric plasma spray employing convolutional neural networks. *Surface and Coatings Technology*, *394*, 125862.

[36] Chen, L. H., Chen, Y. R., Chou, C. Y., Chen, C. H., Ko, C. C., & Tung, K. L. (2017). Inorganic membranes in water and wastewater treatment. In *Sustainable Membrane Technology for Water and Wastewater Treatment* (pp. 121-154). Springer, Singapore.

[37] Shahien, M., Suzuki, M., & Tsutai, Y. (2018). Controlling the coating microstructure on axial suspension plasma spray process. *Surface and Coatings Technology*, *356*, 96-107.

[38] Zhang, Z., Lim, S. H., Chai, J., Lai, D. M. Y., Cheong, A. K. H., Cheong, K. L., ... & Pan, J. S. (2017). Plasma spray of Ti2AlC MAX phase powders: Effects of process parameters on coatings' properties. *Surface and Coatings Technology*, *325*, 429-436.

[39] Prashar, G., & Vasudev, H. (2020). Thermal sprayed composite coatings for biomedical implants: A brief review. *Journal of Thermal Spray and Engineering*, *2*(1), 50-55.

[40] Tan, K., Markovych, S., Hu, W., Shorinov, O., & Wang, Y. (2020). Review of manufacturing and repair of aircraft and engine parts based on cold spraying technology and additive manufacturing technology. *Aerospace technic and technology*, (3), 53-70.

[41] Ghadami, F., Aghdam, A. S. R., Zakeri, A., Saeedi, B., & Tahvili, P. (2020). Synergistic effect of CeO2 and Al2O3 nanoparticle dispersion on the oxidation behavior of MCrAlY coatings deposited by HVOF. *Ceramics International*, *46*(4), 4556-4567.

[42] Verma, R., & Kaushal, G. (2021, May). Cyclic oxidation behaviour and characterization of HVOF deposited inconel 718 coatings at 700° C. In *AIP Conference Proceedings* (Vol. 2341, No. 1, p. 040035). AIP Publishing LLC.

[43] Ahledel, N., Schulz, R., Gariepy, M., Hermawan, H., & Alamdari, H. (2019). Electrochemical corrosion behavior of Fe3Al/TiC and Fe3Al-Cr/TiC coatings prepared by HVOF in NaCl solution. *Metals*, *9*(4), 437.

[44] Widantha, K. W., Basuki, E. A., Martides, E., & Prawara, B. (2021). Effect of hydroxyapatite/alumina composite coatings using HVOF on immersion behavior of NiTi alloys. *Journal of Biomaterials Applications*, 08853282211022531.

[45] Oladijo, O. P., Luzin, V., Maledi, N. B., Setswalo, K., Ntsoane, T. P., & Abe, H. (2020). Residual stress and wear resistance of HVOF Inconel 625 coating on SS304 steel substrate. *Journal of Thermal Spray Technology*, *29*(6), 1382-1395.

[46] Yadaw, R. C., Singh, S. K., Chattopadhyaya, S., Kumar, S., & Singh, R. C. (2018). Tribological behavior of thin film coating-a review. *Int. J. Eng. Technol*, *7*(3), 1656-1663.

[47] Kuroda, S., Kawakita, J., Watanabe, M., & Katanoda, H. (2008). Warm spraying—a novel coating process based on high-velocity impact of solid particles. Science and technology of advanced materials.

[48] Molak, R. M., Araki, H., Watanabe, M., Katanoda, H., Ohno, N., & Kuroda, S. (2014). Warm spray forming of Ti-6Al-4V. Journal of thermal spray technology, 23(1), 197-212.

[49] http://www.hvaf.com/HVAF_Development_History.html

[50] Guo, R. Q., Zhang, C., Chen, Q. E., Yang, Y., Li, N., & Liu, L. (2011). Study of structure and corrosion resistance of Fe-based amorphous coatings prepared by HVAF and HVOF. *Corrosion Science*, *53*(7), 2351-2356.

[51] Liu, S., Sun, D., Fan, Z., Yu, H. Y., & Meng, H. M. (2008). The influence of HVAF powder feedstock characteristics on the sliding wear behaviour of WC–NiCr coatings. *Surface and Coatings Technology*, *202*(20), 4893-4900.

[52] Vardelle, A., Moreau, C., Akedo, J., Ashrafizadeh, H., Berndt, C. C., Berghaus, J. O., ... & Vuoristo, P. (2016). The 2016 thermal spray roadmap. Journal of thermal spray technology, 25(8), 1376-1440.

[53] Korobov, Y., Alwan, H., Soboleva, N., Makarov, A., Lezhnin, N., Shumyakov, V., ... & Deviatiarov, M. (2021). Cavitation Resistance of WC-10Co4Cr and WC-20CrC-7Ni HVAF Coatings. *Journal of Thermal Spray Technology*, 1-13.

[54] Sadeghimeresht, E., Markocsan, N., & Nylén, P. (2016). Microstructural and electrochemical characterization of Ni-based bi-layer coatings produced by the HVAF process. *Surface and Coatings Technology*, *304*, 606-619.

[55] Ganvir, A., Jahagirdar, A. R., Mulone, A., Örnfeldt, L., Björklund, S., Klement, U., & Joshi, S. (2021). Novel utilization of liquid feedstock in high velocity air fuel (HVAF) spraying to deposit solid lubricant reinforced wear resistant coatings. *Journal of Materials Processing Technology*, *295*, 117203.

[56] Guo, H., Zhang, S., Sun, W., & Wang, J. (2019). Differences in dry sliding wear behavior between HVAF-sprayed amorphous steel and crystalline stainless steel coatings. *Journal of Materials Science & Technology*, *35*(5), 865-874.

[57] Mahade, S., Mulone, A., Björklund, S., Klement, U., & Joshi, S. (2021). Novel suspension route to incorporate graphene nano-platelets in HVAF-sprayed Cr3C2–NiCr coatings for superior wear performance. *Journal of Materials Research and Technology*, *13*, 498-512.

[58] Gujba, A. K., Mahdipoor, M. S., & Medraj, M. (2021). Water droplet impingement erosion performance of WC-based coating sprayed by HVAF and HVOF. *Wear*, 203904.

[59] Lyphout, C., & Björklund, S. (2015). Internal diameter HVAF spraying for wear and corrosion applications. *Journal of Thermal Spray Technology*, *24*(1), 235-243.

[60] Liu, F., Li, Z., Fang, M., & Hou, H. (2021). Numerical analysis of the activated combustion high-velocity air-fuel spraying process: a three-dimensional simulation with improved gas mixing and combustion mode. Materials, 14(3), 657.

[61] Jiang, H. R., Li, M. L., Wei, X. S., Ma, T. C., Dong, Y., Ying, C. X., ... & Shen, J. (2019). Numerical investigation of in-flight behavior of Fe-based amorphous alloy particles in AC-HVAF thermal spray process. Journal of Thermal Spray Technology, 28(6), 1146-1159.

[62] Srikanth, A., Basha, G. M. T., & Venkateshwarlu, B. (2020). A Brief Review on Cold Spray Coating Process. *Materials Today: Proceedings*, *22*, 1390-1397.

[63] Lupoi, R., & O'Neill, W. (2010). Deposition of metallic coatings on polymer surfaces using cold spray. *Surface and Coatings Technology*, *205*(7), 2167-2173.

[64] DeForce, B. S., Eden, T. J., & Potter, J. K. (2011). Cold spray Al-5% Mg coatings for the corrosion protection of magnesium alloys. *Journal of Thermal Spray Technology*, *20*(6), 1352-1358.

[65] Prashar, G., & Vasudev, H. (2021). A comprehensive review on sustainable cold spray additive manufacturing: State of the art, challenges and future challenges. *Journal of Cleaner Production*, 127606.

[66] Wang, Z., Cai, S., Jin, K., Wang, X., & Chen, W. (2021). In-flight aggregation and deposition behaviour of particles in low pressure cold spray. *Surface and Coatings Technology*, *409*, 126875.

[67] Rutkowska-Gorczyca, M. (2021). X-ray diffraction and microstructural analysis of Cu–TiO2 layers deposited by cold spray. *Materials Science and Technology*, *37*(7), 711-715.

[67] Prashar, G., & Vasudev, H. (2021). A comprehensive review on sustainable cold spray additive manufacturing: State of the art, challenges and future challenges. *Journal of Cleaner Production*, 127606.

[68] Xie, J., Nélias, D., Berre, W. L., Ogawa, K., & Ichikawa, Y. (2015). Simulation of the cold spray particle deposition process. *Journal of Tribology*, *137*(4).

[69] Assadi, H., Gärtner, F., Stoltenhoff, T., & Kreye, H. (2003). Bonding mechanism in cold gas spraying. *Acta materialia*, *51*(15), 4379-4394.

[70] Kawakita, J., Katanoda, H., Watanabe, M., Yokoyama, K., & Kuroda, S. (2008). Warm Spraying: An improved spray process to deposit novel coatings. *Surface and Coatings Technology*, *202*(18), 4369-4373.

[71] Schmidt, T., Assadi, H., Gärtner, F., Richter, H., Stoltenhoff, T., Kreye, H., & Klassen, T. (2009). From particle acceleration to impact and bonding in cold spraying. *Journal of thermal spray technology*, *18*(5), 794-808.

[72] Schmidt, T., Gärtner, F., Assadi, H., & Kreye, H. (2006). Development of a generalized parameter window for cold spray deposition. *Acta materialia*, *54*(3), 729-742.

[73] Rahmati, S., & Ghaei, A. (2014). The use of particle/substrate material models in simulation of cold-gas dynamic-spray process. *Journal of thermal spray technology*, *23*(3), 530-540.

[74] Assadi, H., Schmidt, T., Richter, H., Kliemann, J. O., Binder, K., Gärtner, F., ... & Kreye, H. (2011). On parameter selection in cold spraying. *Journal of thermal spray technology*, *20*(6), 1161-1176.

[75] Hassani-Gangaraj, M., Veysset, D., Nelson, K. A., & Schuh, C. A. (2018). In-situ observations of single micro-particle impact bonding. *Scripta Materialia*, *145*, 9-13.

[76] Meng, F., Yue, S., & Song, J. (2015). Quantitative prediction of critical velocity and deposition efficiency in cold-spray: A finite-element study. *Scripta Materialia*, *107*, 83-87.

[77] Hassani-Gangaraj, M., Veysset, D., Champagne, V. K., Nelson, K. A., & Schuh, C. A. (2018). Adiabatic shear instability is not necessary for adhesion in cold spray. *Acta Materialia*, *158*, 430-439.

[78] Munagala, V. N. V., Torgerson, T. B., Scharf, T. W., & Chromik, R. R. (2019). High temperature friction and wear behavior of cold-sprayed Ti-6Al-4V and Ti6Al4V-TiC composite coatings. *Wear*, *426*, 357-369.

[79] Yin, S., Jenkins, R., Yan, X., & Lupoi, R. (2018). Microstructure and mechanical anisotropy of additively manufactured cold spray copper deposits. *Materials Science and Engineering: A*, *734*, 67-76.

[80] Yang, K., Li, W., Guo, X., Yang, X., & Xu, Y. (2018). Characterizations and anisotropy of cold-spraying additive-manufactured copper bulk. *Journal of materials science & technology*, *34*(9), 1570-1579.

[81] Chakrabarty, R., & Song, J. (2020). A modified Johnson-Cook material model with strain gradient plasticity consideration for numerical simulation of cold spray process. *Surface and Coatings Technology*, *397*, 125981.

[82] Hemeda, A. A., Zhang, C., Hu, X. Y., Fukuda, D., Cote, D., Nault, I. M., ... & Palko, J. W. (2021). Particle-based simulation of cold spray: Influence of oxide layer on impact process. *Additive Manufacturing*, *37*, 101517.

[83] Gnanasekaran, B., Liu, G. R., Fu, Y., Wang, G., Niu, W., & Lin, T. (2019). A Smoothed Particle Hydrodynamics (SPH) procedure for simulating cold spray process-A study using particles. *Surface and Coatings Technology*, *377*, 124812.

[84] Suresh, S., Lee, S. W., Aindow, M., Brody, H. D., Champagne, V. K., & Dongare, A. M. (2020). Mesoscale modeling of jet initiation behavior and microstructural evolution during cold spray single particle impact. *Acta Materialia*, *177*, 197-206.

[85] Nikbakht, R., Assadi, H., Jahani, K., Saadati, M., & Jodoin, B. (2021). Cold spray deformation and deposition of blended feedstock powders not necessarily obey the rule of mixture. *Surface and Coatings Technology*, *424*, 127644.

[86] Li, W. Y., Li, C. J., & Liao, H. (2010). Significant influence of particle surface oxidation on deposition efficiency, interface microstructure and adhesive strength of cold-sprayed copper coatings. *Applied Surface Science*, *256*(16), 4953-4958.

[87] Rahmati, S., Veiga, R. G., Zúñiga, A., & Jodoin, B. (2021). A Numerical Approach to Study the Oxide Layer Effect on Adhesion in Cold Spray. *Journal of Thermal Spray Technology*, 1-15.

[88] Xie, Y., Yin, S., Chen, C., Planche, M. P., Liao, H., & Lupoi, R. (2016). New insights into the coating/substrate interfacial bonding mechanism in cold spray. *Scripta Materialia*, *125*, 1-4.

[89] Schreiber, J. M. (2016). *Finite Element Implementation of the Preston-Tonks-Wallace Plasticity Model and Energy Based Bonding Parameter for the Cold Spray Process*. The Pennsylvania State University.

[90] Razavipour, M., & Jodoin, B. (2021). Material Model for Predicting Dynamic Response of Copper and Nickel at Very High Strain Rates Under Cold Spray Conditions. *Journal of Thermal Spray Technology*, *30*(1), 324-343.

[91] Nélias, D., Xie, J., Walter-Le Berre, H., Ichikawa, Y., & Ogawa, K. (2014). Simulation of the cold spray deposition process for aluminum and copper using Lagrangian, ALE and CEL methods. *Thermomechanical Industrial Processes: Modeling and Numerical Simulation*, 321-358.

[92] Oyinbo, S. T., & Jen, T. C. (2020). Feasibility of numerical simulation methods on the Cold Gas Dynamic Spray (CGDS) Deposition process for ductile materials. *Manufacturing Review*, *7*, 24.

[93] Song, X., Ng, K. L., Chea, J. M. K., Sun, W., Tan, A. W. Y., Zhai, W., ... & Liu, E. (2020). Coupled Eulerian-Lagrangian (CEL) simulation of multiple particle impact during Metal Cold Spray process for coating porosity prediction. *Surface and Coatings Technology*, *385*, 125433.

[94] Li, W. Y., Yin, S., & Wang, X. F. (2010). Numerical investigations of the effect of oblique impact on particle deformation in cold spraying by the SPH method. *Applied Surface Science*, *256*(12), 3725-3734.

[95] Profizi, P., Combescure, A., & Ogawa, K. (2016). SPH modeling of adhesion in fast dynamics: Application to the Cold Spray process. *Comptes Rendus Mécanique*, *344*(4-5), 211-224.

[96] Bae, G., Xiong, Y., Kumar, S., Kang, K., & Lee, C. (2008). General aspects of interface bonding in kinetic sprayed coatings. *Acta Materialia*, *56*(17), 4858-4868.

[97] Song, X., Ng, K. L., Chea, J. M. K., Sun, W., Tan, A. W. Y., Zhai, W., ... & Liu, E. (2020). Coupled Eulerian-Lagrangian (CEL) simulation of multiple particle impact during Metal Cold Spray process for coating porosity prediction. *Surface and Coatings Technology*, *385*, 125433.

[98] Terrone, M., Lordejani, A. A., Kondas, J., & Bagherifard, S. (2021). A Numerical Framework to Design and Develop Freestanding Porous Structures through Cold Spray Multi-Material Deposition. *Surface and Coatings Technology*, 127423.

[99] Yu, M., Li, W. Y., Wang, F. F., Suo, X. K., & Liao, H. L. (2013). Effect of particle and substrate preheating on particle deformation behavior in cold spraying. *Surface and Coatings Technology*, *220*, 174-178.

[100] Xie, J. (2014). Simulation of Cold Spray Particle Deposition Process. Ph.D. Thesis. L'Institut National des Sciences Appliquées de Lyon.

[101] Karthikeyan, J. (2005). Cold spray technology: the cold spray process has the potential to reduce costs and improve quality in both coatings and freeform fabrication of near-net-shape parts. *Advanced materials & processes*, *163*(3), 33-36.

[102] Mauer, G., Vaßen, R., & Stöver, D. (2007). Comparison and Applications of DPV-2000 and Accuraspray-g3 diagnostic Systems. *Journal of Thermal Spray Technology*, 16(3), 414-424.

[103] Yin, S., Cizek, J., Yan, X., & Lupoi, R. (2019). Annealing strategies for enhancing mechanical properties of additively manufactured 316L stainless steel deposited by cold spray. *Surface and Coatings Technology*, *370*, 353-361.

[104] Sathish, M., Radhika, N., & Saleh, B. (2021). A critical review on functionally graded coatings: Methods, properties, and challenges. *Composites Part B: Engineering*, 109278.

[105] Chen, C., Xie, Y., Yan, X., Yin, S., Fukanuma, H., Huang, R., ... & Liao, H. (2019). Effect of hot isostatic pressing (HIP) on microstructure and mechanical properties of Ti-6Al-4V alloy fabricated by cold spray additive manufacturing. *Additive Manufacturing*, *27*, 595-605.

[106] Bagherifard, S., Monti, S., Zuccoli, M. V., Riccio, M., Kondás, J., & Guagliano, M. (2018). Cold spray deposition for additive manufacturing of freeform structural components compared to selective laser melting. *Materials Science and Engineering: A*, *721*, 339-350.

[107] Khalik, M. A., Zahiri, S. H., Palanisamy, S., Masood, S. H., Gulizia, S., & Faizan-Ur-Rab, M. (2022). Rapid elimination of porosity and brittleness in cold spray additive manufactured grade 2 titanium via in situ electro-plastic treatment. *The International Journal of Advanced Manufacturing Technology*, *119*(1), 773-788.

[108] Amiri, M., Crawford, G. A., & Earthman, J. C. (2021). Quantitative percussion diagnostics for evaluating porosity and surface roughness of cold sprayed and laser deposited materials. *Journal of Materials Research and Technology*, *14*, 312-323.

[109] Singh, A., Singh, P., Pabla, B. S., Singh, H., & Shiva, S. (2022). Parametric analysis to explore the viability of cold spray additive manufacturing to print SS316L parts for biomedical application. *Journal of the Brazilian Society of Mechanical Sciences and Engineering*, *44*(8), 1-22.

[110] Moridi, A., Stewart, E. J., Wakai, A., Assadi, H., Gartner, F., Guagliano, M., ... & Dao, M. (2020). Solid-state additive manufacturing of porous Ti-6Al-4V by supersonic impact. *Applied Materials Today*, *21*, 100865.

[111] Petrovskiy, P., Travyanov, A., Cheverikin, V. V., Chereshneva, A. A., Sova, A., & Smurov, I. (2020). Effect of encapsulated hot isostatic pressing on properties of Ti6Al4V deposits produced by cold spray. *The International Journal of Advanced Manufacturing Technology*, *107*(1), 437-449.

[112] Kim, Y. K., & Lee, K. A. (2022). Effect of carrier gas species on the microstructure and compressive deformation behaviors of ultra-strong pure copper manufactured by cold spray additive manufacturing. *Journal of Materials Science & Technology*, *97*, 264-271.

[113] Fukanuma, H., Ohno, N., Sun, B., & Huang, R. (2006). In-flight particle velocity measurements with DPV-2000 in cold spray. *Surface and Coatings Technology*, *201*(5), 1935-1941.

[114] Tariq, N. H., Gyansah, L., Wang, J. Q., Qiu, X., Feng, B., Siddique, M. T., & Xiong, T. Y. (2018). Cold spray additive manufacturing: A viable strategy to fabricate thick B4C/Al composite coatings for neutron shielding applications. *Surface and Coatings Technology*, *339*, 224-236.

[115] Tang, J., Saha, G. C., Richter, P., Kondás, J., Colella, A., & Matteazzi, P. (2018). Effects of post-spray heat treatment on hardness and wear properties of Ti-WC high-pressure cold spray coatings. *Journal of Thermal Spray Technology*, *27*(7), 1153-1164.

[116] Khun, N. W., Tan, A. W. Y., Sun, W., & Liu, E. (2017). Wear and corrosion resistance of thick Ti-6Al-4V coating deposited on Ti-6Al-4V substrate via high-pressure cold spray. *Journal of Thermal Spray Technology*, *26*(6), 1393-1407.

[117] Machethe, K. E., Popoola, A. P. I., Adebiyi, D. I., & Fayomi, O. S. I. (2017). Influence of SiC-Ti/Al on the microstructural and mechanical properties of deposited Ti-6V-4Al alloy with cold spray technique. *Procedia Manufacturing*, *7*, 549-555.

[118] Wang, Q., Niu, W., Li, X., Han, P., Mao, X., Yang, J., & Zhang, M. X. (2021). Tuning the microstructure and mechanical properties of additive manufactured aluminum matrix composites by cold spray. *Surface and Coatings Technology*, 127847.

[119] Tsaknopoulos, K., Grubbs, J., Siopis, M., Nardi, A., & Cote, D. (2021). Microstructure and Mechanical Property Evaluation of Aluminum F357 Powder for Cold Spray Applications. *Journal of Thermal Spray Technology*, *30*(3), 643-654.

[120] Hutasoit, N., Rashid, R. A., Palanisamy, S., & Duguid, A. (2020). Effect of build orientation and post-build heat treatment on the mechanical properties of cold spray additively manufactured copper parts. *The International Journal of Advanced Manufacturing Technology*, *110*(9), 2341-2357.

[121] Tang, J., Zhao, Z., Guo, M., Liu, H., Ren, Y., Cui, X., ... & Xiong, T. (2022). Microstructure and Mechanical Properties of Ti–Ta Composites Prepared Through Cold Spray Additive Manufacturing. *Acta Metallurgica Sinica (English Letters)*, 1-12.

[122] Ren, Y., Liu, H., Cui, X., Shen, Y., Wang, J., & Xiong, T. (2022). Remarkable improvement in microstructure and mechanical properties of cold sprayed Al deposits via impact forging post-spray treatment. *Materials Today Communications*, *32*, 103951.

[123] Sirvent, P., Garrido, M. A., Sharp, J., Rainforth, W. M., & Poza, P. (2020). Improving the Oscillating Wear Response of Cold Sprayed Ti-6Al-4V Coatings Through a Heat Treatment, *Surface and Coatings Technology*, *399*, 126128.

[124] Voorwald, H. J. C., Souza, R. C., Pigatin, W. L., & Cioffi, M. O. H. (2005). Evaluation of WC–17Co and WC–10Co–4Cr thermal spray coatings by HVOF on the fatigue and corrosion strength of AISI 4340 steel. *Surface and Coatings Technology*, *190*(2-3), 155-164.

[125] Tejero-Martin, D., Rezvani Rad, M., McDonald, A., & Hussain, T. (2019). Beyond traditional coatings: a review on thermal-sprayed functional and smart coatings. *Journal of Thermal Spray Technology*, *28*(4), 598-644.

[126] Samuel, M. P., Mishra, A. K., & Mishra, R. K. (2018). Additive manufacturing of Ti-6Al-4V aero engine parts: qualification for reliability. *Journal of Failure Analysis and Prevention*, *18*(1), 136-144.

[127] Yuan, B., Harvey, C. M., Thomson, R. C., Critchlow, G. W., & Wang, S. (2018). A new spallation mechanism of thermal barrier coatings on aero-engine turbine blades. *Theoretical and Applied Mechanics Letters*, *8*(1), 7-11.

[128] Zhang, Q., Liang, Z. L., Miao, C. A. O., Liu, Z. F., Zhang, A. F., & Lu, B. H. (2017). Microstructure and mechanical properties of Ti6Al4V alloy prepared by selective laser melting combined with precision forging. *Transactions of Nonferrous Metals Society of China*, *27*(5), 1036-1042.

[129] Shunmugavel, M., Polishetty, A., & Littlefair, G. (2015). Microstructure and mechanical properties of wrought and additive manufactured Ti-6Al-4 V cylindrical bars. *Procedia Technology*, *20*, 231-236.

[130] Huang, C. J., Wu, H. J., Xie, Y. C., Li, W. Y., Verdy, C., Planche, M. P., ... & Montavon, G. (2019). Advanced brass-based composites via cold-spray additive-manufacturing and its potential in component repairing. *Surface and Coatings Technology*, *371*, 211-223.

[131] Yin, S., Cavaliere, P., Aldwell, B., Jenkins, R., Liao, H., Li, W., & Lupoi, R. (2018). Cold spray additive manufacturing and repair: Fundamentals and applications. *Additive manufacturing*, *21*, 628-650.

[132] Sova, A., Grigoriev, S., Okunkova, A., & Smurov, I. (2013). Potential of cold gas dynamic spray as additive manufacturing technology. *The International Journal of Advanced Manufacturing Technology*, *69*(9), 2269-2278.

[133] Yan, X., Huang, C., Chen, C., Bolot, R., Dembinski, L., Huang, R., ... & Liu, M. (2019). Additive manufacturing of WC reinforced maraging steel 300 composites by cold spraying and selective laser melting. *Surface and Coatings Technology*, *371*, 161-171.

[134] Gao, X., Li, C., Zhang, D., Gao, H., & Han, X. (2021). Numerical analysis of the activated combustion high-velocity air-fuel (AC-HVAF) thermal spray process: A survey on the parameters of operation and nozzle geometry. *Surface and Coatings Technology*, *405*, 126588.

[135] Gao, X., Li, C., Xu, Y., Chen, X., & Han, X. (2021). Effects of fuel types and process parameters on the performance of an activated combustion high velocity air-fuel (AC-HVAF) thermal spray system. *Journal of Thermal Spray Technology*, 1-16.

[136] Li, C., Gao, X., Zhang, D., Gao, H., Han, X., & Zhang, B. (2021). Numerical investigation on the flame characteristics and particle behaviors in a HVOF spray process using kerosene as fuel. *Journal of Thermal Spray Technology*, *30*(3), 725-738.

[137] Xie, J., Nélias, D., Berre, W. L., Ogawa, K., & Ichikawa, Y. (2015). Simulation of the cold spray particle deposition process. *Journal of Tribology*, *137*(4).

[138] Yildirim, B., Muftu, S., & Gouldstone, A. (2011). Modeling of high velocity impact of spherical particles. *Wear*, *270*(9-10), 703-713.

[139] Li, W. Y., & Gao, W. (2009). Some aspects on 3D numerical modeling of high velocity impact of particles in cold spraying by explicit finite element analysis. *Applied Surface Science*, *255*(18), 7878-7892.

[140] Heuzé, O. (2012). General form of the Mie–Grüneisen equation of state. *Comptes Rendus Mecanique*, *340*(10), 679-687.

[141] Dassault Systemes, 2011, ABAQUS Analysis User's Manuel, 6.11 ed., Simulia.

[142] Yan, X., Li, Q., Yin, S., Chen, Z., Jenkins, R., Chen, C., ... & Liu, M. (2019). Mechanical and in vitro study of an isotropic Ti6Al4V lattice structure fabricated using selective laser melting. *Journal of Alloys and Compounds*, *782*, 209-223.

[143] Yang, Y. (2015). *Temperature-dependent thermoelastic analysis of multidimensional functionally graded materials* (Doctoral dissertation, University of Pittsburgh).

[144] Yildirim, B., Yang, H., Gouldstone, A., & Müftü, S. (2017). Rebound mechanics of micrometre-scale, spherical particles in high-velocity impacts. *Proceedings of the Royal Society A: Mathematical, Physical and Engineering Sciences*, *473*(2204), 20160936.

[145] Goldbaum, D., Shockley, J. M., Chromik, R. R., Rezaeian, A., Yue, S., Legoux, J. G., & Irissou, E. (2012). The effect of deposition conditions on adhesion strength of Ti and Ti6Al4V cold spray splats. *Journal of thermal spray technology*, *21*(2), 288-303.

[146] Suhonen, T., Varis, T., Dosta, S., Torrell, M., & Guilemany, J. M. (2013). Residual stress development in cold sprayed Al, Cu and Ti coatings. *Acta Materialia*, *61*(17), 6329-6337.

[147] Rahmati, S., & Jodoin, B. (2020). Physically based finite element modeling method to predict metallic bonding in cold spray. *Journal of Thermal Spray Technology*, *29*(4), 611-629.

[148] Khodabakhshi, F., Marzbanrad, B., Jahed, H., & Gerlich, A. P. (2018). Interfacial bonding mechanisms between aluminum and titanium during cold gas spraying followed by friction-stir modification. *Applied Surface Science*, *462*, 739-752.

[149] Chen, C., Xie, Y., Huang, R., Deng, S., Ren, Z., & Liao, H. (2018). On the role of oxide film's cleaning effect into the metallurgical bonding during cold spray. *Materials Letters*, *210*, 199-202.

[150] Yin, S., Suo, X., Xie, Y., Li, W., Lupoi, R., & Liao, H. (2015). Effect of substrate temperature on interfacial bonding for cold spray of Ni onto Cu. *Journal of materials science*, *50*(22), 7448-7457.

[151] Legoux, J. G., Irissou, E., & Moreau, C. (2007). Effect of substrate temperature on the formation mechanism of cold-sprayed aluminum, zinc and tin coatings. *Journal of Thermal Spray Technology*, *16*(5), 619-626.

[152] Xie, Y., Planche, M. P., Raoelison, R., Liao, H., Suo, X., & Hervé, P. (2016). Effect of substrate preheating on adhesive strength of SS 316L cold spray coatings. *Journal of Thermal Spray Technology*, *25*(1), 123-130.

[153] Hassani-Gangaraj, M., Veysset, D., Nelson, K. A., & Schuh, C. A. (2019). Impact-bonding with aluminum, silver, and gold microparticles: Toward understanding the role of native oxide layer. *Applied Surface Science*, *476*, 528-532.

[154] Watanabe, Y., Yoshida, C., Atsumi, K., Yamada, M., & Fukumoto, M. (2015). Influence of substrate temperature on adhesion strength of cold-sprayed coatings. *Journal of Thermal Spray Technology*, *24*(1), 86-91.

[155] Khamsepour, P., Moreau, C., & Dolatabadi, A. (2021). Numerical simulation of the effect of particle and substrate preheating on porosity level and residual stress of as-sprayed Ti6Al4V components. *Journal of Thermal Spray Technology*, 1-14.

[156] Li, W. Y., Liao, H., Li, C. J., Bang, H. S., & Coddet, C. (2007). Numerical simulation of deformation behavior of Al particles impacting on Al substrate and effect of surface oxide films on interfacial bonding in cold spraying. *Applied Surface Science*, *253*(11), 5084-5091.

[157] Kim, K., Li, W., & Guo, X. (2015). Detection of oxygen at the interface and its effect on strain, stress, and temperature at the interface between cold sprayed aluminum and steel substrate. *Applied Surface Science*, *357*, 1720-1726.

[158] Yin, S., Wang, X., Li, W., Liao, H., & Jie, H. (2012). Deformation behavior of the oxide film on the surface of cold sprayed powder particle. *Applied Surface Science*, *259*, 294-300.

[159] Wang, X., & Shi, J. (2013). Validation of Johnson-Cook plasticity and damage model using impact experiment. *International Journal of Impact Engineering*, *60*, 67-75.

[160] Banerjee, A., Dhar, S., Acharyya, S., Datta, D., & Nayak, N. (2015). Determination of Johnson cook material and failure model constants and numerical modelling of Charpy impact test of armour steel. *Materials Science and Engineering: A*, *640*, 200-209.

[161] Zhang, Y., Outeiro, J. C., & Mabrouki, T. (2015). On the selection of Johnson-Cook constitutive model parameters for Ti-6Al-4 V using three types of numerical models of orthogonal cutting. *Procedia Cirp*, *31*, 112-117.

[162] Pereira, L. M., Rahmati, S., Zúñiga, A., Jodoin, B., & Veiga, R. G. A. (2021). Atomistic study of metallurgical bonding upon the high velocity impact of fcc core-shell particles. *Computational Materials Science*, *186*, 110045.

[163] Nishimura, K., Kalia, R. K., Nakano, A., Vashishta, P., (2008). Nanoindentation hardness anisotropy of alumina crystal: A molecular dynamics study. *Applied Physics Letters*, *92,* 161904.

[164] Zhang, C., Kalia, R. K., Nakano, A., Vashishta, P., Branicio, P. S., (2008). Deformation mechanisms and damage in α-alumina under hypervelocity impact loading. *Journal of Applied Physics, 103,* 083508.

[165] Khoei, A. R., Khorrami, M. S., (2016). Mechanical properties of graphene oxide: A molecular dynamics study. *Fullerenes, Nanotubes and Carbon Nanostructures*, *24,* 594-603.

[166] Cai, M. B., Li, X. P., Rahman, M., (2007). Study of the temperature and stress in nanoscale ductile mode cutting of silicon using molecular dynamics simulation. *Journal of materials processing technology*, *192,* 607-612.

[167] Almeida, C. M., Prioli, R., Ponce, F. A., (2008). Effect of native oxide mechanical deformation on InP nanoindentation. *Journal of Applied Physics*, *104*, 113509.

[168] Bubar, S. F., Vermilyea, D. A., (1966). Deformation of anodic oxide films. *Journal of the Electrochemical Society*, 1966, *113*, 892.

[169] Propp, M., Young, L., (1979). Adhesion, Ductility, and Fracture of Anodic Oxide Films on Tantalum. *Journal of The Electrochemical Society*, *126*, 624.

[170] A. Banerjee, A., Dhar, S., Acharyya, S., Datta, D., Nayak, N., (2015). Determination of Johnson cook material and failure model constants and numerical modelling of Charpy impact test of armour steel. *Materials Science and Engineering: A*, *640*, 200-209.

[171] Schreiber, J. M., Smid, I., Eden, T. J., Koudela, K., Cote, D., & Champagne, V. (2021). Cold spray particle impact simulation using the Preston-Tonks-Wallace plasticity model. *Finite Elements in Analysis and Design*, *191*, 103557.

[172] Sbayti, M., Ghiotti, A., Bahloul, R., Belhadjsalah, H., & Bruschi, S. (2016). Finite Element Analysis of hot Single Point Incremental forming of hip prostheses. In *MATEC Web of Conferences* (Vol. 80, p. 14006). EDP Sciences.

[172] Dong, E., Yu, W., Cai, Q., Cheng, L., & Shi, J. (2017). High-temperature oxidation kinetics and behavior of Ti–6Al–4V alloy. *Oxidation of Metals*, *88*(5), 719-732.

[173] Guleryuz, H., & Cimenoglu, H. (2009). Oxidation of Ti–6Al–4V alloy. *Journal of Alloys and Compounds*, *472*(1-2), 241-246.

[174] https://spraysensors.tecnar.com/research/dpv/

[175] Munagala, V. N. V., Imbriglio, S. I., & Chromik, R. R. (2019). The influence of powder properties on the adhesion strength and microstructural evolution of cold sprayed Ti6Al4V single splats. *Materials Letters*, *244*, 58-61.

[176] Huang, R., Ma, W., & Fukanuma, H. (2014). Development of ultra-strong adhesive strength coatings using cold spray. *Surface and Coatings Technology*, *258*, 832-841.

[177] Tiamiyu, A. A., Chen, X., Pang, E. L., Sun, Y., Lienhard, J., LeBeau, J. M., ... & Schuh, C. A. (2022). Oxide layer delamination: An energy dissipation mechanism during high-velocity microparticle impacts. *Applied Surface Science*, *574*, 151673.

[178] Venturi, F. Kamnis, S. Hussain, T., (2021). Internal diameter HVOAF thermal spray of carbon nanotubes reinforced WC-Co composite coatings, *Materials & Design*, *202*, 109566.

[179] Pulsford, J. Venturi, F. Pala, Z. Kamnis, S. Hussain, T., (2019). Application of HVOF WC-Co-Cr coatings on the internal surface of small cylinders: Effect of internal diameter on the wear resistance, *Wear*, *432-433*, 202965.

[180] Tzinava, M. Delibasis, K. Allcock, B. Kamnis, S., (2020). A general-purpose spray coating deposition software simulator, *Surface and Coatings Technology*, *399*, 126148.

[181] Katranidis, V. Gu, S. Allcokc, B. Kamnis, S., (2017). Experimental study of high velocity oxy-fuel sprayed WC-17Co coatings applied on complex geometries. Part A: Influence of kinematic spray parameters on thickness, porosity, residual stresses and microhardness, *Surface and Coatings Technology*, *311*, 206-215.

[182] Vo, P., Irissou, E., Legoux, J. G., Yue, S., (2013). Mechanical and Microstructural Characterization of Cold-Sprayed Ti-6Al-4V After Heat Treatment, *Journal of Thermal Spray Technology*, *22*, p 954–964.

[183] Khamsepour, P., Oberste-Berghaus, J., Aghasibeig, M., Moreau, C., Dolatabadi, A., (2022). The Characteristics of In-Flight Ti-6Al-4V Particles and the Coatings Formed by the Inner-Diameter High-Velocity Air-Fuel (ID-HVAF) Process, *Journal of Thermal Spray Technology*.

[184] Shaikh, A., Kumar, S., Dawari, S., Kirwai, S., Patil, A., Singh, R., (2019). Effect of Temperature and Cooling Rates on the Morphology of Ti-6Al-4V Alloy, *Procedia Structural Integrity*, 782-789.

[185] Gupta, A., Khatirkar, R. K., Kumar, A., Parihar, M. S., (2018). Investigations on the effect of heating temperature and colling rate on evolution of microstructure in an titanium alloy, *Journal of Materials Research*, *33*.

[186] Molak, R. M., Araki, H., Watanabe, W., Katanoda, H., Ohno, N., Kuroda, S., (2017). Effects of Spray Parameters and Post-Spray Heat Treatment on Microstructure and Mechanical Properties of Warm-Sprayed Ti-6Al-4V Coatings, *Journal of Thermal Spray Technology*, *26*, 627-647.

Appendix A

Liquid Cold Spray

A.1. Introduction

It is possible to manufacture dense coatings using solid-state deposition techniques. However, the density of the deposits is highly dependent on the deformation of the deposited particles. According to our thesis, particle temperature can thermally soften the deposited particles, which can directly affect their deformation. Another way of enhancing particle deformation upon impact is to increase its kinetic energy which is based on particle mass and its impact velocity. In the context of this discussion, it should be noted that it is not possible to increase particle velocity indefinitely. It is also important that the particle size used for deposition in both cold spray (CS) and high velocity air-fuel (HVAF) be small. In our research center, we have developed a novel CS method known as liquid cold spray (LCS) that allows large metallic particles to be deposited at room temperature while maintaining their phases. This process uses water instead of an inert gas as a propellant. Despite LCS's success in fabricating metallic coatings, wetting the substrate and particles with water negatively affects the deformation of the deposited particles. A numerical analysis based on elastic-plastic theory can be used to determine the effect of the water film on particle deformation accurately since it occurs at strain rates as high as 10-9 s-1. The purpose of this appendix is to discuss two papers that investigated the effects of water film on particle deformation, bonding, and porosity level in copper as-sprayed coatings.

Appendix A contains three subsections. In the first subsection, we briefly discussed the importance of studying the deformation of a particle deposited using LCS. Then, the effect of water film wetting the substrate on particle deformation was investigated. Lastly, we investigated the effects of wetting the particle with a water film on its deformation, oxide layer failure, and bonding area.

Annex 2. The Effect of Water Layer Covering Substrate Surface on the Deformation of the Impacting Particle Deposited by Liquid Cold Spray[5]

A.2.1. Abstract

Cold spray is a deposition method developed for manufacturing metallic coatings by impacting high-velocity metallic powders on a substrate surface at around room temperature. Because of the low temperature of impacted particles, no oxidation or phase transformations occur during spraying. However, the main limitations of cold spray are associated with considerable gas consumption to accelerate the particles and stringent powder size. To address these issues, liquid cold spray (LCS), as a pioneering technology, has been developed with the potential of utilizing water as the propellant for depositing coarse powders. In terms of producing the coatings, LCS is like conventional cold spray. In both techniques, the severe plastic deformation of the deposited particle and the substrate is the main cause of metallurgical bonding. However, the main difference is related to a thin film of water formed on the top of the substrate while LCS is being used. Thus, this research aims to examine the effect of the thin water layer on particle and substrate deformation by elastic-plastic finite-element modeling. Specifically, the deformation of an impacted 50 μm copper particle on a copper substrate covered with a water layer thickness of 3 and 6 μm was examined by the coupled Eulerian-Lagrangian (CEL) method. The results showed that having a 6 μm water film compared to the situation with no water covering the substrate decreased the particle flattening ratio and equivalent plastic strain of the substrate around 4% and 21%, respectively. This reduction in deformation can be related to the portion of the particle's kinetic energy devoted to passing the particle through the water layer. In the end, it is assumed that the particle velocity increased from 500 m/s to 600 m/s before its impact on a substrate covered with a 6 μm water film. The results illustrated that increasing the kinetic energy of the deposited particle can overcome the negative effect of water film and increase the deformation of the particle, particle flattening ratio, and substrate deformation.

A.2.2. Introduction

Cold spray (CS) has been used significantly as a thermal spray or an additive manufacturing technique for producing metallic parts [1-2]. In CS process, metallic particles are deposited using a carrier gas such as nitrogen or helium before impacting the substrate surface [3]. Since the deposited particles impact the substrate surface at a very high velocity and around room temperature, no oxidation and phase transformation occur [4]. However, the main disadvantages of CS are the gas consumption, the need for small particle size, and the high porosity level of additive manufactured samples [4-5]. For reducing gas consumption, in our research center, some attempts have been made to develop a pioneering technology known as liquid cold spray (LCS) for depositing larger metallic particles using a water jet. In LCS process, the solid particle impacts at high velocity on a metallic surface. Hence, the cause of bonding between the deposited particle and the substrate is like conventional CS.

Both the deposited particle and the substrate would deform plastically during the impact, leading to bonding and producing the coatings [6]. To manufacture metallurgical bonding, breaking and ejecting particle and

[5] Khamsepour, P., Akbarnozari, A., Garmeh, S., Moreau, C., & Dolatabadi, A. (2022). The Effect of Water Layer Covering Substrate Surface on the Deformation of the Impacting Particle Deposited by Liquid Cold Spray. Published in the Proceedings of CSME, Edmonton, Alberta, June 2022. DOI: https://doi.org/10.7939/r3-sm40-p514

substrate oxide layer is necessary. After particle impacts the substrate, its deformation is higher in a ring-shaped region known as adiabatic shear instability leading to an increase in temperature. This temperature enhancement would activate thermal softening and ease material deformation. As a result, a material jet can be formed to eject the broken oxide layer [7]. Hence, particle and substrate deformation, which play a crucial role in this process, are defined by particle kinetic energy, type of material, substrate surface properties, particle size, and substrate temperature [4, 8]. All noted parameters' effects are summarized in the critical particle velocity definition. Conclusively, particle and substrate must be deformed significantly for producing bonding, which happens when particle velocity is higher than the critical velocity [4, 8].

Besides the advantages of LCS, the existence of the water jet creates a water film on the substrate surface, which might affect the particle critical velocity and particle and substrate deformation. Conclusively, this paper aims to use proper elastic-plastic modeling to understand the effect of water film on particle and substrate deformation while a 50 μm copper particle is impacted on a copper substrate using LCS. Then, the importance of impact velocity would be examined to reduce the possible effect of water film on particle and substrate deformation.

A.2.3. Numerical Methodology

A.2.3.1. Elastic and Plastic Modeling

First, it is necessary to introduce the utilized elastic and plastic model to understand the water film effect on particle deformation using LCS. Elastic and plastic models are required to be able to study a high strain rate deformation. Hence, for the elastic section, the Mie-Gruneisen equation of state (Eq. 1) and plastic section, Johnson-Cook Modeling (Eq. 2), have been selected. The full description of both noted models are reported in the literature [9-10].

$$P = \frac{\rho_0 c_0^2 \eta}{(1 - s\eta)^2} \left(1 - \frac{\eta \Gamma_0}{2}\right) + \Gamma_0 \rho_0 E_m \tag{1}$$

$$\sigma = \left(A + B\varepsilon_p^n\right)\left(1 + C ln \frac{\dot{\varepsilon}_p}{\dot{\varepsilon}_0}\right)\left(1 - (\frac{T - T_r}{T_m - T_r})^m\right) \tag{2}$$

where, P is total pressure, $\rho_0 c_0^2$ is the elastic modulus at small nominal strains, c_0, s, Γ_0, and ρ_0 represent material constants, E_m is internal energy per unit mass, η (nominal compressive volumetric strain) is equal to $1 - \rho_0/\rho$, and ρ is pressure stress. ε_p, $\dot{\varepsilon}_p$, σ, $\dot{\varepsilon}_0$, T_r, T_m, and T represents equivalent plastic strain, plastic strain rate, flow stress, reference strain rate, reference temperature, melting point, and temperature, respectively. Constants in this model are A, B, C, n, and m [9-10].

A.2.3.2. Finite Element Method

A proper finite-element method such as coupled Eulerian-Lagrangian (CEL) is required to solve the noted models. In this examination, both particle and the substrate are assumed to be Lagrangian, and the water film is an Eulerian part. The initial assembly of the three noted parts is shown in Fig. 1, while a water film with a thickness of 3 μm covers the substrate. Also, a schematic picture of the same condition is represented in Fig. 2, illustrating the used dimension of the particle and substrate. This study has been carried out using ABAQUS/Explicit by considering the used material constants shown in Table 1 [6, 9]. The step has been defined as “Dynamic, Temp-disp, Explicit”, the friction coefficient is 0.3, and the simulation examines the particle and substrate deformation at the first 120 ns after the impact. Particle mesh size is 0.5 μm which falls into an acceptable value compared to the literature [11]. In the end, the mesh type for Lagrangian particle and

substrate is C3D8RT (an 8-node thermally-coupled brick, trilinear displacement, temperature, reduced integration, and hourglass control), and for Eulerian water film is EC3D8RT (An 8-node thermally coupled linear Eulerian brick, reduced integration, hourglass control).

In this simulation, a 50 µm copper particle is deposited on a copper substrate. This particle size equals the smallest size of the copper particles used for manufacturing coatings by LCS in our research center. In the first step, three different conditions have been selected to study the water film effect. In all situations, impact velocity equals 500 m/s and particle and substrate temperature are 298 K. The particle velocity has been chosen above the reported value for critical velocity of a 50 µm copper particle in the literature [8]. The difference between the noted conditions is the water layer. First, the convention CS is assumed to be used, which means no water film covers the substrate. Then by using LCS, first, a 3 µm water film covers the substrate surface. In the end, it is assumed that a 6 µm water film is on the top of the substrate surface. It is worth noting that an accurate thickness of the water film will be studied in our ongoing computational fluid dynamic (CFD) research. Then, by assuming a 6 µm water film on top of the substrate, the particle velocity effect has been examined by changing the velocity from 500 m/s to 600 m/s while the initial temperature remains unchanged. All the noted velocities are higher than the critical value for a 50 µm copper particle noted in the literature [8].

Table 1. Used material constants in the finite-element method [6, 9].

Copper		**Water**	
Property	**Value**	**Property**	**Value**
Thermal Conductivity	386 $W/m.K$	Density	958 kg/m^3
Specific Heat	383 $J/Kg.K$	Speed of Sound	1490 m/s
Density	8930 kg/m^3	Viscousity	1 mPa-s
Shear Modulus	45 GPa	Thermal Conductivity	0.598 $W/m.K$
Melting Point	1356 K	Specific Heat	4.186 $J/g.°C$
Gruneisen's Constant	1.99		
Speed of Sound	3933 m/s		
Hugoniot Slope	1.5		
A	90 MPa		
B	292 MPa		
C	0.025		
m	1.09		
n	0.31		
Reference Strain Rate	1		
Transition Temperature	298		

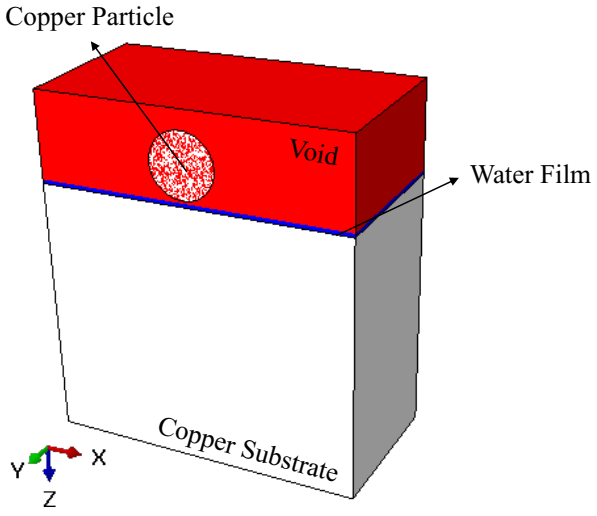

Figure 1. The initial condition of the used finite-element method in this paper.

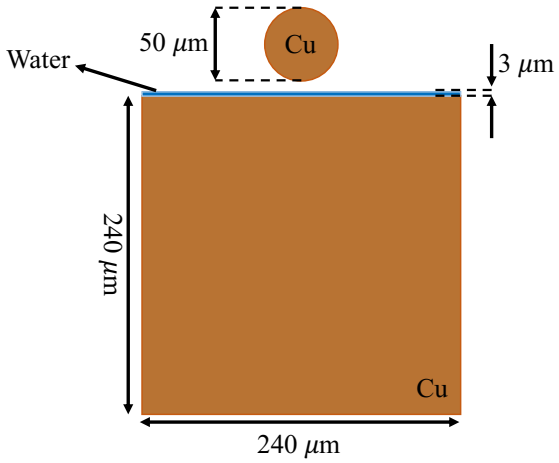

Figure 2. The initial condition examined the water film effect on particle and substrate deformation while a 3 µm water film covers the substrate surface.

A.2.3.3. Flattening Ratio

One way to study the particle deformation deposited by CS is the flattening ratio, which can be calculated using Eq. 3 below [12].

$$Flattening\ ratio = 1 - \frac{Deformed\ Height}{Particle\ Diameter} \tag{3}$$

A.2.4. Results and Discussions

A.2.4.1. Water Film Effect

This section investigates the water film effect on particle and substrate deformation while a 50 µm copper particle is deposited with conventional CS and LCS. In all cases, particle velocity is 500 m/s and particle and substrate temperature are 298 K. First, it is necessary to examine the water film behavior after 120 ns of the initial impact of the particle on the substrate surface, Fig. 3. This figure shows the impacted particle would disperse the water film. As a result, the ejected water film from the surface would have a higher volume while water film thickness increases. Due to the water film behavior, it can be concluded that particle kinetic energy plays a significant role in passing the particle through the water film. In the three noted conditions, the initial kinetic energy is constant regardless of water thickness since the particle size and initial particle velocity remain unchanged. However, Fig. 4 demonstrates the changes in particle velocity by the passage of time. In all cases, particle velocity decreased because of the transformation of kinetic energy into deformation. However, by having a water film on the substrate surface, particle velocity decreased more, meaning that a portion of particle kinetic energy is devoted to passing the particle through the water film. Also, the significant drop at around 20 ns shows the time that particle and substrate started the deformation process. Thus, as the water film thickness increased, the particle would reach the substrate surface with lower kinetic energy, leading to less particle and substrate deformation, Fig. 5 and Fig. 6.

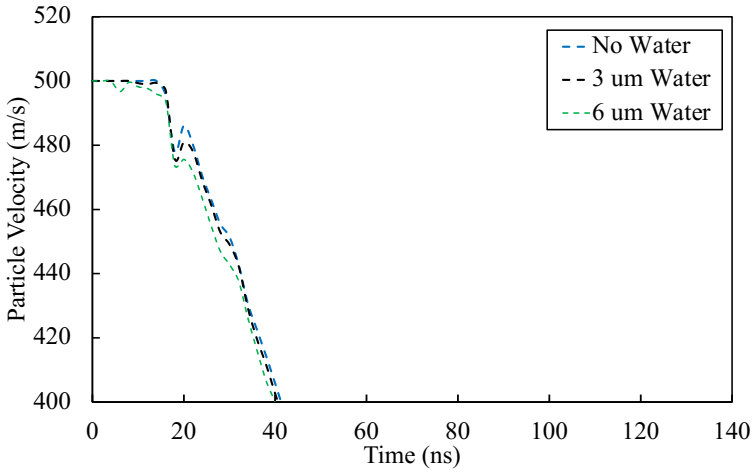

Figure 4. The changes of particle velocity by the passage of time.

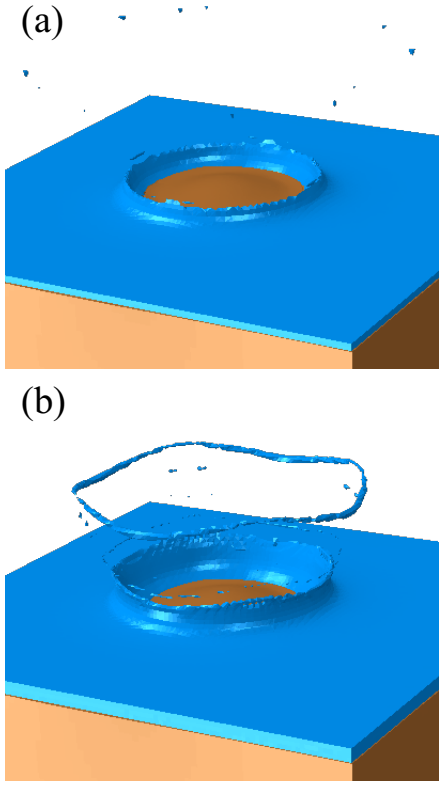

Figure 3. Water film behavior upon the impact of the copper particle by LCS while water film thickness is (a) 3 μm and (b) 6 μm.

Particle and substrate deformation have been examined to profoundly understand the water film effect. Fig. 5 shows that regardless of exiting the water film, both deposited particle and substrate deformed significantly after 120 ns of the impact. However, in Fig. 5, the water layer is cut from the pictures to focus on particle and substrate deformation. By comparing Fig. 5 (a)-(c), it can be understood that having water film and increasing its thickness can reduce the size of the deformed particle. For measuring particle deformation, flattening ratio

can be used. When particle impacts on a surface with no water file, Fig. 6(a), the flattening ratio was 0.42. By having the 3 µm and 6 µm water film covering the substrate, the flattening ratio became 0.4 and 0.38, respectively. As noted, particle impacted the substrate surface with less kinetic energy while the substrate was covered with a water film. Thus, particle deformation would be slightly decreased. On the other hand, it is necessary to investigate substrate equivalent plastic strain (PEEQ) and temperature (TEMP) changes by the passage of time to examine the water film effect on substrate deformation. Fig. 6 demonstrates that substrate plastic strain decreased around 21% while a 6 µm water film covered the substrate compared to when no water existed on the substrate surface, meaning a decrease in substrate deformation. Since having a water film covering the substrate surface decreased substrate plastic strain and substrate deformation, less heat would be produced, which means maximum substrate temperature would reduce, Fig. 6. Conclusively, this decrease in particle and substrate deformation by having a water film covering the substrate is because a portion of particle kinetic energy would be devoted to passing the particle through the water film.

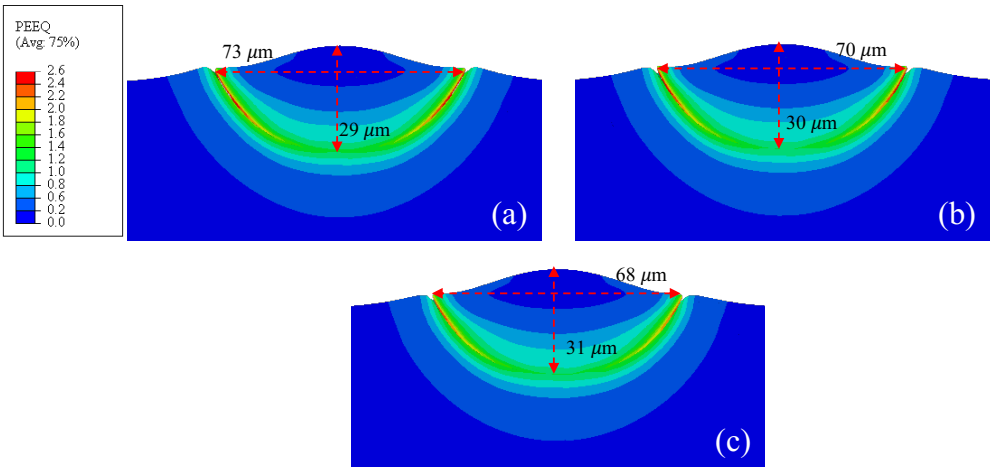

Figure 5. Examine the effect of water film covering the substrate surface on deposited copper particle deformation while the substrate is covered with (a) no water, (b) a 3 µm water film, and (c) a 6 µm water film.

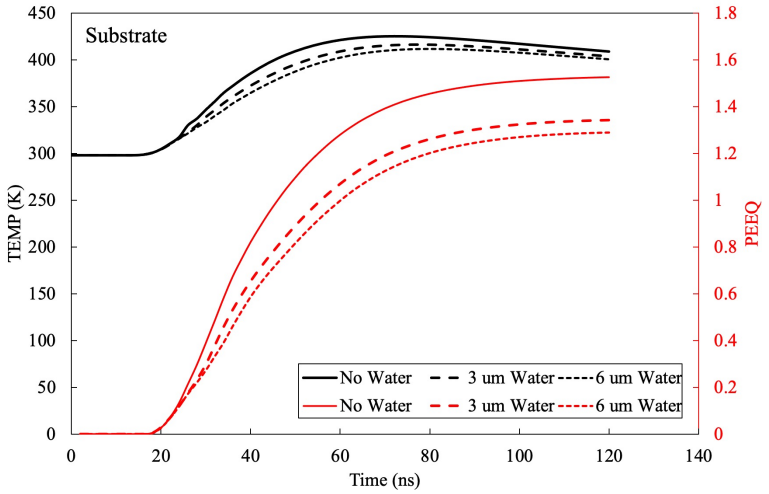

Figure 6. The effect of water film covering the substrate surface on substrate equivalent plastic strain and temperature changes by the passage of time.

A.2.4.2. Particle Velocity Effect

To overcome the negative effect of water film, this section assumes that a 50 µm copper particle is deposited using LCS on a copper substrate covered with a 6 µm water film. The temperature of the particle and substrate are 298 K. The particle velocity is assumed to change from 500 to 600 m/s. Fig. 7 illustrates that increasing particle velocity can enhance particle flattening ratio and particle penetration into the substrate. This enhancement in particle deformation can be shown by studying the particle flattening ratio of 0.42, 0.46, and 0.5 when particle velocity is 500, 550, and 600 m/s, respectively. The changes in equivalent plastic strain by the passage of time will be examined later to study substrate deformation. All these enhancements in particle deformation and reaching a higher flattening ratio than the obtained result for conventional cold spray (Fig. 6(a)) are rooted in enhancing the particle kinetic energy by increasing particle velocity upon its impact on the substrate surface. This shows that increasing particle velocity can increase particle deformation while the substrate surface is covered with a 6 µm water film.

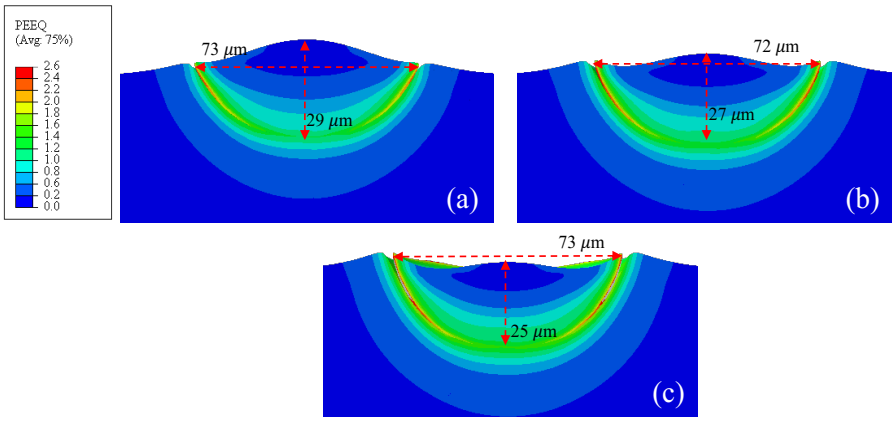

Figure 7. Examine the effect of particle velocity on deposited copper particle deformation after its impact on a copper substrate covered with a 6 µm water film while particle velocity is (a) 500 m/s, (b) 550 m/s, and (c) 600 m/s.

Then, it is necessary to investigate the particle velocity effect on substrate deformation while the copper particle is impacted on a copper substrate covered with water by studying substrate equivalent plastic strain (PEEQ) and temperature (TEMP). Fig. 8 shows that increasing particle velocity and kinetic energy can lead to a higher PEEQ value, which means the substrate has undergone more deformation. For instance, by increasing particle velocity from 500 to 600 m/s, substrate plastic strain rose from 1.2 to 1.6. Also, by having a particle velocity equal to 600 m/s, the substrate deformation becomes more comparing the substrate deformation while the copper particle is deposited using the conventional CS when no water covers the substrate surface. This shows that not only increasing particle velocity can eliminate the water film effect, but it can also increase the deformation even more than the condition with no water film. As a result of having higher deformation by increasing particle velocity, substrate temperature increased, Fig. 9. The maximum temperature is similar when particle impacts at 550 m/s compared to when the particle is deposited at the velocity of 500 m/s using conventional CS. However, by increasing particle velocity up to 600 m/s, maximum substrate temperature rises even more than when no water film covers the substrate due to a higher degree of substrate deformation. This enhancement in temperature is another proof of having higher deformation.

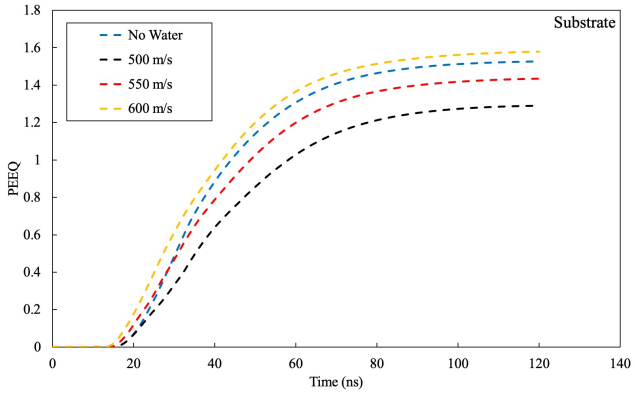

Figure 8. The effect of the particle velocity on the changes of substrate equivalent plastic strain by the passage of time while a copper particle is deposited on a copper substrate surface covered with a 6 µm water film.

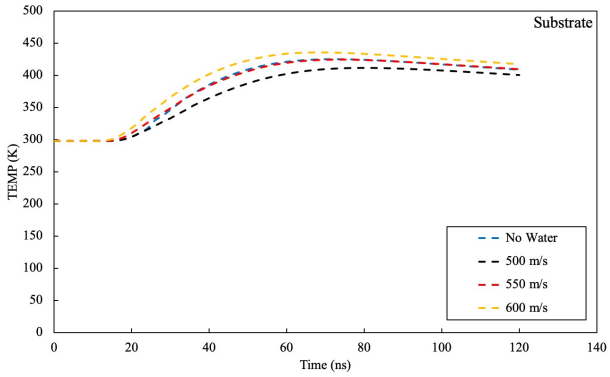

Figure 9. The effect of the particle velocity on the changes of substrate temperature by the passage of time while a copper particle is deposited on a copper substrate surface covered with a 6 µm water film.

To put it into other words, as the particle velocity increases, particle kinetic energy increases at the impact moment that the particle touches the substrate surface. As a result, both the particle and the substrate would go through a higher degree of deformation, leading to eliminating the negative effect of the existing water layer. As it can be seen in both Fig. 7 to Fig. 9, increasing particle velocity to 600 m/s can enhance particle and substrate deformation even more than the time that the copper particle is deposited using conventional CS. However, the primary missing point is the need for examining the possibility of enhancing particle velocity by using LCS experimentally.

A.2.5. Conclusion

One of the main drawbacks of conventional CS is the high level of gas consumption and the impossibility of depositing a larger particle size to increase the deposition rate. A pioneering method known as LCS has been recently developed to address the noted concerns, making it possible to deposit large metallic particles using a water jet. However, the substrate surface is covered with a water film by using LCS due to the existing water jet. Hence, this paper aims to utilize a proper modeling method for studying water film effects on particle and substrate deformation. Then, this paper investigates the potential of particle velocity on eliminating the water film effect. Finally, the main conclusions of the noted study are listed below.

1. A partial part of particle kinetic energy would be devoted to passing the particle through the water film, which leads to an impact with the less initial required energy for the deformation.
2. A 6 μm water film would decrease particle flattening ratio by around 4%, meaning a decrease in particle deformation compared to when no water covers the substrate. Also, increasing particle velocity upon the impact on a substrate covered with a 6 μm water film would increase particle flattening ratio by around 16%, meaning an increase in particle deformation.
3. By comparing the substrate deformation between the conditions with no water film and a 6 μm water film covering the substrate, it was clear that substrate plastic strain decreased around 21%, meaning a decrease in substrate deformation. However, substrate deformation increased significantly by providing more kinetic energy and increasing particle velocity.

A.2.6. Proposed future work

After examining the potential of water film on particle and substrate deformation, experimental investigation can validate the obtained results by studying single splat deformation deposited by LCS. Furthermore, in terms of simulation, an estimation of the thickness of the water film could be achieved by using a proper CFD examination. Also, to make the investigation condition closer to the experiment, consider the water layer around the deposited particle.

A.2.7. References

[1] S. Yin, P. Cavaliere, B. Aldwell, R. Jenkins, H. Liao, W. Li, R. Lupoi, Cold Spray Additive Manufacturing and Repair: Fundamentals and Applications, Additive Manufacturing, vol. 21, pp. 628-650, 2018.

[2] J. G. Legoux, E. Irissou, C. Moreau, Effect of Substrate Temperature on the Formation Mechanism of Cold-Sprayed Aluminum, Zinc and Tin Coatings, Journal of Thermal Spray Technology, vol. 16, 2007.

[3] C. Chen, Y. Xie, X. Yan, S. Yin, H. Fukanuma, R. Huang, R. Zhao, J. Wang, Z. Ren, M. Liu, H. Liao, Effect of Hot Isostatic Pressing (HIP) on Microstructure and Mechanical Properties of Ti6Al4V Alloy Fabricated by Cold Spray Additive Manufacturing, Additive Manufacturing, vol. 27, pp. 595-605, 2019.

[4] P. L. Fauchais, J. V. R. Heberlein, M. I. Boulos, "Thermal Spray Fundamentals from Powders to Parts", Springer, 1st ed., 2015.

[5] X. Yan, C. Huang, C. Chen, R. Bolot, L. Dembinski, R. Huang, W. Ma, H. Liao, M. Liu, Additive Manufacturing of WC Reinforced Maraging Steel 300 Composites by Cold Spray and Selective Laser Melting, Surface and Coating Technology, vol. 371, pp. 161-171, 2019.

[6] J. Xie, D. Nelias, H. W. Berre, K. Ogawa, Y. Ichikawa, Simulation of the Cold Spray Particle Deposition Process, Journal of Tribology, vol. 137, 2015.

[7] H. Assadi, F. Gartner, T. Stoltenhoff, H. Kreye, Bonding Mechanism in Cold Gas Spraying, Acta Materialia, vol. 51, pp. 4379-4394, 2003.

[8] T. Schmidt, F. Gartner, H. Assadi, H. Kreye, Development of a Generalized Parameter Window for Cold Spray Deposition, Acta Materialia, vol. 54, pp. 729-742, 2006.

[9] S. Rahmati, A. Ghaei, The Use of Particle/Substrate Material Models in Simulation of Cold-Gas Dynamic-Spray Process, Journal of Thermal Spray Technology, vol. 23, pp. 530-540, 2014.

[10] Dassault Systemes, 2011, ABAQUS Analysis User's Manuel, 6.11 ed., Simulia.

[11] S. Rahmati, R. G. A. Veiga, A. Zuniga, B. Jodoin, A Numerical Approach to Study the Oxide Layer Effect on Adhesion in Cold Spray, Journal of Thermal Spray Technology, 2021.

[12] H. Assadi, T. Schmidt, H. Richter, J. -O. Kliemann, K. Binder, F. Gartner, T. Klassen, H. Kreye, On Parameter Selection in Cold Spraying, Journal of Thermal Spray Technology.

Annex 3. The Effect of Water Film Surrounding the Deposited Particle on Bonding Area: A Numerical Study [6]

A.3.1 Abstract

Cold spray (CS) is a thermal spray method that deposits solid particles at high velocity at about room temperature using gases such as nitrogen or helium. Despite of CS's unique advantages, it is expensive to operate due to its high gas consumption and the need for small particle sizes for deposition. To enhance cost-effectiveness, liquid cold spray (LCS) has been developed with the capability of depositing large particles with a wider size cut by using water as a propellant. Though LCS has demonstrated success in manufacturing copper coatings, it raises questions about how wetting of particles and/or substrate surfaces can affect adhesion. This paper addresses these concerns using a finite element method based on elastic-plastic theory. Results demonstrate that wetting the deposited particle reduces both particle and substrate deformation. Water film wetting the particle primarily affects the bonding area due to its presence in the interfacial area between the particle and substrate. In order to avoid interfacial water, this paper investigates the effect of four parameters: particle velocity, particle size, water film thickness, and water temperature. The results demonstrates that the volume of interfacial water is reduced by increasing particle impact velocity and particle size and decreasing water film thickness. A rise in water temperature does not affect the amount of interfacial water; however, evaporation of interfacial water can increase.

A.3.2. Introduction

Cold spraying (CS) is a thermal spray technique that sprays solid-state particles onto surfaces using a gas propellent such as nitrogen or helium. The low temperature of CS makes it possible to manufacture coatings without oxidation or phase transformation [1-6]. When deposited particles impact substrates, both deform severely in order to produce bonding [7-9]. As a consequence of this deformation, particle and substrate temperatures increase in a ring-shaped region called the adiabatic shear instability (ASI). In ASI region, deformation of the particle and substrate will lead to failure of their oxide layer. These broken oxide pieces need to be ejected by using a jet of material, which is produced by the tensile force at the edge of the contact area. This results in two new metallic surfaces forming a metallurgical bond between the deposited particle and the substrate in ASI region [8, 10-11].

A wide range of materials have been deposited by CS, either during coating production or for repairing damaged samples [12-15]. As a result of copper's high ductility, it has received considerable attention both numerically and experimentally in the development and understanding of CS processes [16-19]. Studies have shown that porosity levels and mechanical properties of as-sprayed samples are strongly correlated with spraying parameters, which include propellant type

[6] This paper has been accepted for publication in the Journal of Thermal Spray Technology in March 2023.

[12-20]. It has recently been discovered that a new type of propellant (water) can be used to deposit large particles of a broader size cut [21-22]. This technique, which offers the possibility of being more cost-effective than CS, is known as liquid cold spray (LCS) [23]. In this spraying system, water is pressurized and heated up to 600 MPa and 400°C, respectively, before flowing through a small orifice to form a high-speed jet of water and vapor. It is intended to use this jet to accelerate copper particles for the purpose of manufacturing thick copper coatings with particle size up to 150 μm, Figure 1. The ideal purpose of LCS is to transfer all the momentum of the water jet to the large particles. Thus, the particles imping on substrate surface at very high velocities while the water jet would become a mist of vapor and water droplets. This mist of vapor and water droplets would have a stagnation flow on the substrate surface instead of bow-shock which cannot affect the particle velocity negatively [23].

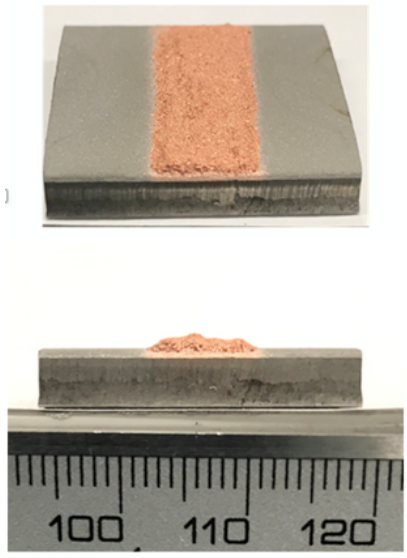

Figure 1. A sample of a copper coating deposited using LCS [23].

Even though LCS is still in the developmental stages and has succeeded in manufacturing copper coatings, some concerns have been raised about using water as propellent on particle deformation, bonding, and adhesion strength. Due to particle deformation occurring at a high strain rate, experimental studies of particle deformation and bonding formation are not feasible. Thus, numerical investigations based on elastic-plastic models have received considerable attention [19, 24].

Other fields of science have examined the impact of wet particles using both experimental and numerical methods [25-3]. However, to the author's knowledge, no literature has been published regarding the effect of water surrounding an in-flight particle on its plastic deformation. According to our previous research, the water film covering the substrate surface can have a negative effect on particle and substrate deformation. As the thickness of water on the substrate surface increases, particle and substrate deformation decrease significantly. However, it was shown that it is possible to overcome the water film effect by increasing the velocity of the deposited particles [32]. The use of CS in water-filled environments and repairing water pipelines has been studied previously [33-34]. CS coatings were deposited in both papers in water-containing environments. CS coatings

in this research have a similar structure to conventional CS coatings but have lower porosity and surface roughness [33-34].

As a continuation of our previous study [32] and to investigate the drawbacks of using water as propellent on coating build up and deposited particle deformation, in this paper investigates the effect of a water film surrounding deposited particles on its deformation and bonding. To achieve this goal, an elastic-plastic modeling has been used along with Coupled Eulerian-Lagrangian (CEL) analysis to investigate the deformation of a 50 μm wet copper particle deposited by LCS toward a dry copper substrate.

A.3.3. Numerical Methodology

A.3.3.1. Elastic and Plastic Models

To understand the finite element method, it is necessary to explain the types of models used to study the elastic and plastic sections of particle and substrate deformation. For the study of elastic and plastic sections, respectively, Mie- Gruneisen equations of state (EoS) (Eq. 1) and Johnson-Cook Model (Eq. 2) have been chosen. An in-depth description of the noted models can be found in the literature [24, 35].

$$P = \frac{\rho_0 c_0^2 \eta}{(1-s\eta)^2} \left(1 - \frac{\Gamma_0 \eta}{2}\right) + \Gamma_0 \rho_0 E_m \quad (1)$$

$$\sigma = \left(A + B\varepsilon_p^n\right)\left(1 + C ln \frac{\dot{\varepsilon}_p}{\dot{\varepsilon}_0}\right)\left(1 - \left(\frac{T - T_r}{T_m - T_r}\right)^m\right) \quad (2)$$

where, P represents total pressure, $\rho_0 c_0^2$ is the elastic modulus at small nominal strains, c_0, s, Γ_0, and ρ_0 are material constants, E_m is internal energy per unit mass, η which is nominal compressive volumetric strain equals to $1 - \rho_0/p$, and p is pressure stress. ε_p, $\dot{\varepsilon}_p$, σ, $\dot{\varepsilon}_0$, T_r, T_m, and T are equivalent plastic strain, plastic strain rate, flow stress, reference strain rate, reference temperature, melting point, and temperature, correspondingly. A, B, C, n, and m are material constants [24, 35].

A.3.3.2. Finite Element Method

The models above were solved using ABAQUS/Explicit alongside the Coupled Eulerian-Lagrangian (CEL) finite element method to study the deformation of a particle deposited using LCS. In this method, it is assumed that both the particle and substrate are Lagrangian, whereas the water film is Eulerian. Hence, a 50 μm diameter wet copper particle surrounded by a water film with the thickness of 3 μm is impacted on a dry copper substrate, Figure 2(a). It is worth noting that when particle size effect is under examination, the particle size would be 50, 60, or 70 μm. The dimension that was retained in this examination is shown in Figure 2(b). Table 1 below provides the material constants that are used to define the water and copper properties at room temperature [24, 35]. It is worth noting that ABAQUS/Explicit considered linear $U_s - U_p$ Hugoniot form of the Mie-Grüneisen equation of state as the constitutive model for considering water behavior during simulation [33, 36]. In the end, after water exits the nozzle, it would

transform to a mist of vapor water. This helps to assume that no pressure would be applied from impinging water droplets on the substrate surface.

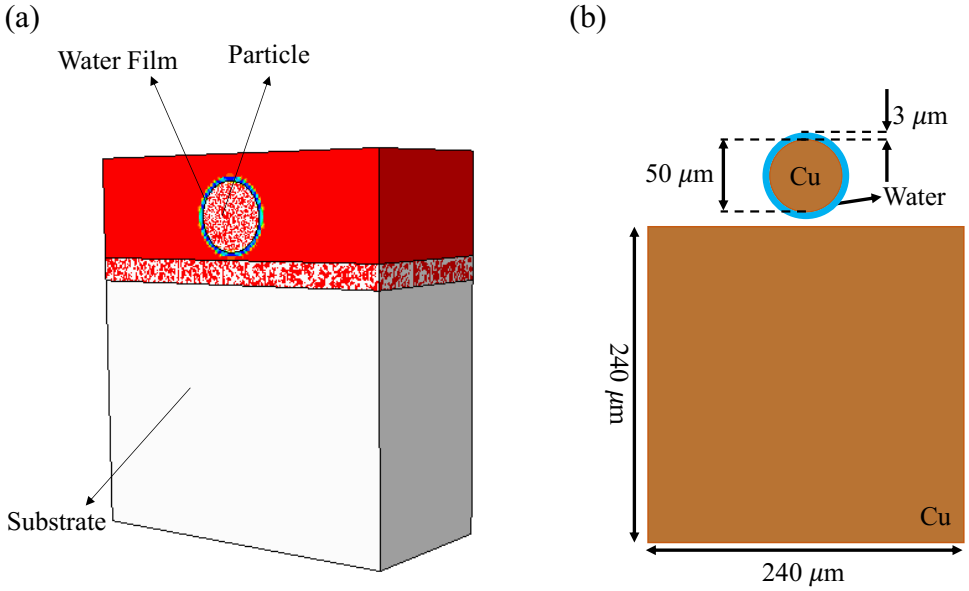

Figure 2. (a) the CEL initial conditions, (b) the dimension used of studying particle water film effect on particle deformation.

Table 1. Used material constants in the finite element analysis [24, 35, 33].

Copper		**Water**	
Property	**Value**	**Property**	**Value**
Thermal Conductivity	386 $W/m.K$	Density	958 kg/m^3
Specific Heat	383 $J/Kg.K$	Speed of Sound	1490 m/s
Density	8930 kg/m^3	Viscousity	1 mPa-s
Shear Modulus	45 GPa	Thermal Conductivity	0.598 $W/m.K$
Melting Point	1356 K	Specific Heat	4.186 $J/g.K$
Gruneisen's Constant	1.99		
Speed of Sound	3933 m/s		
Hugoniot Slope	1.5		
A	90 MPa		
B	292 MPa		
C	0.025		
m	1.09		
n	0.31		
Reference Strain Rate	1 $/s$		
Transition Temperature	298 K		

Following the design and assembly of the parts, a dynamic-explicit solver has been selected for solving the problem for a duration of 120 ns. The friction coefficient is considered to be 0.3 [35]. It is important to note that the mesh size of both the particle and water layers is 0.5 µm, which falls within an acceptable range when compared to previously reported values [20). The mesh type of Lagrangian parts is C3D8RT (an 8-node thermally-coupled brick, trilinear displacement,

temperature, reduced integration, and hourglass control) and the mesh type of the Eulerian part is EC3D8RT (An 8-node thermally coupled linear Eulerian brick, reduced integration, hourglass control).

In Table 2, the initial conditions for studying the effect of particle velocity, particle size, water film thickness, and water film temperature on particle deformation are listed. In this paper, both particle and substrate temperatures were 298 K. Since LCS has been able to produce metallic coatings using particle deformation, the impact velocities need to be higher that critical value [10]. On the other hand, it is worth noting that experimental method has been used to examine in-flight particles velocity in LCS. It has been shown that particle velocity increases with the increase in water pressure [21-22]. To be more specific, for a 180 μm and 300 μm copper particle would be as high as 880 m/s and 800 m/s when water pressure is 380 ksi [21-22]. In the experimental examination in our research facility, the velocity of water and particle velocity have been measured. The results show that the particle velocity around 500 m/s and above, based on water pressure and particle size, and it is close to the velocity of the water jet [23]. Thus, the selected values for particle velocity in this paper falls in an acceptable range. According to the critical velocity measurement (Eq. 3), selected particle velocities are greater than the value required for depositing a 50 μm copper particle using CS, Figure 3 [10]. In the end, the flattening ratio (Eq. 4) has been selected as an indicator to measure particle deformation where Δh is the difference between particle deformed height and particle initial diameter (d_o) [10, 37-38]. The temperature noted in the section on "particle water film temperature" is chosen as a way to be close to room temperature while allowing a more detailed study of how water temperature affects interfacial water volume.

$$v_{cr} = 900.\, d_0^{-0.19} \tag{3}$$

$$Flattening = \frac{\Delta h}{d_o} \tag{4}$$

Table 2. Used initial conditions to study particle water film effect on particle deformation.

Studying Parameter	Particle Velocity (m/s)	Particle Water Film Temperature (K)	Particle Water Film Thickness (μm)	Particle Size (μm)
Particle Velocity	**500**	298	3	50
	550	298	3	50
	600	298	3	50
Particle Water Film Thickness	500	298	**1**	50
	500	298	**2**	50
	500	298	**3**	50
Particle Water Film Temperature	500	**298**	3	50
	500	**303**	3	50
	500	**313**	3	50
Particle Size	500	298	3	**50**
	500	298	3	**60**
	500	298	3	**70**

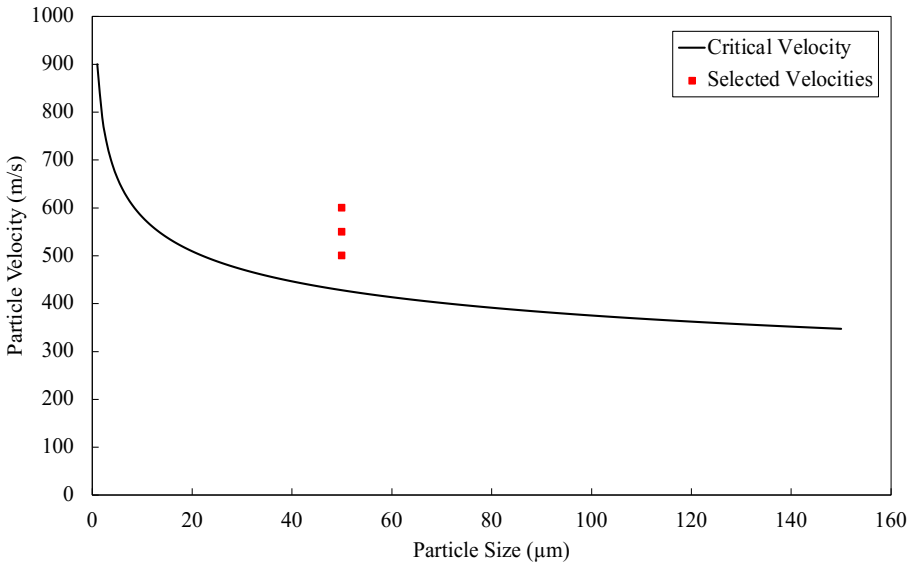

Figure 3. Critical velocity estimate for copper particles as a function of particle size.

When particles are deposited using LCS, a water film covers the substrate surface in addition to the particle water layer. This paper, however, focuses exclusively on particle water film to gain a deeper understanding of its influence on particle deformation and the bonding area.

A.3.4. Result and Discussion

A.3.4.1. The Effect of Surrounding Water on the Deformation of Particles and Substrates

Now that it is clear LCS can successfully produce copper coatings, it is necessary to examine the effect of water film wetting the particle on its deformation. To do so, first, the impact of a wet copper particle covered with a 3 μm water film at a velocity of 500 m/s on particle and substrate deformation has been investigated. The results have been compared with those of our previous study, which did not involve the presence of a water film [32]. To emphasize the deformed shape of the particle, the water has been removed from the images in Fig.4. Figure4 shows that regardless of the presence of water, the shapes of the severely deformed particle and substrate are nearly identical. Also, Fig 4 illustrates that the distribution of the equivalent plastic strain (PEEQ) is similar in both cases, but its value is higher in the circular region known as ASI.

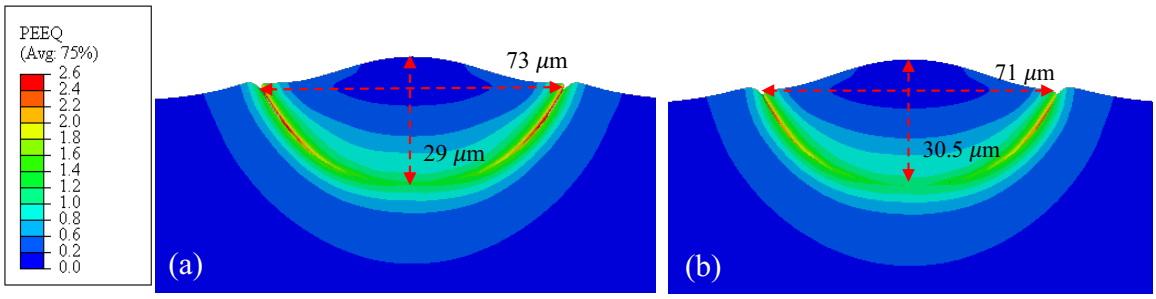

Figure 4. Particle and substrate deformed shape after 120 ns of the impact of a 50 µm wet copper particle on a dry copper substrate while (a) using CS [32] and (b) using LCS while particle is surrounded by a 3 µm water film when impact velocity is 500 m/s.

It is necessary to analyze the impact of water on particle deformation by measuring the flattening ratio and the ratio of the maximum deformed width to the initial diameter (WD) of the deposited particle, Figure 5. Figure 5 shows that having water surrounding the particle, the flattening ratio can be reduced by 4.7% and the WD can be decreased by 2.8%, meaning that the particle's width has been reduced by 2 µm. Overall, wet particles deform less than dry particles despite the same initial conditions. It is imperative that particle velocity plays a key role in enhancing the wet particle deformation in order to make it similar to the condition in which it is dry. Therefore, when impact velocity is increased from 500 m/s to 550 m/s, wet particles flatten more than dry particles impacted at 500 m/s.

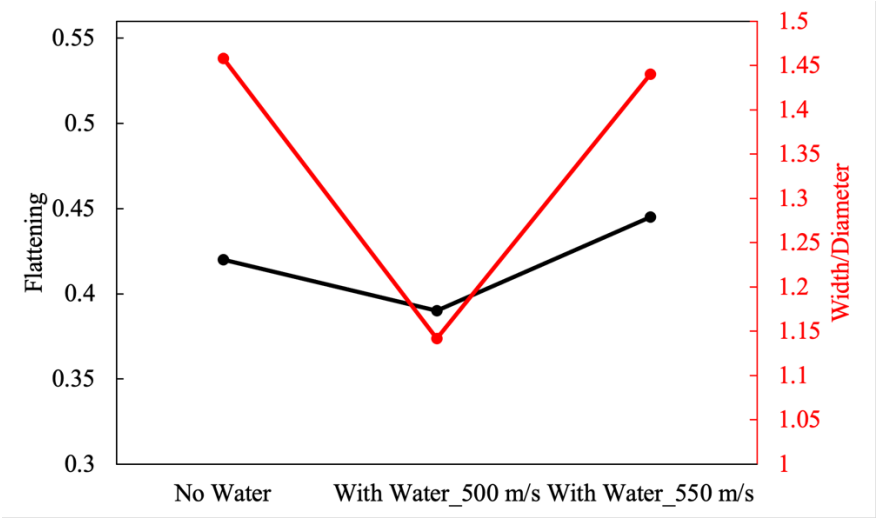

Figure 5. Studying particle deformation using flattening ratio and the ratio of particle deformed width over particle initial diameter.

As a next step, we need to determine how impacting a wet particle affects substrate deformation. As a result, the temperature and equivalent plastic strain of a specific node in ASI region have been selected, Figure 6. Results demonstrate that the deposition of a wet copper particle at 500 m/s decreased substrate equivalent plastic strain by 20.3 %, leading to a slight decrease in substrate temperature. It is worth noting that the decrease in substrate equivalent plastic strain corresponds to a decrease in substrate deformation. However, by impinging the wet particle at 550 m/s, both

substrate plastic strain and temperature become close to those when a dry particle is deposited at 500 m/s.

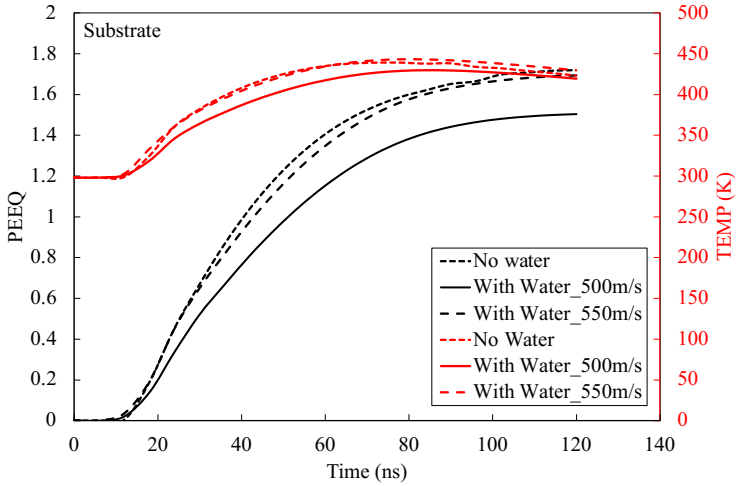

Figure 6. Studying substrate deformation using equivalent plastic strain (PEEQ) and temperature (TEMP).

There is no doubt that wet particles reduce deformation of the particle itself and. It is therefore necessary to discover what is causing this decline. Due to the fact that increasing impact velocity enhances deformation to a point similar to when a dry particle impacts a dry substrate, it is expected the change in velocity during deformation is responsible for this reduction in deformation. Thus, the impact velocity (velocity perpendicular to the substrate surface) must be studied in detail throughout the entire 120 ns of this numerical study, Figure 7. Figure 7 presents only the first 40 ns of velocity changes to enhance the focus of the study. When the particle is wet, the particle velocity is lower at around 20 ns, when the particle and substrate start their deformation. The reason for this is that a part of the particle's kinetic energy is dedicated to passing through the water.

Based on the results discussed above, a wet particle in LCS needs 50 m/s more velocity than a dry particle in CS to exhibit the same deformation. This deformation causes the oxide layer to fail, the material jet to form, and the particle to bond to the substrate. Therefore, wetting a particle or substrate with water could increase the critical velocity required for bonding between a particle and a substrate. It is, therefore, consistent with findings in the literature that the surface characteristics of the substrate and the particle can influence critical velocity [10, 11].. For a detailed understanding of the water effect on critical velocity, the oxide layer behavior needs to be analyzed, which is beyond the scope of this paper.

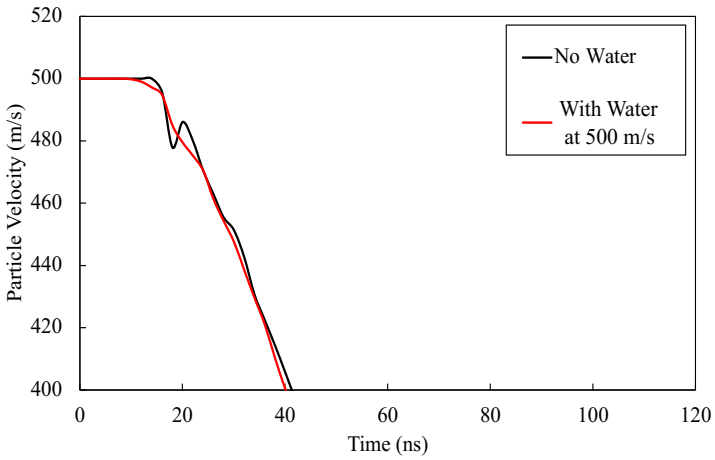

Figure 7. Studying particle velocity by the passage of time.

In the following step, it is necessary to examine the water film behaviour after 120 ns of impact, Figure 8. Figure 8 (a) showed that water film dispersed significantly. However, by examining the contact area (Figure 8 (b)), a portion of the water would remain at the interface between the particle and the substrate (red arrows), which will be referred to as "interfacial water". It has been shown in Figure 9 that interfacial water (shown by white color) is found at regions with higher plastic strain and temperature, commonly called ASI, which has the potential to bond particles to substrates. As a consequence, not only does water wetting increase critical velocity but also leads to interfacial water, which negatively affects the bonding area and adhesive strength. A numerical investigation of particle initial conditions such as impact velocity, water layer thickness, and water temperature are necessary to avoid interfacial water in the bonding area.

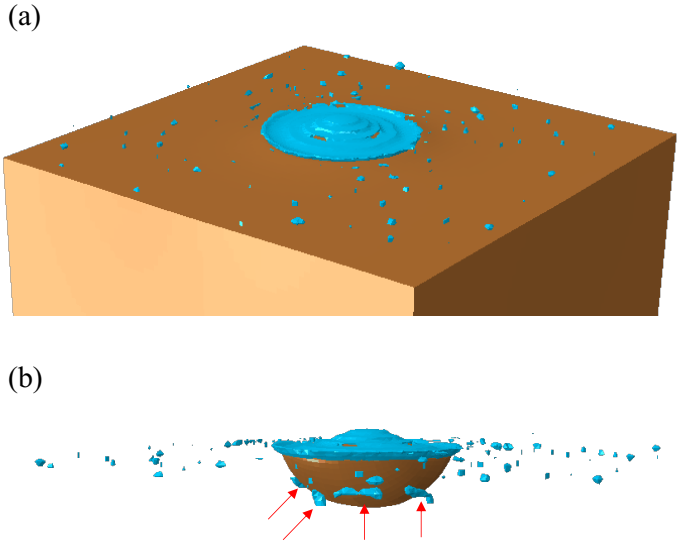

Figure 8. (a) Particle water layer behavior after 120 ns of the impact and (b) existing interfacial water at the contact area when impact velocity is 500 m/s.

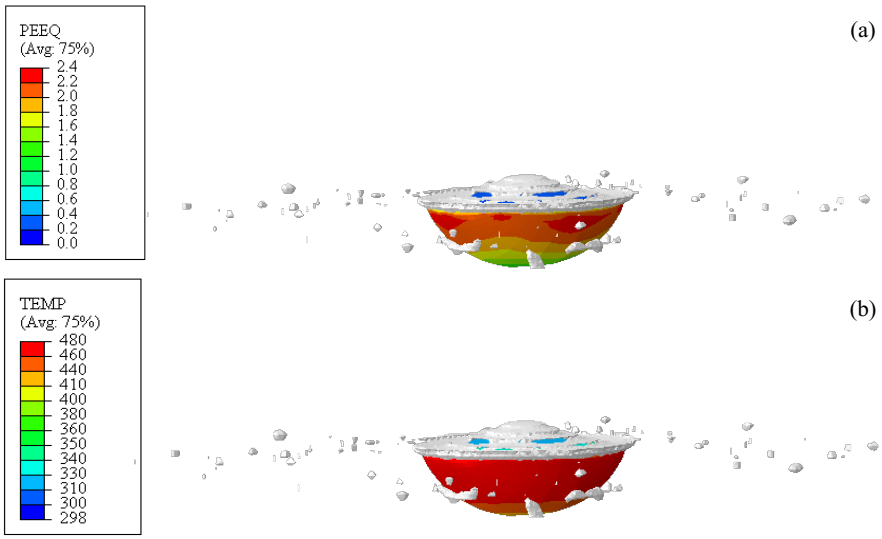

Figure 9. (a) Particle equivalent plastic strain and (b) temperature distribution after 120 ns of the impact of a 50 µm wet copper particle on a dry copper substrate at the velocity of 500 m/s using LCS.

A.3.4.2. Particle Velocity Effect

In the following section, impact velocity will be examined in more detail as the first parameter that can affect the interfacial water volume. To do so, it is assumed that a 50m copper particle is surrounded by a 3 µm water film and was deposited using LCS at three different speeds (500, 550, and 600 m/s) at 298 K. As the particle velocity is increased, the particle flattens and penetrates the substrate more readily, Figure 10. To examine the effect of water films on particle deformation, the particle flattening ratio and the ratio of deformed particle width to initial particle diameter (PWID) were selected as indicators, Figure 11. As the particle velocity was increased from 500 to 600 m/s, the flattening ratio increased by 20% and the PWID increased by 2.7%. It can be concluded from these results that increasing particle velocity enhances particle deformation by providing more kinetic energy to the particles.

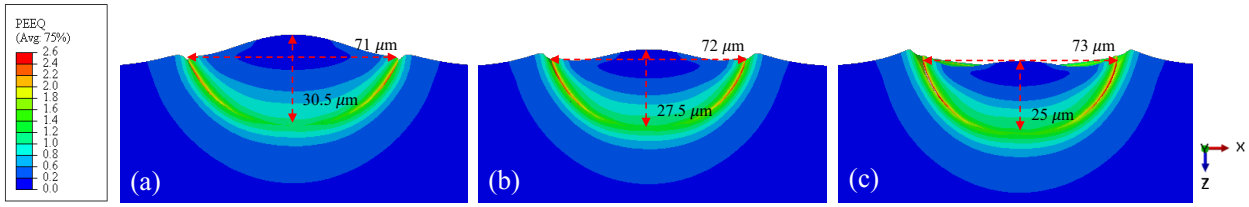

Figure 10. Particle and substrate deformed shape after 120 ns of the impact of a 50 µm wet copper particle on a dry copper substrate while particle velocity is (a) 500 m/s, (b) 550 m/s, and (c) 600 m/s.

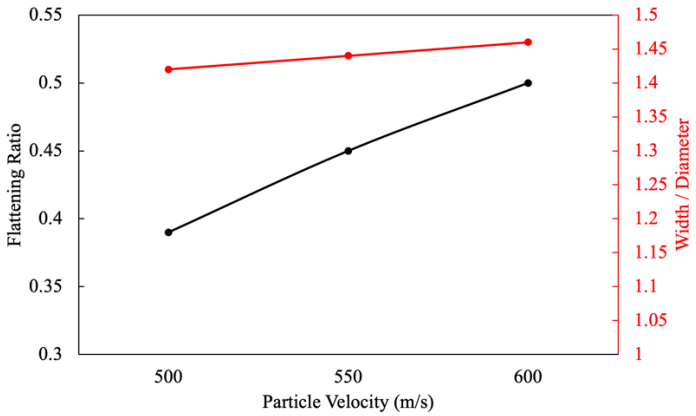

Figure 11. Studying a wet particle deformation using flattening ratio and PWID.

As the next step, the contact area was examined for the presence of interfacial water. As shown in Figure 12, increasing particle velocity does not cause interfacial water to disappear; however, it can decrease the quantity of it. To measure this decrease, the ratio of interfacial water volume to initial water film volume was calculated using the technique described in the literature [38], Figure 13. Results show that the amount of interfacial water decreased by 68% when particle velocity increased from 500 m/s to 600 m/s. The reason for this is that increasing particle velocity increases the amount of kinetic energy required to disperse the same volume of initial water film. Hence, increasing particle velocity can decrease the volume of interfacial water and enhance the bonding area. However, since it is not practicable to increase particle velocity indefinitely, it may be necessary to combine some other factors, such as water film thickness, to further decrease interfacial water volume.

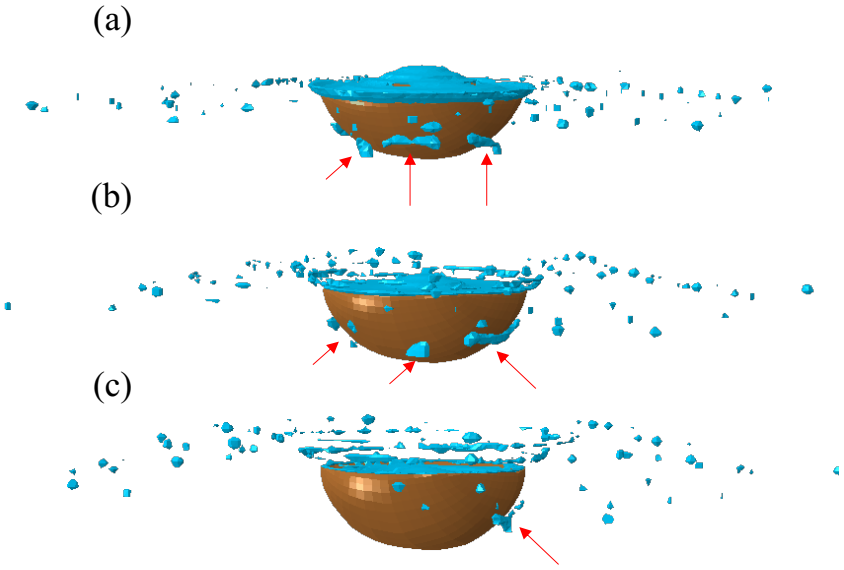

Figure 12. Studying interfacial water at the contact area while impact velocity is (a) 500 m/s, (b) 550 m/s, and (c) 600 m/s and initial water film thickness is 3 µm.

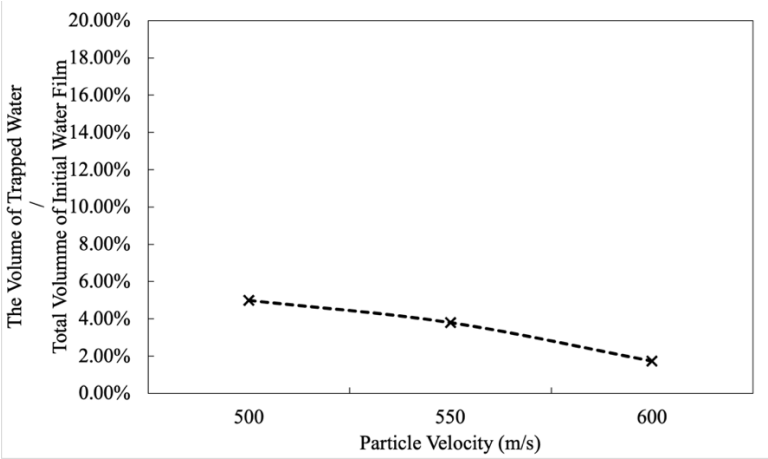

Figure 13. Studying particle velocity effect on the volume of interfacial water by examining the ratio of the volume of the interfacial water to the volume of the initial water film.

A.3.4.3. Particle Size Effect

As indicated above, increased kinetic energy from increasing impact velocity can lead to improved particle deformation as well as decrease the volume of trapped water. Kinetic energy can also be increased by particle size. This section explores the effects of particle size on the velocity of a 3 µm water impact assuming a 50, 60, or 70 µm wet particle on a 500 m/s substrate. Figure 14 illustrates how kinetic energy changes during 120 ns of impact. Due to its larger size and higher mass, 70 µm has a higher kinetic energy than other objects. The deformed shape of each particle is shown in Figure 15. As shown in Figure 15 and Figure 16, the flattening ratio shows that the 500 m/s impact velocity cannot easily deform the larger particle.

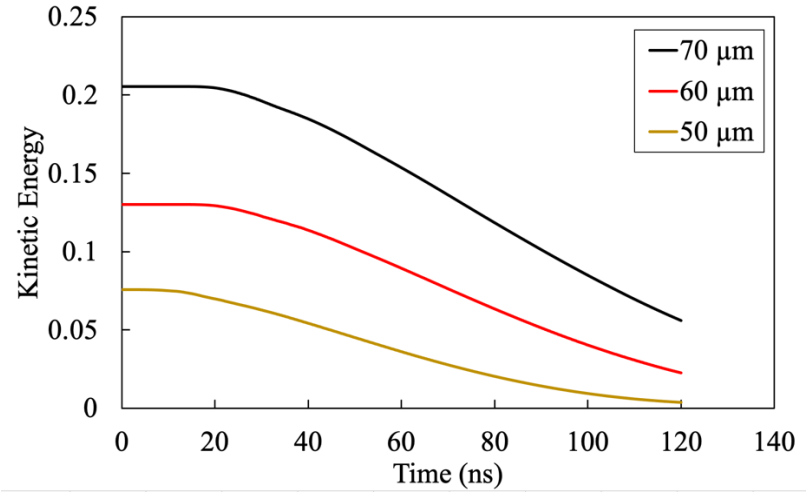

Figure 14. The effect of particle size in the changes of kinetic energy.

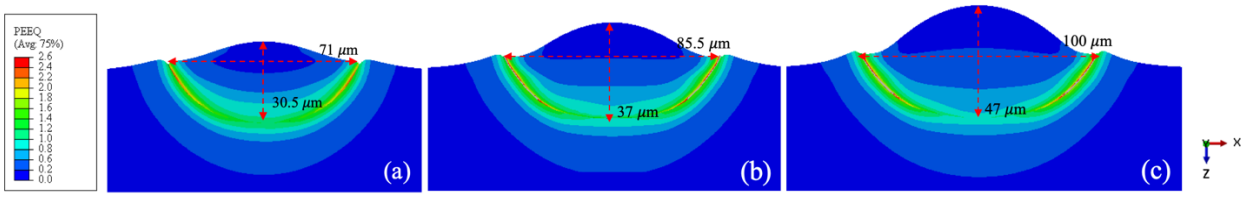

Figure 15. Particle and substrate deformed shape after 120 ns of the impact of a (a) 50 µm (b) 60 µm, and (c) 70 µm wet copper particle on a dry copper substrate while particle velocity is 500 m/s.

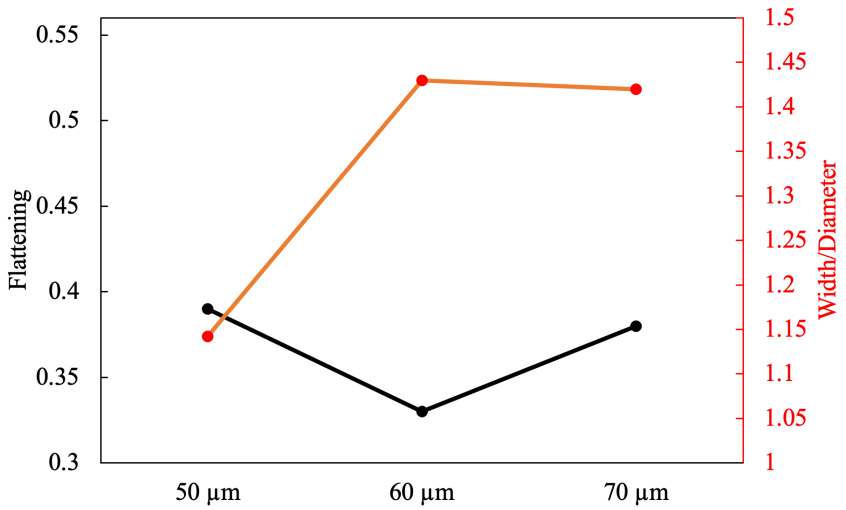

Figure 16. Studying a wet particle deformation using flattening ratio and PWID.

Following this, it is necessary to examine the effect of particle size on the volume of interfacial water, Figure 17. The results show that interfacial water exists regardless of particle size. However, increasing the size of deposited particle from 50 m to 70 m would decrease the proportion of interfacial water volume to the volume of the initial water layer by approximately 30%, Figure 18. Thus, larger particles combined with higher impact velocity can decrease the interfacial water volume. Afterward, it is necessary to examine the effect of water layer characteristics, such as thickness and temperature, on the volume of interfacial water.

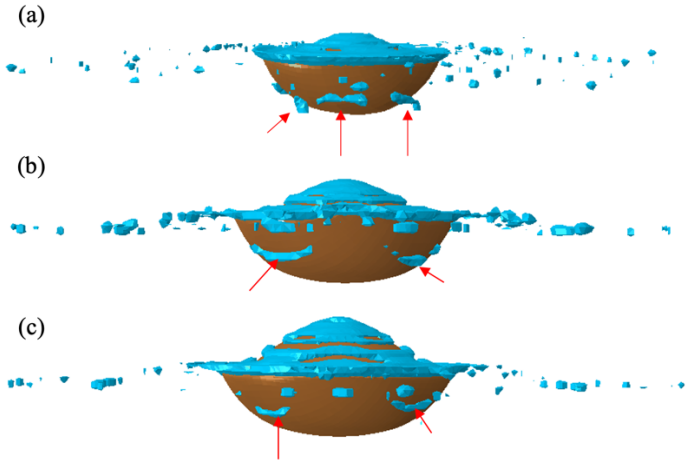

Figure 17. Studying interfacial water at the contact area while impact velocity is 500 m/s initial water film thickness is 3 µm and particle size is (a) 50 µm (b) 60 µm, and (c) 70 µm.

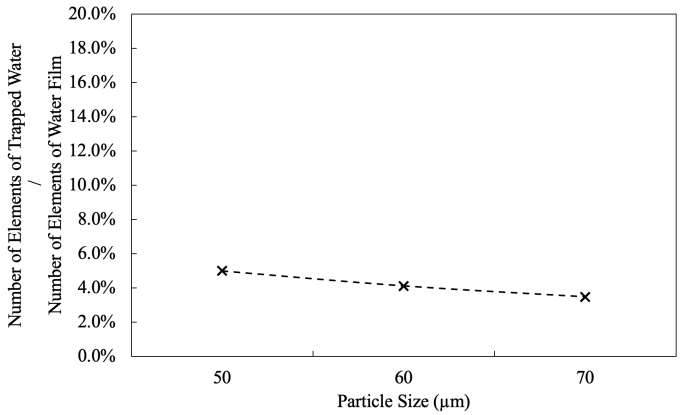

Figure 18. Studying particle size effect on the volume of interfacial water by examining the ratio of the volume of the interfacial water to the volume of the initial water film.

A.3.4.5. Particle Water Film Thickness Effect

To investigate the effect of water film thickness on the interfacial water volume, it is assumed that a 50 µm copper particle surrounded with a water film with the thickness of 1, 2, or 3 µm is deposited at a velocity of 500 m/s. When the water thickness was increased from 1 µm to 3 µm, the deformed shape of the particles remained almost identical with a decreased of 7.1% in the flattening ratio, Figures 19 and 20. This is based on the drop in particle velocity at 20 ns after impact when the particle begins to deform severely is more when the water thickness is 3 µm, Figure 21. This is because the same kinetic energy is used to disperse more water volume. Conclusively, increasing water film thickness reduces particle kinetic energy and, as a result, reduces particle deformation.

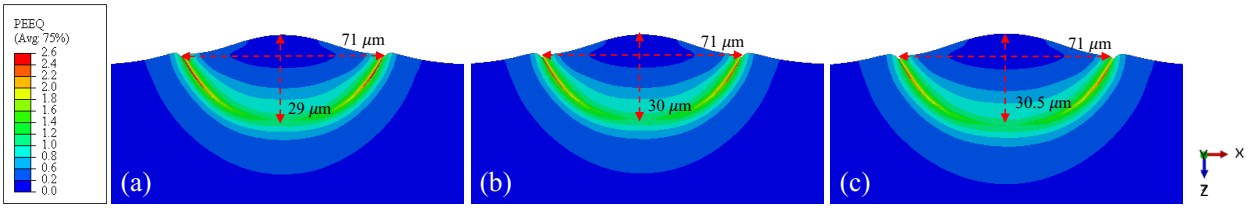

Figure 19. Particle and substrate deformed shape after 120 ns of the impact of a 50 µm wet copper particle on a dry copper substrate while water film thickness is (a) 1 (b) 2, and (c) 3 µm.

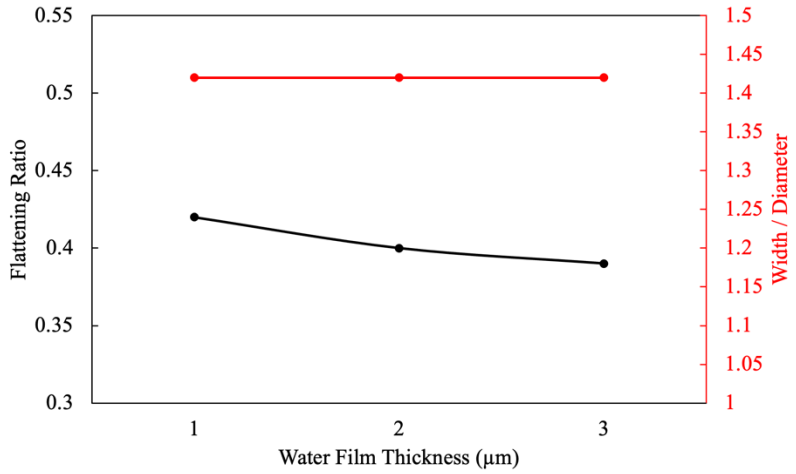

Figure 20. Studying particle deformation using flattening ratio and PWID.

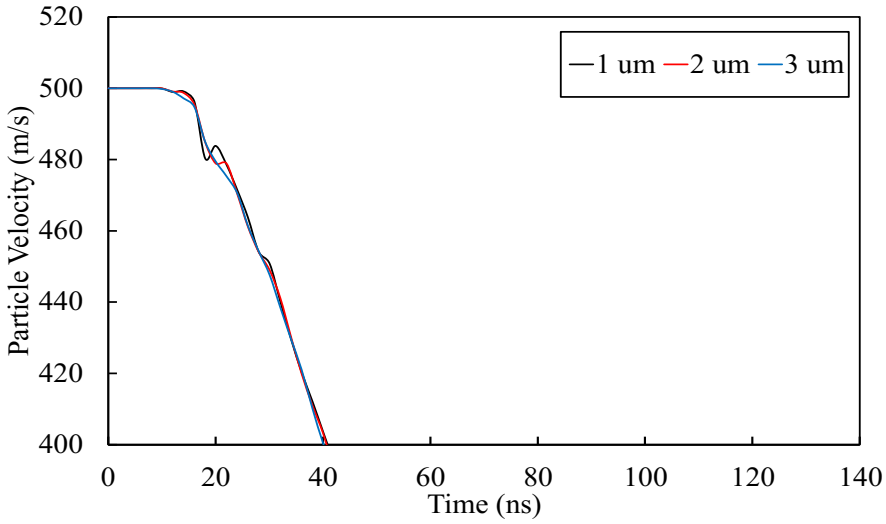

Figure 21. Studying particle velocity by the passage of time.

It was understood that particle deformation plays an important role in the volume of interfacial water. Since increasing water thickness decreases particle deformation, it is necessary to examine the contract area to determine if a thinner water layer resulted in interfacial water. Figure 22

illustrates that regardless of the initial thickness of the water film, interfacial water exists (red arrows). However, by increasing the initial thickness of the water film, the amount of interfacial water appeared to increase. Furthermore, the ratio of interfacial water volume to initial water volume was estimated using the method described in the literature [3], Figure 23. Based on the results, this ratio increased by 22.5% when the thickness of the water film was increased from 1 µm to 3 µm. As explained above, increasing water film thickness results in decreasing particle velocity and kinetic energy upon impact and increase interfacial water volume. Hence, to solve the problem of interfacial water, it is possible to consider decreasing a water film thickness as a factor that could be associated with increasing particle velocity.

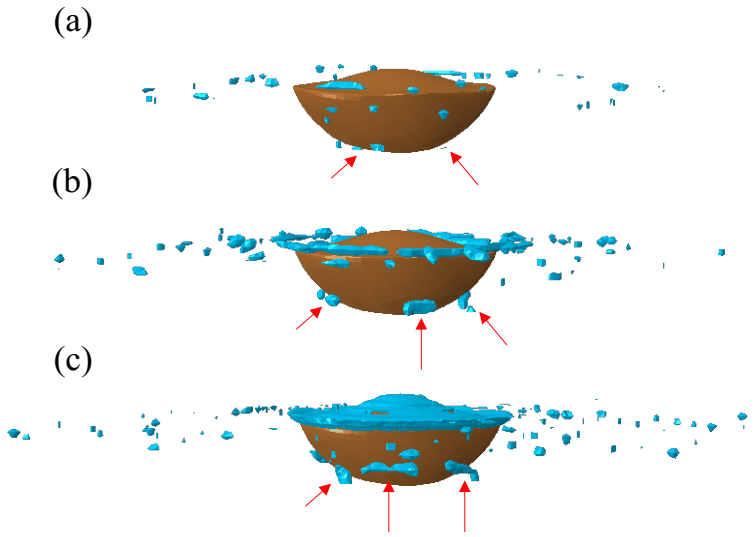

Figure 22. Studying interfacial water at the contact area while water film thickness is (a) 1 (b) 2, and (c) 3 µm and impact velocity is 500 m/s.

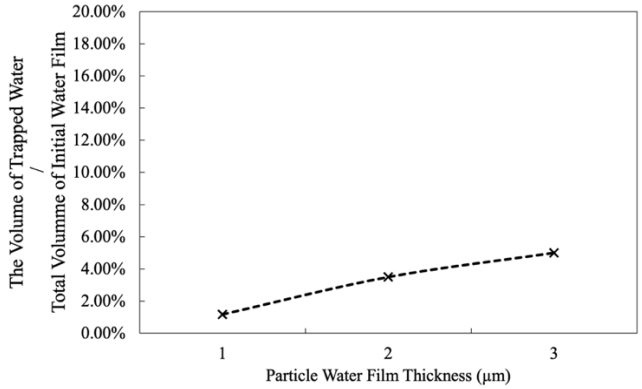

Figure 23. Studying particle water film thickness effect on the volume of interfacial water by examining the ratio of the volume of the interfacial water to the volume of the initial water film.

A.3.4.4. Water Film Temperature Effect

The final parameter that might affect the volume of interfacial water is water temperature. For studying its effect, a 3 µm particle water film temperature effect on interfacial water was studied in this section while particle and substrate temperatures were 298 K, particle velocity was 500 m/s, and water film temperatures were 298, 303, or 313 K. This slight increase in water temperature was chosen for a more detailed examination of its effect. According to the results, increasing the temperature of the water film does not affect particle deformed shape, Figure 24. According to Figure 25 and Figure 26 approximately 5% of the initial water film would be trapped in the contact area regardless of the water film's initial temperature. Therefore, an increase in the temperature of the water film has no effect on the ratio between the interfacial water volume and the initial water volume, Figure 26. Accordingly, the water film's initial temperature does not affect the bonding area by decreasing the volume of the interfacial water under the mentioned initial conditions. However, increasing water film temperature might lead more interfacial water to be evaporated and provide more area for the bonding. Hence, it is necessary to examine water temperature after 120 ns of the impact.

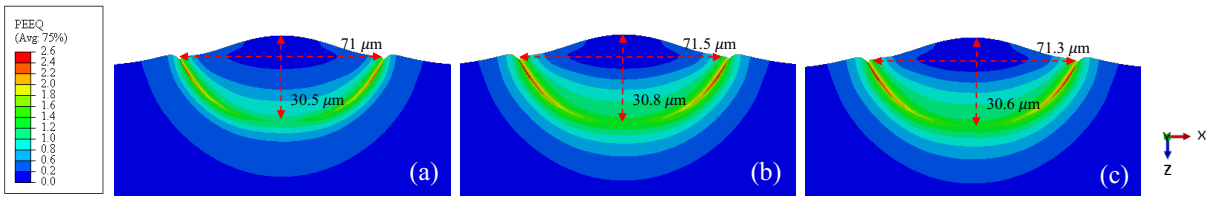

Figure 24. Particle and substrate deformed shape after 120 ns of the impact of a 50 µm wet copper particle on a dry copper substrate while water film temperature is (a) 298, (b) 303, and (c) 313 K.

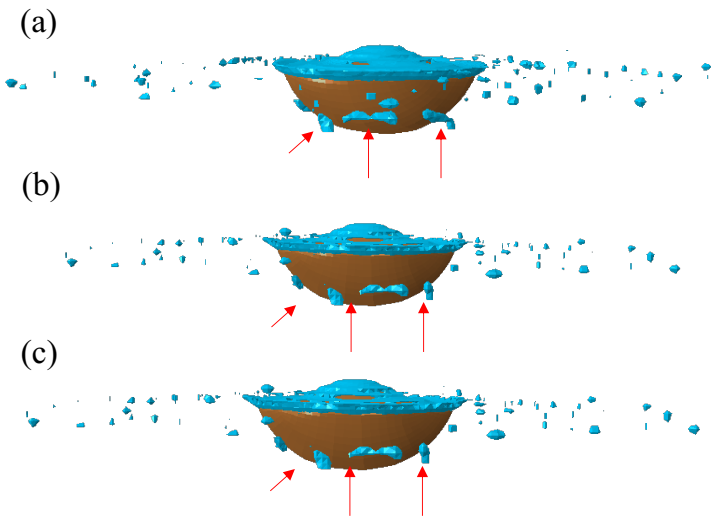

Figure 25. Studying interfacial water at the contact area while water film temperature is (a) 298, (b) 303, and (c) 313 K and impact velocity is 500 m/s.

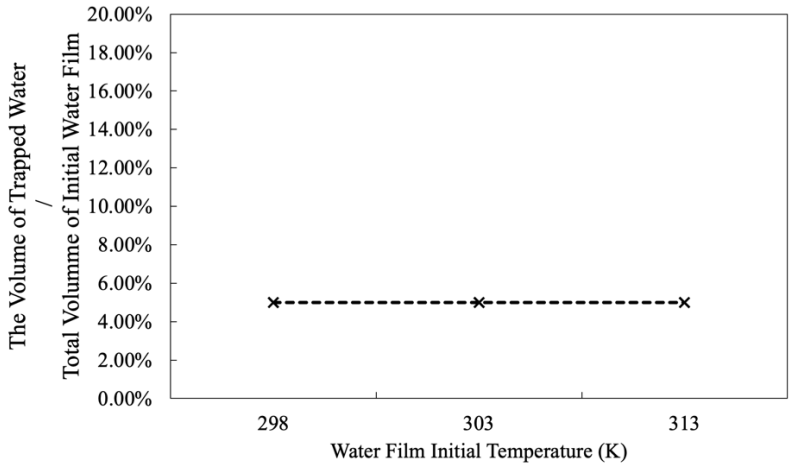

Figure 26. Studying particle water film temperature effect on the volume of interfacial water by examining the ratio of the volume of the interfacial water to the volume of the initial water film.

As shown in Figure 27, after 120 ns of the impact, the temperature of the interfacial water increased, especially in the contact area. A portion of the interfacial water reached a temperature above 373 K, indicating that some of it may be evaporating. It is worth noting that in Figure 27, the particle is shown with white color to produce better contrast whiles studying the temperature of particle water layer. As shown in Figure 28, increasing the water film initial temperature from 298 to 313 K significantly increased the ratio of evaporated water volume to interfacial water volume by 90 %. Without the use of a proper numerical analysis based on CFD, it is not possible to examine evaporated water behavior in greater detail. Therefore, if the evaporated water was able to escape the contact area, increasing the temperature of the water film would be considered as an additional factor contributing to a decrease in the amount of water present at the interface.

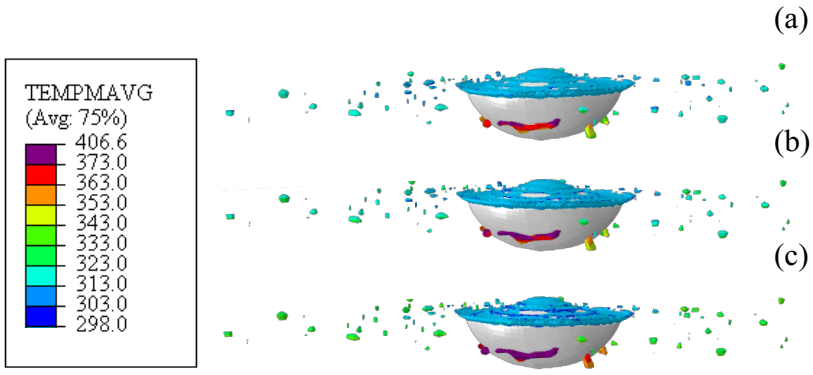

Figure 27. Studying evaporated interfacial water (shown by purple color) while water film initial temperature is (a) 298, (b) 303, and (c) 313 K and impact velocity is 500 m/s.

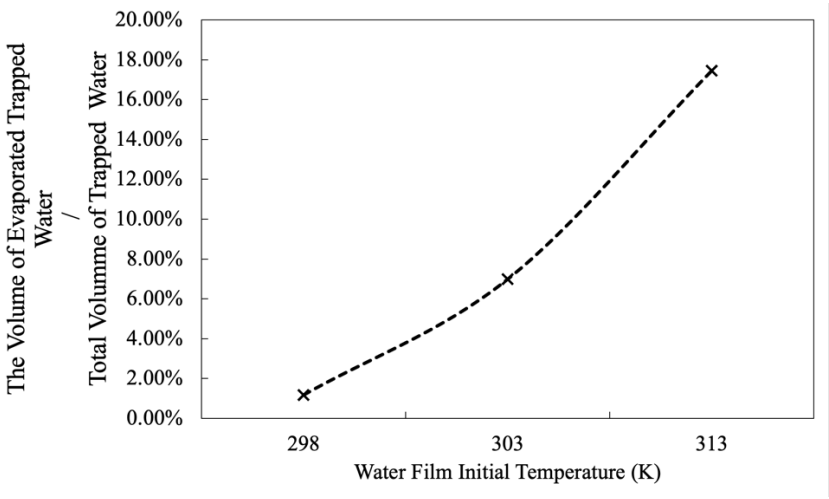

Figure 28. Studying the ratio of evaporated interfacial water volume to total interfacial water volume.

A.3.5. Conclusion

To overcome the problems inherent in CS, such as the high gas consumption and the need of using small particle size for deposition, and reduce the cost of operation, LCS has been developed using water as the propellant. The use of water would result in wetting the deposited particle and forming a water film on the surface of the substrate. Since substrate and particle surface affects critical velocity [10-11, 39], wetting them might affect particle deformation, bonding formation, and coating buildup. In this paper, as a continue of our previous work [32], we only investigate the effects of wetting the deposited particle with a water film on the bonding area using an elastic-plastic numerical analysis.

The presence of a water film not only negatively affects particle and substrate deformation, but also increases the critical velocity needed for bonding to occur. Additionally, interfacial water caused by the impact of a wet particle negatively affected bonding areas between the particle and substrate. These two main outcomes illustrate that LCS can negatively affect the bonding of the particle to the substrate. To overcome this problem, the effect of some possible changes that can apply experimentally was examined numerically in this paper. First, increasing particle velocity and size were shown to decrease interfacial water volume. When the water film thickness is increased, the amount of interfacial water is also increased. Interfacial water does not change in volume when the water film temperature is increased; however, the amount of interfacial evaporated water increases. All attempts show that it is possible to decrease the amount of interfacial water; however, it is not possible to completely avoid it. On the other hand, due to the limitations of ABAQUS/Explicit, it was unclear whether evaporated water escaped the contact area. Consequently, a thinner, elevated temperature water film would be preferred to wet the deposited particle at a higher velocity to enhance the bonding area for a solid particle deposited using LCS.

A.3.6. Future Work

Beside the ongoing experimental work for developing LCS, for a better understanding of the effects of using water as a propellant on particle deformation and coating build up, it would be necessary to develop an accurate CFD model to study in-flight particle characteristics, flow field, and predict the exact thickness of the water film around the particle and on the substrate surface. In addition, a CFD simulation is required to capture the behavior of evaporated interfacial water in the contact area and the pressure of the jet during deposition and on the substrate surface. Additionally, it is important to investigate the effect of interfacial water on bonding by examining the oxide layer failure of both wet particle and wet substrate.

A.3.7. Acknowledgment

The authors would like to express their gratitude to Polycontrols (Brossard, QC, Canada) for their financial support in this project.

A.3.8. References

[1] X. Yan, C. Huang, C. Chen, R. Bolot, L. Dembinski, R. Huang, W. Ma, H. Liao, M. Liu, Additive Manufacturing of WC Reinforced Maraging Steel 300 Composites by Cold Spray and Selective Laser Melting, *Surface and Coating Technology*, 2019, 371, p 161-171.

[2] F. Khodabakhshi, B. Marzbanrad, H. Jahed, A. P. Gerlich, Interfacial Bonding Mechanisms between Aluminum and Titanium during Cold Gas Spraying Followed by Friction-Stir Modification, *Applied Surface Science*, 2018, 462, p 739-752.

[3] D. Goldbaum, J. M. Shockley, R. R. Chromik, A. Rezaeian, S. Yue, J. Legoux, E. Irissou, The Effect of Deposition Conditions on Adhesion Strength of Ti and Ti6Al4V Cold Spray Splats, *Journal of Thermal Spray Technology*, 2012, 21.

[4] S. Bagherifard, S. Monti, M. V. Zuccoli, M. Riccio, J. Kondas, M. Guagliano, “Cold Spray Deposition for Additive Manufacturing of Freeform Structural Components Compared to Selective Laser Melting”, *Material Science and Engineering A*, 2018, 721, p 339-350.

[5] C. Chen, Y. Xie, X. Yan, S. Yin, H. Fukanuma, R. Huang, R. Zhao, J. Wang, Z. Ren, M. Liu, H. Liao, Effect of Hot Isostatic Pressing (HIP) on Microstructure and Mechanical Properties of Ti6Al4V Alloy Fabricated by Cold Spray Additive Manufacturing, *Additive Manufacturing*, 2019, 27, p 595-605.

[6] P. L. Fauchais, J. V. R. Heberlein, M. I. Boulos, "Thermal Spray Fundamentals from Powders to Parts", Springer, 1st ed., 2015.

[7] S. Rahmati, B. Jodoin, Physically Based Finite Element Modeling Method to Predict Metallic Bonding in Cold Spray, *Journal of Thermal Spray Technology*, 2020, 29, p 611-629.

[8] Y. Xie, S. Yin, C. Chen, M. Planche, H. Liao, R. Lupoi, New Insights into the Coating/Substrate Interfacial Bonding Mechanism in Cold Spray, *Scripta Materialia*, 2016, 125, p 1-4.

[9] W. Li, H. Liao, C. Li, H. Bang, C. Coddet, Numerical Simulation of Deformation Behavior of Al Particles Impacting on Al Substrate and Effect of Substrate Oxide Films on Interfacial Bonding in Cold Spraying, *Applied Surface Science*, 2007, 253, p 5084-5091.

[10] T. Schmidt, F. Gartner, H. Assadi, H. Kreye, Development of a Generalized Parameter Window for Cold Spray Deposition, *Acta Materialia*, 2006, 54, Pages 729-742.

[11] M. Hassani-Gangaraj, D. Veysset, V. K. Champagne, K. A. Nelson, C. A. Schuh, Adiabatic Shear Instability is not Necessary for Adhesion in Cold Spray, *Acta Materialia*, 2018, 158, p 430-439.

[12] C. J. Huang, H.J. Wu, Y. C. Xie, W. Y. Li, C. Verdy, M. P. Planche, H. J. Liao, G. Montavon, Advanced Brass-Based Composites via Cold-Spray Additive-Manufacturing and its Potential in Component Repairing, *Surface and Coating Technology*, 2019, 371, p 211-223.

[13] S. Yin, P. Cavaliere, B. Aldwell, R. Jenkins, H. Liao, W. Li, R. Lupoi, Cold Spray Additive Manufacturing and Repair: Fundamentals and Applications, *Additive Manufacturing*, 2018, 21, p 628-650.

[14] A. Sova, S. Grigoriev, A. Okunkova, I. Smurov, Potential of Cold Gas Dynamic Spray as Additive Manufacturing Technology, *The International Journal of Advanced Manufacturing Technology*, 2013, 69, p 2269-2278.

[15] N. H. Tariq, L. Gyansah, J. Q. Wang, X. Qiu, B. Feng, M. T. Siddique, T. Y. Xiong, Cold Spray Additive Manufacturing: A Viable Strategy to Fabricate Thick B4C/Al Composite Coating for Neutron Shielding Application, *Surface & Coating Technology*, 2018, 339, p 224-236.

[16] J. Xie, "Simulation of cold spray particle deposition process", Thèse, Le Grade de Docteur, L'institut national des sciences appliquées de Lyon, 2014.

[17] R. Chakrabarty, J. Song, Crystal Plasticity Finite Element Investigation of Deformation of Single Crystal Copper During Cold Spay, *Additive Manufacturing*, 2022, 49.

[18] Y. Kim, K. Lee, Effect of Carrier Gas Species on the Microstructure and Compressive Deformation Behaviors of Ultra-Strong Pure Copper Manufactured by Cold Spray Additive Manufacturing, *Journal of Materials Science & Technology*, 2022, 97, p. 264-271.

[19] C. Chen, Y. Xie, X. Yan, S. Yin, H. Fukanuma, R. Huang, R. Zhao, J. Wang, Z. Ren, M. Liu, H. Liao, Effect of Hot Isostatic Pressing (HIP) on Microstructure and Mechanical Properties of Ti6Al4V Alloy Fabricated by Cold Spray Additive Manufacturing, *Additive Manufacturing*, 2019, 27, p 595-605.

[20] S. Rahmati, R. G. A. Veiga, A. Zuniga, B. Jodoin, A Numerical Approach to Study the Oxide Layer Effect on Adhesion in Cold Spray, *Journal of Thermal Spray Technology*, 2021.

[21] T. Butler, Liquid Accelerated Cold Spray, Cold Spray Action Team (CSAT), May 2011.

[22] T. Butler, Liquid Accelerated Cold Spray, Cold Spray Action Team (CSAT), October 2012.

[23] A. Akbarnozari, S. Garmeh, F. Ben Attouil, A. Dolatabadi, S. Desaulniers, L. Pouliot, C. Moreau, Recent Advance in Liquid Cold Spray (LCS), North American Cold Spray Conference 2022, New Orleans.

[24] S. Rahmati, A. Ghaei, The Use of Particle/Substrate Material Models in Simulation of Cold-Gas Dynamic-Spray Process, *Journal of Thermal Spray Technology*, 2014, 23, p 530-540.

[25] B. Buck, Y. Tang, N. G. Deen, J. A. M. Kuipers, S. Heinrich, Dynamics of Wet Particle-Wall Collisions: Influence of Wetting Condition, *Chemical Engineering Research and Design*, 2018, 135, p 21-29.

[26] L. Zhang, C. Wu, Discrete Element Analysis of Normal Elastic Impact of Wet Particles, *Powder Technology*, 2020, 362, p 628-634.

[27] D. Wu, P. Zhou, G. Wang, T. Howes, W. Chen, A Theoretical Study of Particle Coalescence Criteria for Inelastic Collision of Wet Particles, *Chemical Engineering Science*, 2021, 243, p 116770.

[28] T. Kondo, K. Ando, Simulation of High-Speed Droplet Impact Against a Dry/Wet Rigid Wall for Understanding the Mechanism of Liquid Jet Cleaning, *Physics of Fluids*, 2019, 31.

[29] B. Buck, Y. Tang, S. Heinrich, N. G. Deen, J. A. M. Kuipers, Collision Dynamics of Wet Solids: Rebound and Rotation, *Powder Technology*, 2017, 316, p 218-224.

[30] C. Henry, J. Minier, Progress in Particle Resuspension from Rough Surfaces by Turbulent Flows, *Progress in Energy and Combustion Science*, 2014, 45, p 1-53.

[31] B. Buck, J. Lunewski, Y. Tang, N. G. Deen, J. A. M. Kuipers, S. Heinrich, Numerical Investigatoin of Collision Dynamics of Wet Particles via Force balance, *Chemical Engineering Research and Design*, 2018, 132, p 1143-1159.

[32] P. Khamsepour, A. Akbarnozari, S. Garmeh, C. Moreau, A. Dolatabadi, The Effect of Water Layer Covering Substrate Surface on the Deformation of the Impacting Particle Deposited by Liquid Cold Spray, Canadian Society for Mechanical Engineering International Congress 2022, Alberta, Canada.

[33] Y. Liu, C.X. Li, X.F. Huang, K. Ma, X.T. Luo, and C.J. Li, Effect of Water Environment on Particle Deposition of Underwater Cold Spray, *Applied Surface Science,* 2020, 506, 144542.

[34] Y. Meng, H. Saito, C. Bernard, Y. Ichikawa, K. Ogawa, Parametric Study to Repair Leaks in Water Pipe Using the Low-Pressure Cold Spray Technique, *Journal of Thermal Spray Technology*, 2022, 31, p 2560–2576.

[35] J. Xie, D. Nelias, H. W. Berre, K. Ogawa, Y. Ichikawa, Simulation of the Cold Spray Particle Deposition Process, *Journal of Tribology*, 2015, 137.

[36] Dassault Systemes, 2011, ABAQUS Analysis User's Manuel, 6.9 ed., Simulia.

[37] OC. Oxdemir, JM. Conahan, S. Muftu, Particle Velocimetry, CFD, and the Role of Particle Sphericity in Cold Spray, *Coatings*, 2020, 10.

[38] P. Khamsepour, C. Moreau, A. Dolatabadi, Numerical Simulation of the Effect of Particle and Substrate Pre-Heating on Porosity Level and Residual Stress of As-Sprayed Ti6Al4V Components, *Journal of Thermal Spray Technology*, 2021.

[39] H. Assadi, T. Schmidt, H. Richter, J. -O. Kliemann, K. Binder, F. Gärtner, T. Klassen, H. Kreye, On Parameter Selection in Cold Spraying, *Journal of Thermal Spray Technology*, 2011, 20, p 1161-1176.